Obliquities of stars from the study of transiting exoplanets and eclipsing binaries

by

Vedad Kunovac Hodžić



UNIVERSITY OF BIRMINGHAM

A thesis submitted for the degree of
Doctor of Philosophy

Solar and Stellar Physics Group
School of Physics and Astronomy
College of Engineering and Physical Sciences
University of Birmingham
October 2021

UNIVERSITY OF BIRMINGHAM

University of Birmingham Research Archive
e-theses repository



This unpublished thesis/dissertation is under a Creative Commons Attribution 4.0 International (CC BY 4.0) licence.

You are free to:

Share — copy and redistribute the material in any medium or format

Adapt — remix, transform, and build upon the material for any purpose, even commercially.

The licensor cannot revoke these freedoms as long as you follow the license terms.

Under the following terms:



Attribution — You must give appropriate credit, provide a link to the license, and indicate if changes were made. You may do so in any reasonable manner, but not in any way that suggests the licensor endorses you or your use.

No additional restrictions — You may not apply legal terms or technological measures that legally restrict others from doing anything the license permits.

Notices:

You do not have to comply with the license for elements of the material in the public domain or where your use is permitted by an applicable exception or limitation.

No warranties are given. The license may not give you all of the permissions necessary for your intended use. For example, other rights such as publicity, privacy, or moral rights may limit how you use the material.

Unless otherwise stated, any material in this thesis/dissertation that is cited to a third-party source is not included in the terms of this licence. Please refer to the original source(s) for licencing conditions of any quotes, images or other material cited to a third party.

Abstract

Obliquities of stars from the study of transiting exoplanets and eclipsing binaries

Vedad Kunovac Hodžić

In this thesis I study stellar obliquities across a range of companion masses, and in new regimes, that aims at constraining theories of planet formation and evolution. I begin in Chapter 1 with an introduction to the state of the field of extrasolar planets, key discoveries that have motivated previous studies on the misalignments between planetary orbits and stellar spins, and highlight the gaps in our knowledge where this thesis aims to make an impact. In Chapter 2, I outline the models and tools that underpin the analysis of transit light curves and high-resolution spectra in subsequent chapters. In Chapter 3, I apply these tools to the discovery of binary systems of various mass ratios. Two such systems are rare brown dwarfs whose discoveries help calibrate models of sub-stellar evolution, and the connection to giant planet formation and evolution. In Chapters 4–6, I present new measurements of stellar obliquities across a range of companion masses. In Chapter 4 I consider two systems hosting small planets. I demonstrate a misalignment the stellar spin and the orbit of a planet twice the size of Earth. This discovery is consistent with some disc-free migration scenarios, and provides the first observational evidence of its kind that super-Earths may form far from their star. In Chapter 5, I consider a sample of 13 giant planets orbiting cool stars in weak-tide regimes. I show that their host stars display a variety of obliquities, contrary to similar planets orbiting closer to their star. Such an effect is consistent with the expectation from tidal evolution, but has not yet been tested on this scale. In Chapter 6, I study the spin angular momentum of the primary component of a binary star hosting a circumbinary planet. I demonstrate that the star is aligned with the binary and planet orbit, providing an important constraint on the formation of binary stars and circumbinary planets. Finally, in Chapter 7, I conclude and offer some thoughts on future prospects.

Dedication

To my mother for her love, support, and the confidence she instilled in me.
None of this would have been possible if not for her courage and strength.

Acknowledgements

Funding for this thesis was jointly provided by the School of Physics and Astronomy, College of Engineering and Physical Sciences, a Birmingham Doctoral Scholarship, and a Fulbright Scholarship from the U.S.-Norway Fulbright Foundation.

This thesis would not have been possible without the support from family, friends, and mentors that I have received over the years.

First and foremost I would like to express a deep gratitude to my supervisor, Amaury Triaud, for his unwavering support in both professional and personal matters; for his insight, mentorship, friendship, advice, and enthusiasm that have made my PhD a thoroughly enjoyable experience.

I would like to thank the other members of my research group, past and present: Bill Chaplin and Guy Davies for insightful discussions; and the other PhD students and postdocs, for the laughs, the commisery, the memes, but most of all for making me look forward to coming to the office every day.

Thank you to my collaborators, especially Daniel Fabrycky and David Martin for also being supportive mentors and excellent hosts while I spent time at The University of Chicago.

The circumstances and events that led me to this thesis is thanks to the advice and help from various people over the years, in particular Max Grönke and Johannes Sahlmann whom I am deeply grateful to.

Finally, a warm and loving thanks to all the friends I made in Birmingham, who reminded me to have fun and made the past four years into something I will cherish forever. In particular I wish to thank all my housemates in 688 for creating a home; James and Sonja for the support, dancing, and late night chats over a bowl of Weetabix; and Samantha for reminding me to take holidays, and for holding my hand.

Declaration

I declare that the thesis has been composed by myself and that the work has not been submitted for any other degree or professional qualification. I confirm that the work submitted is my own, except where work which has formed part of jointly-authored publications has been included. My contribution to co-authored publications has been explicitly indicated below, and in the sections of the thesis. I confirm that appropriate credit has been given within this thesis where reference has been made to the work of others.

This thesis includes five articles that are published in refereed astronomical journals. Three of the published articles are my own where I am lead author (Chapters 3.2, 4.2, 6). In addition, Chapter 5 is a manuscript in preparation which I am also leading. Two articles in this thesis are co-authored publications where I made a significant contribution to the analysis and manuscript. My role in all published work included in this thesis is outlined below.

The work presented in Chapter 3.1 was previously published in *Nature Astronomy, 4, 650* as *An eclipsing substellar binary in a young system discovered by SPECULOOS* by Triaud et al. (2020). I carried out the global light curve and radial velocity analysis that provided the orbital and physical parameters of the binary system, co-led the follow-up efforts of this system by predicting new eclipse timings, and contributed to the manuscript.

The work presented in Chapter 3.2 was previously published in *Monthly Notices of the Royal Astronomical Society, 481, 5091* as *WASP-128 b: a transiting brown dwarf in the dynamical-tide regime* by Hodžić et al. (2018). I carried out all data analysis except for the spectroscopic analysis and wrote the manuscript.

The work presented in Chapter 3.3 was previously published in *Monthly Notices of the Royal Astronomical Society, 507, 4132* as *TOI-1259 Ab - a gas giant planet with 2.7 per cent deep transits and a bound white dwarf companion* by Martin et al. (2021). I carried out the analysis of the radial velocity data and all ground- and space-based transit light curves, and contributed to the manuscript.

The work presented in Chapter 4.2.1 was previously published in *Monthly Notices of the Royal Astronomical Society, 502, 2893* as *Orbital misalignment of the super-Earth πMen c with the spin of its star* by Kunovac Hodžić et al. (2021). I came up with the intial idea. I wrote the observing proposal to secure the data with some help from my supervisor on the scientific rationale. I carried out all data reduction, analysis, and wrote the manuscript. My supervisor wrote Section 4.2 in the published article (Section 4.2.5 in this thesis).

The work presented in Chapter 6 was previously published in *Monthly Notices of the Royal Astronomical Society, 497, 1627* as *The EBLM project - VII. Spin-orbit alignment for the circumbinary planet host EBLM J0608-59 A/TOI-1338 A* by Kunovac Hodžić et al. (2020). I took the initiative to publish this archival data, carried out all data analysis, and wrote the manuscript.

Contents

Abstract iii

Dedication v

Acknowledgements vii

Declaration ix

Contents xi

List of Publications xv

List of Figures xvii

1 Introduction 1
- 1.1 Methods for exoplanet detection . . . 3
  - 1.1.1 The Doppler (radial velocity) method: measuring planet masses . . . 3
  - 1.1.2 The transit method: measuring planet sizes . . . 7
- 1.2 Demographics of exoplanets . . . 9
  - 1.2.1 Giant planets . . . 9
  - 1.2.2 Small planets . . . 11
- 1.3 Planet formation and migration . . . 11
  - 1.3.1 Formation of rocky cores and super-Earths . . . 12
  - 1.3.2 Gas giant planet formation . . . 13
  - 1.3.3 Brown dwarf and binary star formation . . . 13
  - 1.3.4 Planetary migration . . . 14
- 1.4 Observational clues to planetary formation and migration . . . 17
  - 1.4.1 Measuring obliquities of exoplanet host stars . . . 18
  - 1.4.2 Obliquity trends of planet-hosting stars . . . 23
  - 1.4.3 Tidal evolution in hot Jupiter systems . . . 25
- 1.5 How this thesis addresses some of these questions . . . 27

2 Photometric light curves and high-resolution spectroscopy 31
- 2.1 Light curves of exoplanets and binary stars . . . 31
  - 2.1.1 Science from transit light curves . . . 31
  - 2.1.2 Limb darkening . . . 34
  - 2.1.3 Science from binary star light curves . . . 35
- 2.2 Methods for the analysis of high-resolution spectra . . . 36
  - 2.2.1 Spectrograph overview . . . 38
  - 2.2.2 Cross-correlation functions . . . 38
  - 2.2.3 Science from radial velocity orbits . . . 41

2.2.4 Modelling the Rossiter-McLaughlin effect . . . 44
2.3 Statistical inference . . . 50
2.3.1 Noise sources in astronomy . . . 51
2.3.2 Correlated noise models . . . 51
2.3.3 Goodness of fit, parameter estimation, and model selection . . . 53
2.3.4 Bayesian inference with Markov chain Monte Carlo . . . 54
2.4 Software developed during this thesis . . . 56
2.4.1 `amelie`: Bayesian inference of light curves and radial velocities of transiting exoplanets and eclipsing binaries . . . 56
2.4.2 `olio`: The *reloaded* Rossiter-McLaughlin method . . . 62

3 Discovery and characterisation of new exoplanets and brown dwarfs 67
3.1 An eclipsing substellar binary in a young triple system discovered by SPECULOOS . . . 67
3.1.1 An unexpected discovery . . . 67
3.1.2 Contribution . . . 68
3.1.3 Main article . . . 71
3.1.4 Methods . . . 74
3.1.5 Further developments and future work . . . 79
3.2 WASP-128 b: a transiting brown dwarf in the dynamical-tide regime . . . 79
3.2.1 Introduction . . . 81
3.2.2 Observations . . . 82
3.2.3 Data analysis . . . 82
3.2.4 Results . . . 83
3.2.5 Discussion . . . 83
3.2.6 Conclusion . . . 85
3.3 TOI-1259 Ab: a gas giant transiting a K dwarf with a white dwarf companion . . . 88
3.3.1 Contribution . . . 88
3.3.2 Introduction . . . 89
3.3.3 Observations . . . 90
3.3.4 Analysis and results . . . 92
3.3.5 Discussion . . . 98
3.3.6 Additional analysis . . . 106

4 Stellar obliquities in Earth and super-Earth systems 109
4.1 Rossiter-McLaughlin campaigns on TRAPPIST-1 observed with CARMENES . . . 110
4.1.1 Observations . . . 110
4.1.2 Rossiter-McLaughlin modelling . . . 111
4.1.3 Results . . . 112
4.1.4 Further observations . . . 112
4.1.5 Conclusion and further developments . . . 114
4.2 Orbital misalignment of the super-Earth π Men c with the spin of its star . . . 117
4.2.1 An opportune moment for jumping onto the *TESS* bandwagon . . . 117
4.2.2 Introduction . . . 120
4.2.3 ESPRESSO data analysis . . . 121
4.2.4 Results . . . 126
4.2.5 Discussion . . . 127
4.2.6 Conclusion . . . 129
4.2.7 Appendix A: TESS photometric anaysis . . . 131

5 A miscellany of planetary misalignments 139

5.1 Target selection . . . 140
5.1.1 WASP-29 b . . . 143
5.1.2 WASP-68 b . . . 143
5.1.3 WASP-89 b . . . 143
5.1.4 WASP-99 b . . . 143
5.1.5 WASP-106 b . . . 144
5.1.6 WASP-107 b . . . 144
5.1.7 WASP-129 b . . . 144
5.1.8 WASP-130 b . . . 144
5.1.9 WASP-131 b . . . 145
5.1.10 WASP-139 b . . . 145
5.1.11 WASP-166 b . . . 145
5.2 Observations . . . 146
5.2.1 HARPS spectroscopy . . . 146
5.2.2 CORALIE spectroscopy . . . 146
5.2.3 *TESS* photometry for WASP-99 b . . . 147
5.3 Spectroscopic stellar parameters . . . 148
5.4 Transit modelling of WASP-99 b . . . 148
5.5 Radial velocity orbit analysis . . . 149
5.6 Spectroscopic transit analysis . . . 150
5.6.1 Retrieving the spatially resolved light . . . 150
5.6.2 Modelling the stellar surface velocity . . . 154
5.7 Results . . . 154
5.7.1 WASP-129 b is a newly eccentric planet . . . 154
5.7.2 Radial velocity drifts . . . 155
5.7.3 Rotation and stellar obliquities . . . 155
5.8 Discussion . . . 160
5.8.1 The origin of misalignments . . . 160
5.8.2 Tidal realignment . . . 160
5.8.3 Origins of our sample . . . 162
5.9 Conclusion . . . 162

6 Alignment of a star with the orbit of its binary companion and circumbinary planet 165
6.1 Background . . . 165
6.2 Introduction . . . 168
6.3 Observations . . . 169
6.4 Line profile analysis . . . 169
6.5 Results and discussion . . . 171
6.6 Conclusions . . . 173

7 Final remarks 175
7.1 Conclusions . . . 175
7.2 Future prospects . . . 177
7.2.1 Young systems . . . 177
7.2.2 Sub-Neptunes and multiplanetary systems . . . 178
7.2.3 True obliquities . . . 178

Bibliography 179

List of publications

First, a note on the names I have published under. In my first published work [1] I used my family name, Hodžić, which has been my legal name throughout this degree. In subsequent publications [2–8] I have used Kunovac Hodžić to include my mother's family name for personal reasons.

[8] *TOI-1259Ab - a gas giant planet with 2.7 per cent deep transits and a bound white dwarf companion*, MNRAS (2021), 507, 4132
Martin, D. V., El-Badry, K., **Kunovac Hodžić, V.**, Triaud, A. H. M. J., Angus, R., Birky, J., Foreman-Mackey, D., Hedges, C., Montet, B. T., Murphy, S. J., Santerne, A., Stassun, K. G., Stephan, A. P., Wang, J., Benni, P., Krushinsky, V., Chazov, N., Mishevskiy, N., Ziegler, C., Soubkiou, A., Benkhaldoun, Z., Boisse, I., Battley, M., Miller, N. J., Caldwell, D. A., Collins, K., Henze, C. E., Guerrero, N. M., Jenkins, J. M., Latham, D. W., Levine, A., McDermott, S., Mullally, S. E., Ricker, G., Seager, S., Shporer, A., Vanderburg, A., Vanderspek, R., & Winn, J. N.

[7] *The EBLM project - VIII. First results for M-dwarf mass, radius, and effective temperature measurements using CHEOPS light curves*, MNRAS (2021), 506, 306
Swayne, M. I., Maxted, P. F. L., Triaud, A. H. M. J., Sousa, S. G., Broeg, C., Florén, H.-G., Guterman, P., Simon, A. E., Boisse, I., Bonfanti, A., Martin, D., Santerne, A., Salmon, S., Standing, M. R., Van Grootel, V., Wilson, T. G., Alibert, Y., Alonso, R., Anglada Escudé, G., Asquier, J., Bárczy, T., Barrado, D., Barros, S. C. C., Battley, M., Baumjohann, W., Beck, M., Beck, T., Bekkelien, A., Benz, W., Billot, N., Bonfils, X., Brandeker, A., Busch, M.-D., Cabrera, J., Charnoz, S., Collier Cameron, A., Csizmadia, S., Davies, M. B., Deleuil, M., Deline, A., Delrez, L., Demangeon, O. D. S., Demory, B.-O., Dransfield, G., Ehrenreich, D., Erikson, A., Fortier, A., Fossati, L., Fridlund, M., Futyan, D., Gandolfi, D., Gillon, M., Guedel, M., Hébrard, G., Heidari, N., Hellier, C., Heng, K., Hobson, M., Hoyer, S., Isaak, K. G., Kiss, L., **Kunovac Hodžić, V.**, Lalitha, S., Laskar, J., Lecavelier des Etangs, A., Lendl, M., Lovis, C., Magrin, D., Marafatto, L., McCormac, J., Miller, N., Nascimbeni, V., Olofsson, G., Ottensamer, R., Pagano, I., Pallé, E., Peter, G., Piotto, G., Pollacco, D., Queloz, D., Ragazzoni, R., Rando, N., Rauer, H., Ribas, I., Santos, N. C., Scandariato, G., Ségransan, D., Smith, A. M. S., Steinberger, M., Steller, M., Szabó, G. M., Thomas, N., Udry, S., Walter, I., Walton, N. A., & Willett, E.

[6] *Orbital misalignment of the super-Earth π Men c with the spin of its star*, MNRAS (2021), 502, 2893
Kunovac Hodžić, V., Triaud, A. H. M. J., Cegla, H. M., Chaplin, W. J., & Davies, G. R.

[5] *The TESS light curve of the eccentric eclipsing binary 1SWASP J011351.29+314909.7 - no evidence for a very hot M-dwarf companion*, MNRAS (2020), 498, L15
Swayne, M. I., Maxted, P. F. L., **Kunovac Hodžić, V.**, & Triaud, A. H. M. J.

[4] *The EBLM project - VII. Spin-orbit alignment for the circumbinary planet host EBLM J0608-59 A/TOI-1338 A*, MNRAS (2020) , 497, 1627
Kunovac Hodžić, V., Triaud, A. H. M. J., Martin, D. V., Fabrycky, D. C., Cegla, H. M., Collier Cameron, A., Gill, S., Hellier, C., Kostov, V. B., Maxted, P. F. L., Orosz, J. A., Pepe, F., Pollacco, D., Queloz, D., Ségransan, D., Udry, S., & Welsh, W. F.

[3] *TOI-1338: TESS' First Transiting Circumbinary Planet*, AJ (2020), 159, 253
Kostov, V. B., Orosz, J. A., Feinstein, A. D., Welsh, W. F., Cukier, W., Haghighipour, N., Quarles, B., Martin, D. V., Montet, B. T., Torres, G., Triaud, A. H. M. J., Barclay, T., Boyd, P., Briceno, C., Cameron, A. C., Correia, A. C. M., Gilbert, E. A., Gill, S., Gillon, M., Haqq-Misra, J., Hellier, C., Dressing, C., Fabrycky, D. C., Furesz, G., Jenkins, J. M.,

Kane, S. R., Kopparapu, R., **Kunovac Hodžić, V.**, Latham, D. W., Law, N., Levine, A. M., Li, G., Lintott, C., Lissauer, J. J., Mann, A. W., Mazeh, T., Mardling, R., Maxted, P. F. L., Eisner, N., Pepe, F., Pepper, J., Pollacco, D., Quinn, S. N., Quintana, E. V., Rowe, J. F., Ricker, G., Rose, M. E., Seager, S., Santerne, A., Ségransan, D., Short, D. R., Smith, J. C., Standing, M. R., Tokovinin, A., Trifonov, T., Turner, O., Twicken, J. D., Udry, S., Vanderspek, R., Winn, J. N., Wolf, E. T., Ziegler, C., Ansorge, P., Barnet, F., Bergeron, J., Huten, M., Pappa, G., & van der Straeten, T.

[2] *An eclipsing substellar binary in a young triple system discovered by SPECULOOS*, Nature Astronomy (2020), 4, 650

Triaud, A. H. M. J., Burgasser, A. J., Burdanov, A., **Kunovac Hodžić, V.**, Alonso, R., Bardalez Gagliuffi, D., Delrez, L., Demory, B.-O., de Wit, J., Ducrot, E., Hessman, F. V., Husser, T.-O., Jehin, E., Pedersen, P. P., Queloz, D., McCormac, J., Murray, C., Sebastian, D., Thompson, S., Van Grootel, V., & Gillon, M.

[1] *WASP-128b: a transiting brown dwarf in the dynamical-tide regime*, MNRAS (2018), 481, 5091

Hodžić, V., Triaud, A. H. M. J., Anderson, D. R., Bouchy, F., Collier Cameron, A., Delrez, L., Gillon, M., Hellier, C., Jehin, E., Lendl, M., Maxted, P. F. L., Pepe, F., Pollacco, D., Queloz, D., Ségransan, D., Smalley, B., Udry, S., & West, R.

List of Figures

1.1 Elements of a Keplerian orbit. The massless particle (*grey*) moves clockwise in an elliptical orbit. The system is illustrated top-down, with the centre and focus of the ellipse denoted as a red dot and cross, respectively. The semi-major axis of the elliptical orbit is a and is the distance from the centre to the largest separation in the orbit. The eccentricity (ellipticity) of the orbit is given by e, with the product ae being the distance from the centre of the ellipse to its focus. The particle is closest to the focus at point π, which is the periastron. The system is viewed from the right, and the line perpendicular to the line-of-sight connecting the orbit through the focus of the ellipse is the line of nodes. For a non-circular orbit the argument of periastron, ω, is the angle from periastron to where the line of nodes intersects the orbit in the direction of the particle motion. 4

1.2 The inclination of the orbit. The orbit of a planet relative to the star is illustrated from the side (*edge-on*), and the observer sits to the right. The orbital plane can be inclined to the line of sight by the inclination angle i. When $i = 0°$ the system is observed face-on, and no radial velocity motion is seen from the observer's point of view. The radial velocity semi-amplitude is highest when the orbit is viewed edge-on ($i = 90°$). When $i \approx 90°$ the planet is likely to transit the star. 4

1.3 The radial velocity reflex motion of a star due to a planet on a circular orbit ($e = 0$). *Top:* The (exaggerated) orbit of a planet and star around the centre of mass is illustrated top-down at four times during a complete orbit, $t_0 - t_3$. The grey arrow denotes the direction of motion. The star is the star-shaped symbol and its colour denotes the radial velocity direction, with red and blue taken to mean maximum and minimum radial velocity. Purple colour denotes zero radial velocity motion because the star is moving only tangentially to the line of sight. *Bottom:* The radial velocity curve of the star observed over two complete orbits. The colour gradient is to show when the light is redshifted (star is moving away from the observer) and blueshifted (star is moving towards the observer). The times $t_0 - t_3$ are marked on the curve, which correspond to the positions in the orbits in the top panels. Half of the peak-to-peak radial velocity amplitude is K, and the radial velocity curve repeats every orbital period, P. . 6

1.4 Transit light curve caused by a Jupiter-sized planet passing in front of a Sun-like star. The loss of light is proportional to the size ratio, while the transit duration ($T_14 = t_4 - t_1$) and ingress durations ($\tau = t_2 - t_1 = t_4 - t_3$) provide constraints on the impact parameter $b = a \cos i / R_\star$ and hence the orbital inclination, as well as the stellar density (see Chapter 2.1.1). This diagram was created using `starry` (Luger et al. 2019). 7

1.5 The radii (*top*), masses (*bottom*), and orbital periods of confirmed exoplanets as of April 2021, obtained from the NASA Exoplanet Archive. Darker regions indicate a higher density of planets. 10

1.6 The geometry of a star in relation to a planet orbit. The observer views the system along the z axis (labelled *observer*). The axis normal to the planet's orbital plane is labelled *orbit*, and the stellar rotation axis is labelled *spin*. The angle between the observer and *orbit* is the orbital inclination, i, while the angle between the observer and *spin* is the stellar inclination, $i_\star$. The obliquity of the star is the angle ψ. The Rossiter-McLaughlin effect measures the sky-projected obliquity, λ. Credit: Josh Winn and Simon Albrecht (Albrecht et al. 2021). . . 19
1.7 Radial velocity anomalies during transit due to the Rossiter-McLaughlin effect. The Rossiter-McLaughlin effect is shown for a planet with $b = 0.4$ for three values of the angle between the stellar rotation axis and planet orbital axis. From left to right: $\lambda = 0°$, $\lambda = 60°$, and $\lambda = 160°$. 21
1.8 Projected obliquities of planet-hosting stars (planet-star misalignments) as of September 2020. *Top:* The full sample with planet masses consisting of 155 measurements, most of which have been made using the Rossiter-McLaughlin effect. Some notable patterns are annotated in the data. Each of the planet-star pairs along the vertical axis serve as a visual aid of the relevant architecture for a particular value of $|\lambda|$. Note that these illustrations assume $i_\star = 90°$, though the real value is in most cases unconstrained (and likely different) since only the projection of the obliquity is measured. *Bottom left:* The stellar effective temperatures of the sample. *Bottom right:* The orbital separation of the sample. Points with an inverted color scheme denotes planets that are eccentric, which here is determined as those that have e larger than three times the uncertainty on e. 24

2.1 The transit depth depends on the size of the planet relative to the star. Larger planets (*solid circle and line*) cause deep transits, while smaller planets (*dashed and dotted*) cause shallower transits. In addition, the distance of the transit chord (*shaded region*) from the centre of the star, i.e. the impact parameter b, changes the total transit duration as well as the ingress/egress times. This figure was created using `starry` (Luger et al. 2019). 33
2.2 The intensity across the stellar disc is not uniform; it is lowest at the limb and increases towards the centre, referred to as limb darkening. Limb darkening is strongest for stars observed at blue wavelengths (e.g. g' band, $\lambda \approx 500\,\mathrm{nm}$) and causes the transit to look U-shaped. Stars observed at redder wavelengths (r', i', z' bands, $\lambda > 600\,\mathrm{nm}$) have less pronounced limb darkening, and the transits appear more flat-bottomed. This figure was created using `starry` (Luger et al. 2019). 35
2.3 An example of an eclipsing binary star system consisting of a low-mass star ($m_2 = 0.2\,M_\odot$, $T_\mathrm{eff} = 3000\,\mathrm{K}$) orbiting a Sun-like primary ($m_1 = 1.1\,M_\odot$, $T_\mathrm{eff} = 6000\,\mathrm{K}$). In a circular binary the secondary eclipse occurs $P/2$ ($\phi = 0.5$) after the primary eclipse (*solid line*). The same is true for eccentric orbits with $|\omega| = 90°$ (*dashed line*), but here the durations of the primary and secondary eclipse differ and can constrain $e \sin\omega$. Eccentric binaries with $|\omega| \neq 90°$ have secondary eclipses that are displaced from $\phi = 0.5$ (*dotted line*) which can constrain $e \cos\omega$. In addition, the secondary eclipse depth measures the temperature ratio of the stars. This figure was created using ELLC. 37
2.4 *Left:* An image of a cross-dispersed echelle spectrum taken with the red camera of ESPRESSO on the VLT. The target star is π Mensae. The y direction is the main dispersion direction, while the x direction is the cross-dispersion direction. *Right:* A zoomed-in part of the detector showing three different spectral orders of the stellar light (*continuous bands*) and reference light (*bright dots*). The dark regions within the bands show absorption. 39

2.5 *Top:* The 1D spectrum obtained from co-adding all spectral orders shown in the echellogram in Figure 2.4. The continuum (*coloured line*) follows Planck's law (black-body radiation), and a few prominent absorption lines are marked. The high-resolution spectrum also contains thousands of non-saturated absorption lines (*grey lines*) which are used to measure the Doppler shift. The red parts of the spectrum shows significant absorption due to water and molecular oxygen in Earth's atmosphere. *Bottom:* A zoomed inset of a small region of the spectrum, showing the details of some absorption lines in the grey forest. 40
2.6 The radial velocity of a star can be determined from cross-correlating absorption lines in a stellar spectrum (*left, black*) with expected line positions using a binary template (*blue*). The resulting cross-correlation function (CCF, *right*) is an average stellar line profile in velocity space, and the radial velocity is determined from the centre of a Gaussian fit to the CCF. Figure adapted from Roy et al. (2016). 41
2.7 Radial velocity curves of a Sun-like star hosting a Jupiter-mass planet with $P = 3$ days. Each panel shows the circular orbit (*dashed line*) and eccentric orbit ($e = 0.3$, *solid line*) with the same semi-amplitude K, but different values of ω. The systemic velocity here is $\gamma = 0\,\mathrm{km\,s^{-1}}$. These models were calculated using ELLC (Maxted 2016). 42
2.8 The radial velocity orbits of two stars with masses $m_1 = 1\,M_\odot$, $m_2 = 0.7\,M_\odot$, and orbital elements $P = 4\,\mathrm{d}$, $i = 90°$, $e = 0.2$, $\omega = 90°$, orbiting their common centre of mass. Spectra from unresolved binary stars of similar brightness may show two sets of absorption lines from which radial velocities of both stars can be derived. The ratio of their radial velocity semiamplitudes measures the mass ratio of the stars from which model-independent (minimum) masses can be obtained. This figure was generated using ELLC (Maxted 2016). . 45
2.9 Transits produces a change in the line profile of rotating stars. The deficit light (*dotted line*) is Doppler shifted according to the local surface velocity on the star, i.e. that which is occulted by the planet, v_{occ}. The line profile from the visible disc (*solid line*) is therefore perturbed relative to an unocculted surface (*dashed line*), which displaces the line centre to create a net radial velocity shift. This figure was created using `starry` (Luger et al. 2019). 46
2.10 Simulated CCFs of the stellar light hidden by a transiting planet. The grey scale refers to the flux so that dark areas correspond to absorption, i.e. the local CCF core. The four transit contacts are shown as horizontal black dashed lines. The light hidden by the planet is Doppler shifted by the local surface velocity on the star, which is determined by the projected rotation $v \sin i_\star$ (*vertical black dashed lines*) and spin-orbit angle λ. The true model ($\lambda = 0°$) is shown as a solid white line. The impact of varying λ is shown as dotted white lines. This figure was generated using OLIO (Section 2.4.2). 49
2.11 A fit to the low-mass eclipsing binary system J0113+31 using AMELIE. 61
2.12 Demonstration of surface velocity models computed with OLIO for rotation (*left*) and centre-to-limb convective blueshift variation (*right*). *Left:* The rigid-body model (*solid line*) is computed with $v \sin i_\star = 3\,\mathrm{km\,s^{-1}}$, $\lambda = 45°$. The differential rotation model (*dashed*) is computed with $v_{\mathrm{eq}} = 3\,\mathrm{km\,s^{-1}}$, $i_\star = 60°$, $\lambda = 45°$, and $\alpha = 0.2$. *Right:* The convective blueshift models are expressed as polynomials in the brightness-weighted distance from the stellar centre, $\langle\mu\rangle$, with linear coefficient $300\,\mathrm{m\,s^{-1}}$ for the linear model (*dotted*), and an additional quadratic coefficient of $100\,\mathrm{m\,s^{-1}}$ (*dash-dotted*). 65

3.1 A spectrum of 2M1510 A taken with the UVES instrument on the VLT, revealing splitting at the locations of the absorption lines at approximately 8186 Å and 8197.7 Å due to the composite spectrum from both brown dwarfs. Note that there is an error in the wavelength label, the numbers are in units of Å. The black line corresponds to the spectral data, the red line is the forward model, the blue line is the residual of the fit with grey lines corresponding to the 1σ uncertainties on the data. Figure by courtesy of Adam Burgasser. 68

3.2 *Top:* The projected separation between the two brown dwarfs during their orbit. The dash-dotted line is the equivalent curve if the eccentricity was zero. The dotted line shows the separation curve for the minimum inclination needed for a primary eclipse to occur, which is i=89.1°. The two insets are zoomed in on the expected position where primary eclipse would occur, and where secondary eclipse occurs. The red line in the insets denote the minimum separation needed for there to be an eclipse. *Bottom:* A visual representation of the projected separation at the expected times of primary (*left*) eclipse (inferior conjunction, Chapter 2.1.1) and secondary eclipse (*right*, superior conjunction). The darker object is the primary component. 69

3.3 The two panels show the brightness of 2M1510 A as a function of time with errors. The green regions are possible orbital solutions within 2σ. The first panel (*left*) shows the detected eclipse, and the second panel (*right*) shows how a second eclipse was narrowly missed, leading to two distinct orbital solutions, placing the eclipse either just before or after the observations. 70

3.4 Data demonstrating that 2M1510 A is a substellar eclipsing binary. **a**, SPECULOOS photometric data (black points) and their 1σ uncertainties showing the observed 4 % grazing eclipse. The red solid line is the best-fit model from the joint global fit with its 2σ confidence region (red shaded region). Below are the residuals of the best fit ($O - C$). **b**, The phase-folded radial velocity orbit of the brown dwarf primary (blue) and secondary (orange). A systemic velocity of $-12.9\,\mathrm{km\,s^{-1}}$ has been subtracted from the values. Individual points are measurements (UVES, circles; NIRSPEC, diamonds) with their 1σ uncertainties. Solid lines indicate the joint global fit with 2σ uncertainty regions shaded. Below are the residuals of the best fit ($O - C$). **c**, Radial velocity observations and models as in **b**, but shown as a function of time. The vertical dashed line on day 7961.5 indicates the epoch of the secondary eclipse displayed in **a**. These combined data allow us to measure the masses of the two brown dwarfs and their combined radius. 72

3.5 Mass-radius diagram showing the position of the 2M1510 Aab eclipsing pair (shown in black with their 1σ uncertainties). The red-shaded areas separate the tracks of the Exeter/Lyon evolutionary models with ages labelled. Circles delineate mass/radius measurements obtained for previously detected double-line eclipsing binaries, with their colour corresponding to the age estimated for each binary. Dark dots depict mass/radius measurements for interferometric measurements, single-line eclipsing binaries and transiting exoplanets. The young brown dwarfs 2M0535 AAB and RIK 27b are labelled. 2M1510 As parameters are consistent with the 45 ± 5 Myr age of the Argus moving group, just below a 40-Myr isochrone highlighted in black. 2M1510 Aab, our double-line eclipsing system, is in an area of parameter space with no equivalent systems. Literature measurements are reported in Supplementary Tables 5 and 6. 73

3.6 Radius and luminosity measurements as a function of system age, for stars, brown dwarfs and giant exoplanets with their 1σ uncertainties. **a**, Radius versus age; **b**, luminosity versus age. Each line corresponds to a model of a given mass. Stellar masses (pink lines) are labelled in units of $M_\odot$, whereas brown dwarf (khaki lines) and exoplanet masses (blue lines) are labelled in units of M_{Jup}. Dots following a similar colour scheme are systems reported in the literature. We note that directly imaged planetary mass objects do not have measured radii. 2M1510 Aa and Ab are represented as a single black point, and along with 2M0535 AB and RIK 72b are the smallest and least massive objects with measured masses, radii and age (panel **a**). Together, they form an empirical isochrone for masses close to $40\,M_{\mathrm{Jup}}$. Models for $30\,M_{\mathrm{Jup}}$, $40\,M_{\mathrm{Jup}}$ and $50\,M_{\mathrm{Jup}}$ are depicted as bolder lines. In panel **b** we note that the bolometric luminosity (and the J, H and K magnitudes) of 2M1510 Aab fall under the $0.038\,M_\odot$ ($40\,M_{\mathrm{Jup}}$) track as measured from dynamical masses. 73

3.7 Transits of WASP-128 taken with the *Euler* (*green*) and TRAPPIST (*vermillion*) telescopes. The points correspond to detrended data binned to 5 min, and the coloured lines are the best-fitting models. The residuals of the fit are shown in the lower panel. 84
3.8 The radial velocity motion of WASP-128 due to its brown dwarf companion, folded on the best-fitting period. The blue points correspond to RV measurements taken with CORALIE (*circles*) and HARPS (*triangles*). The solid line is the best-fitting model. The residuals of the fit are shown in the lower panel. 84
3.9 Mass-radius diagram placing WASP-128 b (*vermillion*) in the context of the other known transiting brown dwarfs. Objects are from Bayliss et al. (2017) and references therein, including the recent discovery of Kepler-503b (Cañas et al. 2018). The shaded area outlines isochrones for substellar objects from the COND03 models (Baraffe et al. 2003). 85
3.10 Transit depths of all confirmed transiting exoplanets as a function of the planet's equilibrium temperature (where such a value has been calculated). The colour indicates the mass of the host star in solar masses. The triangle demarcates TOI-1259 with 2.7 % deep transits. 91
3.11 SDSS image of the planet host TOI-1259A and its bound white dwarf companion TOI-1259B. The image is centred on TOI-1259A at RA $18^{h}48^{m}24.07^{s}$, Dec $79°15'21.76''$. 92
3.12 Spectral energy distribution of TOI-1259A. The red symbols represent the observed photometric measurements, where the horizontal bars represent the effective width of the passband. The blue symbols are the model fluxes from the best-fit (Kurucz 1979) atmosphere model (black). 93
3.13 Top: Systematics-Insensitive Periodogram (SIP) for TOI-1259b.The periodogram is calculated for both the corrected light curve (the black line) and the background (BKG) pixels (the blue line). There is a strong peak in the SIP at 28 d, which is attributed to the rotation of the planet host and denoted by a red-dashed line. The background pixels show no evidence of any periodicity, suggesting that the 28 d signal is both real and intrinsic to the target. Note that these periodograms are not normalized by the measurement errors. Bottom: The light curve for TOI-1259. The grey points show the raw data TESS data, and the black points show the data corrected using `TESS-sip`, showing a clear periodicity. 93
3.14 Parameters of the WD and its progenitor, obtained from fitting the SED. We compare constraints obtained when assuming the initial-final mass relations (IFMR) from El-Badry & Rix (2018) and Williams et al. (2009). For this figure we assume a hydrogen atmosphere, but in Table 4 we also show results for a potential helium atmosphere. Values listed on the diagonal are based on the El-Badry & Rix (2018) IFMR. Contours enclose 68 and 95 per cent probability. The total age of the WD and thus, presumably, the age of the system is at least 3 Gyr. The age uncertainty is dominated by uncertainty in the mass and pre-WD age of the progenitor. 95
3.15 Generalized Lomb-Scargle (GLS) periodogram of the 19 SOPHIE RV points (top) and the residuals to the circular Keplerian fit (bottom). The highest peak for the observations corresponds to the transiting planet orbital period at 3.45 d. There are also harmonics at integer fractions of this period. Note that these periodogram does not include any information from the photometry. The RV detection alone is significant, above a 1 per cent false alarm probability (FAP). For reference, we show the 27.8 d rotation period of the host star with a red-dashed line, at which there is no power in the GLS. The GLS periodogram of the residuals shows no significant peak above a 10 per cent FAP. 96
3.16 *Upper panel:* Nine sectors of *TESS* PDCSAP photometry of TOI-1259. The blue model is the Gaussian process model. *Middle panel:* The light curve after removing the Gaussian process model, showing transits only, with the transit model overlaid in orange. *Bottom panel:* Residuals from the best-fitting full model. 98

3.17 Phase folded and detrended light curve of the primary transit after removing the Gaussian process model. We show the unbinned data in blue, and the data averaged in 10 min bins in blue/white points. The orange line is the best-fitting transit model, with a maximum depth of 2.7 per cent. 98
3.18 Transit light curves of TOI-1259 b followed up with small (<50 cm s^{-1}) ground-based telescopes with various filters. For each light curve, we show the raw data in the top panel (*grey*) overlaid with data binned in 10 min intervals (*black*). The best-fitting model is shown as a solid blue line, which consists of a Gaussian process (GP) model (*dashed*) and transit model (*dotted*). The 1σ uncertainty of the GP model is indicated by the shaded region. The middle panels are 'cleaned' light curves after removing the GP model, and the bottom panels are residuals from the best-fitting model. 99
3.19 *Top:* The light curve folded on the phase of the planet orbit, with data points binned in 20 min intervals. The grey highlighted area is the transit duration. The expected secondary eclipse depth is 63 ppm, which is comparable to the noise. There is no apparent signal at $\phi = 0.5$, where one could expect a secondary eclipse for a circular orbit. There is a tentative signal centred on $\phi = 0.64$ with a duration that is consistent with a secondary eclipse, however, this implies an eccentricity of roughly 0.2–0.3 that is incompatible with the RV data. 100
3.20 SOPHIE RV (*black*) with the 99th percentile models from a joint fit with the *TESS* photometry encapsulated in the blue region. The RV are indicative of a 0.44 $M_{\rm Jup}$ planet, and are in phase with the transits observed by *TESS*. 100
3.21 Transit Spectroscopy Metric (TSM) from Kempton et al. (2018) for all confirmed transiting exoplanets as a function of their equilibrium temperature (where such a value has been calculated). The TSM is calculated using equation (3). The colour scale is the planet radius. TOI-1259Ab has a TSM of 180, making it ideal for atmospheric follow-up. In particular, it has one of the highest TSM values for a planet cooler than 1000 K and of Jupiter-size or less. 101
3.22 Posteriors for the e and ω using constraints from various sources. *Blue:* Constrained by the radial velocity data (joint fit with photometry). *Orange:* Constraint from comparing the stellar density derived from two different sources. *Gray:* Constraint from approximate location and duration of the candidate secondary eclipse in Figure 11 (Section 3.3.5). 106
3.23 Transit spot-crossing events for TOI-1259 Ab. *Top:* A view of the SAP flux from *TESS* of TOI-1259 A. *Middle:* A closer look on the first sector of *TESS* data, highlighting the locations of two adjacent transits in blue and orange. *Bottom:* A closer look at each transit. The first transit (*blue*) occurs first, and encounters a spot in the second half of the transit. The second transit (*orange*) encounters a spot earlier than the previous transit. 108

4.1 Posterior distributions (*black*) for $v \sin i_\star$ and λ from our four runs where either was fit, with prior distribution (*red*) where applicable. *Top:* Prior on $v \sin i_\star = 6 \pm 2$ km s^{-1} from spectroscopic line broadening (Barnes et al. 2014). *Upper middle:* Prior on $v \sin i_\star = 1.855 \pm 0.095$ km s^{-1} from *K2* periodic signal interpreted as rotation (Luger et al. 2017; Vida et al. 2017). *Lower middle:* No prior. *Bottom:* No prior, fix $\lambda = 0°$ (alignment). 113
4.2 The data and their best Rossiter-McLaughlin fits. *Top:* From left to right we show individual fits for TRAPPIST-1 b,c,g. The data are given as coloured dots, with best-fit models in the same colour, and errorbars in gray. The 2σ credible interval is given as a coloured shaded area, while the transit duration is shaded in gray. *Bottom:* The data and models normalised to the stellar disc, allowing us to stack observations in the same frame. Gray dots and errors are the individual data, with binned data and errors in red, binning the stellar disc into 12 equidistant points. The residuals of the fit are shown in the bottom panel. 114
4.3 Lomb-Scargle periodogram of the combined *ESPRESSO* radial velocity data. The orange curve shows the heavily smoothed spectrum and reveals an estimate of $\nu_{\rm max} \simeq 2900$ µHz. In blue, we denote the frequency of maximum oscillation for the Sun for comparison. 122

4.4 *Top: ESPRESSO* data from run A (*left*) and run B (*right*). The orange line is the best fit from our combined Rossiter-McLaughlin model and GP model (oscillations and 'background' variability). The shaded area is the 68 per cent (1σ) credible interval of the fit. *Upper middle:* The data after removing the contribution from oscillations in our GP model. *Lower middle:* The data after further removing the contribution from the longer-term variability in our GP model. *Bottom:* Residuals of the fit. The grey, shaded regions denote the transit duration. 124
4.5 Radial velocity scatter as function of bin width for run A (*blue*) and run B (*orange*). The black dashed line denotes the expectation from whit enoise scaling. 125
4.6 CCF residuals and planet traces for run A (*top*) and run B (*bottom*). In each figure, the upper panel shows the residual profiles obtained from subtracting the binned CCFs from the out of transit reference CCF (CCF_{out}).The green colours denote in-transit data, getting darker with time. The grey residuals are binned CCFs outside of transit. In the lower panels, the trace of the planet across the stellar disc is shown, where the grey solid lines denote the transit ingress and egress, while the white dotted lines denote the stellar rest velocity and transit mid-point. 125
4.7 *Upper panel:* The local surface velocities obtained from fitting Gaussian profiles to the in-transit residual CCFs, shown as blue circles and orange squares for runs A and B, respectively. The red shaded area denote the 50th-99th percentiles of the models generated from the posterior distribution of the fit. As a reference, the grey line denotes the $\lambda = 0°$ line, which shows that alignment is firmly rejected. *Lower panel:* The residuals from the best-fitting model. 127
4.8 *TESS* data folded on the transit period after removing the best-fitting GP model (*blue points*), and binned to 10 min averages (*blue/white points*). We also show the best-fitting transit model (*orange line*). 129
4.9 Comparison of the transit depth and planet radius posterior distributions from the MCMC sampling from each sector, and the full combined fit using all sectors (*grey, filled*) using a transit and GP model. We also show the posterior distribution from Damasso et al. (2020) (*pink, filled*) for comparison. These results are consistent with the previously reported values from Huang et al. (2018) and Gandolfi et al. (2018). 129
4.10 *TESS* data (*black points*) from sectors 1, 4, 8, 11, 12, and 13 fitted with the GP model and transit model (*orange line*) described in Section 4.2.7. In the lower panel of each sector, we show the residuals from the best fit. 133
4.11 Observing conditions and CCF observables for *ESPRESSO* run A (*blue*) and run B (*orange*). From top to bottom: CCF contrast, CCF FWHM, SNR at 550 nm, airmass, seeing, and bisector inverse slope (BIS). The grey vertical lines denote the transit ingress and egress. . . 134
4.12 Gaussian fits to the 15 min binned residual line profiles from run A. The orange shading denotes the 1σ of the model. 134
4.13 Gaussian fits to the 15 min binned residual line profiles from run A. The orange shading denotes the 1σ of the model. 135
4.14 Gaussian fits to the 15 min binned residual line profiles from run A. The orange shading denotes the 1σ of the model. 135
4.15 Gaussian fits to the 15 min binned residual line profiles from run B. The orange shading denotes the 1σ of the model. 136
4.16 Gaussian fits to the 15 min binned residual line profiles from run B. The orange shading denotes the 1σ of the model. 136
4.17 Gaussian fits to the 15 min binned residual line profiles from run B. The orange shading denotes the 1σ of the model. 137
4.18 Comparison of the fitted local depth and width from the residual line profiles for runs A and B. 137

5.1 Key planetary, stellar, and orbital parameters for the sample considered in this work. 140

5.2 Fits to the radial velocity orbits for all planets in our sample. The yellow line and shaded regions are the best-fitting models and the 68 % credible interval, respectively. CORALIE data are shown as red squares, while HARPS data are shown as green circles. Data taken during transit spanning twice the transit duration are not included in the fit and not shown in these figures. In addition to the transit data, all HARPS data shown here (*green*), with the exception of WASP-139 b and WASP-166 b, is previously unpublished and has allowed better constraints on the eccentricities. 151
5.3 Sensitivity of the spectroscopic $v \sin i_\star$ prior on the fitted $v \sin i_\star$ (*top*) and λ (*bottom*) values. The prior (*yellow*) is applied for the vertical axes and is derived from a spectroscopic analysis of the combined CORALIE and HARPS data. The uncertainties denote the 68 % credible interval. Labels: [1]WASP-29 b [2]WASP-68 b [3]WASP-89 b [4]WASP-99 b [5]WASP-105 b [6]WASP-106 b [7]WASP-107 b [8]WASP-129 b [9]WASP-130 b [10]WASP-131 b [11]WASP-132 b [12]WASP-139 b [13]WASP-166 b. Note that the prior values (yellow) are from the new spectroscopic analysis. The fits using $v \sin i_\star$ priors (y-axis) were done before the spectroscopic analysis and therefore used $v \sin i_\star$ from literature. 152
5.4 Velocity of the stellar surface transited by the planet. The dark regions represent local absorption line profiles on the star that are Doppler shifted by the stellar rotation. The white lines and shaded regions are the best-fitting surface velocity model and the 3σ (99.7 %) credible interval, respectively. Each panel covers the transit duration only and is therefore centered at the transit mid-point. Grey areas denote missing data. 153
5.5 Systems where a statistically significant drift is detected. The yellow line and shaded regions are the best-fitting linear or quadratic polynomial models and the 68 % credible interval, respectively. CORALIE data are shown as red squares, while HARPS data are shown as green circles. The constant systemic velocity offset and radial velocity orbits due to known planets have been removed. 156
5.6 Projected obliquities as functions of stellar effective temperature (*top*) and scaled separation (*bottom*). Literature measurements (*blue*) are obtained from TEPCat, and measurements from this work are shown in yellow. The data for WASP-166 b has been previously published, but has not been analysed with the reloaded Rossiter-McLaughlin method. Labels: [1]WASP-29 b [2]WASP-68 b [3]WASP-89 b [4]WASP-99 b [5]WASP-105 b [6]WASP-106 b [7]WASP-107 b [8]WASP-129 b [9]WASP-130 b [10]WASP-131 b [11]WASP-132 b [12]WASP-139 b [13]WASP-166 b. 161

CHAPTER 1

INTRODUCTION

When faced with the daunting task of writing a doctoral thesis, one of the many choices one has to make is how to introduce the topic. Over the years I have witnessed numerous approaches across various areas of astrophysics. Yet in the true spirit of an astronomer looking at their shoddy data, I have seen a trend. Many start at the *beginning*, which is loosely interpreted. Science has its basis in philosophy, so naturally some take the philosophical angle and begin their story in Ancient Greece. Others begin by deriving fundamental equations and relations that their research area is based on, be it asteroseismic scaling relations, two-body orbits, the evolution of matter and structures in the universe, or Einstein's field equations. Unfortunately, I never had much interest in philosophy, so there will be no deep musings about our place in the universe through the lens of philosophers of old. Moreover, it is in my opinion that nobody reads a doctoral thesis[a] for its introduction to, say, Kepler's laws of planetary motion, when there is no shortage of publicly available books and lecture notes on the topic that likely provide a much better explanation than any doctoral candidate ever could. Lastly, my most important inspiration for writing this thesis is my mother, who despite her numerous redeeming qualities is not a scientist nor academic. As a result I have attempted to write this Chapter in a way that is (more or less) approachable for her — that is if she was proficient in English.

Nevertheless, while I hate to become part of the statistic, I, too, will start at the beginning. Not only that, but *my* beginning is yet another cliché within the field of exoplanets, because I will start with the discovery of the first planet orbiting a star like the Sun. The reason for this is very simple. It is very rare in astronomy for a research field to have been born within one's own lifetime, yet this is exactly what happened with the new field of *exoplanets* when a 4-day period Jupiter-mass companion to the solar-type star 51 Pegasi was discovered in 1995 (Mayor & Queloz 1995). At the time, only one or two handful of astronomers in Canada, Switzerland, and the USA searched for these new, alien worlds. Today, at the

[a] I could end the sentence here.

time of writing 26 years later, several thousand researchers around the world study exoplanets in one form or another, spanning areas in astronomy, physics, chemistry, biology, geology, and atmospheric science.

Although I have started this story at the origin of the exoplanetary science field, I am not going to go through the process of detailing the main findings from 26 years worth of research. Suffice to say that in this time we have discovered 4383 confirmed planets[b], and that these exoplanets exhibit a great diversity in properties such as mass, radius, orbital separations, and system architectures – much more so than what we find in our own solar system. The solar system consists of eight planets: four interior rocky planets, and four exterior gas giants, all of which are remarkably coplanar. The orbital planes of all the planets line up with the Sun's equator to within ~6° (Souami & Souchay 2012; Bailey et al. 2016), whereas the variation in mutual inclination between the planets themselves is less than one degree.[c]

In contrast, most of the exoplanets we have discovered do not adhere to the rules of the solar system. The most common exoplanets have masses and sizes between that of Earth and Neptune (Figure 1.5), for which we do not have a solar system analog (Howard et al. 2010; Mayor et al. 2011; Fressin et al. 2013; Petigura et al. 2018). Some stars host a single Jupiter-mass planet orbiting its star at just a tenth of the Sun-Mercury separation (e.g. 51 Peg b), many of which have orbits that are severely misaligned with the axis of rotation of its star, or even orbit in the opposite direction of the stellar rotation (Triaud et al. 2010; Winn et al. 2010a; Albrecht et al. 2012; Winn & Fabrycky 2015; Triaud 2018). In those systems that contain multiple planets, the planets appear to have similar sizes[d] and do not show the diversity of sizes found in the solar system (Weiss et al. 2018). Recently, both planets of a multiple planet system have even been found to orbit in the opposite direction of their star's rotation (Hjorth et al. 2021).

It is clear, then, that our initial theories on how planets form and evolve — which were based on the solar system alone, prior to the discovery of exoplanets — cannot adequately explain the diversity of planetary systems that we observe. Why do some systems have one planet, while others have up to seven and eight planets (Gillon et al. 2017; Shallue & Vanderburg 2018)? How do Jupiter-mass planets end up so close to their star, where they complete an orbit in a matter of days? Do they form there, or is their proximity a result of orbital evolution? If the latter, what factors influence the evolution of their orbits? Why are some planetary orbits grossly inclined with respect to the rotation axis of their star? Are these questions connected?

In this Chapter, I will review some of the observed properties of exoplanets — and also of brown dwarfs and low-mass binary systems — with which they share many similarities. I will further discuss how these properties have influenced new theories on the formation, migration, dynamical and tidal evolution of such systems. Lastly, I will outline how my original research described in Chapters 3 to 6 can help constrain some of these theories, and thus help answer questions such as the ones laid out in the previous paragraph.

[b] NASA Exoplanet Archive, 23 April 2021

[c] The exception to this is the closest planet to the Sun, Mercury, whose inclination undergoes chaotic evolution (Laskar 1994; Batygin et al. 2015)

[d] Whether this is astrophysical in origin or due to observational bias is a contentious topic (Zhu 2020; Weiss & Petigura 2020; Murchikova & Tremaine 2020)

In order to accurately interpret the observed exoplanet population in Figure 1.5, we first need an understanding of how the exoplanets presented in this figure are discovered. For example, someone who has never seen such a diagram before may remark on the fact that so many of the discovered planets are on short orbits ($\lesssim$10 days), compared to our innermost planet Mercury which has an orbital period of 88 days. It is worth spending a bit of time to understand this and other patterns in the figure. Accordingly, I will start by giving a conceptual overview of the most important methods we use to detect exoplanets and the biases they introduce. Later, in Chapter 2, I will describe these techniques in more detail, in particular the science we can extract from their observations.

1.1 Methods for exoplanet detection

A number of methods have been developed for detecting exoplanets since the inception of the field. The four main techniques are the radial velocity method, transit method, and those that rely on microlensing, astrometry, and direct imaging of exoplanets. While astrometry has not yet been widely applied to detect planets, this technique is expected to yield several thousand Jupiter-mass companions on wide orbits once the final data release of the *Gaia* mission becomes public (date TBD, Collaboration et al. 2016). Direct imaging accounts for roughly 50 detections. The microlensing technique is behind ~150 planetary detections, but offers very little chance of further study due to the transient nature of the method. Beyond these main methods, 17 planets have been discovered in multiplanetary systems by measuring transit timing variations (TTVs), and a few giant planets have been discovered by studying their tidal influence on the star's light curve. Indeed, the most successful methods for exoplanet detections are then the radial velocity method and transit method, which have yielded 960 (20 %) and 3432 (72 %) planet discoveries, respectively.[e]

1.1.1 The Doppler (radial velocity) method: measuring planet masses

1.1.1.1 Conceptual overview

Although the mass of a typical solar-type star is ~1000 times higher than a Jupiter-mass planet companion, the planet does not strictly orbit the star. They both orbit the *centre of mass* of the system, although the centre of mass of a typical star-planet system is within the star itself. If these two bodies move only due to the influence of their mutual gravitational fields, their orbits are described by Kepler's laws of planetary motion. These orbits take place in a two-dimensional plane which can be oriented randomly in three-dimensional space, and a full characterisation of the orbit requires knowledge of six orbital elements: the separation (semi-major axis) of the binary system, a; eccentricity (ellipticity) of the orbit, e ($e = 0$ for circular orbits); inclination of the orbit relative to the plane of the sky, i; longitude of periastron, ω, i.e. the orientation of the orbit within its own plane if $e \neq 0$; longitude of the ascending node, Ω, i.e. the position in the orbit where the orbital plane intersects the sky plane; and time of periastron passage $t_{\rm peri}$,

[e] All numbers are from http://exoplanet.eu as of July 2021.

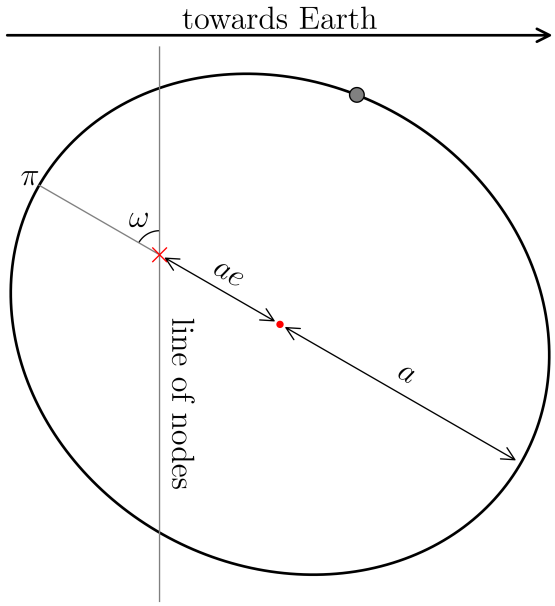


Figure 1.1: Elements of a Keplerian orbit. The massless particle (*grey*) moves clockwise in an elliptical orbit. The system is illustrated top-down, with the centre and focus of the ellipse denoted as a red dot and cross, respectively. The semi-major axis of the elliptical orbit is a and is the distance from the centre to the largest separation in the orbit. The eccentricity (ellipticity) of the orbit is given by e, with the product ae being the distance from the centre of the ellipse to its focus. The particle is closest to the focus at point π, which is the periastron. The system is viewed from the right, and the line perpendicular to the line-of-sight connecting the orbit through the focus of the ellipse is the line of nodes. For a non-circular orbit the argument of periastron, ω, is the angle from periastron to where the line of nodes intersects the orbit in the direction of the particle motion.

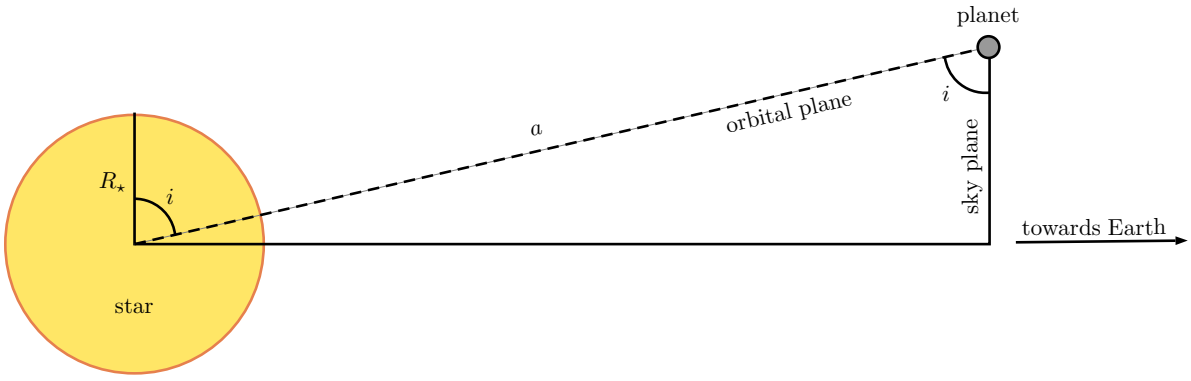


Figure 1.2: The inclination of the orbit. The orbit of a planet relative to the star is illustrated from the side (*edge-on*), and the observer sits to the right. The orbital plane can be inclined to the line of sight by the inclination angle i. When $i = 0°$ the system is observed face-on, and no radial velocity motion is seen from the observer's point of view. The radial velocity semi-amplitude is highest when the orbit is viewed edge-on ($i = 90°$). When $i \approx 90°$ the planet is likely to transit the star.

which is a reference time when the planet reaches the point in its orbit closest to the star (see Figure 1.1 and Murray & Correia 2010).

As we will see in Chapter 2, we can infer a, e, ω, $t_{\rm peri}$, as well as the orbital period, P just from measuring the velocity of the two bodies along our line of sight, i.e. *radial velocity*, as a function of time. Measuring the radial velocity of an object relies on the Doppler effect. Electromagnetic waves (such as visible light) are shifted to longer or shorter wavelengths when the emitting source is moving away or towards an observer, respectively, such as when when a star moves in response to the gravitational pull due to an orbiting planet (Lovis & Fischer 2010). When observing the spectrum of a star, the effect of Doppler shift due to the movement of the star will shift the position of its known spectral absorption lines relative to the rest frame. The magnitude of the velocity shift is given by the (non-relativistic) Doppler formula (Lovis & Fischer 2010; Perryman 2011)

$$\Delta v = \frac{\Delta\lambda}{\lambda_0}\, c = \frac{(\lambda - \lambda_0)}{\lambda_0}\, c, \tag{1.1}$$

where λ_0 is the rest wavelength where a given atomic species in the stellar atmosphere will absorb light, λ is the observed wavelength, and c is the speed of light. Thus in a star-planet system the planet will gravitationally tug on its star over the course of an orbit, changing the star's radial velocity, which we can measure from the positional shifts in the absorption lines using the Doppler equation in 1.1.

This method to detect exoplanets was not the first. The first three confirmed exoplanets were found orbiting the pulsar PSR B1257+12 (Wolszczan & Frail 1992; Wolszczan 1994): a rapidly spinning neutron star with an extreme magnetic field. Pulsars emits electromagnetic radiation along its magnetic poles, which if pointed towards the Earth arrive at extremely regular intervals. The presence of the planets was inferred by measuring periodic deviations in the arrival of the pulsar timings on Earth, caused by the changing light travel time due to the gravitational influence of the planets. Although this was a momentous discovery, the planets were likely formed in the aftermath of the supernova that created the neutron star, and thus did not necessarily represent a solar system that formed similarly to our own (Wolszczan & Frail 1992). Moreover, the low occurence of pulsars with magnetic poles facing Earth prevents scaling the method to find a large sample of planets. In contrast, when the Doppler method was used to detect 51 Pegasi b in 1995 (Mayor & Queloz 1995), it not only represented the first exoplanet orbiting a *main sequence* star like our Sun; it also demonstrated a feasible detection method that can be applied to the abundance of known solar-type stars. Ultimately, this discovery went on to create a new branch of astronomy focused on the discovery and characterisation of planets orbiting other stars, for which it was recognised with the Nobel Prize in Physics in 2019.

1.1.1.2 Trends from Doppler planets

Since the amplitude of the radial velocity variation of a star from the Doppler method is a response to the gravitational pull of the planet, the signature encodes information about the planet mass and its distance from the star since the gravitational force is proportional to m/a^2 (Murray & Correia 2010). It should be noted, however, that the radial velocity has no information on the size of the planet. Massive planets that

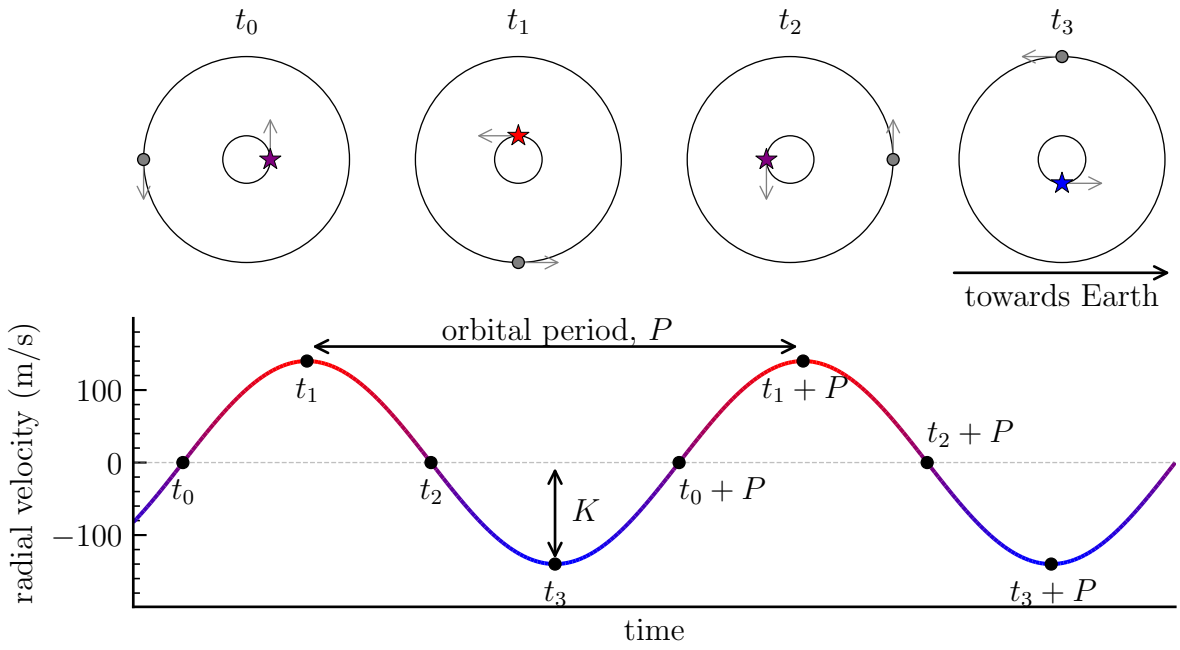


Figure 1.3: The radial velocity reflex motion of a star due to a planet on a circular orbit ($e = 0$). *Top:* The (exaggerated) orbit of a planet and star around the centre of mass is illustrated top-down at four times during a complete orbit, $t_0 - t_3$. The grey arrow denotes the direction of motion. The star is the star-shaped symbol and its colour denotes the radial velocity direction, with red and blue taken to mean maximum and minimum radial velocity. Purple colour denotes zero radial velocity motion because the star is moving only tangentially to the line of sight. *Bottom:* The radial velocity curve of the star observed over two complete orbits. The colour gradient is to show when the light is redshifted (star is moving away from the observer) and blueshifted (star is moving towards the observer). The times $t_0 - t_3$ are marked on the curve, which correspond to the positions in the orbits in the top panels. Half of the peak-to-peak radial velocity amplitude is K, and the radial velocity curve repeats every orbital period, P.

are close to the star create a high amplitude signal, and the opposite effect occurs for lower mass planets further from the star. As a result, the Doppler method is extremely successful at identifying close-in planets with masses down to a few times that of Earth's, corresponding to a radial velocity amplitude of just $\lesssim 1\,\mathrm{m\,s^{-1}}$ (Leleu et al. 2021; Rajpaul et al. 2021). This is illustrated in the lower panel of Figure 1.5, showing the masses of planets on orbits shorter than ~100 days. Beyond this ($P > 100\,\mathrm{d}$) the radial velocity semi-amplitude starts diminishing, and thus we are only sensitive to giant planets on long orbits. The absence of low-mass planets on longer orbits is therefore an observational bias, and does not indicate that those planets do not exist.

It should be noted, however, that the radial velocity is only a one-dimensional projection of a three-dimensional velocity vector, and thus does not constrain the orientation of the orbit in the sky plane (Ω), or the inclination of the orbit relative to the sky plane (i). Since i is generally unknown for a planet discovered by the Doppler method, there is a degeneracy between the inclination of the orbit and the mass of the planet: larger amplitude radial velocity variation can be caused by either a more massive planet, or by viewing the orbit closer to edge-on ($i \sim 90°$), or conversely for a smaller amplitude variation. Most of the masses of the planets reported in the lower panel of Figure 1.5 are therefore only lower limits denoted

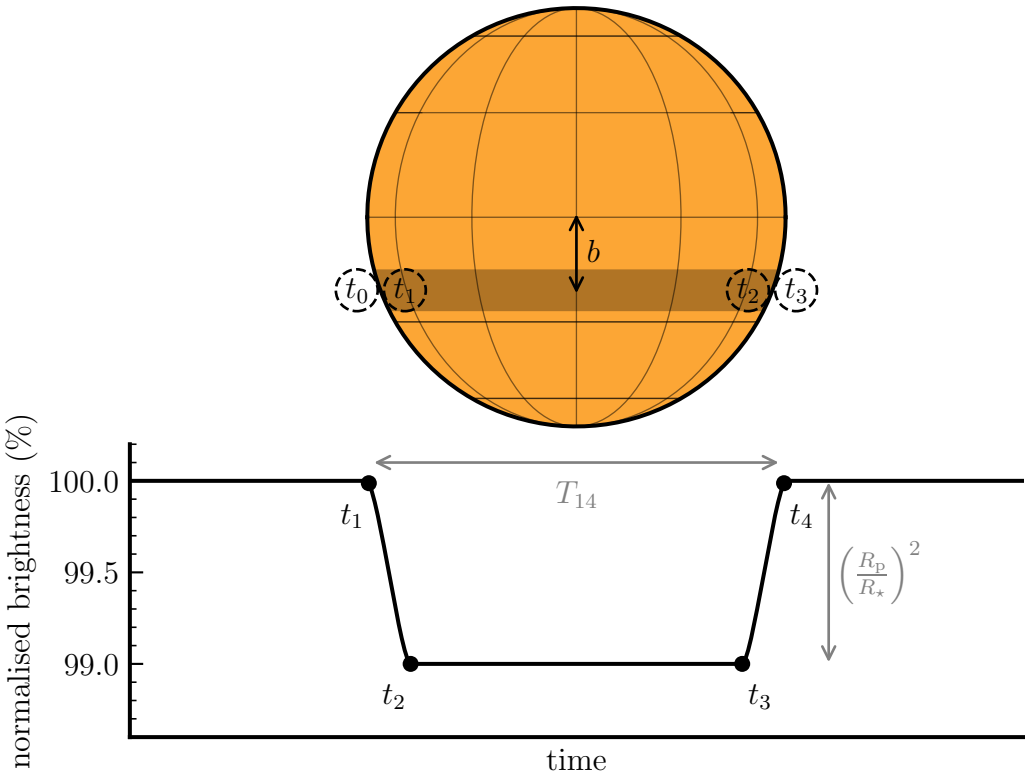


Figure 1.4: Transit light curve caused by a Jupiter-sized planet passing in front of a Sun-like star. The loss of light is proportional to the size ratio, while the transit duration ($T_14 = t_4 - t_1$) and ingress durations ($\tau = t_2 - t_1 = t_4 - t_3$) provide constraints on the impact parameter $b = a \cos i / R_\star$ and hence the orbital inclination, as well as the stellar density (see Chapter 2.1.1). This diagram was created using `starry` (Luger et al. 2019).

as $m \sin i$. Although this makes it difficult to infer the absolute mass of any given Doppler planet, a lower mass limit is enough to make an astrophysical interpretation of a population of planets like in Figure 1.5, because we know that the distribution of inclinations in planetary systems should be uniform in $\cos i$ (Winn 2010).

1.1.2 The transit method: measuring planet sizes

1.1.2.1 Conceptual overview

By far the most successful method for exoplanet discovery has been the transit method. The idea is simple: the inclinations of planetary orbits as seen from our line of sight are distributed uniformly in $\cos i$ (Winn 2010). A small fraction of these planets will have inclinations $i \approx 90°$, i.e. the system would be seen roughly edge-on from Earth. In these systems the planets would periodically pass in front of the star as seen from our point of view, causing a *transit* (similar to the Venus and Mercury transits within the solar system). Transits block out part of the stellar disc making it appear dimmer, thus by monitoring the brightness of stars (*photometry*) over time we can detect planets by finding *repeated* dimmings in the *light curve* of the star.

Figure 1.4 shows a diagram of a transit light curve, which here represents a Jupiter-sized planet transiting a star of the same size as the Sun. A transit light curve is characterised by four contact points, t_1 to t_4. The times between $t_1 - t_2$ and $t_3 - t_4$ are the *ingress* and *egress*, respectively, which describe the times at which the transit is partial. The transit is full between $t_2 - t_3$ when $b < 1$. Using simple distance travel calculations, one can show that the ingress/egress durations provide a measure of the scaled planet radius, $t_2 - t_1 = t_4 - t_3 = R_\mathrm{p} P/(\pi a)$, while the time between first and third contacts (or second and fourth) provide a measure of the scaled radius of the star $t_3 - t_1 = t_4 - t_2 = R_\star P/(\pi a)$. The orbital period P can be determined by measuring the time between successive transits. The total transit duration $T_{14} = t_4 - t_1$ is also directly observed from the light curve and also constrains the dimensionless parameter $a/R_\star$ as well as the impact parameter b, and hence the inclination i of the orbit (Chapter 2.1.1). The loss of light due to the transit is proportional to the ratio of sizes between the planet and star, $R_\mathrm{p}/R_\star$, thus the transit method also measures the size of the planet given the radius of the star, without having to know the size of the orbit.

The geometric transit probability, i.e. the probability that a planet orbit is inclined in such a way that it will transit, is inversely proportional to the semi-major axis, a (Haswell 2010; Winn 2010). Planets that are closer to the star are more likely to be transiting, compared to planets further from the star. For a giant planet on a 4-day orbit that is randomly oriented in space, the transit probability is ~10 %. In contrast, if we imagine an alien civilisation observing our Sun, the probability they would see any of our own planets transiting is <1 % for all our planets except Mercury (1.2 %). Note that these are just *geometric* transit probabilities, and do not take into account how often planets of a certain size at a given orbital period occur in nature (i.e. the occurence rate), which further reduces the chance at detecting transiting planets. As a result of the low probability of observing a transit, transit surveys that search for planets need to observe thousands of stars simultaneously to increase their chances of detection. It is also for this reason that the method is so successful, as it allows simultaneous monitoring of even hundreds of thousands of stars (as was done for the *Kepler* spacecraft, Borucki et al. 2010), whereas the Doppler method is restricted to one star at a time (and also works in a fundamentally different way).

Contrary to the Doppler method, the transit method can typically not constrain the mass of the planet, but the observation of a transit ensures $i \approx 90°$ which allows an absolute mass determination for Doppler planets. As we have seen, transits hold information on the size of the planet because the loss of light during transit is proportional to the area the planet covers on the stellar disc. As a result the two methods are perfectly complementary and together they can be used to constrain the bulk density of the planet to determine its bulk composition.

1.1.2.2 Trends from transiting planets

The sizes of the planets discovered by the transit method is shown in the upper panel of Figure 1.5. Because of the geometric transit probability discussed above, the transit method is most sensitive to planets on close orbits to the star, which is one factor that explains why most of these have orbital periods $\lesssim$10 days. Another factor is that most transit surveys — e.g. WASP (Pollacco et al. 2006), HATNet

(Bakos et al. 2004), HATS (Bakos et al. 2013), and KELT (Pepper et al. 2007) — observe from the ground and can only observe for ~8 hours per night. Transits that happen outside of night time will therefore not be visible, and so ground-based surveys have to observe a group of stars for several months on average to be able to detect recurring transits of planets on close orbits. Planets beyond 10 d orbits are more difficult to catch transiting from the ground. There are a few contributing effect to this. One important reason is that there is an order of magnitude fewer planets on 10 d orbits compared to a few day orbits (Santerne et al. 2016). In addition to this, short nights, bad weather, technical interruptions, and fewer transits means that it is difficult to observe repeated transits from the ground, which is key to detect a periodic signal. Therefore most transiting planets on wider orbits are discovered by space telescopes, in particular *Kepler* (Borucki et al. 2010), which stared at a fixed patch of the sky uninterrupted for four years.

Ground-based surveys are mostly sensitive to giant planets as these produce the deepest transit signals. As a result these surveys have been quite successful in discovering *hot Jupiters*, i.e. giant planets on close orbits to their star (<10 d), shown as the population in the upper left part of the radius diagram in Figure 1.5. The smaller planets in Figure 1.5 — those smaller than Neptune — are almost exclusively discovered by telescopes in space, such as CoRoT (Baglin et al. 2006), *Kepler*, and the currently active *TESS* mission (Ricker et al. 2015). Notably exceptions to this are planets orbiting M dwarf stars, such as TRAPPIST-1 (Gillon et al. 2017). One of the benefits of a space telescope is that it allows observations without interference from Earth's atmosphere, which is one of the limiting factors that prevents us detecting small transit signals from the ground.

1.2 Demographics of exoplanets

Now that we have familiarised ourselves with the detection methods we can study the different populations of planets that have been uncovered in Figure 1.5. There are three main populations of planets apparent in the mass diagram: *(i)* hot Jupiters (high mass, large radius, short period, Santerne et al. 2016), *(ii)* cold Jupiters (high mass, large radius, long period, Wittenmyer et al. 2020), and *(iii)* sub-Neptunes/super-Earths (low mass, small radius, Mayor et al. 2011). The cold Jupiters are not apparent in the radius diagram because of the low transit probability at long orbital periods, as discussed in the previous Section.

In the Sections below we will refer to giant planets as those that are Jovian or Neptunian worlds, i.e. those with a mass in the range ~0.1–13 $M_{\rm Jup}$, and radii between ~0.3–2 $R_{\rm Jup}$. Where I refer to small planets, I mean those that are Terran or sub-Neptunian, with masses between ~1–20 $M_\oplus$ and radii between ~1–3 $R_\oplus$ (Chen & Kipping 2017).

1.2.1 Giant planets

Hot Jupiters are thought to be physically similar to Jupiter — from which they derive their name — but they orbit much closer to their star (P < 10 days). They are the most well studied class of planets due to

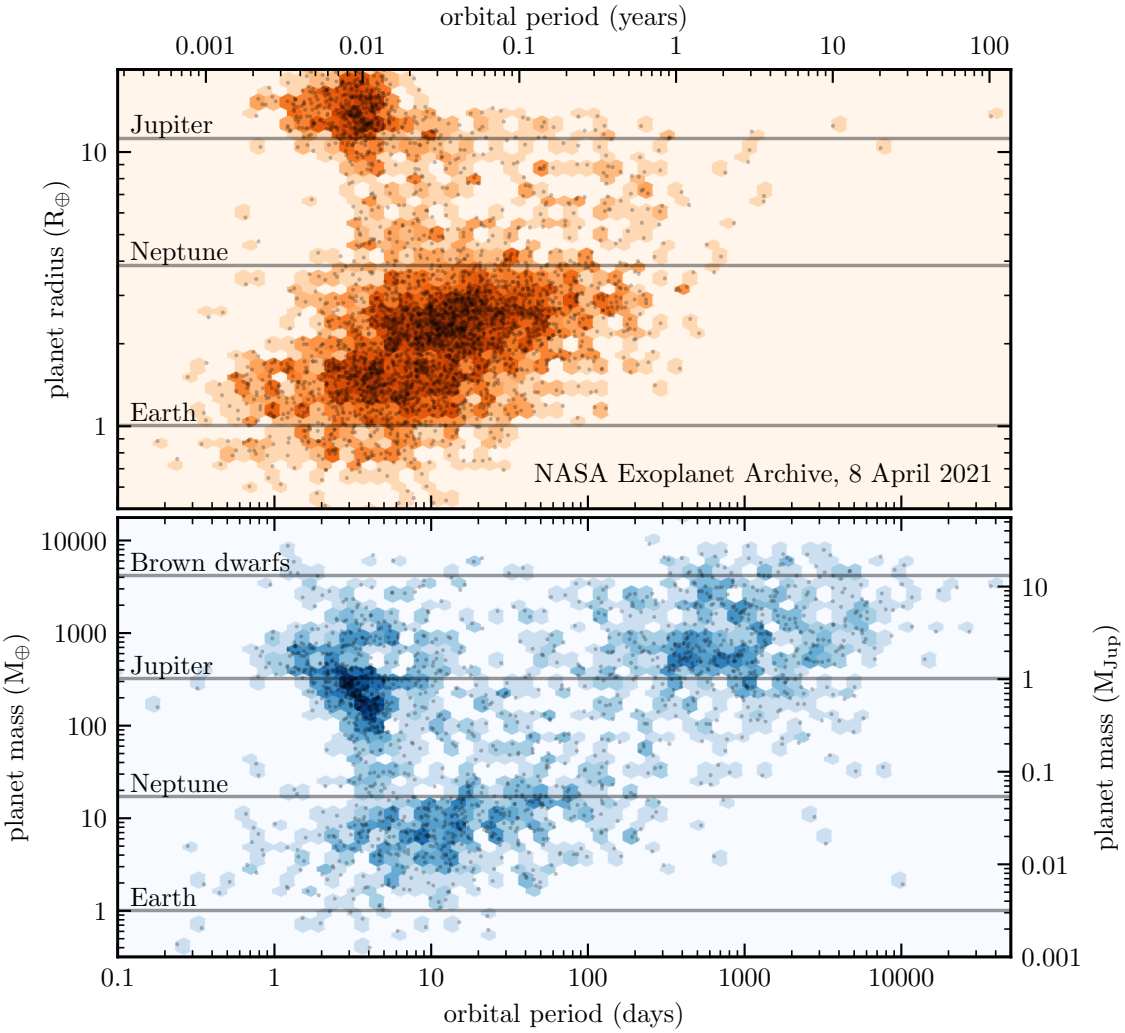


Figure 1.5: The radii (*top*), masses (*bottom*), and orbital periods of confirmed exoplanets as of April 2021, obtained from the NASA Exoplanet Archive. Darker regions indicate a higher density of planets.

their high mass, large radius, and proximity to the star, all of which has enabled a detailed study. They are (likely) comprised of a solid core ($\gtrsim 10\,M_\oplus$) with a significant gas envelope that is predominantly made up of H/He (Chabrier et al. 2014; D'Angelo et al. 2010). Given their proximity to the star they are strongly irradiated, which has facilitated the detection of various atomic and molecular species in their atmospheres such as Na, K, H_2O, TiO, and many, many others (see Birkby 2018 for a review); studies of atmospheric dynamics such as measurements of their albedo, heat redistributions, and wind speeds (Demory et al. 2013; Ehrenreich et al. 2020). Despite their abundance in Figure 1.5, hot Jupiters are rare; only 0.5 % of Sun-like stars host them (Mayor et al. 2011; Wright et al. 2012; Santerne et al. 2016), thus they are over-represented in the diagram due to the transit and radial velocity method being biased towards finding short period planets.

Another giant planet population in Figure 1.5 are the cold Jupiters, which more closely resemble Jupiter because they are more widely separated from their star ($P > 300$ days). Not much is known about these planets as their long orbital periods prevents a detailed study despite being the most common

population of *giant* planets, with an occurence rate of 4–11 % (Wittenmyer et al. 2020).

An interesting aspect in Figure 1.5 is the low density region between the hot and cold Jupiters, i.e. giant planets with orbital periods between 10 days and ~100 days which are sometimes referred to as warm Jupiters. Giant planets at these orbital periods are roughly as common as hot Jupiters with an occurrence rate of about 1 % (Santerne et al. 2016), but there is some evidence that hot and warm Jupiters are distinctly different outcomes of planet formation. Half of warm Jupiters have *nearby* small planets, while hot Jupiters do not[f] (Huang et al. 2016).

1.2.2 Small planets

One of the greatest discoveries to have come from space based transit surveys, in particular *Kepler*, was that planets with masses and sizes between that of Earth and Neptune (~5–20 $M_\oplus$, ~2–4 $R_\oplus$) orbiting their host star closer than Mercury does the Sun (~3–100 d) are the most common planets in the universe (Fressin et al. 2013). This is particularly interesting in the context of the solar system, where we have no known equivalent planet. In fact, looking at the radius diagram in Figure 1.5, Neptune-sized planets are quite unlikely to form. The small planet population is most commonly referred to as sub-Neptunes, or super-Earths. Formally speaking, sub-Neptunes and super-Earths may be distinguished; sub-Neptunes are thought to be scaled-down versions of Neptune (sometimes also called mini-Neptunes), i.e. they have a solid core with a thin H/He gas envelope that only makes up a few per-cent of its total mass. On the other hand, super-Earths are scaled-up versions of Earth, thought to be predominantly rocky where any atmosphere makes up a negligible fraction of its total mass. However, the line separating the two is blurry and is an active area of research (c.f. the radius valley; Fulton et al. 2017; Van Eylen et al. 2018), thus in practice the terms sub-Neptunes and super-Earths are sometimes used interchangeably.

One of the key factors that separates sub-Neptunes on close orbits from hot Jupiters is that small planets are frequently part of multiplanet systems where two or more planets orbit the star. These neighbouring planets are often observed to form orbital resonances, where the ratio of orbital periods between the outer and inner planet equal some integer fraction. Common orbital resonances are 2:1, 3:2, and 3:1, though more complex resonances between neighbouring planets have been observed (see e.g. Figure 6 in Winn & Fabrycky 2015).

In the next Section I will examine the qualitative differences between hot Jupiter and sub-Neptune systems in the context of their formation and subsequent radial migration, which may explain some of the differences in architectures that we see between sub-Neptunes and gas giants.

1.3 Planet formation and migration

In this Section we will look at some physical processes that might have led to the distribution of exoplanets seen in Figure 1.5. Stars are born from the gravitational collapse of overdense clumps of interstellar molecular clouds. These clouds consists of both gas (mostly H_2) and dust (micrometre-sized

[f] There is only one exception to this rule, WASP-47b (Becker et al. 2015).

grains of silicates and water ice) in an approximate 100:1 mass ratio, both which play important roles in the formation of stars and planets (Chambers 2010; Roberge & Kamp 2010). As the gas cloud contracts under gravity it starts to rotate faster due to conservation of angular momentum, which flattens the gas cloud into a disc that surrounds the central protostar, i.e. a circumstellar disc. Once the star has accreted enough material to attain hydrostatic equilibrium (entering the pre-main sequence phase), the remaining material makes up a protoplanetary disc wherein planets are born (Chambers 2010; D'Angelo et al. 2010; Roberge & Kamp 2010).

1.3.1 Formation of rocky cores and super-Earths

In the initial stages of terrestrial planet formation tiny micrometre-sized dust grains collide and stick together by electrostatic forces to form larger particles, all of which tend to grow at similar rates. Though there is some uncertainty around the exact mechanism for the next stage, these building blocks continue to collide and grow into planetesimals of several hundred metres to a few kilometres (comets, asteroids) (Chambers 2010). Planetesimals continue to collide, which can result in either growth or fragmentation depending on the impact velocity and strength of the body. Once planetesimals reach sufficient mass, they tend to grow much faster as they gravitationally attract nearby objects to increase the chance of collision and growth (Chambers 2010). This means that larger planetesimals grow faster than smaller ones, until each region in the disc is dominated by a single large body called a planetary embryo (Chambers 2010; Lambrechts & Johansen 2012). The entire system may at this point contain a few tens to hundreds of embryos (or *oligarchs*) of Mars mass or similar ($0.1\,M_\oplus$) (Raymond et al. 2014). The growth of these oligarchs is slower, but they continue to grow by accreting smaller planetesimals near their orbit, clearing out more of the immediate area. The timescale at this stage of formation is roughly $\lesssim$2 Myr (Kokubo & Ida 2002; Chambers 2010; Raymond et al. 2014). Up until this stage dynamical interactions between oligarchs that would otherwise excite their eccentricities are instead damped due to gas drag and dynamical friction from smaller planetesimals (Chambers 2010; Raymond et al. 2014).

The final stage of terrestrial planet formation is late-stage growth. During this phase the Mars-sized embryos acquire thick atmospheres from the surrounding gas. Planetesimals that pass through the atmosphere are slowed, which increases the rate of growth. Soon thereafter the protoplanetary disc disperses such that there is no longer enough gas or planetesimals to damp the dynamically excited eccentricities and inclinations of the oligarchs. Neighbouring embryos may therefore end up on crossing orbits, thus late-stage growth is a chaotic phase characterised by pairwise collisions of giant embryos, and is also where the architecture of planetary systems are set, such as their masses, semimajor axes, eccentricities and inclinations (Raymond et al. 2014), notwithstanding any tidal evolution, see Section 1.4.3. This stage may go on for 10 Myr–100 Myr; in fact Earth is believed to have taken ~30 Myr to form based on measurements of radioactive isotopes in meteorites (Kleine et al. 2002, 2009).

Planetesimal or pebble accretion such as described above can form planets up to a few tens of $M_\oplus$ in the mid to outer part of the disc (>3 AU) where there is enough solid material, in particular water ice, to form the planetary cores (Chambers 2010; Raymond et al. 2014). However, most of the super-Earths

observed in exoplanet systems have separations (<1 AU), many of them even orbiting their star within 10 days (hot super-Earths, see Figure 1.5). One of the most important questions is then whether these super-Earths formed where we observe them (*in situ formation*), or whether they formed at large distances and migrated inwards. In situ formation would require the inner protoplanetary disc (within 1 AU) to have a mass upwards of a few tens of Earth masses to provide enough solid material to form the multiple super-Earth planetary systems that we observe. Yet this is difficult to reconcile with current models of the radial density profile of protoplanetary discs, which might suggest that they migrated to their current positions instead (see Raymond et al. 2014 and references therein). In fact, super-Earths orbiting binary stars (circumbinary orbit) *must* have migrated since *in-situ* formation is ruled out (Orosz et al. 2012; Paardekooper et al. 2012; Martin 2018). Nevertheless, in-situ models of super-Earths formation are successful in reproducing some of the observed trends (Lee et al. 2014; Lee & Chiang 2017).

1.3.2 Gas giant planet formation

Observations indicate the (gaseous) protoplanetary disc dissipates over a timescale of 2 Myr–10 Myr (Mamajek 2009). Since giant planets most likely attain their significant gas envelope from the surrounding disc, they have to form within this time and therefore much faster than smaller planets. Early Doppler surveys noted that hot Jupiters are most frequently found around metal-rich stars, the so-called planet-metallicity relation (Santos et al. 2004; Valenti & Fischer 2005). This suggests Jupiter-mass planets have a central solid core, presumably made of various silicates and ices, and therefore form via the core accretion scenario. Core accretion consists of building a massive protoplanetary core, followed by rapid gas accretion onto the core. To achieve runaway gas accretion the core mass needs to reach $\sim 10\,M_\oplus$ before the gas disperses, i.e. within a few Myr (D'Angelo et al. 2010). Giant planet cores grow by the same principles as described in Section 1.3.1 but need to have access to more material and grow much faster than the timescales for terrestrial planets. Rapid core growth can be aided by a continuous influx of pebbles transported from the outer disc to the inner disc (Lambrechts & Johansen 2012), but other factors may also influence the core growth. We refer the reader to Pollack et al. 1996; D'Angelo et al. 2010; Chabrier et al. 2014 for more information on giant planet formation.

Core growth is most favourable beyond the system's snow line because of the abundance of solids in the form of water ice. The snow line refers to the distance from the star where water cannot exist in liquid form, which is around 3 AU from the Sun in the solar system. Unlike the hot super-Earths, in-situ formation of hot Jupiters is considered extremely unlikely due to the lack of solids at <0.1 AU, thus the prevailing evidence suggests they formed beyond the snow line and migrated to their current positions (Bodenheimer et al. 2000; Ida & Lin 2004).

1.3.3 Brown dwarf and binary star formation

Brown dwarfs are defined as substellar objects with masses between $\sim$13–80 $M_{\rm Jup}$, and are able to sustain deuterium burning in their core (Chabrier et al. 2014). Field (solitary) brown dwarfs are thought to form similarly to stars, but are unable to reach sufficient mass to ignite hydrogen fusion. Since the dawn of the

exoplanet era, a number of brown dwarfs orbiting Sun-like stars have been discovered as a byproduct of the search for exoplanets, both in Doppler (Sahlmann et al. 2011) and transit surveys (e.g. Chapter 3, Hodžić et al. 2018, see also Carmichael et al. 2020, 2021 and references therein). The formation of brown dwarf *companions* to stars may therefore occur in a different way. In this scenario a massive protoplanetary disc surrounding the star may become gravitationally unstable such that it starts to contract and accrete nearby gas in the process (Kratter & Matzner 2006; Chabrier et al. 2014). In both these scenarios brown dwarfs do not have solid cores and thus they are naturally distinct from planets due to their different formation processes.

The discovery of several massive hot Jupiters (e.g. HAT-P-2b, Bakos et al. 2007) with masses upwards of $10\,M_{\rm Jup}$ have cast doubts on this orderly picture, showing that core accretion may be able to produce objects that fall into the brown dwarf regime. Another piece of evidence that complicates the picture is that there is a distinct lack of brown dwarfs with intermediate masses between ~40–55 $M_{\rm Jup}$ often referred to as the brown dwarf desert (Grether & Lineweaver 2006; Sahlmann et al. 2011; Ma & Ge 2014; Triaud et al. 2017), but the frequency of brown dwarfs with masses on either side of this valley increases rapidly. These observations could indicate that the low and high-mass brown dwarfs constitute two separate populations: the low mass brown dwarfs predominantly form via core accretion, while the higher mass brown dwarfs do so from fragmentation of the protoplanetary disc. The two populations would conceivably have some overlap which could indicate some giant planets could also form via disc fragmentation (Chabrier et al. 2014).

Binary stars, in particular those that are considered close binaries ($a \lesssim 10\,$AU), are also thought to form from fragmentation due to disc instability (Kratter & Lodato 2016). In this case they clear out an inner cavity within the original circumstellar disc, forming a *circumbinary* disc that surrounds both stars from which they accrete their gas (Tokovinin & Moe 2020). Planet formation can also happen in circumbinary discs, as evidenced by discoveries of over a dozen transiting circumbinary planets to date (see e.g. Chapter 3, Kostov et al. 2020), with ongoing efforts to detect circumbinary planets with the Doppler method (Martin et al. 2019). Most of the hitherto detected circumbinary planets orbit at or shortly beyond the nearest stable orbit, found at roughly six times the binary orbital period. However, in-situ formation at such close separations in binary systems can be excluded due to large velocity shear, thus they *must* have migrated there, presumably through disc interaction. Binary systems therefore offer a great laboratory to test planetary formation theories. Binaries on wider orbits may instead form from core fragmentation in the original protostellar nebula in which case they accrete from their respective circumstellar discs (Kratter & Lodato 2016), but can end up on close orbits through Kozai cycles with tidal friction (Fabrycky & Tremaine 2007).

1.3.4 Planetary migration

As alluded to in the previous sections, planet embryos are continuously perturbed by their environment during formation, e.g. from gas drag or interactions with other embryos or outer giant planets. These interactions can change their orbits significantly, in particular their semimajor axis which is referred to

as radial *migration* (Ward 1997). However, once planet embryos reach sufficient mass, gas drag becomes a negligible effect. Radial migration of planet bodies during the gaseous disc phase is instead driven by gravitational interactions with the surrounding disc (Lubow & Ida 2010). These interactions generate torques on the planet that are either directed inwards or outwards, depending on local disc conditions, though there is a tendency for migration to be directed towards the star (Lubow & Ida 2010). Migration can also occur after the gas has dissipated, which is referred to as disc-free migration, and is often due to gravitational perturbations from neighbouring planets or stars (e.g. Fabrycky & Tremaine 2007; Chatterjee et al. 2008). Migration in one form or another is thought to have played a crucial role in producing hot Jupiters, as they are unlikely to have formed in-situ (Bodenheimer et al. 2000). In the following we will examine the different mechanisms for shrinking planetary orbits.

Disc migration

Planet migration due to interaction with the disc often boils down to two regimes: *(i)* planets that are not massive enough to clear a gap in the disc, and *(ii)* planets that have enough mass to clear a gap, which affects the density distribution in the disc. The first scenario is referred to as Type I migration and is the regime for terrestrial planet cores, while the second scenario is referred to as Type II migration and is the regime of giant planets.

Type I. When discussing the orbits of planets embedded within discs, it is important to remember that the gas in the disc near the planet is also moving at (near) Keplerian velocities. Thus the relative angular velocity difference between a planet ($\Omega_{\rm p}$) and the local gas ($\Omega_{\rm gas}$) is usually small. The orbital frequency of the disc varies with distance r from the star as (Lubow & Ida 2010)

$$\Omega(r) = \sqrt{\frac{GM_\star}{r^3}}, \tag{1.2}$$

where G is the gravitational constant and $M_\star$ is the stellar mass, as before. The orbital frequency of the planet is then $\Omega(a)$ where a is the semi-major axis. When the gas passes in the vicinity of the planet it gravitationally interacts and exchanges energy and angular momentum in the process. Gas that orbits just interior to the planet moves faster (Equation 1.2) and the gravitational interaction with the planet causes the gas to lose angular momentum. Gas that orbits exterior to the planet is slower, but here the gravitational interaction increases the angular momentum of the gas. In this way angular momentum is continuously moved to the outer parts of the disc, while material flows inwards (Lynden-Bell & Pringle 1974; Lubow & Ida 2010). For small planets the gravitational torques, or equivalently the Hill sphere, are not large enough to clear a gap in the disc as the gas is constantly replenished by inwards-moving gas arising from turbulent viscosity (Lubow & Ida 2010). This is the Type I migration scenario. Multiple inwards-migrating planets will naturally form a resonant chain, which can explain some resonant multiple planet systems (Raymond et al. 2014; Gillon et al. 2017).

With this picture in mind, there are two dominant torques that drive migration in the Type I scenario: *(i)* Lindblad torques and *(ii)* corotation torques (Goldreich & Tremaine 1979, 1980). Both of these

torques arise due to resonances in the velocities between the gas and planet. Lindblad resonances occur when gas that passes by the vicinity of a planet satisfies the condition $\Omega_{\rm gas}/m\Omega_{\rm p} = m/(m \mp 1)$, i.e. the orbital frequency of the disc is related to that of the planet by an integer m (Lubow & Ida 2010). For each m (except $m = 1$) there are two Lindblad resonances, one inside the planet orbit (minus sign in the denominator on the right hand side) and one outside the orbit (plus sign). These resonances excite spiral density waves in the gas that propagate outwards from the planet, carrying angular momentum and energy. The inner resonance therefore creates a torque on the planet that pushes it outwards, and likewise the outer resonance pushes it inwards (Goldreich & Tremaine 1979). For a given m the outer resonance location is slightly closer to the planet than the inner resonance, thus the net effect tends to be inwards migration (Ward 1997; Lubow & Ida 2010).

Gas that is on the same orbit as the planet will interact differently and gives rise to another torque due to resonance from corotation ($\Omega_{\rm gas}(r) = \Omega_{\rm p}$) (Goldreich & Tremaine 1979). If we consider the motion of the gas (moving at Keplerian velocity) in the inertial frame of the planet, gas particles that are slightly outside the orbit of the planet will have a lower velocity and thus appear to approach the planet. These particles will then be deflected by the planet onto an interior (faster) orbit, surrendering angular momentum to the planet. Since the particles are now on an interior orbit, they will appear to be moving away from the planet (taking a U-turn) until they catch up with the planet from behind. Again they are deflected by the gravitational potential of the planet onto an exterior orbit (another U-turn), but have now regained the angular momentum (Lubow & Ida 2010). These particles move in closed *horseshoe* orbits and — unlike Lindblad resonances — cannot exchange angular momentum with the disc outside of the coorbital region. In the case of a uniform disc density profile, the net effect is zero torque on the planet (Lubow & Ida 2010). However, the density of the disc varies as a function of radius (Roberge & Kamp 2010), which will impart some turbulent viscous torques on the disc (Goldreich & Tremaine 1979; Lubow & Ida 2010). These torques break the symmetry of particles on horseshoe orbits, allowing angular momentum exchange with the outside disc, which in turn can exert a continuous torque on the planet that causes it to migrate (Lubow & Ida 2010). The timescale for Type I migration is roughly 10^5 years, which is currently too fast compared to the lifetime of the disc (Lubow & Ida 2010). It is worth noting that corotation torques account for only a few tens of percent of the Lindblad torques, thus the latter is more important (Ward 1997; Lubow & Ida 2010).

Type II. In the Type I regime the planet continuously pushes material away from its orbit due to an exchange of angular momentum, but its mass is too small to clear a gap. Once a planet reaches a mass beyond $\gtrsim 0.2\,M_{\rm Jup}$ (giant planets) its tidal torques on the nearby gas is larger than viscous torques, which creates a gap in the disc along the planet's orbit (Lin & Papaloizou 1986; Lubow & Ida 2010). The torque acting on the planet is in this case still provided by turbulent viscosity which acts to close the gap, and this is referred to as Type II disc migration. The timescale for Type II migration is tied to the viscous evolution of the disc, roughly 10^5 years, again too fast considering the abundance of giant planets on separations beyond 1 AU in Figure 1.5 (Lubow & Ida 2010). The population of hot Jupiters indicate that

migration must be halted at some point, for example when they reach the inner cavity where it may be stopped by magnetic field interaction or tidal interaction with the star (Lubow & Ida 2010).

Disc-free migration

A number of other mechanisms can cause planets to migrate after the disc has dissipated, all of which fall under the wide umbrella of disc-free migration (e.g. Rasio & Ford 1996; Fabrycky & Tremaine 2007; Chatterjee et al. 2008; Naoz et al. 2011b; Petrovich et al. 2019). Disc-free migration is dynamical in nature; it is caused by gravitational interactions between the planet and other substellar or stellar objects in the system. These processes generally boil down to two steps: *(i)* the planet gains a highly eccentric orbit due to some dynamical mechanism, and *(ii)* the eccentric orbit brings the planet sufficiently close to the star at periastron such that tidal friction causes the semimajor axis to decay over time (Section 1.4.3). There are a number of dynamical effects that can place the planet on eccentric orbits:

Planet-planet scattering. When multiple planets migrate via tidal interaction with the protoplanetary disc they naturally form a resonant chain (Raymond et al. 2014). These resonances can excite both eccentricities and mutual inclinations in the planets that are damped by the disc during the gas phase (Lubow & Ida 2010). However, after the disc has dissipated eccentricity excitations may lead to crossing orbits that lead to instabilities in their orbits (Matsumura et al. 2010). During such an event they receive a gravitational boost which further raises their eccentricities and inclinations and can lead to one of the planets being ejected from the system, while the other ends up on a very eccentric orbit (Rasio & Ford 1996; Chatterjee et al. 2008).

Secular chaos. Planets on wide orbits can induce long-term (secular) perturbations in the orbits of inner planets, which can grow their eccentricities and inclinations to high values and cause instability in planetary systems (Wu & Lithwick 2011; Naoz et al. 2011a).

Kozai-Lidov. Distant massive planets or stellar companions that are inclined by $\gtrsim 40°$ to the inner planet and star binary can excite Kozai oscillations in the inner orbit, which is a periodic exchange between eccentricity and inclination (Lidov 1962; Kozai 1962; Wu & Murray 2003; Fabrycky & Tremaine 2007). The timescale for these oscillations is given by (Fabrycky & Tremaine 2007)

$$\tau_{\text{Kozai}} = \frac{P_{\text{outer}}^2}{P_{\text{inner}}}(1 - e_{\text{outer}}^2)^{3/2} \tag{1.3}$$

1.4 Observational clues to planetary formation and migration

Most planetary systems that we observe are several billion years (Gyr) old; only a couple dozen known planetary systems are ~100 Myr or younger and can thus be considered actively forming or very recently formed (see Chapter 7.2.1). Since we are unlikely to observe planetary systems during their formation (except for a few candidates in young planet-forming discs, ALMA Partnership et al. 2015), our knowledge of the processes that created the planets and the mechanisms that caused them to potentially migrate (i.e. change the size of their orbit) is almost entirely based on what we can observe at present-day.

As we saw in in the previous Section, the theories therein describe viable pathways for how planets can form and migrate. Each of these might predict different outcomes for how the final orbits of the putative planets might look like, how many planets should be created, and perhaps what their atmospheric composition would be. Our job is to gather observational clues that can be traced back to the conditions at formation. This way we might be able to answer the question whether nature shows a preference for one type of process over another.

Some of the observables that can inform us of the formation of planets include (but are not limited to) the amount of metals[g] (metallicity) in atmospheres of planet-hosting stars (Santos et al. 2004; Fischer & Valenti 2005; Osborn & Bayliss 2020), elemental abundances (or often ratios of abundances, e.g. C/O) in the atmospheres of planets (Madhusudhan 2012), the number of planets in the system, their masses and sizes, and in particular their orbital elements (e.g. Mayor et al. 2011; Fressin et al. 2013). Each of these are active research areas in exoplanetary science, but most relevant to this thesis is the study of planetary orbits, where the angle between the angular momentum vectors of the stellar spin and planetary orbit, i.e. *stellar obliquity*, ψ, is of particular interest (Winn & Fabrycky 2015; Triaud 2018). An illustration of the relevant geometry is shown in Figure 1.6.

One of the key differences between disc migration and disc-free migration is that the orbits of the planets that migrate through disc interaction are expected to be aligned with the stellar spin, assuming the disc itself is in the plane of the stellar equator (Batygin 2012). Disc-free scenarios, on the other hand, are dynamical in nature and produces highly eccentric and inclined planets relative to the star. Measuring the stellar obliquity may in theory offer a distinction between these two scenarios. However, one can imagine that planetary migration happens as a mix of different processes, for example partial disc-migration followed by high eccentricity tidal migration, or secular interaction that produces mutually inclined planets triggering Kozai oscillations and high eccentricity tidal migration (Nelson et al. 2017; Nagasawa et al. 2008). A further complication is that some theories are able to produce inclined planets from disc interaction alone, either by gravitational interaction with a warped outer disc (Terquem & Ajmia 2010; Terquem 2013), or due to a distant stellar companion tilting the disc with respect to the star (Lai et al. 2011; Batygin 2012; Lai 2014; Zanazzi & Lai 2018). Measuring the stellar obliquity may therefore not offer an explanation for the origin of individual systems, but it may still offer clues to the dominant migration mechanism of exoplanets (Nelson et al. 2017).

1.4.1 Measuring obliquities of exoplanet host stars

Practically all stars that we can observe are spatially unresolved in our telescopes. This means that the light that we receive from the star — whether we study its brightness or spectrum — is an average over its visible hemisphere, so-called *disc-integrated* light. This means that we cannot in general *see* the orientation of the star. Yet there are certain aspects in the light curve and spectrum of stars that is sensitive to the stellar inclination, $i_\star$. One such observable is the projected rotational velocity of the star, $v \sin i_\star$, which can be the dominant broadening mechanism in absorption spectra (Gray 1984; Doyle et al.

[g] In astronomy, "metals" are taken to mean any elements heavier than helium.

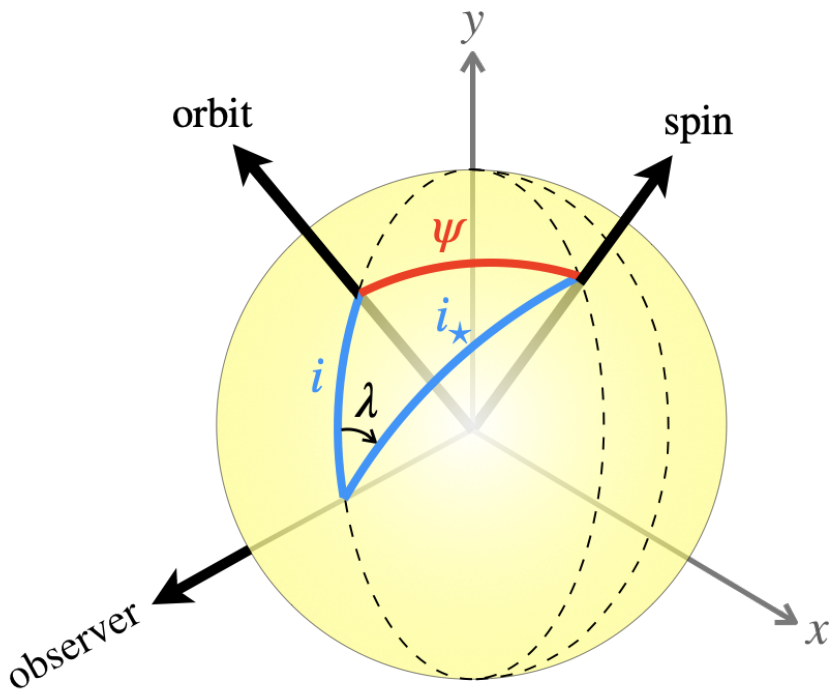


Figure 1.6: The geometry of a star in relation to a planet orbit. The observer views the system along the z axis (labelled *observer*). The axis normal to the planet's orbital plane is labelled *orbit*, and the stellar rotation axis is labelled *spin*. The angle between the observer and *orbit* is the orbital inclination, i, while the angle between the observer and *spin* is the stellar inclination, $i_\star$. The obliquity of the star is the angle ψ. The Rossiter-McLaughlin effect measures the sky-projected obliquity, λ. Credit: Josh Winn and Simon Albrecht (Albrecht et al. 2021).

2014). Another is the rotational splitting in frequency spectra of stars obtained from long-duration and high-frequency brightness measurements (Chaplin et al. 2013; Huber et al. 2013). Moreover, if the planet is transiting then we know that $i \approx 90°$, which together can place constraints on the obliquity (Triaud 2018). Note that $i_\star$ is the inclination of the *star*, not to be confused with the inclination of the orbit, i, which we introduced in Section 1.1.1. The difference between $i_\star$ and i is shown in Figure 1.6. In this figure, "orbit" refers to the angular momentum vector of the orbit, which is normal to the orbital plane of the planet. The angle between this vector and the observer's line of sight is the orbital inclination, i.[h] Likewise, "spin" refers to the stellar spin angular momentum vector, which is the axis around which the star rotates and is perpendicular to the stellar equator. The angle between this vector and the observer is $i_\star$. The angle between the two angular momentum vectors is the stellar obliquity, ψ (Albrecht et al. 2021). Since we cannot observe the obliquities of stars directly, we have to rely on indirect methods to measure $i_\star$ (Chaplin et al. 2013; Huber et al. 2013), or in most cases λ (Triaud 2018) which is the two-dimensional line-of-sight projection of the (true) obliquity ψ, which is also illustrated in Figure 1.6. Here we will give an overview of the most important methods that have been developed to constrain the obliquities of stars.

[h]Note that i is measured between 0°–90°, therefore even though we measured i as the angle between the sky-plane and orbital plane in Figure 1.2, the angle between the observer and orbital angular momentum vector in Figure 1.6 is equivalent.

The Rossiter-McLaughlin effect

The most successful method for determining obliquities of stars is the Rossiter-McLaughlin effect, which forms the foundation of this thesis (Rossiter 1924; McLaughlin 1924). This effect is a radial velocity signal that occurs during a planetary transit, and thus relies on the Doppler effect that we described in Section 1.1.1. All stars rotate, and regardless of the orientation of the star the rotational velocity will always have a line-of-sight component as long as we do not view the star along its poles (when $i_\star = 0°$ or 180°). This means that one hemisphere of the star will have a velocity component towards the observer and the light from this hemisphere will appear blueshifted, while the other hemisphere will appear to move away from the observer and thus be redshifted (Triaud 2018). In the absence of a transit, the two hemispheres cancel and the net result is no radial velocity change. With this in mind, the effect of a planetary transit is best illustrated with an example, but is also shown conceptually in Figure 1.7. Suppose the star rotates according to the principle of right-hand rotation, and the planet orbits in the same direction such that the two angular momenta are aligned. At the start of a transit, the planet will block light from the star that is blueshifted, causing a net redshift. This redshift of the light causes a positive radial velocity contribution. As the planet moves towards the other hemisphere, the net effect changes until it is now covering the red hemisphere, causing a net blueshift and thus a negative radial velocity contribution. If the two angular momenta are *not* aligned, the planet will spend unequal time on the red and blue hemispheres, which will cause an asymmetry in the radial velocity (Ohta et al. 2005; Giménez 2006; Hirano et al. 2011; Boué et al. 2013). Thus the shape of the Rossiter-McLaughlin effect is sensitive to the projected obliquity, often called spin-orbit angle, λ, which has been measured for numerous systems to date (e.g. Queloz et al. 2000b; Winn et al. 2005; Hébrard et al. 2008; Triaud et al. 2010; Albrecht et al. 2012; Mancini et al. 2018, see also Triaud 2018 and references therein).

The semiamplitude of the Rossiter-McLaughlin effect scales with (Triaud 2018)

$$K_{\mathrm{RM}} \propto v \sin i_\star \left(\frac{R_\mathrm{p}}{R_\star}\right)^2 \sqrt{1-b^2}, \tag{1.4}$$

where $v \sin i_\star$ is the projected stellar rotational velocity; $R_\mathrm{p}/R_\star$ is the ratio of the radii of the planet and star; and b is the aforementioned transit impact parameter. Figure 1.7 shows what the Rossiter-McLaughlin effect might look like for a typical hot Jupiter system with $\lambda = 0°$ (aligned), 60° (misaligned), and 160° (retrograde, planet orbits opposite direction of stellar rotation).

Asteroseismology

Another powerful method that can constrain stellar obliquities of planet-hosting stars is from the study of stellar oscillations, i.e. asteroseismology. This has in large only become possible in the recent decade due to the availability of long (4 yr), continuous time-series photometry from the *Kepler* spacecraft, see for example Chaplin et al. (2013); Huber et al. (2013); Van Eylen et al. (2014); Campante et al. (2016); Kamiaka et al. (2019). Asteroseismology is the study of stellar pulsations, which were first discovered in the Sun (Leighton et al. 1962). In stars like the Sun, turbulent motion near the surface layers

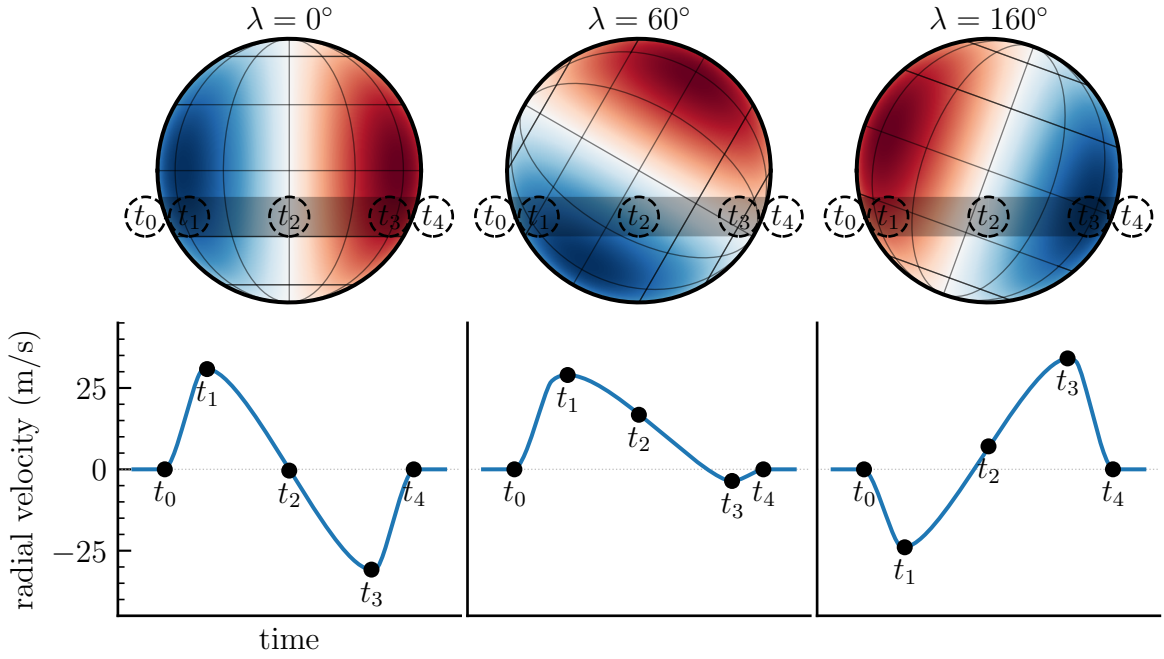


Figure 1.7: Radial velocity anomalies during transit due to the Rossiter-McLaughlin effect. The Rossiter-McLaughlin effect is shown for a planet with $b = 0.4$ for three values of the angle between the stellar rotation axis and planet orbital axis. From left to right: $\lambda = 0°$, $\lambda = 60°$, and $\lambda = 160°$.

excite sound (pressure) waves that propagate through the stellar interior, carrying information about the stellar structure. These acoustic waves can interfere and form resonant frequencies (standing waves) that cause the outer layers of the star to expand and contract on timescales of a few minutes (Basu & Chaplin 2017). The oscillation of the surface layers causes a Doppler signal as shown in Figure 4.4 (see also e.g. Bouchy et al. 2005; Farr et al. 2018), but the expansion and contraction also changes the temperature of the star which in turns affects its intensity, causing brightness variations over the pulsation timescales. Thus monitoring the brightness of stars over a long period of time (as done when searching for transiting exoplanets) can also reveal a rich spectrum of frequencies at which a star pulsates, which carries information about the stellar interior and can constrain the mass, radius, age (Basu & Chaplin 2017), rotation (Hall et al. 2021), and helium content in the star (Basu et al. 2004). The frequency spectrum of the star consists of radial and non-radial pulsation modes. Non-radial modes in rotating stars are sensitive to the viewing angle, $i_\star$, such that stars that are viewed close to $i_\star = 90°$ show rotational splitting, while stars that are viewed pole-on $i_\star \approx 0°$ present as a single-peaked mode (Gizon & Solanki 2003; Ballot et al. 2006, 2008).

Stellar rotation

One of the primary ways of measuring the rotation of stars is by measuring the broadening of its absorption lines due to rotation. This method measures $v \sin i_\star$, which is the equatorial velocity of the star projected onto our line of sight, thus we are unable to differentiate between the velocity v and stellar inclination $\sin i_\star$. Nevertheless, $v \sin i_\star$ alone can provide a powerful diagnostic for planetary formation

when comparing such measurements for a population of planet-hosting stars to a control sample. This is because stars that are aligned with their transiting planets will on average have higher $v \sin i_\star$ than stars that are oblique (Schlaufman 2010; Louden et al. 2021).

Another method that has matured in the recent decade due to *Kepler* is measurements of the rotation period from photometric variability due to spots on the stellar surface (McQuillan et al. 2014; Mazeh et al. 2015; Angus et al. 2018). Spots are dark regions of strong magnetic activity on the surface of stars which can rotate in and out of view as they get carried around with the stellar rotation. In doing so, the brightness of the star will typically vary on a similar timescale as the rotation. An example of this is shown in Chapter 3.3. Here, too, the amplitude of the brightness variability will depend on the inclination, thus when considering a large sample of stars can also provide useful constraints on the obliquity (Mazeh et al. 2015).

The degeneracy between v and $\sin i_\star$ can be lifted by combining measurements of $v \sin i_\star$ with an independent measurement of the rotation period $P_{\rm rot}$ (e.g. from photometry), as well as a measurement of the stellar radius, $R_\star$ (Masuda & Winn 2020). The radius might be based on spectroscopic parameters, or derived from parallax measurements and the Stefan-Boltzmann law. Then one obtains the stellar inclination (Masuda & Winn 2020)

$$i_\star = \sin^{-1}\left(\frac{v \sin i_\star}{2\pi R_\star / P_{\rm rot}}\right),$$

which has allowed studies on the obliquities of stars hosting small planets (Winn et al. 2017; Muñoz & Perets 2018).

Transit spot-crossing events

If a planet transits a spotted star while a spot is facing us, the planet may fully or partially occult the spot which causes a temporary brightening of the star during transit, which presents as an anomaly in the transit light curve (Désert et al. 2011). An example of this effect is shown in the bottom panels of Figure 3.23. One can analyse the timings of these spot-crossing events in relation to the rotational phase of the star to deduce the spin-orbit angle (Sanchis-Ojeda et al. 2012), use a geometric model of the spotted star to model the transit light curve (Désert et al. 2011; Sanchis-Ojeda et al. 2011; Sanchis-Ojeda & Winn 2011; Sanchis-Ojeda et al. 2013), or look for correlations in successive transit light curves from the advancement of a spot (Dai et al. 2018).

Gravity darkening/brightening

Stars that rotate very rapidly ($v \sin i_\star \gtrsim 50\,\mathrm{km\,s^{-1}}$) have oblate shapes due to strong centrifugal forces that creates additional outwards pressure at the equator. The polar regions of the star will have higher surface gravity than the equator, which in turn requires higher temperatures and pressures to maintain hydrostatic equilibrium. The effect is that the poles of rapidly rotating stars appear brighter than the equator. Thus if the orbit of a planet is misaligned with the star such that it transits several latitudes, the

transit light curve will appear asymmetric, and this asymmetry can constrain both λ and $i_\star$, allowing a measurement of the true obliquity ψ (Barnes 2009; Masuda 2015).

1.4.2 Obliquity trends of planet-hosting stars

Spin-orbit angle measurements of hot Jupiters have a fascinating history. The first measurement was made on HD 209458 b using the Rossiter-McLaughlin effect (Queloz et al. 2000b). The planet was found to be aligned with the spin of its star, with a projected obliquity of $|\lambda| = 3.^\circ9 \pm 19.^\circ5$, which was later refined to $\lambda = -4.^\circ4 \pm 1.^\circ4$ (Winn et al. 2005). The alignment was unsurprising at the time, given the expectation from the solar system and contemporary planet formation theories. More measurements came as new transiting exoplanets were discovered, all which appeared to follow the same trend as before, namely that hot Jupiters are aligned with the stellar spin (see Winn et al. 2010a, and references therein).

The narrative started shifting with the discovery of the misaligned orbit of XO-3, with $\lambda = 37.^\circ3 \pm 3.^\circ7$ (Hébrard et al. 2008; Winn et al. 2009a). Soon after, a flurry of other misaligned systems were announced including some planets on retrograde orbits (Winn et al. 2009b; Triaud et al. 2010). As the sample of projected obliquity measurements grew a few trends started appearing in the obliquity distribution. Figure 1.8 shows the range of observed projected obliquities that have been measured in exoplanet systems up to September 2020. The measurements come from a combination of the methods above, although the vast majority were made using the Rossiter-McLaughlin effect. This method is most sensitive to giant planets on short orbits around rapidly rotating stars, which explains the surplus of measurements on Jupiter-mass planets. In the following I will summarise what we have learned from studying the obliquities of hot Jupiter systems, which I define to be in the mass range 0.1–10 $M_{\rm Jup}$. I will first start by removing measurements that have an uncertainty on λ higher than 50° in order to paint a clearer picture.

Dependence on stellar temperature. One of the important results that came from studying the obliquities of stars is that the spin-orbit angle seems to have a strong dependence on the effective temperature of the star, $T_{\rm eff}$[i] (Winn et al. 2010a). This pattern is shown in the bottom left panel of Figure 1.8. Hot Jupiters orbiting cold stars tend to have low obliquity (i.e. star and planet are aligned and prograde), while those orbiting hot stars tend to have a wider range of obliquities, including many that are on retrograde orbits (Triaud et al. 2010). The cut-off temperature between these two populations is measured to be $T_{\rm cut} = 6090^{+150}_{-110}$ K (Dawson 2014; McQuillan et al. 2014).

Dependence on planet mass. Another pattern that arises from the ensemble of stellar obliquities is the dependence on planet mass. In the top panel of Figure 1.8 I show that the obliquity decreases as a function of planet mass for hot Jupiters. Beyond $\sim$3 $M_{\rm Jup}$ there is a distinct lack of retrograde planets (Hébrard et al. 2011; Dawson 2014). Studying this dependency in detail is important for future work, but is difficult to do simply due to the rarity of massive hot Jupiters (Santerne et al. 2016).

[i] Alternatively the pattern can be seen as a dependence on stellar mass since the two are correlated, but $T_{\rm eff}$ is easier to measure empirically (Schlaufman 2010).

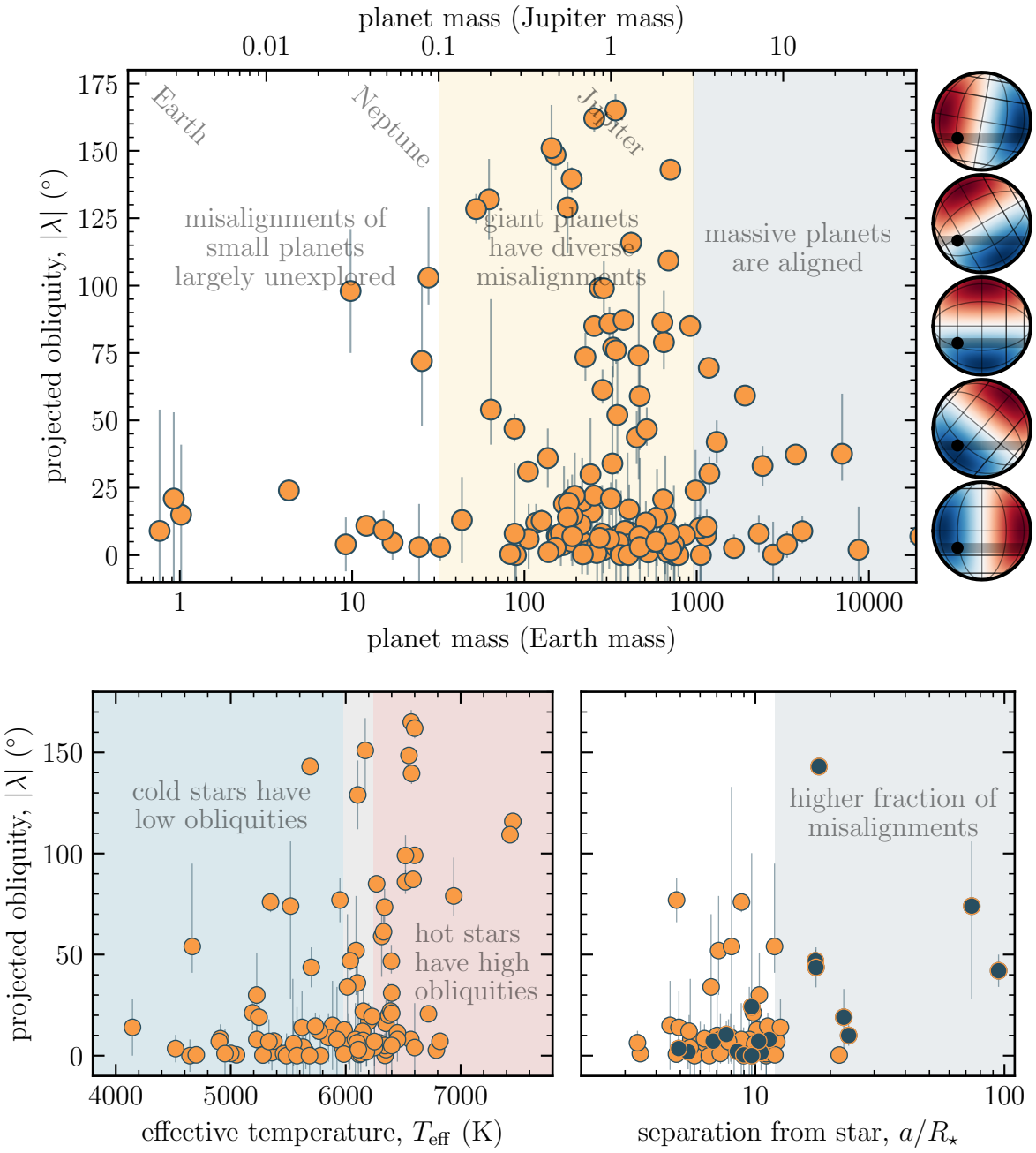


Figure 1.8: Projected obliquities of planet-hosting stars (planet-star misalignments) as of September 2020. *Top:* The full sample with planet masses consisting of 155 measurements, most of which have been made using the Rossiter-McLaughlin effect. Some notable patterns are annotated in the data. Each of the planet-star pairs along the vertical axis serve as a visual aid of the relevant architecture for a particular value of $|\lambda|$. Note that these illustrations assume $i_\star = 90°$, though the real value is in most cases unconstrained (and likely different) since only the projection of the obliquity is measured. *Bottom left:* The stellar effective temperatures of the sample. *Bottom right:* The orbital separation of the sample. Points with an inverted color scheme denotes planets that are eccentric, which here is determined as those that have e larger than three times the uncertainty on e.

Dependence on star-planet separation. A third important pattern in the data is the dependence on the distance between the planet and star (Albrecht et al. 2012; Anderson et al. 2015). In many cases it makes sense to denote the separation in units of the stellar radius, $a/R_\star$, sometimes referred to as the *scaled separation*. In the bottom right panel of Figure 1.8 I plot the obliquities of cold stars ($T_{\rm eff}$ = 4000–6100 K) with hot Jupiters as a function of their scaled separation. Hot Jupiters within about 10 stellar radii from the star are frequently found on aligned orbits. Beyond this, however, the fraction of misaligned systems increases, and they tend to be eccentric (Triaud 2018).

1.4.3 Tidal evolution in hot Jupiter systems

In this Section we will look at some processes that might help explain the patterns seen in Figure 1.8. Celestial bodies such as planets and stars are not point masses; they have a finite size, which means that the gravitational pull on each body is not uniform. In systems where the orbital separation is sufficiently small relative to the sizes of the bodies, the gravitational attraction deforms the objects from their usual spherical shape which are referred to as *tidal forces* (Zahn 1975, 1977). The effects of tidal deformation can be seen in the ocean tides on Earth which are induced by the Moon (and Sun), or the heat generated within Io as tidal energy induced by Jupiter is dissipated in Io's interior, giving rise to its volcanic activity. Tidal forces are also apparent outside of the solar system, for example in binary star systems where the tidal deformation is so strong that it has pronounced effects on their light curve or radial velocity curve (Masuda & Hirano 2021).

Hot Jupiters, too, are massive and close enough to their star that they can influence its properties through tidal interaction, and this is currently a leading theory for several of the obliquity trends outlined in the above paragraphs (Winn et al. 2010a; Albrecht et al. 2012; Dawson 2014). The planet raises an ellipsoidal bulge on the star, which slightly lags behind the planet. Since there is a delay in the tidal response from the planet, it gives rise to an angular force that resists the relative motion between the spin and orbital angular momentum vectors. A torque is also generated that couples the spin of the star to the orbit of the planet, allowing an exchange of energy and angular momentum. This enables a transfer of orbital angular momentum from the orbit to the spin that can spin up the star (Collier Cameron & Jardine 2018; Penev et al. 2018; Hodžić et al. 2018), or align of the stellar spin vector with the orbital angular momentum vector if they were initially misaligned (Barker & Ogilvie 2009a; Winn et al. 2010a; Ogilvie 2014).

Such tidal forcing ultimately results in an energy loss as the tide dissipates in the convective region of the star due to turbulent fluid motion. As a result the orbital elements continuously evolve over time until the planet and star are synchronised. For a typical hot Jupiter system this means: *(i)* synchronisation of the planet spin with the orbit (tidal locking), *(ii)* circularisation of the orbit ($e = 0$), *(iii)* alignment of stellar spin axis and planet orbital axis ($\psi = 0$), and *(iv)* (if the orbital period is smaller than the stellar spin period) synchronisation of the stellar spin with the orbit ($P = P_\star$). The timescale τ for tidal

synchronisation follow a relation of the form (Ogilvie 2014)

$$\tau \propto \frac{M_\star}{M_\mathrm{p}} \left(\frac{a}{R_\star} \right)^5 , \tag{1.5}$$

i.e. it is a strong function of the orbital separation relative to the stellar radius, and to some degree the mass ratio. More generally, however, the rates of change of *(i) – (iv)* differ in a way that depends on the angular momentum of each component. The total angular momentum L of the system consists of contributions from the stellar spin, orbit, and planet spin. In a typical hot Jupiter system their relative contributions roughly follow $L_\mathrm{star} \gtrsim L_\mathrm{orbit} >> L_\mathrm{planet}$. Thus tidal locking of the planet happens first, followed by circularisation ($\tau_e \sim 100\,\mathrm{Myr}$), spin-orbit alignment ($\tau_\psi \sim 1\,\mathrm{Gyr}$), then synchronisation of the stellar spin rate with the orbit ($\gg 1\,\mathrm{Gyr}$). A final relevant timescale is the inspiral time, which is the lifetime of a hot Jupiter. This measures how long the planet survives before having surrendered so much angular momentum through tidal dissipation that its orbit reaches the Roche limit where it gets tidally destroyed. This timescale is similar to that of τ_ψ, thus synchronisation of the spin rate usually does not happen in hot Jupiter systems. There is evidence for stars being spun up by their hot Jupiters, though not yet to the point where they are synchronised (Collier Cameron & Jardine 2018; Penev et al. 2018).

Tidal influence on the obliquity

An issue with the obliquity damping scenario is that the star has a very large moment of inertia, which requires a significant transfer of angular momentum; so much in fact that the planet would have to trade all of its orbital angular momentum to reorient the star. In simple terms the planet would be destroyed as it spirals towards the star, which contradicts our observations. As a solution to this problem, Winn et al. (2010a) suggest the outer convective layer of the star is sufficiently decoupled from the stellar interior, and only the outer layer participates in the tidal realignment, thus saving the planet from having to surrender all of its angular momentum. Recent work has identified a component of the tidal potential that affects the obliquity but not the orbital separation, which provides another potential explanation (Lai 2012; Anderson et al. 2021).

How do tides cause the observed stratification by stellar temperature on stellar obliquities? Albrecht et al. (2012) argue the contrast in obliquities between hot and cold stars can be explained by their difference in stellar structure. Tidal energy is dissipated in the convective envelope of stars, thus the depth of the convective zone may play an important role. Hot stars have very thin outer convective envelopes that enables only weak tidal coupling, therefore lowering the tidal dissipation efficiency and increasing the time needed to dampen the obliquity. Cold stars, on the other hand, have deep convective envelopes that allows tidal realignment to happen on relatively short timescales.

Dawson (2014) later argued that the convective zone indeed is important, but not because of the tidal dissipation efficiency, but because of the natural spin evolution of stars. The temperature cut-off, T_cut, also corresponds to the Kraft break (Kraft 1967), which separates stars by their angular momentum evolution. Stars below the Kraft break (cold stars) have deep convective envelopes which generates their magnetic field. The magnetic field carries material away from the surface with the stellar wind, which

in turn causes the star to lose spin angular momentum in a process called *magnetic braking* (McQuillan et al. 2014; Hall et al. 2021). Hot stars, on the other hand, have only thin outer convective envelopes and thus weaker magnetic dynamos such that braking is weakened. Cold stars therefore slow down as they age and lose angular momentum, which reduces the energy and time needed for tidal realignment (Dawson 2014).

The planetary mass cut-off for retrograde planets in the top panel of Figure 1.8 can too be attributed to tidal realignment since the timescale shortens for higher mass planets (Equation 1.5). This trend also holds when selecting hot stars only, demonstrating that hot stars are not immune to tidal dissipation. A similar argument can be used for the trend with orbital separation in the bottom right panel of Figure 1.8. Tidal synchronisation depends most sensitively on the orbital separation, $(a/R_\star)^5$, thus planets on wider orbits ($a/R_\star \gtrsim 12$) take much longer to tidally realign stars, which is why we see a higher fraction of misaligned systems at such separations.

Tidal evolution in binary star systems

Since this thesis is partially devoted to the study of (low-mass) binary stars (Chapter 6), it is useful to also briefly discuss tidal evolution in binary star systems. In the previous section we considered a system comprised of a star and a hot Jupiter. In such cases the angular momentum in the stellar spin is similar or higher than the orbital angular momentum. In a low-mass binary star system, however, the angular momentum in the orbit is typically the largest contribution to the total angular momentum of the system, i.e. $L_{\rm orbit} >> L_{\rm star,1} > L_{\rm star,2}$ (Zahn 1977). This has an impact on the tidal evolution of binary systems compared to planets. Similarly to planets, tidal evolution has three relevant effects on a binary: (i) alignment of stellar spin axes, (ii) synchronization of stellar rotation rates, and (iii) circularisation of the orbit (Zahn 1977). Because of the distribution of angular momentum in a binary system, (i) and (ii) happen on similar timescales, while eccentricity damping is typically the slowest process (Triaud et al. 2017). In an eccentric system the tidal response is not constant due to the binary separation varying over the course of an orbit. Because of this the stellar rotation rates do not exactly synchronise with the orbit, instead they reach a pseudosynchronous state where the rotation of the star is slightly below the orbital motion at periastron (Hut 1981).

1.5 How this thesis addresses some of these questions

As we have seen from Figure 1.8 and in Section 1.4.3, tidal forcing is believed to cause the orbital parameters to evolve with time, and the timescale for this evolution strongly depends on the star-planet separation, and to a somewhat lesser extent the mass ratio, as given in Equation 1.5. By this logic, planets that are more widely separated from their star, or planets that are low-mass, experience tidal evolution over a much longer timescale. In some cases the timescale surpasses the age of the universe and therefore the age of the system, which means that tidal evolution in such systems has only a small impact on the

evolution of certain orbital elements. In turn, such systems may more closely represent the outcome of planet formation and dynamical evolution.

From the current sample of measured spin-orbit angles it is unclear to what extent the distribution has been shaped due to tides. Hot stars, as we have seen, seem more resilient to tidal effects from their planetary companion, which is likely due the large spin angular momentum they retain most of their lives (Dawson 2014). However, they are not completely immune, as evidenced by a population of aligned hot Jupiters orbiting hot stars. Cold stars tend to host hot Jupiters that are aligned with the spin, though many of these planets orbit close to the star where realignment occurs quickly. Further from the star there is some evidence that the population is different, as would be expected from tidal theory, but the sample size is small due to the difficulty of finding and observing planets at longer orbital periods. The work presented in Chapter 5 is aimed at increasing the sample size of more widely separated giant planets orbiting cool stars. I provide obliquity measurements and eccentricity limits for 13 giant planets whose separations $a/R_\star$ range from 7.9–22.8 . With these new measurements the distribution of spin-orbit angles appear to be closer to planets orbiting hot stars, as one might expect, though we caution that this is work that is still in progress.

One of the most scientifically interesting avenues for further research into spin-orbit misalignments is to extend the current sample to the sub-Neptune regime. This is important for several reasons. First, while hot Jupiters are unlikely to form in-situ and therefore almost certainly experience some form of migration (Nelson et al. 2017), the picture is less clear for planets smaller than Neptune which are far less massive. There is some debate on whether they form in situ (~0.1 AU, Lee et al. 2014) or undergo large-scale migration — due to disc interaction or otherwise — from the outer system (Izidoro et al. 2017; Raymond et al. 2018). Second, sub-Neptunes frequently appear in multiple planet systems, which is of obvious interest in the context of our solar system and its evolution. They frequently make up compact resonant chains which are unlikely to arise from certain disc-free migration theories (Raymond et al. 2018), and therefore provide additional constraints on the mechanisms for migration. A third reason is that these planets have negligible tidal influence on their host star, which can alleviate some of the complications that arise from studying the obliquities of stars hosting hot Jupiters (Chapter 1.4.3). My work in Chapter 4 is a step in this direction, which concerns measurements of the Rossiter-McLaughlin effect in two systems with low-mass planets. The first is TRAPPIST-1, which is a multiplanetary system with seven Earth-mass planets orbiting an ultracool M dwarf star (Gillon et al. 2017). The second system is π Men, which is a naked-eye star hosting a close-in super-Earth, and a far-out giant planet/brown dwarf companion.

Studying the evolution of binary systems can also be useful to learn about planet formation. One application of this is reported in Chapter 3.3, which concerns the discovery of a hot Jupiter to a main-sequence K dwarf with a white dwarf companion. Few exoplanet systems are known to have bound stellar remnants, but their study is important to provide context to the final stage in the evolution of Sun-like stars.

Another application is the study of brown dwarfs which are similar to giant planets in many aspects,

including their formation, atmospheric composition, and orbital evolution. In Chapter 3.2 I announce a discovery of a brown dwarf companion to a Sun-like star, which adds another piece to the puzzle on how their formation and evolution compares to that of giant planets. In addition, masses, ages, and radii of young directly imaged planets are typically inferred from models that are based on brown dwarf cooling curves. In Chapter 3.1 I make an important contribution to a discovery of a brown dwarf eclipsing binary which is a member of a young moving group aged ~45 Myr. This discovery provides an accurate age, dynamical masses, and empirical radii — all of which are important to calibrate sub-stellar evolution models used in the study of giant planet evolution.

A final application is that there are now more than a dozen known circumbinary planets, where the planet orbits both components of a binary star system. I participated in such a discovery in Kostov et al. (2020) by observing for the BEBOP circumbinary planet survey on the HARPS spectrograph, which contributed some data to the discovery paper. As discussed earlier, these planets tend to pile up at ~6× the binary orbital period where planet formation is suppressed, so if they formed from the same disc as the binary the planets must significantly shrink their orbits to arrive at their present-day location (Section 1.3.3). To date, all circumbinary planets have been discovered via transit photometry, which is significantly biased towards co-planar systems. Yet circumbinary discs in polar configurations relative to the inner binary have been observed (Kennedy et al. 2019), thus motivating an exploration of the spin-orbit alignments of binaries hosting circumbinary planets (Winn et al. 2011). In Chapter 6 I therefore present a measurement of the spin-orbit alignment of the inner low-mass eclipsing binary hosting the circumbinary planet TOI-1338 Ab, which is only the third measurement of its kind. This work is part of a larger, ongoing work to explore the primary star obliquities in low-mass eclipsing binary systems.

Chapter 2

Photometric light curves and high-resolution spectroscopy

In this Chapter I describe the data, models, and statistical methods that underpin the analysis presented in the remaining Chapters. In Section 2.1 I start by introducing various aspects of exoplanet transit modelling. I continue in Section 2.2 by describing observations with high-resolution spectrographs, the data obtained from these spectra, and how to model them for the purposes of this thesis. In Section 2.3 I describe the statistical methods employed throughout this thesis for the data analysis. Finally, in Section 2.4 I present some software that was developed over the course of this thesis that has been used throughout the remaining Chapters.

2.1 Light curves of exoplanets and binary stars

2.1.1 Science from transit light curves

The distance between a star and a planet varies as over the course of an elliptical orbit. Solving the equations of motion for two bodies under the influence of Newtonian gravity one can find that the separation expressed in polar coordinates is (Murray & Correia 2010)

$$r = \frac{a(1-e^2)}{1+e\cos\theta}. \tag{2.1}$$

The variable θ is the *true anomaly* and is a function of time, describing the angle of the current position in the orbit with respect to the direction of periapsis. In Figure 1.1 it is the angle connecting the ellipse focus with the positions of the planet and periapsis. We can transform this expression into Cartesian coordinates where the xy-plane is in the orbital plane and periastron is in the x direction. After rotating this reference frame by the angles ω and i, our new coordinate system has the xy-plane in the sky plane,

and z points towards Earth. If we set $\Omega = 180°$ we have (Winn 2010)

$$x = -r\cos(\omega + \theta) \tag{2.2}$$

$$y = -r\sin(\omega + \theta)\cos i \tag{2.3}$$

$$z = r\sin(\omega + \theta)\sin i. \tag{2.4}$$

The separation of the star and planet projected onto the sky-plane (xy-plane) is then given by

$$\delta = \sqrt{x^2 + y^2} = \frac{a(1 - e^2)}{1 + e\cos\theta}\sqrt{1 - \sin^2(\omega + \theta)\sin^2 i}. \tag{2.5}$$

Eclipses occur when the separation on the sky is smaller than the sum of the radii of the two objects, i.e. $\delta < R_\star + R_\mathrm{p}$. The eclipses are centered on the local minima of δ. However, finding the minima of Equation 2.5 is an expensive computation, therefore a common approximation in exoplanet science is to set the midpoints of eclipses at conjunctions, which are defined by $x = 0$. This approximation is reasonable for the vast majority of exoplanet systems as the ingress and egress durations are approximately equal, but breaks down for very close-in eccentric and grazing planets where they can differ (Winn 2010). In such systems the time difference between conjunctions and minimum of projected separation can be up to 10 minutes, and indeed a handful of exoplanet systems have differences larger than 30 s, well above the detectable level (Eastman et al. 2019).

From Equation 2.2 we see that conjunctions occur when $\theta = \pi/2 - \omega$ and $\theta = 3\pi/2 - \omega$. The planet is in front (i.e. transiting) when Equation 2.4 is positive (recall z is pointing towards Earth), which (approximately) happens when $\theta = \pi/2 - \omega$. This is called inferior conjunction. The planet is in superior conjunction when it is behind the star (i.e. occultation), which is (approximately) centered on $\theta = 3\pi/2 - \omega$.

The impact parameter b is the sky-projected distance at conjunctions, shown as the distance between the transit chord and the centre of the star in Figure 2.1. Using Equation 2.5 with $\theta = \pi/2 - \omega$ this becomes

$$b = \frac{a}{R_\star}\cos i\left(\frac{1 - e^2}{1 \pm e\sin\omega}\right), \tag{2.6}$$

where "+" is used for transits, and "−" for occultations. The impact parameter is in units of $R_\star$ and has values between 0 and $1 + k$, where $k = R_\mathrm{p}/R_\star$ is the radius ratio between the planet and star. When $b < 1$ the entire planet covers the stellar disc and the four transit contact points are discernable, as shown in Figure 1.4. When $1 < b < 1 + k$ the transit is only partial (*grazing*) and therefore the second and third contacts do not occur. The effect of the impact parameter on the transit light curve is illustrated in Figure 2.1. Higher impact parameters shorten the total transit duration T_{14}, but increases the ingress/egress duration relative to the full transit duration ($t_3 - t_2$). One can show that the total transit duration is (Winn 2010)

$$T_{14} = \frac{P}{\pi}\sin^{-1}\left(\frac{R_\star}{a}\frac{\sqrt{(1 + k)^2 - b^2}}{\sin i}\right)\frac{\sqrt{1 - e^2}}{1 \pm e\sin\omega}. \tag{2.7}$$

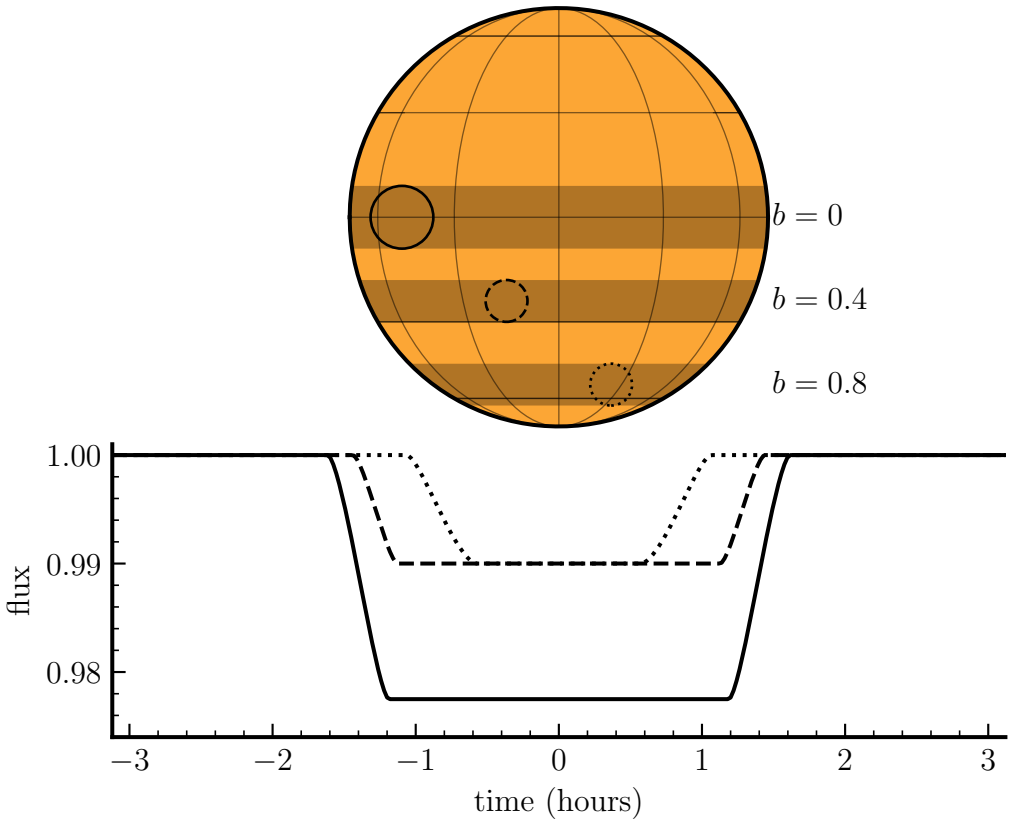


Figure 2.1: The transit depth depends on the size of the planet relative to the star. Larger planets (*solid circle and line*) cause deep transits, while smaller planets (*dashed and dotted*) cause shallower transits. In addition, the distance of the transit chord (*shaded region*) from the centre of the star, i.e. the impact parameter b, changes the total transit duration as well as the ingress/egress times. This figure was created using `starry` (Luger et al. 2019).

Note that the expressions in Equations 2.7 and 2.6 are also approximations. The true values can be calculated numerically at a computational cost, but doing so offers little advantage. The differences are up to $\delta T_{14} = 27\,\mathrm{s}$ and $\delta b \approx 10^{-4}$ at worst case among known exoplanet systems, which in both cases is lower than typical uncertainties on these parameters (Eastman et al. 2019).

The transit duration can also provide a measure of the mean stellar density. One can rearrange Kepler's third law to show that

$$\rho_\star = \frac{3\pi}{GP^2(1+q)}\left(\frac{a}{R_\star}\right)^3. \tag{2.8}$$

In exoplanet systems the mass ratio $q = M_\mathrm{p}/M_\star$ is negligible ($q \sim 10^{-3}$) for a giant planet around a Sun-like star), so $\rho_\star$ only depends on the orbital period which is observed from repeated transits, and the scaled separation $a/R_\star$ which can be measured from the transit duration by rearranging Equation 2.7. Keen readers may notice that the transit duration in Equation 2.7 is also dependent on the eccentricity e, and indeed e and $R_\star/a$ are degenerate in determining the transit duration. Most often the eccentricity will therefore have to be constrained by other means, for example from a radial velocity curve or the observation of a secondary eclipse. Frequently one uses time scales of tidal evolution to argue that the

planet should have circularised within its current age, therefore justifying a circular model. If this is not possible, prior knowledge of the distribution of eccentricities in exoplanet systems may be used so that our ignorance of e is reflected in the final uncertainty of $a/R_\star$ and other derived parameters (Kipping 2013; Van Eylen & Albrecht 2015; Van Eylen et al. 2019).

Alternatively, transits may still constrain the eccentricity if the stellar density is determined by other means, for example by combining measurements of the stellar surface gravity and the stellar radius. The surface gravity g (most often denoted in cgs units as $\log g$) is readily derived from a spectroscopic analysis since g determines the shape of absorption lines (Gray 2005), while the stellar radius can be found from parallax measurements. Then the density of the star is

$$\rho_\star = \frac{3}{4\pi G}\frac{g}{R_\star}. \tag{2.9}$$

Compared to a circular orbit, any eccentricity will to first order change the transit duration (Dawson & Johnson 2012). Then e may be constrained by comparing the stellar density from Equation 2.8 assuming a circular orbit, with that from Equation 2.9 (Dawson & Johnson 2012).

The combination of a transit and radial velocity curve yields an absolute planet mass instead of the minimum mass $m \sin i$ since i is known from the transit. The combination of the mass and radius also yields a bulk density — provided the stellar dimensions are known — which can constrain the overall composition of planets using thermal evolution models (Lopez et al. 2012). Combining Doppler planets and their transits can also determine the surface gravity of the planet, g_p, using just observables, with no assumption on the absolute dimensions of the star. Using the definition of the mass function and surface gravity in Equations 2.23 and 2.9 one can find (Southworth et al. 2007)

$$g_\mathrm{p} = \frac{2\pi}{P}\frac{\sqrt{1-e^2}}{}\left(\frac{a}{R_\mathrm{p}}\right)^2 \frac{K}{\sin i}. \tag{2.10}$$

2.1.2 Limb darkening

The light curves presented in Figure 2.1 are computed assuming a uniform intensity distribution across the stellar disc. In reality, however, stars exhibit limb darkening: an effect where the central part of the star is brighter than its limb due to opacity effects associated with our viewing angle. The intensity profile across the disc varies with the distance from the stellar centre, $\mu = \sqrt{1-x^2-y^2}$ (Winn 2010). A common approach is to describe the intensity profile $I(\mu)$ as a quadratic function of μ, such as

$$I(\mu) = 1 - u(1-\mu) - v(1-\mu)^2, \tag{2.11}$$

where u, v are limb darkening coefficients. The effect of limb darkening on the transit light curve is illustrated in Figure 2.2. Qualitatively it is clear that the transits become more rounded compared to the box-shape resulting from a uniform disc intensity profile. The exact shape depends on the optical filter; blue bands (e.g. g') have pronounced limb darkening resulting in a "U"-shape, compared to red and near-infrared wavelengths (z') which has a flatter portion during total transits. The limb darkening coefficients also depend on stellar properties, in particular T_eff, $\log g$ and Fe/H which are available from a

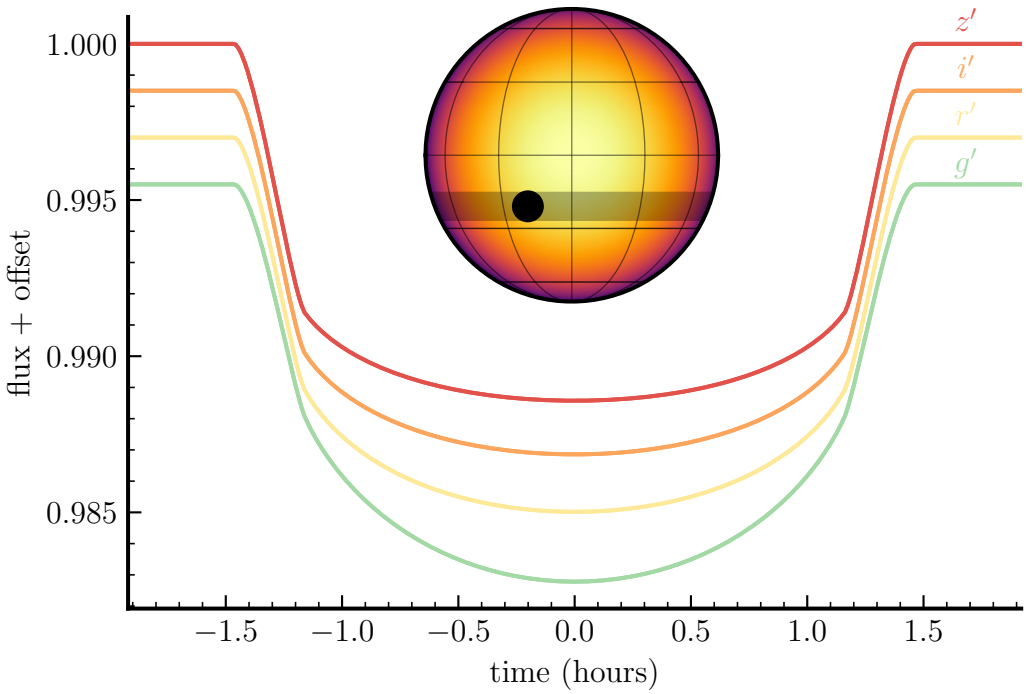


Figure 2.2: The intensity across the stellar disc is not uniform; it is lowest at the limb and increases towards the centre, referred to as limb darkening. Limb darkening is strongest for stars observed at blue wavelengths (e.g. g' band, $\lambda \approx 500\,\mathrm{nm}$) and causes the transit to look U-shaped. Stars observed at redder wavelengths (r', i', z' bands, $\lambda > 600\,\mathrm{nm}$) have less pronounced limb darkening, and the transits appear more flat-bottomed. This figure was created using `starry` (Luger et al. 2019).

stellar spectrum. The limb darkening coefficients can then be calculated by interpolating grids of stellar atmosphere models (e.g. Claret & Bloemen 2011; Husser et al. 2013), but can in some cases be measured directly from a high signal-to-noise transit light curve (e.g. Maxted 2018). Several codes are available for computing limb darkening coefficients using the former approach, e.g. `EXOFAST` (Eastman et al. 2013) and `LDTK` (Parviainen & Aigrain 2015), both of have been used throughout this thesis.

Although the quadratic limb darkening law in Equation 2.11 is most often used, there is no physical reason for this choice. The choice of limb darkening law is often based on the data. Some evidence suggests that another 2-parameter model such as the power-2 law can more adequately fit high SNR light curves such as from *Kepler* (Maxted 2018), while others advocate for a 4-parameter model (Claret 2000). Low SNR light curves do not necessarily warrant a limb darkening model with a high number of parameters. In these cases it might make more sense to use a linear model which omits the final term in Equation 2.11.

2.1.3 Science from binary star light curves

Light curves of eclipsing binary stars can provide additional constraints on their orbital and physical parameters that are not easily obtainable in exoplanet systems (Torres et al. 2010). The main reason for this is that in a binary system the secondary component is self-luminous. The occultation of the secondary star by the primary star then produces a secondary eclipse that is detectable even with modest

sized apertures, see Figure 2.3. Assuming the secondary is fully occulted the secondary eclipse depth is (Hilditch 2001)

$$\delta_{\rm sec} = \frac{l_2}{l_1} = k^2 \left(\frac{J_2}{J_1}\right), \tag{2.12}$$

where $J_2/J_1 = S$ is the *surface brightness ratio* of the two stars. Since the secondary star is fully occulted, Equation 2.12 is also the light ratio l_2/l_1 of the two stars, i.e. the fractional brightness of the secondary compared to the primary. The surface brightness is the brightness per unit area on the star, which is related to the temperature ratio of the two stars via the Stefan-Boltzmann law

$$\frac{J_2}{J_1} = \left(\frac{T_2}{T_1}\right)^4. \tag{2.13}$$

The secondary eclipse depth therefore measures the temperature ratio of the two stars, or the temperature of one star given a temperature for the other. Since the secondary is self-luminous this also means that the primary eclipse depth is no longer just dependent on the size ratio of the two bodies, but also on the flux ratio. The primary eclipse depth is then (Hilditch 2001; Winn 2010)

$$\delta_{\rm pri} = k^2 \left(1 - \frac{l_2}{l_1}\right). \tag{2.14}$$

In a circular orbit the primary and secondary eclipse occur exactly $P/2$ apart. In elliptical orbits, however, the time between primary and secondary eclipse depends sensitively on e and ω. The true anomaly during superior conjunction is offset by $\pi/2$ from primary eclipse. Solving Equations 2.20 and 2.19 with respect to time, the time difference between eclipses is given by (Kopal 1959; Hilditch 2001)

$$\Delta t = \frac{P}{2\pi}\left(\pi + 2\arctan c + \sin\left(2\arctan c\right) + \frac{2e\cos\omega}{\tan^2 i}\right), \tag{2.15}$$

with $c = e\cos\omega/\sqrt{1-e^2}$. The final term in Equation 2.15 is a correction term for $i < 90°$ and can in many cases be neglected for eclipsing binaries (de Kort 1954). The time difference Δt then provides a determination of the quantity $e\cos\omega/\sqrt{1-e^2}$. Equation 2.7 also shows that the durations of primary and secondary eclipse differ, and indeed their ratio also provide a constraint of the form (Hilditch 2001)

$$e\sin\omega = \frac{d-1}{d+1}, \tag{2.16}$$

where d is the ratio of the primary eclipse duration to the secondary eclipse duration. Equations 2.15 and 2.16 can then be combined to separate e and ω (e.g. de Kort 1954).

2.2 Methods for the analysis of high-resolution spectra

Stars emit a range of electromagnetic radiation, but most stars like the Sun emit most of their light in the visible regime which is what our human eyes have adapted to. The wavelength regime of visible light spans from about 380 nm (blue light) to 700 nm (red light), and the combination of these colors form "white" light, which is what we see from the Sun. A spectrograph is an instrument that disperses light into

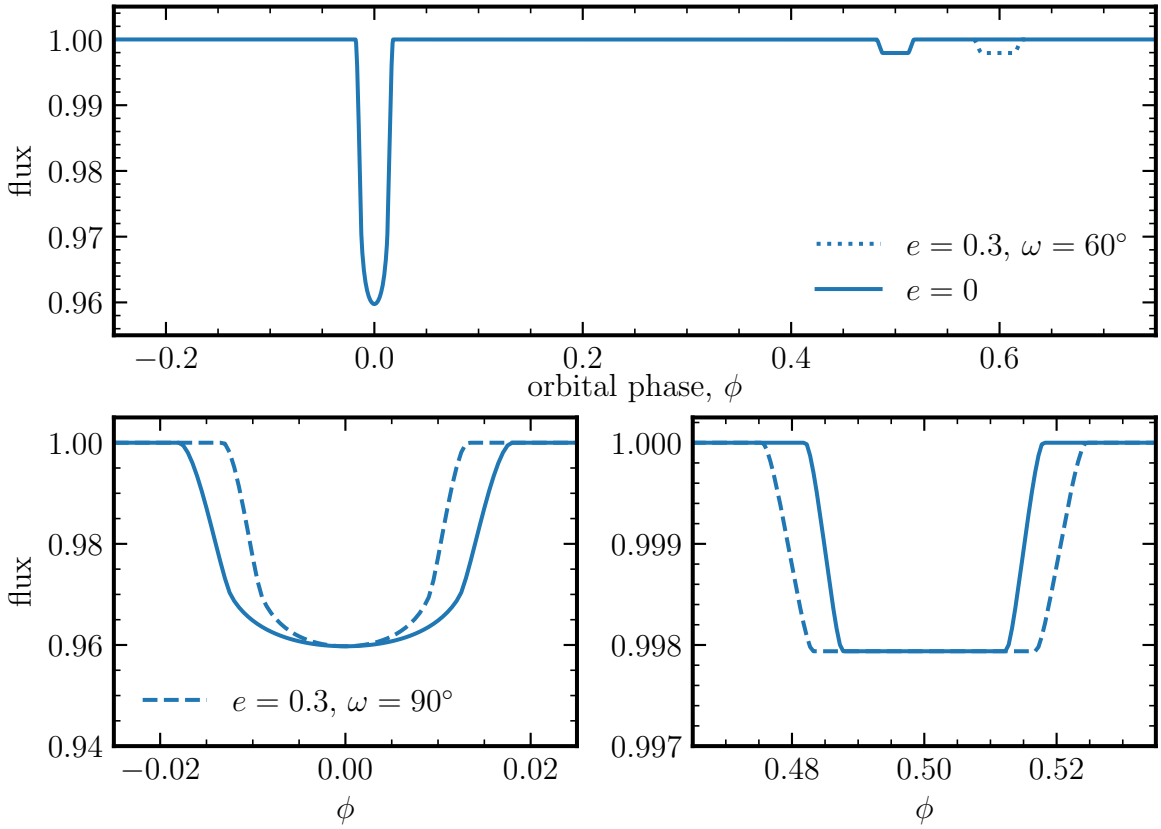


Figure 2.3: An example of an eclipsing binary star system consisting of a low-mass star ($m_2 = 0.2\,M_\odot$, $T_{\rm eff} = 3000\,\mathrm{K}$) orbiting a Sun-like primary ($m_1 = 1.1\,M_\odot$, $T_{\rm eff} = 6000\,\mathrm{K}$). In a circular binary the secondary eclipse occurs $P/2$ ($\phi = 0.5$) after the primary eclipse (*solid line*). The same is true for eccentric orbits with $|\omega| = 90°$ (*dashed line*), but here the durations of the primary and secondary eclipse differ and can constrain $e \sin\omega$. Eccentric binaries with $|\omega| \neq 90°$ have secondary eclipses that are displaced from $\phi = 0.5$ (*dotted line*) which can constrain $e \cos\omega$. In addition, the secondary eclipse depth measures the temperature ratio of the stars. This figure was created using ELLC.

its constituent wavelengths, called a *spectrum*. Spectra are useful for studying emission and absorption lines in various astronomical objects such as comets, planets, stars, galaxies, and the interstellar medium, which can tell us about the physics of these objects. Absorption lines arise because electrons in certain elements or molecules have energy transitions associated with a specific narrow wavelength region. For example, one of the most prominent absorption lines in the spectrum of the Sun absorbs light at a wavelength of 656.3 nm, which corresponds to the energy difference when an electron transitions from the third to the second lowest energy level in the hydrogen atom, also called Hα.

Spectrographs are often characterised by their resolving power, R, which measures their ability to resolve features in a spectrum. The resolving power is defined as $R = \lambda/\Delta\lambda$, where $\Delta\lambda$ is the smallest wavelength difference that can be resolved at wavelength λ (Gray 2005). The first generation of exoplanet spectrographs had $R \approx 45\,000$ and were one of the first modern high-resolution spectrographs (Baranne et al. 1996). The first generation of such spectrographs could resolve spectral features with widths of just 0.12 Å, whereas current high-resolution exoplanet spectrographs such as HARPS, ESPRESSO and EXPRES can reach $R = 110\,000$–$190\,000$ (Mayor et al. 2003; Pepe et al. 2020; Blackman et al. 2020). As

we saw in Equation 1.1, due to the Doppler effect the observed wavelength of a given absorption line can be shifted relative to the rest frame, which gives us the radial velocity of the object. The radial velocity variation of a star induced by a hot Jupiter can be $\sim$100 m s^{-1}, which corresponds to a wavelength shift of $\Delta\lambda = \Delta v \lambda_0 / c = 0.002$ Å at 550 nm, i.e. about 60× smaller than what the best spectrographs could resolve at the dawn of the exoplanet era. Then how were they able to detect planets?

2.2.1 Spectrograph overview

Most high-resolution optical spectrographs optimised for exoplanet science are built on similar principles. The telescope focuses light from the star onto a series of optical elements (mirrors, prisms, collimators) where it may also be corrected for color-dependent atmospheric dispersion, before ultimately guiding the light into an optical fiber which feeds the spectrograph (Gray 2005). The light is then fed into a dispersing element that separates the white light into its constituent wavelengths. A commonly used dispersing element in modern high-resolution spectrographs is the echelle grating. The advantage of the echelle grating is that the groove tilt (blaze angle) is very high and is illuminated by the light at a steep angle which produces higher diffraction orders, as opposed to just the first order that a standard grating would give (Gray 2005). However, the various orders overlap in the spectral direction, so to separate the orders from one another a cross-disperser is used to spread the light along the spatial direction as well. The cross-dispersed (2D) spectrum is then imaged onto the detector and is sometimes referred to as an echellogram. In Figure 2.4 I show an image of such a cross-dispersed high-resolution spectrum, which is what the raw data looks like coming out of the ESPRESSO spectrograph on the VLT (Pepe et al. 2020). The y direction in the left panel is the main dispersion direction, while the x direction corresponds to the cross-dispersion direction which allows higher orders to be observed. A zoomed inset is shown in the right panel, showing subsets of three spectral orders. The bands of light is that from the star, which has darker regions that correspond to absorption. In most modern high resolution spectrographs dedicated to exoplanets, a second fiber is used to to supply a simultaneous reference spectrum on which the observed stellar spectrum is calibrated to extremely high precision, and which can help keep track of long-term velocity drifts. The reference spectrum is oftentimes generated by either a ThAr lamp, Fabry-Perot interferometer, or Laser Frequency Comb (LFC). The dots in the zoomed inset of Figure 2.4 is a reference spectrum from a Fabry-Perot interferometer, which creates a rich forest of emission lines at regular intervals.

The pixel positions of each echelle order on the detector are traced and identified by means of diffraction theory in order to form a 1D spectrum. The reduced and calibrated 1D high-resolution spectrum of the echellogram in Figure 2.4 is shown in Figure 2.5.

2.2.2 Cross-correlation functions

An optical high-resolution spectrum of a star similar to the Sun, as shown in Figure 2.5, contains several features. The first is the overall shape of the spectrum outside of absorption lines. This is the continuum of the star, shown as the coloured line. Its shape is due to black-body radiation as described by Planck's law.

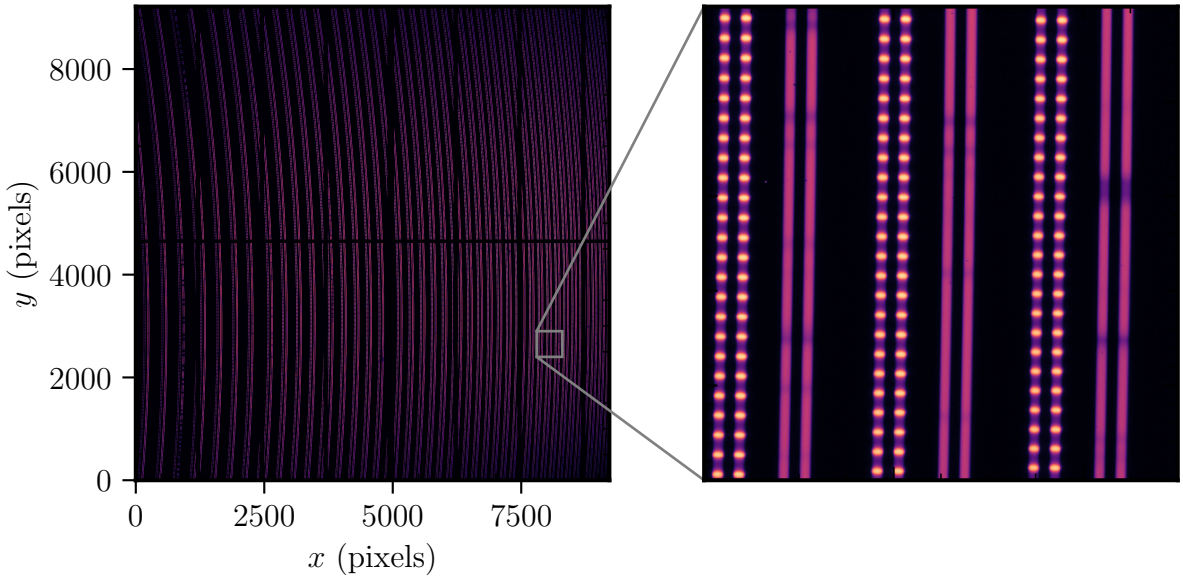


Figure 2.4: *Left:* An image of a cross-dispersed echelle spectrum taken with the red camera of ESPRESSO on the VLT. The target star is π Mensae. The y direction is the main dispersion direction, while the x direction is the cross-dispersion direction. *Right:* A zoomed-in part of the detector showing three different spectral orders of the stellar light (*continuous bands*) and reference light (*bright dots*). The dark regions within the bands show absorption.

The continuum is interrupted by several prominent absorption lines which are also marked in Figure 2.5, such as the aforementioned Hα, but also Ca II H & K and others (Gray 2008). In addition to these, such spectra also contain a rich forest of several thousand narrow absorption lines shown in grey, most of which are due to various iron (Fe) transitions. Earlier in this Section we mentioned that the wavelength shift due to the Doppler velocity induced by a hot Jupiter on its parent star was significantly less than the resolution of the spectrographs. This wavelength shift is what is expected for a single absorption line. The Doppler shift affects all absorption lines in the spectrum, thus if we can measure the velocity shifts of several thousand absorption lines, their average might be enough to precisely measure the Doppler shift, even if the resolution for any single one line is not enough. In fact, this is what allowed the detection of exoplanets with the Doppler method (Baranne et al. 1996).

One of the pioneering methods for utilising the Doppler information in the thousands of available absorption lines in stellar spectra is by the use of the cross-correlation function (CCF; Baranne et al. 1996). The cross-correlation method uses a binary mask which acts as a template spectrum of the star. The mask is zero in the continuum, but has a non-zero value at the expected locations of selected absorption lines with some characteristic width. This mask is then correlated with the spectrum in velocity space (via the Doppler formula) in order to build an average master absorption line at high signal-to-noise, as demonstrated in Figure 2.6 (Baranne et al. 1996). Not all lines are included in the cross-correlation, however. Absorption lines have a characteristic width and depth which vary depending on the absorber and the transition levels within an element. The mask is therefore weighted by the expected depth of the absorption line. In addition, some of the prominent Fraunhofer lines (e.g. Hα, Ca II H and K) are

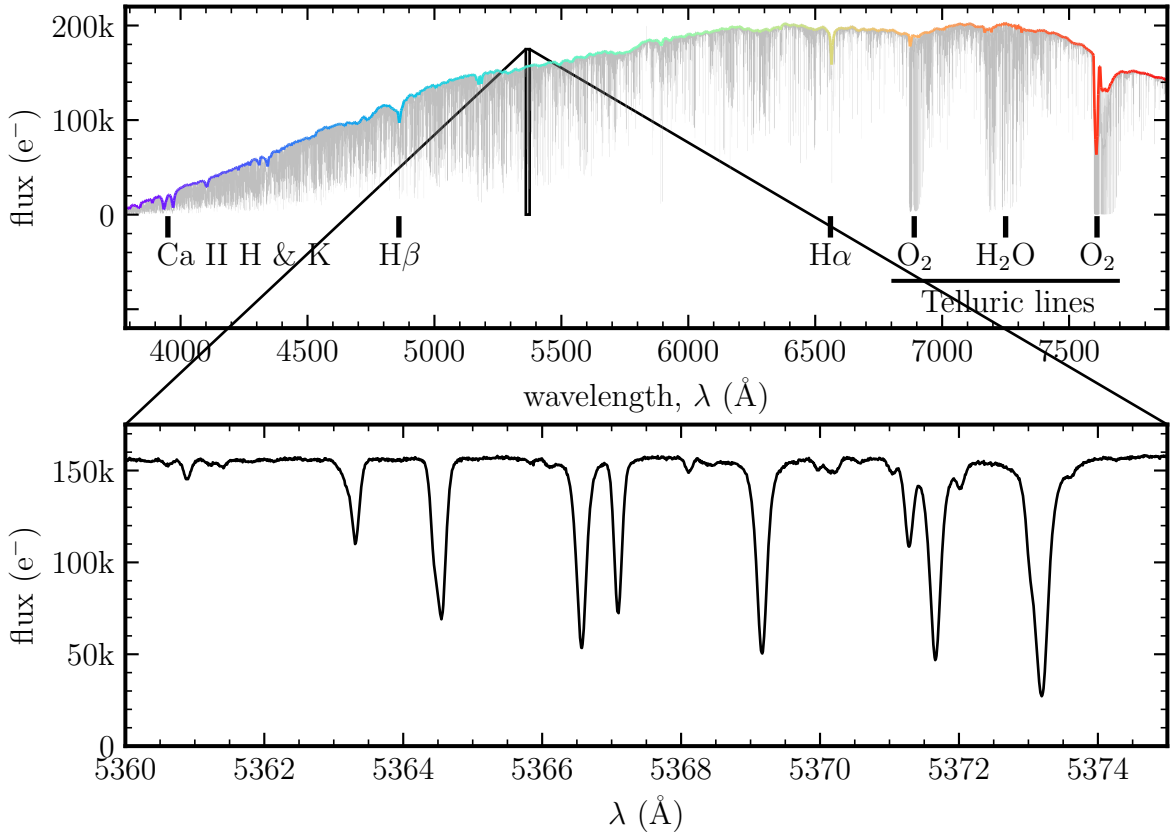


Figure 2.5: *Top:* The 1D spectrum obtained from co-adding all spectral orders shown in the echellogram in Figure 2.4. The continuum (*coloured line*) follows Planck's law (black-body radiation), and a few prominent absorption lines are marked. The high-resolution spectrum also contains thousands of non-saturated absorption lines (*grey lines*) which are used to measure the Doppler shift. The red parts of the spectrum shows significant absorption due to water and molecular oxygen in Earth's atmosphere. *Bottom:* A zoomed inset of a small region of the spectrum, showing the details of some absorption lines in the grey forest.

saturated, meaning photons at those wavelengths are almost fully absorbed and form very deep lines (Gray 2008). Due to associated opacity effects, some of the Fraunhofer lines are much wider than than the nonsaturated Fe lines, which degrades the radial velocity precision we can achieve (Bouchy et al. 2001). Most lines that are cross-correlated are therefore Fe lines (Baranne et al. 1996).

The shape of an absorption line (or CCF) is called a *profile*, and is most often modelled as a Gaussian, Lorentzian, or a mixture of both (Voigt profile). In exoplanet science, most often a Gaussian model is adopted. CCF profiles have a characteristic width and depth, measured by the FWHM and contrast of a Gaussian profile. The centre of the Gaussian (the mean) denotes the observed radial velocity of the star, as indicated in Figure 2.6. There are several sources contributing to the broadening (FWHM) of CCFs. Absorption lines are broadened due to line formation (thermal and pressure broadening), stellar rotation, large and small scale convective effects such as macroturbulence (Doyle et al. 2014), microturbulence, convective blueshift (Cegla et al. 2018), and broadening due to the instrumental resolution. For exoplanet applications the rotation of the star is perhaps the most useful among these, and is denoted by $v \sin i_\star$, i.e.

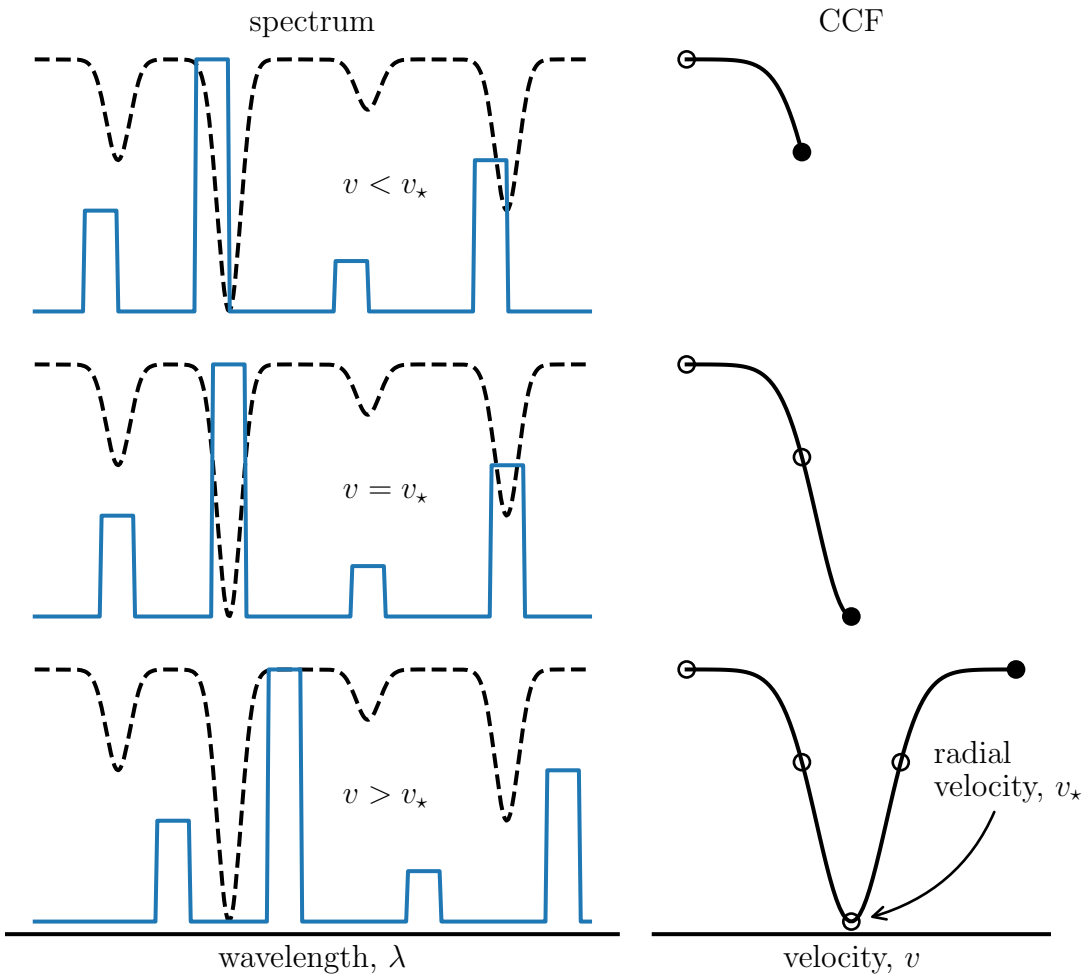


Figure 2.6: The radial velocity of a star can be determined from cross-correlating absorption lines in a stellar spectrum (*left, black*) with expected line positions using a binary template (*blue*). The resulting cross-correlation function (CCF, *right*) is an average stellar line profile in velocity space, and the radial velocity is determined from the centre of a Gaussian fit to the CCF. Figure adapted from Roy et al. (2016).

the projected rotational velocity at the equator of the star.

The broadening of absorption lines has adverse effects on the radial velocity precision. If we assume the lines are approximately Gaussian shaped, the radial velocity precision follows (Lovis & Fischer 2010)

$$\sigma_{\mathrm{RV}} \sim \frac{\sqrt{\mathrm{FWHM}}}{\mathrm{C} \cdot \mathrm{SNR}}, \tag{2.17}$$

where C is the contrast (amplitude of the line), and SNR is the signal-to-noise ratio in the continuum, $\mathrm{SNR} = N_{e^-}/\sqrt{N_{e^-}} = \sqrt{N_{e^-}}$ when the dominant source of noise is due to photon noise.

2.2.3 Science from radial velocity orbits

The radial velocity observations above can be repeated over time to map out the orbit of a star due to the gravitational pull of its planet (or stellar) companion around their centre of mass. The radial velocity orbit can be described by solving the equations of motion of two bodies moving in their mutual gravitational

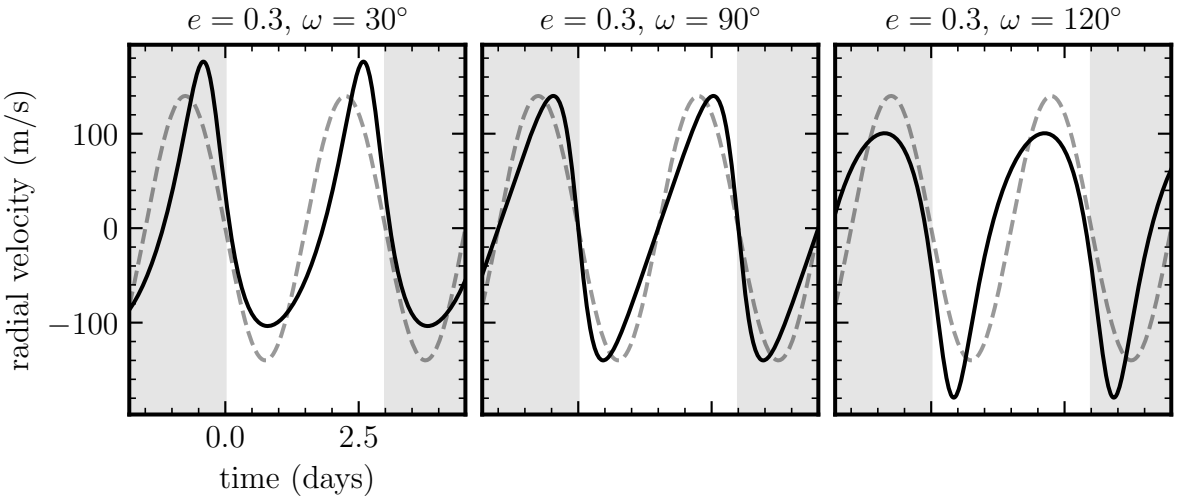


Figure 2.7: Radial velocity curves of a Sun-like star hosting a Jupiter-mass planet with $P = 3$ days. Each panel shows the circular orbit (*dashed line*) and eccentric orbit ($e = 0.3$, *solid line*) with the same semi-amplitude K, but different values of ω. The systemic velocity here is $\gamma = 0\,\mathrm{km\,s^{-1}}$. These models were calculated using ELLC (Maxted 2016).

fields (Murray & Correia 2010; Hilditch 2001). The radial velocity of either component is then (Hilditch 2001)

$$v_{\mathrm{rad}} = \frac{2\pi a \sin i}{P(1-e^2)^{1/2}}[\cos(\theta+\omega) + e\cos\omega] + \gamma, \tag{2.18}$$

where $a = a_1$ if we consider the star, and $a = a_2$ for the companion. The variables P, i, e and ω are the orbital period, orbital inclination, eccentricity and argument of periastron as described in Section 1.1.1. The first three are shared between both components, while ω for the planet and star have opposite signs (Eastman et al. 2019). The factor $2\pi a \sin i/P\sqrt{(1-e^2)}$ in Equation 2.18 is also known as the radial velocity semi-amplitude, K, shown in Figure 1.3. Thus for a circular orbit ($e = 0$), the radial velocity orbit in Equation 2.18 is just a cosine curve with amplitude K, as shown in Figure 1.3. For $e > 0$ the radial velocity curve becomes increasingly skewed and its shape is modulated by ω, with examples given in Figure 2.7 which shows how the geometry of the orbit within its own plane affects the radial velocity. The systemic velocity γ is (usually) a constant compared to the timescales of orbits, and describes the radial velocity of the system due to its orbit around the galaxy.

The variable θ is the *true anomaly* and describes the angle of the current position in the orbit with respect to the direction of periapsis. In Figure 1.1 it is the angle connecting the ellipse focus with the positions of the planet and periapsis. The true anomaly is a function of time, but its solution is not straightforward because the orbital velocity varies throughout an elliptical orbit. However, it can be related to two other angles; the eccentric anomaly, E, which is further related to the mean anomaly, M. The mean anomaly $M = n(t - t_0)$ does not have a simple geometric interpretation, but it is simple to calculate as it is related to the mean motion $n = 2\pi/P$ and has a constant angular increment with time. The eccentric anomaly is easier to conceptualise: if an elliptical orbit has semi-major axis a, then E is the angle swept out by an equivalent circular orbit with the same semi-major axis. The mean and eccentric

anomalies are then related by (Murray & Correia 2010)

$$M = E - e \sin E, \tag{2.19}$$

which is referred to as Kepler's equation. This is a transcendental equation and can only be solved numerically by iteration, for example by using a Newton-Raphson method to find the roots to the equation $E - e \sin E - M = 0$. The eccentric anomaly is then related to the true anomaly by (Murray & Correia 2010)

$$\tan \frac{\theta}{2} = \sqrt{\frac{1+e}{1-e}} \tan \frac{E}{2}, \tag{2.20}$$

which can be used in Equation 2.18 to describe a Keplerian radial velocity orbit as a function of time. There are a number of open source software packages that implement efficient numerical solvers for Equation 2.19 and are thus used to calculate radial velocity curves. Many of these packages are combined with transit light curve packages such as those described in Section 2.1.1 in order to jointly and self-consistently model transit light curves and radial velocity data (Maxted 2016; Foreman-Mackey 2019; Eastman et al. 2019).

From a radial velocity curve one can directly measure P, K, e, ω and t_p. One can also easily determine γ, though it is often considered a nuisance parameter and not of importance for most applications. The five primary parameters can be used to derive other orbital parameters of interest. Notably, the radial velocity curve measures the semi-amplitude of the primary star, K, which is related to its (projected) semi-major axis relative to the barycentre (Equation 2.18)

$$a_1 \sin i = \frac{\sqrt{1-e^2}}{2\pi} KP. \tag{2.21}$$

Moreover, using Kepler's third law one can determine the orbital separation $a = a_1 + a_2$ using

$$G(m_1 + m_2) = \frac{4\pi^2 a^3}{GP^2} \tag{2.22}$$

in the limit that the planet mass $m_2 \ll m_1$, and m_1 can be determined from other observations or stellar evolution models. Another quantity of interest is the mass function

$$f(m) = \frac{m_2^3 \sin^3 i}{(m_1 + m_2)^2} = \frac{P}{2\pi G} K^3 (1-e^2)^{3/2} \tag{2.23}$$

which can be derived using the above relations and using the centre of mass definition $a_1 m_1 = a_2 m_2$. The mass function is fully determinate from the radial velocity curve. Moreover, if one is willing to assume that $m_2 \ll m_1$ (which is a reasonable assumption for most planets orbiting Sun-like stars), then Equation 2.23 can be used to determine the *minimum* planet mass $m_2 \sin i$. If the planet is transiting the star, then i can be determined from the transit light curve and the true mass follows, along with a determination of the bulk density using the radius measurement from the transit light curve.

The orbital elements from a radial velocity curve can also be used to predict the time of transit, i.e. inferior conjunction. A number of planetary systems that were discovered with the Doppler method have

also been found to be transiting, e.g. HD 209458 b (Charbonneau et al. 2000) and 55 Cnc e (Winn et al. 2011)). Indeed, this is even expected as the detection of Doppler planets is biased towards high-inclination systems as these produce the largest radial velocity semi-amplitudes. The true anomaly during periastron is $\theta(t_\mathrm{p}) = 0$ as per its definition, while during inferior conjunction it is $\theta(t_\mathrm{c}) = \pi/2 - \omega$. The eccentric and mean anomalies can then be calculated to find t_c given t_p and vice-versa using Equations 2.20 and 2.19, i.e. (Murray & Correia 2010)

$$t_\mathrm{c} = t_\mathrm{p} + \frac{P}{2\pi}(E - e\sin E), \tag{2.24}$$

$$E = 2\tan^{-1}\left[\tan\left(\frac{\theta_\mathrm{c}}{2}\right)\sqrt{\frac{1-e}{1+e}}\right], \tag{2.25}$$

$$\theta_\mathrm{c} = \frac{\pi}{2} - \omega \tag{2.26}$$

Spectroscopic binaries

In binary systems consisting of two stars of similar brightness, their composite spectrum may contain spectral lines from both stars, dubbed a double-lined binary, or SB2. The extra set of absorption lines from the secondary star then move in anti-phase to those of the primary star due to their orbital motion. In such spectroscopic binaries radial velocities of both stars can be obtained (Figure 2.8), for example from a two-dimensional cross-correlation technique (Zucker & Mazeh 1994), which allows for additional constraints on the system. In particular, the ratio of their radial velocity semiamplitudes directly gives the mass ratio of the system, i.e.

$$\frac{K_1}{K_2} = \frac{m_2}{m_1} = q, \tag{2.27}$$

where the subscripts 1 and 2 refer to the primary and secondary component, respectively.[a] The orbital separation $a = a_1 + a_2$ can be determined from K_1 and K_2 using Equation 2.21, which means Equation 2.22 can be solved for m_1 since $m_2 = m_1 q$. Spectroscopic binaries therefore allow a *model-independent* measurement of the masses of stars (e.g. Triaud et al. 2020), which can be used to calibrate relations between mass and other observables, such as temperature, radius, luminosity (Torres et al. 2010), or asteroseismic scaling relations.

2.2.4 Modelling the Rossiter-McLaughlin effect

The transit of a planet (or any object) in front of a rotating star produces a change in the stellar line profile. A line profile from a star can be thought of as the sum of numerous local lines originating from all areas of the stellar disc. The velocity field across the stellar disc varies for a rotating star, ranging from $-v\sin i_\star$ to $+v\sin i_\star$. Lines originating from different areas of the disc may therefore have different Doppler shifts according to the local stellar surface radial velocity. During transit the total line profile will have a deficit

[a] Note that in the case of a star-planet system that we have investigated previously, K_1 would refer to K, and K_2 would not be observed because planets are generally not self-luminous. However, K_2 has been detected in high-resolution transmission spectra of hot Jupiters from measuring the Doppler shifts of molecular absorption lines such as CO (Snellen et al. 2010).

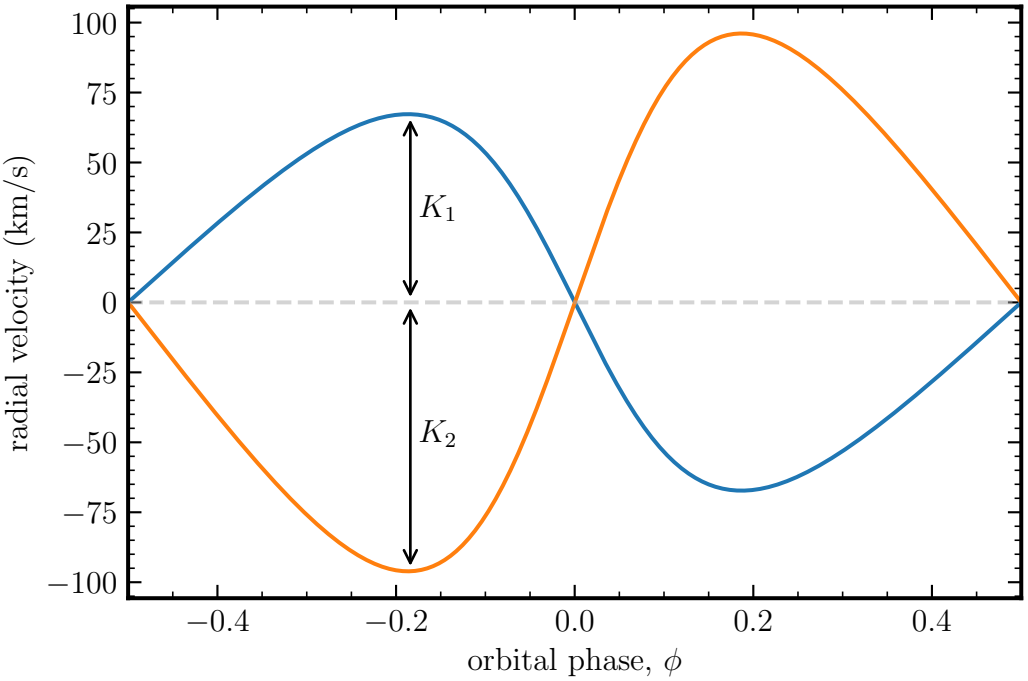


Figure 2.8: The radial velocity orbits of two stars with masses $m_1 = 1\,M_\odot$, $m_2 = 0.7\,M_\odot$, and orbital elements $P = 4\,\mathrm{d}$, $i = 90°$, $e = 0.2$, $\omega = 90°$, orbiting their common centre of mass. Spectra from unresolved binary stars of similar brightness may show two sets of absorption lines from which radial velocities of both stars can be derived. The ratio of their radial velocity semiamplitudes measures the mass ratio of the stars from which model-independent (minimum) masses can be obtained. This figure was generated using ELLC (Maxted 2016).

of light at a velocity given by the local surface velocity on the disc occulted by the planet. This deficit manifests as a "bump", or distortion, in the line profile that moves from $-v \sin i_\star$ to $+v \sin i_\star$, assuming the orbital and stellar spin axes are aligned and the planet transits along the stellar equator, as shown in Figure 2.9 (Triaud 2018).

The distortion of the stellar line profile during transit gives rise to a wholesale Doppler shift of the stellar radial velocity, which was first discovered in eclipsing binary systems by Rossiter (1924) and McLaughlin (1924) and is therefore dubbed the Rossiter-McLaughlin effect. This velocimetric effect is shown in Figure 1.7 for different configurations of the sky-projected angle between the orbital and stellar spin axes, λ, which in most applications is the parameter of interest. The Rossiter-McLaughlin effect also determines the sky-projected rotation of the star, $v \sin i_\star$, which is another important parameter can be used as a proxy for ages of stars with deep convective envelopes due to their spin angular momentum evolution from magnetic braking (Mamajek & Hillenbrand 2008). Besides these, the amplitude of the effect also depend on the area covered by the planet $(r/R_\star)^2$, and impact parameter b because the radial component of the velocity field becomes smaller as our viewing angle increases towards the limb (Triaud 2018). In most cases, however, b and $r/R_\star$ are already precisely known from a photometric transit light curve, thus modelling the Rossiter-McLaughlin effect boils down to adjusting two parameters: $v \sin i_\star$ and λ. The effect of limb darkening must also be taken into account, though the choice of limb darkening model and coefficients is a higher-order effect. The Rossiter-McLaughlin effect is furthermore

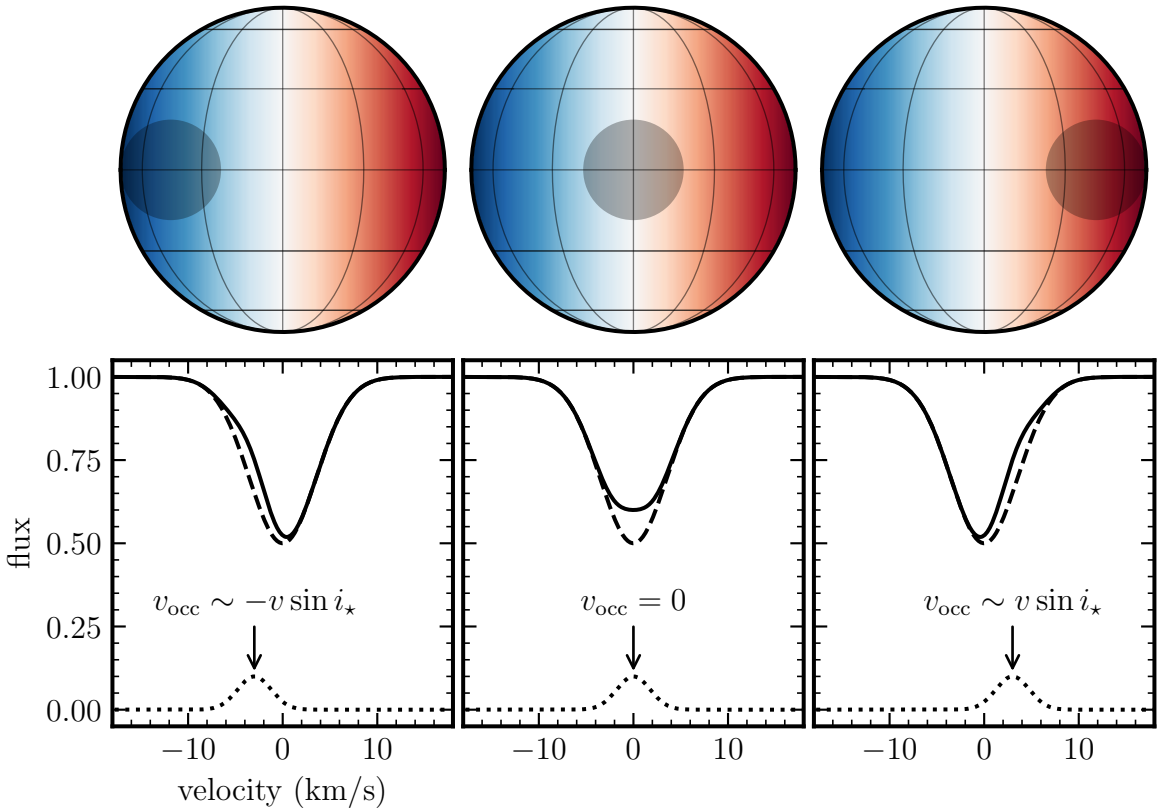


Figure 2.9: Transits produces a change in the line profile of rotating stars. The deficit light (*dotted line*) is Doppler shifted according to the local surface velocity on the star, i.e. that which is occulted by the planet, $v_{\rm occ}$. The line profile from the visible disc (*solid line*) is therefore perturbed relative to an unocculted surface (*dashed line*), which displaces the line centre to create a net radial velocity shift. This figure was created using `starry` (Luger et al. 2019).

superimposed onto the slope of the radial velocity orbit during transit, which also needs to be taken into account by either using the known radial velocity elements, or freely fitting a first order polynomial to account for the slope and systemic velocity on the night of transit, or higher-order polynomials for additional effects (Montet et al. 2020).

Velocimetric (classical) models

There are several models for computing the Rossiter-McLaughlin effect in the literature, but — perhaps alarmingly — each may infer different values of $v \sin i_\star$ and λ when applied to the same dataset (Brown et al. 2017). This is because the observed shape of the Rossiter-McLaughlin effect also depends on how the radial velocity is computed. A common analytical model is that of Ohta et al. (2005) and Giménez (2006), which assumes the spectrograph resolution is sufficiently low such that the asymmetry of the line profile is not resolved. These models then compute the mean brightness-weighted velocity of the stellar disc by integrating over the unocculted area. Under such assumptions the solution is analytic, and may be a reasonable model for slowly rotating stars and where the size of the transiting body is small compared to the host. The analytical model of Ohta et al. (2005) is easy to compute and is included in several

software packages, such as the `PyAstronomy` package[b] and ELLC (Maxted 2016).

However, there are at least two widely used methods for computing radial velocities. One is the CCF technique (Baranne et al. 1996) outlined in Section 2.2.2, where the radial velocity is the mean of a Gaussian fit to the CCF. The other is the iodine-cell technique where the observed stellar spectrum is modelled with a Doppler shifted theoretical spectrum, and the iodine absorption lines are used as a reference scale (Butler et al. 1996). Neither of these are particularly well described by the brightness-weighted mean surface velocity (Winn et al. 2005). The effect on the radial velocity due to an asymmetry in the line profile is treated differently depending on which method is used and results in different shapes of the Rossiter-McLaughlin curve. Modelling a dataset with the "wrong" model can therefore systematically bias the value of $v \sin i_\star$ and λ, leading to different interpretations of the system geometry (Brown et al. 2017). This motivated the development of several new Rossiter-McLaughlin models specific to the two reduction techniques. Radial velocities obtained during transit with the CCF technique may be better decribed by the model of Boué et al. (2013), wherein they derive an analytical expression for the centre of a Gaussian fit to a CCF that is asymmetric due to the planet. The models of Hirano et al. (2010, 2011) may instead be better suited to describe radial velocities derived with the iodine-cell technique, and has the advantage of taking into account additional broadening mechanisms such as macroturbulence (Doyle et al. 2014). The Boué et al. (2013) model is implemented in the publicly available ARoME library[c], which is written in Fortran with a C interface. The Hirano et al. (2011) model is to the author's knowledge not publicly available as a software package. The most popular programming language within exoplanet science is `Python`, therefore it would be useful to the community if both of these models were to be implemented in a single software package.

One of the main difficulties with modelling the Rossiter-McLaughlin effect is that a degeneracy arises between $v \sin i_\star$, λ and b when b tends to zero. For systems seen edge-on, models cannot distinguish between a system with high $v \sin i_\star$ and low obliquity ($\lambda \approx 0°$) vs. the opposite case. In these situations the degeneracy can be lifted by applying a constraint on $v \sin i_\star$ derived from other sources, for example from rotational broadening of spectral lines. However, measurements of $v \sin i_\star$ obtained from spectra and the Rossiter-McLaughlin effect are sometimes found to disagree significantly, which further complicates the picture (e.g. Triaud et al. 2009). The reasons behind this are not fully understood, but may be related to using the "wrong" Rossiter-McLaughlin model for a given dataset, or poor understanding of other line broadening mechanisms (e.g. macroturbulence, Doyle et al. 2014) which may dominate the broadening for slow rotators. A constraint on $v \sin i_\star$ can also be made by combining observations of $R_\star$, the stellar rotation period $P_{\rm rot}$ and its inclination $i_\star$, though $i_\star$ is difficult to obtain without first knowing $v \sin i_\star$ (Masuda & Winn 2020).

Another related issue is how to interpret a non-detection of the Rossiter-McLaughlin effect. Not detecting the radial velocity anomaly during transit can be interpreted in a few different ways. *i)* The rotation of the star is so low that the maximally expected Rossiter-McLaughlin amplitude is below the

[b] `https://pyastronomy.readthedocs.io/en/latest/`
[c] `http://www.astro.up.pt/resources/arome/`

noise in the data; *ii)* the star has a high inclination; *iii)* the planet is transiting parallel to and close to the projected spin axis of the star (polar orbit); and *iv)* a combination of the above. For high-b systems a non-detection due to *(iii)* is less likely as all values of λ cause a signal as long as the stellar rotation is above the noise.

Modelling the line profiles

One way of circumventing the issues outlined above is to analyse the line profiles directly instead of relying on the final radial velocity product. These types of techniques fall under several names such as line profile tomography, Doppler tomography, or Doppler shadow methods, all of which refer to the same basic principle (Albrecht et al. 2007, 2009; Collier Cameron et al. 2010a,b). The line profile is typically modelled as a Gaussian with some width σ determined by various broadening components, such as natural broadening, rotation, spectrograph resolution, and in some cases macroturbulence (Collier Cameron et al. 2010a). A time-dependent Gaussian component is then added to the line profile model, which represents the light obscured by the planet. The peak of the planet-obscured light is the sub-planet velocity v_p and its movement can be tracked across the velocity field of the star given a set of parameters $\boldsymbol{\theta} = \{v \sin i_\star,\ \lambda,\ i,\ a/R_\star\}$, shown as the dark trace in Figure 2.10, which is sometimes referred to as the Doppler shadow. Note that the trace represents the moving bump in Figure 2.9 labelled v_occ. We set the xy plane in the sky such that y is parallel to the projected spin axis and z points towards Earth. We then have that the planet's position on the stellar disc for $e = 0$ is given by

$$x_\mathrm{p} = \frac{a}{R_\star} \sin(2\pi\phi), \tag{2.28}$$

$$y_\mathrm{p} = -\frac{a}{R_\star} \cos(2\pi\phi) \cos i, \tag{2.29}$$

where ϕ is the orbital phase of the planet and $a/R_\star$ and i have their usual meanings. If we rotate the xy plane by λ, the planet's x coordinate in this new frame is given by $x_\perp = x_\mathrm{p} \cos\lambda - y_\mathrm{p} \sin\lambda$. The sub-planet velocity is then given by (Collier Cameron et al. 2010a; Cegla et al. 2016)

$$v_\mathrm{p} = x_\perp v \sin i_\star. \tag{2.30}$$

Doppler shadow methods are particularly useful on stars that rotate very rapidly since the radial velocity precision decreases rapidly as the line profile is broadened. The method therefore excels in determining projected obliquities in systems where the star is typically too hot to extract precise radial velocities (Johnson et al. 2014; Gaudi et al. 2017). The added benefit of Doppler shadow methods is that it avoids any assumption on the method for deriving radial velocities. Line-profile techniques are also more robust against non-detections. As we saw for the velocimetric case, non-detections can happen when the planet transits an area of low or zero surface velocity, which does not deform the line profile and therefore does not cause a net radial velocity change. Line-profile techniques instead work on the flux, therefore if a planet transits the star the flux drop may still be significant regardless of whether the centre of the residual line profile is at zero, although strong correlations between $v \sin i_\star$, λ and b remain.

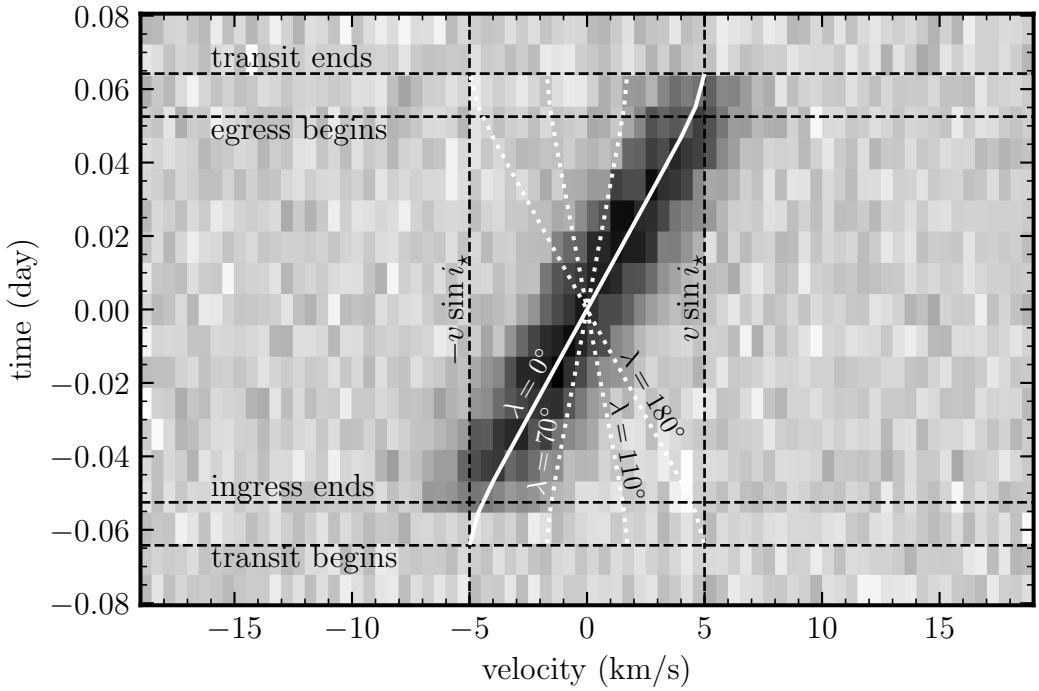


Figure 2.10: Simulated CCFs of the stellar light hidden by a transiting planet. The grey scale refers to the flux so that dark areas correspond to absorption, i.e. the local CCF core. The four transit contacts are shown as horizontal black dashed lines. The light hidden by the planet is Doppler shifted by the local surface velocity on the star, which is determined by the projected rotation $v \sin i_\star$ (*vertical black dashed lines*) and spin-orbit angle λ. The true model ($\lambda = 0°$) is shown as a solid white line. The impact of varying λ is shown as dotted white lines. This figure was generated using OLIO (Section 2.4.2).

A non-detection in this case would instead mean that there is no difference in the residual line profiles between in-transit spectra and out-of-transit spectra.

Despite the many strengths of Doppler shadow methods, they too come with some assumptions. The stellar line profile is often modelled as a Gaussian (Collier Cameron et al. 2010a), which is not strictly accurate, in particular when rotational broadening is significant, but also partly due to the asymmetry introduced in the line profile due to convective blueshift (Cegla et al. 2018). Moreover, various iterations of these methods also assume a common width and depth for the planet-occulted line profile, which is generally not true as as *i)* the shape of the local line profile changes as a function of distance from the centre (Beeck et al. 2013), and *ii)* stellar surfaces are generally inhomogeneous due to spots, plages, and faculae which can impact the shape of local lines (Cegla et al. 2018; Cegla 2019).

The reloaded Rossiter-McLaughlin method

The reloaded Rossiter-McLaughlin technique was developed to address some of the issues in the previous section, in particular the assumption of line profile shapes (Cegla et al. 2016). The technique is intended for CCFs computed from spectra obtained with stabilised high-resolution spectrographs. The basic premise of the method is to create a mean out-of-transit "master" line profile which is used as a reference template for individual line profiles. The missing light during transit is then retrieved by subtracting

the master line profile from in-transit CCFs. Using the observed CCFs as a template means that no assumption is made on its shape. In order to create the master template, the CCFs need to be brought to the same reference frame, which involves resampling the CCF onto a grid that is corrected for any differences in radial velocity (e.g. due to the Keplerian orbit). Moreover, in order to properly account for the missing light during transit, the CCFs need to be scaled by a transit model since individual spectra are not normalised to a reference source and are therefore on an arbitrary scale.

The residual CCFs (representing the sub-planet light in Figure 2.9) is typically fit with Gaussian profiles whose centre denote the local surface velocity on the star. Each residual CCF is also fit with its own width and depth, which allows for centre-to-limb variation in the line profile (Cegla et al. 2018). The local surface velocities obtained from the previous step are modelled by calculating the mean brightness-weighted sub-planet velocity, which is obtained using a grid-based approach by summing cells that are both within the stellar disc and occulted by the planet. By default the star is assumed to rotate as a rigid body as in Equation 2.30, but the model can easily accommodate both differential rotation, and a model for the centre-to-limb convective blueshift variation (Cegla et al. 2016).

The reloaded Rossiter-McLaughlin method is a promising technique that has the potential to tease out even the smallest detectable signals (e.g. Kunovac Hodžić et al. 2021) and is expected to be instrumental in studying the obliquities of stars hosting multiple (small) planets, which have so far largely eluded detection. However, this method, too, comes with downsides. The main issue in its current state is the awkward two-step process where the residual line profiles are first calculated assuming some orbital parameters P, t_0, K, followed by line profile modelling given some parameters $v \sin i_\star$, λ, i and $a/R_\star$ (Cegla et al. 2016). This means that uncertainties on parameters from the first step are not formally propagated to the uncertainty in the final values of $v \sin i_\star$ and λ. Another issue is that when working on very small signals, the nightly variation in the depth (and width) may be comparable to the reduction in flux due to the transit, which can bias our inference of $v \sin i_\star$ and λ. Future iterations of this method are therefore expected to address some of these issues which will aid the study of obliquities of stars hosting small planets.

2.3 Statistical inference

Much of this Chapter has hitherto been concerned with the models we use to describe the physics of transits, radial velocity orbits, and the Rossiter-McLaughlin effect; but so far we have avoided talking about *data*. Astronomical observations are at the core of this thesis, and this Section is dedicated to how we reconcile our models to observations in order to infer the physical properties about exoplanets and their stars, which is referred to as *parameter estimation*. We will start this section by introducing the origins of noise in astronomical data, before moving on to parameter estimation, model selection, and finally some notes on how to deal with correlated noise in the data.

2.3.1 Noise sources in astronomy

Most areas of astronomy rely on the measurement of a discrete number of photons arriving at a detector. In optical astronomy the most common detector is the charge-coupled device (CCD), where photons are converted to electrons upon interaction with a semiconductor material. Electrons are collected in charge potentials underneath each pixel during an exposure. At the end of the image acquisition the CCD counts the number of electrons in each pixel and converts this to a digital number on the computer which we use in our analysis (Haswell 2010).

The counting of discrete independent events, such as photon arriving at a CCD, or the number of electrons they excite, has an inherent uncertainty that follows Poisson statistics. If the number of photo-electrons in a given pixel is N (the signal), then the uncertainty σ on that number is $\sqrt{N}$. A fundamental concept in astronomy is the signal-to-noise ratio, sometimes expressed as SNR or S/N. If the signal is from the source *only* then we are only limited by photon noise and the signal-to-noise ratio is then

$$\mathrm{SNR} = N/\sqrt{N} = \sqrt{N}. \tag{2.31}$$

In practice, N contains contributions from *all* sources, not just from the astronomical source. Some important "white" noise sources are the sky background, read-out noise, and dark current (Haswell 2010). In practice the contributions from these sources to the signal is removed in post-processing, but their uncertainty still remains. The SNR is then

$$\mathrm{SNR} = \frac{N_{\mathrm{star}}}{\sqrt{N_{\mathrm{star}} + N_{\mathrm{sky}} + N_{\mathrm{read}} + N_{\mathrm{dark}}}}. \tag{2.32}$$

Modern instruments typically produce very low read-out noise, and are frequently cooled down to cryogenic temperatures to minimise dark current. The dominant source of noise in many cases is then that from the object itself such that the signal is photon noise limited.

2.3.2 Correlated noise models

The noise sources in the previous Section are so-called "white" noise, i.e. it is Gaussian and therefore independent between each measurement. Although individual measurement errors are well described by Gaussian noise (due to counting statistics), other environmental and astrophysical processes can introduce signals into the data that *are* correlated. These signals are not typically accounted for in simple transit and radial velocity models, and not taking these effects into account can lead to retrieved parameters that deviate significantly from their true values.

The simplest approach to "dealing" with this problem is to assume that the individual measurement errors are underestimated, and therefore allow for an additional error term σ_{jitter} in the fit. This error term is often referred to as the "jitter" and is added in quadrature to the normal measurement errors, i.e. $s^2 = \sigma^2 + \sigma^2_{\mathrm{jitter}}$. For data that is in relative units (e.g. transit light curves) rather than absolute (e.g. radial velocities), the adjusted parameter is an error scaling term such that the total error is now a vector, $s^2 = \sigma^2 + f(x, \boldsymbol{\theta})^2\sigma^2_{\mathrm{jitter}}$ where $f(x, \boldsymbol{\theta})$ is the (transit) model generated by a set of parameters

$\boldsymbol{\theta}$. Allowing for a jitter term adjusts the uncertainty on the measurements to reconcile the model with the data, even if the model does not capture the correlated signal. This will not be adequate if correlated noise is significant, but including a white noise term is in most cases recommended anyway given the formal uncertainties are typically calculated from photon noise, which is a best-case scenario.

Transit light curves captured with ground-based telescopes can have correlated signals over timescales of the night or shorter due to observing the star at different airmass, fluctuations in sky brightness, and movement of the target star on the CCD. In these cases a common approach is to model these variations using a combination of low order (1-3) polynomials using the sky brightness count, airmass, target pixel x and y positions, and/or aperture FWHM as the independent variable (e.g. Delrez et al. 2014; Hodžić et al. 2018). Another frequently used method is to divide a light curve into several smoothly varying chunks that are each modelled with a cubic spline, which can offer great flexibility if one is not concerned with removing astrophysical variability.

A relatively recent method for modelling a range of correlated signals in exoplanet data is the use of Gaussian processes (GPs) (Rasmussen & Williams 2006; Roberts et al. 2013). Exoplanet transit light curves and radial velocity data may exhibit complex astrophysical, instrumental and environmental signals that are challenging or impossible to model with traditional parametric models. In these areas, GPs offer a flexible model that can be used to model stellar activity and rotation (Haywood et al. 2014; Gillen et al. 2014; Rajpaul et al. 2015; Grunblatt et al. 2015; Angus et al. 2018), stellar pulsations (Farr et al. 2018; Kunovac Hodžić et al. 2021), or a range of signals in exoplanet data believed to be of non-astrophysical origin (Suárez Mascareño et al. 2020). Stellar signals such as rotation are quasi-periodic due to evolving spot groups, and modelling the spot locations, sizes and temperature contrasts is a highly degenerate task (Ikuta et al. 2020). Light curves obtained with space telescopes can have complex correlated signals due to the changing attitude and orbit of the spacecraft, which is also difficult to correct for (Stevenson et al. 2012; Luger et al. 2016).

These signals and others can all be well described by Gaussian processes, which is a method by which the signal is parametrised by the covariance between data points. A suitable covariance kernel function $\boldsymbol{K}(x_i, x_j)$ is adopted given the characteristics of the data, which defines the covariance between any two locations x_i and x_j. In time-series analysis x might represent time, and the covariance elements might be determined by how much time has passed in between each observation, i.e. $|x_i - x_j|$, so that points that are closer in time are more correlated than those that are far apart. An example of a covariance function is the widely used squared-exponential kernel (Roberts et al. 2013)

$$k(x_i, x_j) = A \exp\left[-\left(\frac{x_i - x_j}{\tau}\right)^2\right], \tag{2.33}$$

where A and τ are *hyperparameters* that represent a characteristic amplitude and timescale for the signal, respectively. The GP is also characterised by a mean function μ, which in this context might represent a transit light curve model or a radial velocity curve. The prior distribution of the GP then contains any function drawn from the multivariate Gaussian distribution given by $\mathcal{N}(\mu, \boldsymbol{K})$, where $\boldsymbol{K}$ is the covariance matrix given by Equation 2.33. The GP is therefore a distribution over *functions* which allows incredible

flexibility in the model given just a few hyperparameters for the covariance function, in this case A and τ. The prior distribution is then conditioned on the observed data to get the predictive distribution of the GP. The hyperparameters can be adjusted in a fit by calculating the marginal log likelihood (Rasmussen & Williams 2006), which is marginalised over all function values from the posterior predictive distribution.

2.3.3 Goodness of fit, parameter estimation, and model selection

We will now consider the process of adjusting model parameters to obtain the best fit to data. In the simplest case we determine a goodness-of-fit statistic such as the χ^2-statistic (pronounced chi-squared, Andrae et al. 2010)

$$\chi^2 = \sum_{i=1}^{N} \left(\frac{d_i - f(x_i;\, \boldsymbol{\theta})}{\sigma_i} \right)^2 , \tag{2.34}$$

where the subscript i denotes the i-th index of the data consisting of N measurements, and d and σ denote the data and measurement error, respectively. This can represent either brightness measurements or radial velocities as discussed previously in this Chapter. The function $f(x_i;\, \boldsymbol{\theta})$ is generated from a parameter vector $\boldsymbol{\theta}$ and has the independent variable x, which typically represents time since we have thus far mostly worked in the time domain. In the case of simple linear regression we have $\boldsymbol{\theta} = \{a,\, b\}$ and $f(x;\, a, b) = ax + b$. The χ^2-statistic computes the residuals given a best-fitting model, normalised by the measurement uncertainties σ which are assumed to be independent and normally (Gaussian) distributed. The probability distribution of the residuals from the χ^2 statistic then follows a χ^2-distribution of k degrees of freedom, which is a special case of the gamma function (Gelman et al. 2003). When the number of data points N is large, $k \approx N$ and the distribution approaches the normal distribution.

In some cases one may only be interested in the best-fitting model (maximum likelihood) to the data in order to find some parameter(s) of interest. This involves minimising Equation 2.34, i.e. finding the set of parameters that generates a model that minimises the dispersion in the residuals. In practice this is done by an iterative procedure whereby a user specifies an initial guess for $\boldsymbol{\theta}$, and each parameter is iteratively displaced by some value in order to search the parameter space for minima of the χ^2-statistic (Gelman et al. 2003). If the initial guess is reasonably close to the global minimum, least squares minimisation procedures such as the Levenberg-Marquardt algorithm (Moré 1978) can be fast and robust. The `python` package `scipy` (Virtanen et al. 2020) implements several algorithms for least squares minimisation.

Another important use case of statistical inference is to do model comparison, i.e. hypothesis testing (Andrae et al. 2010). For example, given a radial velocity data set of N points, does the data favour an eccentric orbit, or a circular one? How many planets? Alternatively, when we are working very close to the noise, does the data contain a statistically significant signal or is it commensurate with a random realisation of noise? The χ^2-statistic also gives a way of quantifying the significance of a detection compared to the null hypothesis where the signal is purely due to chance. Given a measurement of χ^2 with k degrees of freedom, the chance probability can be calculated using online calculator[d]. If needed

[d] e.g. https://www.fourmilab.ch/rpkp/experiments/analysis/chiCalc.html

and if k is large, the chance probability may then be used to estimate the significance in units of standard deviations of a normal distribution using an online table[e].

Within various areas of astronomy the *reduced* χ^2-statistic ($\chi^2_{\rm red}$) has traditionally taken center-stage in determining the goodness of a fit and in model comparison (Andrae et al. 2010). The reduced chi-squared is obtained by dividing the χ^2 by the degrees of freedom, k. A $\chi^2_{\rm red} = 1$ indicates the model provides a good fit, $\chi^2_{\rm red} > 1$ is taken to mean a bad fit, and $\chi^2_{\rm red} < 1$ is an overfit, i.e. the model is too complex for the data. The problem with $\chi^2_{\rm red}$ is in knowing what k is. For a data set with N measurements described by a model with p parameters, the degrees of freedom is usually assumed to be $k = N - p$. As pointed out by Andrae et al. (2010), however, this is only true for linear models where the basis functions are linearly independent. Both limb-darkened transit models and radial velocity models are non-linear, which makes effective number of independent parameters and hence k impossible to estimate, this is especially true if priors are applied (Andrae et al. 2010). Moreover, $\chi^2_{\rm red}$ inherits the uncertainty from the measurements, which is not typically taken into account when reporting $\chi^2_{\rm red}$. For large N, the uncertainty on $\chi^2_{\rm red}$ is $\sqrt{2/N}$, which can be significant for small datasets (Andrae et al. 2010). As a result the reduced chi-squared can be a poor estimate of the goodness-of-fit and model comparison.

Another metric for model selection — one that is frequently used throughout this thesis — is the Bayesian Information Criterion (BIC, Schwarz 1978a). The BIC is defined as

$$\mathrm{BIC} = p \ln N - 2 \ln \mathcal{L}_{\rm max}, \tag{2.35}$$

where p, N are defined as above, and $\mathcal{L}_{\rm max}$ is the maximum likelihood under a likelihood function (Gelman et al. 2003). For most applications in exoplanet science the Gaussian likelihood function is used (Equation 2.38) so that $\mathcal{L}_{\rm max}$ is obtained by essentially minimising χ^2 in Equation 2.34. The BIC alleviates some of the issues with $\chi^2_{\rm red}$ as it is independent of the priors. However, it is only valid when $N \gg p$ and is therefore not reliable for small datasets. The BIC compares two models with different number of parameters p under the same likelihood function. It is a metric that quantifies the improvement of a fit obtained by using a more complex model (increasing p), but is penalised by introducing more free parameters. One example of this is to compute the BIC for a circular model vs. an eccentric model (which also fits for e and ω). The lowest BIC is preferred, and implies a better fit, a model with fewer parameters, or both. The BIC is closely related to the Akaike Information Criterion (AIC), but has a stronger penalty on p than AIC.

2.3.4 Bayesian inference with Markov chain Monte Carlo

In many practical applications one is not only interested in the parameters $\boldsymbol{\theta}$ that produce the best-fitting model (the model that minimizes χ^2), but also the uncertainty on each parameter by taking into account the uncertainty of all other parameters and the correlations between them (i.e. marginalisation). This is commonly achieved with Markov chain Monte Carlo (MCMC) methods which operate on principles of

[e] e.g. http://www.z-table.com

Bayesian probability. Bayes' theorem states that the log probability that the parameters $\boldsymbol{\theta} = \{\theta_0, \theta_1, ..., \theta_n\}$ describe the data y is given by (Gelman et al. 2003)

$$\overbrace{\ln p(\boldsymbol{\theta} \mid y)}^{\text{log probability}} \propto \overbrace{\ln p(\boldsymbol{\theta})}^{\text{log prior}} + \overbrace{\ln p(y \mid x, \boldsymbol{\theta})}^{\text{log likelihood}}, \tag{2.36}$$

where the first and second terms are the natural logarithms of the prior and likelihood, respectively. Bayes' theorem therefore offers an elegant way of combining our prior beliefs of a parameter and using new data to update our knowledge. Parameter estimation is carried out in several steps.

(i) A set of parameters $\{\theta_0, \theta_1, ...\theta_n\}$ is generated, where each θ_i is drawn from a prior distribution which is parameter-dependent. Prior distributions incorporate any information we have on a parameter before we have seen the data. In exoplanet data modelling each parameter commonly has some physical significance and should therefore be restricted to physical values. As an example, imagine we are modelling a radial velocity curve which is a function $f(t, \boldsymbol{\theta})$ where $\boldsymbol{\theta} = \{P,\ t_0,\ K,\ \gamma,\ \sigma_{\text{jitter}}\}$ and we have implicitly set $e = 0$. The radial velocity semi-amplitude K is defined to be positive, so a prior distribution for K could be the uniform distribution between $[0, \infty)$, though in practice the upper limit can safely be set to a finite value and can be informed by e.g. the absence of a secondary spectrum, which translates to a rough limit on the companion mass and hence K. A uniform prior just discards parameter draws that are outside the bounds and do not inform the log probability since all values within the uniform distribution are equally probable. These types of priors are sometimes called non-informative priors, but in reality all prior distributions carry some kind of information. Alternatively, the orbital period P may already be known precisely from several transit light curves, in which case a Gaussian prior distribution may be justified for P with mean and standard deviation given from the transit light curve analysis. In this case the log prior probability is informed by how far the random variable P_{draw} is from the expected mean value μ_P scaled by its standard deviation σ_P, i.e.

$$\ln p(P) = -\frac{1}{2}\left(\frac{P_{\text{draw}} - \mu_P}{\sigma_P}\right)^2 \tag{2.37}$$

(ii) The parameters $\boldsymbol{\theta}$ are used to generate a model $f(x, \boldsymbol{\theta})$ that is compared to the data y. In the Bayesian framework we use a likelihood function to compute the likelihood that the observed data y with Gaussian variance s^2 is a random realisation of the mean function (model) $f(x, \boldsymbol{\theta})$. Most commonly the Gaussian likelihood function is adopted, which reads (Gelman et al. 2003)

$$\ln p(y \mid x, \boldsymbol{\theta}) \equiv \ln \mathcal{L} = -\frac{1}{2}\sum_{i=0}^{N}\left[\frac{(y_i - f(x_i, \boldsymbol{\theta}))^2}{s_i^2} + \ln(2\pi s_i)\right]. \tag{2.38}$$

The measurement uncertainty s is defined as in Section 2.3.2 and can include a white noise scaling term in addition to the formal measurement uncertainties. Keen readers may recognise that first term within the bracket of the likelihood function is the χ^2 as defined in Equation 2.34.

(iii) The log posterior probability in Equation 2.36 is computed by summing the prior probability for all parameters together with the likelihood of each measurement under the current model. The new log

posterior probability is then compared to the previous value to evaluate whether the current parameters are a better fit to the data and new parameter draws are then informed by whether the likelihood increases or decreases. Steps *(i)* – *(iii)* are repeated several thousands or millions of times (Monte Carlo sampling) to form a Markov chain. Once the chain has converged the equilibrium distribution represents the posterior probability distribution of all the parameters, i.e. all combination of parameters that are compatible with the data (Gelman et al. 2003). The exact details of how each Markov chain accepts or rejects steps, and how it responds to variation in the log probability depends on the specific MCMC sampler; the details of which are outside the scope of this work. The two samplers that are used in this thesis are the affine-invariant ensemble sampler (Goodman & Weare 2010) and the No-U-Turn Sampler (Hoffman & Gelman 2014). The former sampler is implemented in the widely used `python` package EMCEE, whereas the latter is implemented in the probablistic modelling framework PYMC3.

2.4 Software developed during this thesis

2.4.1 `amelie`: Bayesian inference of light curves and radial velocities of transiting exoplanets and eclipsing binaries

Motivation

When I first started my doctorate degree in September 2017 my supervisor and I had not yet settled on a definitive topic. The reason for this was due to the fact that I had been granted the luxury of choice, which meant I felt like a child in a sweet shop and was unable to decide on a topic for the first six months. In the first six to eight months of my PhD we therefore decided to take advantage of a couple of opportunities that had recently presented themselves. The first opportunity was that in the few months leading up to the start of my PhD the SPECULOOS Southern Observatory in Paranal, Chile — where Birmingham is a partner institution — had discovered an eclipse in the light curve of a known field brown dwarf. Follow-up spectra of this system determined that these were in fact *two* brown dwarfs of near equal mass orbiting each other, which would make it only the second known eclipsing brown dwarf binary system. I began working on the data for this system, which meant that I needed to write a code that had the capability of performing MCMC analyses using light curves and radial velocities of binary stars (Chapter 3.1). While there was no shortage of publicly available eclipsing binary models at the time (e.g. JKTEBOP; Southworth 2013), the binary star community relied on old codes that were written in Fortran or C. The exoplanet community consists of a relatively young crowd owing to the research field itself being only a few decades old, and as a result the `python` programming language has become the standard. The few binary star light curve models that *did* include a `python` interface (e.g. ELLC, Maxted 2016; `eb`, Irwin et al. 2011) for the most part lack MCMC capability and/or flexibility in including additional models for light curve detrending.

The second opportunity was a transiting brown dwarf companion to a Sun-like star discovered by the WASP survey, where my supervisor was a team member and had led follow-up efforts for some time

already. This would be the second project I would work on in my PhD (Chapter 3.2). The brown dwarf in this system is faint compared to the host star, which means the system is modelled as a single-line binary, similar to exoplanet systems. Several publicly available limb darkened transit models had become popular at the time (e.g. BATMAN, Kreidberg 2015), but these did not generally come with MCMC capability, and those that did, such as `EXOFAST` Eastman et al. 2013 required an IDL license and lacked support for modelling multiple planet systems.

There was therefore a need for a flexible fitting code with MCMC capabilities that could *(i)* fit eclipse light curves of double-lined binaries and their radial velocities, either separately or jointly, and *(ii)* fit transit light curves and radial velocities of exoplanet systems (single-lined binaries), either separately or jointly, with support for multiple planets, and *(iii)* do ground-based light curve corrections for sky background, airmass, and others. In response to these needs I started developing a piece of software that I named AMELIE. AMELIE is based on several publicly available software packages. The light curves and radial velocity models are computed using the eclipsing binary light curve model ELLC (Maxted 2016), which is a Fortran-compiled code with a `python` front-end. The MCMC sampling is carried out by the widely used EMCEE package, which is a `python` implementation of the affine-invariant ensemble sampler by Goodman & Weare (2010).

AMELIE has gone through a series of changes since its initial version. The very first version was written for the analysis of double-lined binaries (Triaud et al. 2020, Chapter 3.1), with functionality for single-lined binaries/exoplanets added for the work outlined in Hodžić et al. (2018) (Chapter 3.2). In my next project I analysed the Rossiter-McLaughlin effect in TRAPPIST-1 observed with CARMENES (Chapter 4.1), which saw the added support for modelling orbit of multiple planets, and the Rossiter-McLaughlin effect using the Ohta et al. (2005) model implemented in ELLC. Finally, functionality to add Gaussian process regression with CELERITE was added for the work published in Kunovac Hodžić et al. (2021) (Chapter 4.2.1).

As one can imagine, adding all this functionality to a software risks making the code bloated and hard to maintain, and this was exactly the case with AMELIE after some time. With new functionality came also difficulty to uphold backwards compatibility due to a code structure that did not scale very well to larger projects. These first versions also used a parameter file in the `yaml` format as input to the fit, which specified parameters, priors, data files, and everything else for the fit. Modern coding is now frequently carried out within the `jupyter` ecosystem, which is clunky for a code based on input edited within a text file. For these reasons, AMELIE underwent a complete revamp of the code structure and was re-written from scratch (several times in fact). It is now more similar to a scripting language found in other open-source codes in the exoplanet community, such as ASTROPY, LIGHTKURVE, and EXOPLANET (see example below). This allows for a more stable code that should be more amenable to new functionality, but this also means that some of the previous features in AMELIE such as certain light curve detrending functionality and Gaussian process regression has not yet been implemented in this new version. The current version of AMELIE — which is not yet intended for public use — can be found on Github.[f]

[f] https://github.com/vedad/amelie

Example guide

As an example of using AMELIE I will here demonstrate how the code was used to analyse a *TESS* light curve of the low-mass eclipsing binary system J0113+31 as part of the work published in Swayne et al. (2020).

We start by importing some basic packages and AMELIE, and define some initial parameters taken from the original discovery paper of this system (Gómez Maqueo Chew et al. 2014).

```
import numpy as np
import amelie

guess = {
        "period" : (14.28052, 0.003), # value and initial error
        "tpri"   : (1778.70064, 0.0002),
        "k"      : (0.1558824, 0.0008),
        "rsum"   : (0.0616481, 0.00075),
        "J"      : (0.06827, 0.0025),
        "fs"     : (-0.5480691, 0.01),
        "fc"     : (0.0874486, 0.002),
        "cosi"   : (0.01575, 0.001),
        "jitter" : (80e-6, 20e-6),
        "ustar"  : [0.4, 0.3]
}
```

Next we name the primary star for internal bookkeeping, create a limb darkening object and assign it to a photometric band we call `tess`, which we are going to use when specifying the photometric data later.

```
primary = amelie.Primary(name="J0113+31")

ld = amelie.Power2LimbDark(guess["ustar"])
primary.add_channel('tess', ld)
```

Now we define a companion and its parameters. Each parameter is given a ‘`value`‘ and nothing more if the parameter should be fixed. If the parameter should be fit, an initial ‘`error`‘ is given which is used to disperse the MCMC walkers around ‘`value`‘. If the parameter is fit, the upper and lower ‘`bounds`‘ can be specified, and/or Gaussian priors by using the keywords ‘`mu`‘ and ‘`sd`‘ for the mean and uncertainty, respectively.

```
companion = amelie.Companion(name="{0}b".format(target))

companion.set_parameter('P', value  = guess["period"][0],
                             error  = guess["period"][1],
                             bounds = (period-0.1, period+0.1)
                        )
companion.set_parameter('Tpri', value  = guess["tpri"][0],
                                error  = guess["tpri"][1],
                                bounds = (guess["tpri"][0]-0.05, guess["tpri"][0]+0.05)
```

```
                        )
companion.set_parameter('k', value  = guess["k"][0],
                             error  = guess["k"][1],
                             bounds = (0.1, 0.2)
                        )
companion.set_parameter('rsum', value  = guess["rsum"][0],
                                error  = guess["rsum"][1],
                                bounds = (0.03, 0.08)
                        )
companion.set_parameter('J', value  = guess["J"][0],
                             error  = guess["J"][1],
                             bounds = (0, 0.2)
                        )
companion.set_parameter('cosi', value  = guess["cosi"][0],
                                error  = guess["cosi"][1],
                                bounds = (0, 0.15)
                        )
companion.set_parameter('f_s', value  = guess["fs"][0],
                               error  = guess["fs"][1],
                               bounds = (-1, 1)
                        )
companion.set_parameter('f_c', value  = guess["fc"][0],
                               error  = guess["fc"][1],
                               bounds = (-1, 1)
                        )

# Set a requirement that it has to eclipse
companion.set_parameter('b', bounds=(0, 1+k))

# Companions is a list to accommodate additional companions in the case of multiple planets
companions = [companion]

system = System(primary=primary, companions=companions)
```

The ‘`system`‘ object brings together the different companions and their orbits, and tracks their parameter values as they are updated in the MCMC sampling, and directly computes the log posterior probability given the priors and data.

Finally, we assign data to our model and specify some options in the fitting. Note that the variables `x,y,yerr` are not defined within the current scope, but represent arrays for the time stamps, normalised flux, and uncertainty, respectively. The ‘`in_transit`‘ flag only computes the model values in-transit and interpolates values outside, which speeds up the computation. The exposure time ‘`t_exp`‘ can be set to correct for finite integration time, with the related ‘`oversample`‘ option which determines the number of points to oversample each exposure. For modelling out-of-transit variability, ‘`knot_spacing`‘ can be specified to a number in units of days, which uses cubic spline interpolation in segments of ‘`knot_spacing`‘ at each step in the MCMC.

```
# Additional parameters for the light curve model
lckwargs = {
            "in_transit"   : True,
            "t_exp"        : 2/60/24,
            "oversample"   : 3,
            "knot_spacing" : 0.5
}

# Extra white noise term for the TESS data
jitter = amelie.Parameter('jitter', value  = guess["jitter"][0],
                           error  = guess["jitter"][1],
                           bounds = (0, 1e-3)
                 )

system.data.add_light_curve(x, y, y_err=yerr, channel='tess', jitter=jitter, **lckwargs)

# Update some parameters that were defined after the instance creation
system.update()
```

The call to '`add_light_curve()`' of the '`data`' submodule adds the photometric light curve to be fit and specifies which band it is such that is uses the correct limb darkening object specified before, as well as a jitter term to inflate the uncertainties. This way if another sector of *TESS* data were to be included, the new sector could have its own jitter term but the same limb darkening parameters, as one would expect. Adding radial velocity data fitting to this system is easy easy and just requires two additional calls. First, the semi-amplitude K needs to be fit in this case, which can be done in the same way as the other parameters. Second, the radial velocity data needs to be specified, which can be done in a similar way to the photometry, but this time calling the '`add_radial_velocity()`' function of the '`data`' submodule. The photometric and radial velocity offsets are calculated by default for each specified data set using a weighted average of the residuals from the current model to the data.

Markov chain Monte Carlo sampling is then as easy as

```
walkers = 200
steps = 1000
system.sample(steps, walkers, threads=4) # 'threads' specifies the number of threads used in
    multiprocessing
```

After discarding the first 800 steps as burn-in, we can draw 50 random parameter samples from the posterior distribution and see how it looks, shown in Figure 2.11.

```
plt.figure()
plt.plot(x, y, '.')

discard = 800

for i in range(50):
    random_ints = np.random.randint(0,int(walkers*(steps-discard)))
    p = system.sampler.get_chain(flat=True, discard=discard)[random_ints,:]
```

```
    system._set_all_parameters(p)

    lc = system.get_channel('tess').get_light_curve(x, system.companions, **lckwargs)
    m = ~system.companions[0]._in_transit_mask(x) # transit mask
    trend = system.get_spline(x, y/light_curve, yerr, mask=m) # spline trend

    plt.plot(x, lc*trend(x), lw=0.5, color='C1')

plt.title("J0113+31")
plt.xlabel('time (days)')
plt.ylabel('relative flux')
```

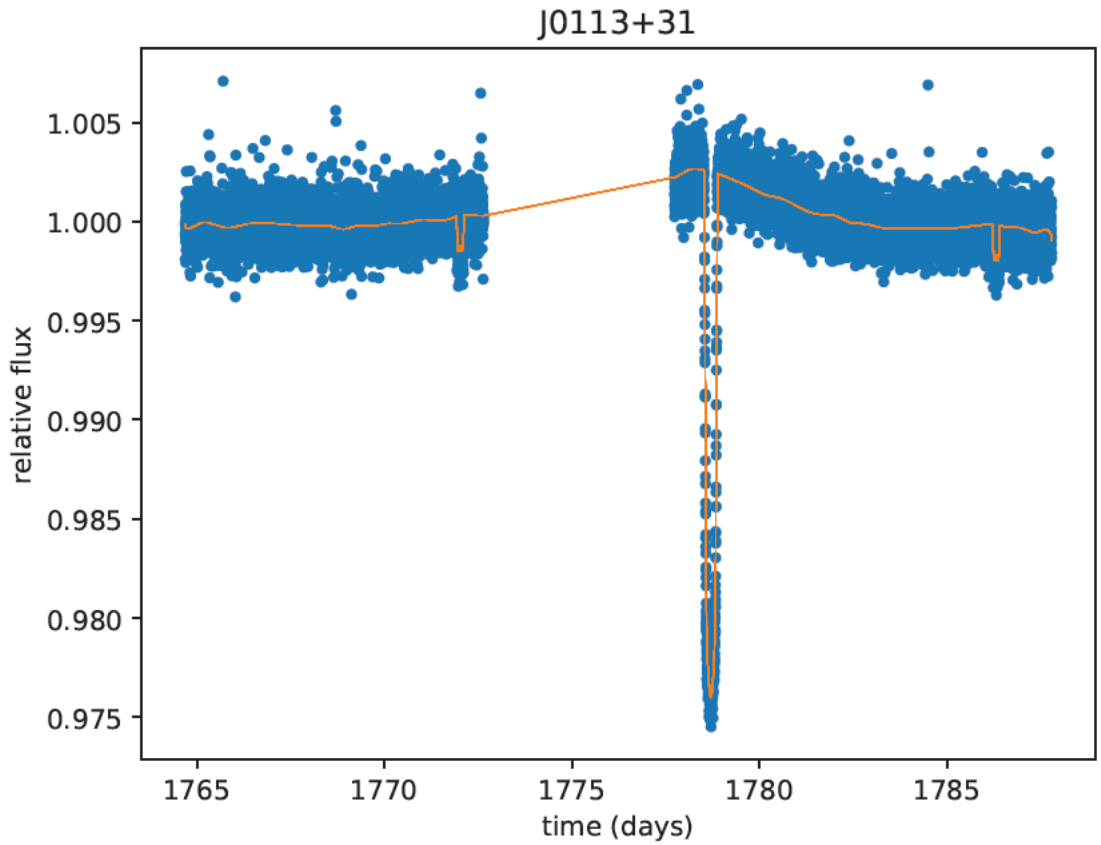


Figure 2.11: A fit to the low-mass eclipsing binary system J0113+31 using AMELIE.

Current state and future of AMELIE

The motivation for the new version of AMELIE was to use it to characterise a sample of two dozen low-mass eclipsing binaries that had been discovered and followed up with WASP over the years. *TESS* had recently started its science observations and provides primary and secondary eclipses for these systems, and the WASP team had secured significant radial velocity follow-up using the CORALIE spectrograph. This sounded like the perfect use case for AMELIE, so I started working on this project and on revamping AMELIE during my Fulbright Scholarship at the University of Chicago, which ran from September 2019

to March 2020. However, the completion of this project was at the time hindered due to the COVID-19 pandemic and wanting to move on to other projects, which is why it is not reported in this thesis. During this time and since then several new codes started getting popular, such as JULIET (Espinoza et al. 2019), EXOFASTV2 (Eastman et al. 2019), ALLESFITTER (Günther & Daylan 2019), and EXOPLANET (Foreman-Mackey 2019). The first two of these are widely used for exoplanet analysis and have limited or no support for binaries. ALLESFITTER is built on the ELLC eclipsing binary model similar to AMELIE, but implements nested sampling (Speagle 2020), MCMC sampling (Foreman-Mackey et al. 2013), and various other functionality. EXOPLANET implements most of the functionality that AMELIE was set out to do, especially when support for secondary eclipses and modelling detached eclipsing binaries was added in mid-2020. The biggest strength of EXOPLANET is however the engine on which it was built — THEANO, now renamed to AESARA — which allows for building models in the PYMC3 framework. This is an enormous benefit because model building in PYMC3 is *dynamic*, which means the user can add arbitrary (analytical) models to the analysis of light curves or radial velocities, where other codes are relatively rigid and can only offer those that are already implemented in the code. In addition, models in PYMC3 have access to Hamiltonian Monte Carlo samplers (e.g. NUTS; Hoffman & Gelman 2014) which offers a significant improvement in convergence times over the sampler implemented in EMCEE. For these reasons I already started using EXOPLANET in Kunovac Hodžić et al. (2021) and in several projects since then, including some parts of Chapter 5.

EXOPLANET has lots of advantages for modelling exoplanet data and its repertoire is ever increasing. Yet, the limb darkened transit model in EXOPLANET is analytical and the star is modelled as a sphere, whereas eclipsing binary models such as ELLC allows for non-spherical shapes due to tidal deformation and can include the effects of ellipsoidal variation, spots, Doppler boosting, beaming, and reflection. Therefore, there may still be a place for AMELIE in the future, providing the above features can be implemented in user-friendly way to take full advantage of the ELLC model.

2.4.2 `olio`: The *reloaded* Rossiter-McLaughlin method

Motivation, description and future vision

As outlined in Section 2.2.4, the reloaded Rossiter-McLaughlin method that was first introduced in Cegla et al. (2016) implemented a new technique (though based on familiar principles) for the analysis of cross-correlation functions from stabilised spectrographs. As we push towards studying the obliquities of stars with small transiting planets (Chapter 4) new techniques such as this and future iterations of it are expected to be important. This became clear in my analysis of the Rossiter-McLaughlin effect of π Men c, outlined in Section 4.2.1, which is when I started developing a code for the reloaded Rossiter-McLaughlin model which I eventually named OLIO. OLIO is being developed on Github[g] and an initial public version is available from the `python` Package Index, PyPI[h].

[g] https://github.com/vedad/olio
[h] https://pypi.org/

There are three main elements to reloaded Rossiter-McLaughlin analyses. The first part consists of manipulating the CCFs in a series of ways to retrieve the local stellar light behind the planet (Section 2.2.4). Some of the basic steps include normalisation and resampling (interpolation) of the CCFs to get the difference between the reference CCF and in-transit CCFs. The second step consists of a fit to the local stellar CCFs retrieved from the previous step, which finds the radial velocity of the stellar surface at each epoch. The third step is modelling the surface radial velocities from the previous step which is a function of the geometry of the star in relation to the line of sight and the planet's path across the stellar disc (Collier Cameron et al. 2010b).

Certain aspects of the first two steps could be implemented as helper functions in OLIO to simplify the analysis for the user — this is in fact planned for subsequent releases. In general, however, very early versions of OLIO demonstrated that a streamlined approach of feeding in a sequence of CCFs to the code that will then spit out local surface velocities does not always work well for all data, and also has the danger of making the code inflexible and a "black box". For this reason, this approach is not implemented in the current version. The preferred approach is instead to create comprehensive documentation (TBD) to guide users through the necessary steps, and instead concentrate on providing the necessary models and functions to perform the analysis, such as those found for e.g. LIGHTKURVE (Lightkurve Collaboration et al. 2018), EXOPLANET (Foreman-Mackey 2019) and numerous other codes.

The third and final step is not unique to the reloaded technique, it is in fact a necessary ingredient for all Rossiter-McLaughlin models since all require the sub-planet velocity during transit (Ohta et al. 2005; Hirano et al. 2011; Boué et al. 2013; Cegla et al. 2016). Yet I was surprised to find that I was unable to locate any public `python` code which implemented the necessary equations for just returning stellar surface velocities. For this reason, version 0.0.1 of OLIO is a bare-bones implementation of a model that calculates the stellar surface velocity over the transit chord. Future releases of OLIO will build on this to include several widely-used velocimetric Rossiter-McLaughlin models, such as those in Giménez (2006), Hirano et al. (2011), Boué et al. (2013), which to my knowledge are not publicly available in the `python` language from any other code as of yet.

Various versions of OLIO has been used in Kunovac Hodžić et al. (2020) and Kunovac Hodžić et al. (2021) which are outlined in Chapters 6 and 4.2, respectively, as well as the article in preparation in Chapter 5.

Example guide

In the following I demonstrate some of the features of OLIO v0.0.1. Computing a model of the stellar surface velocity along the transit chord starts with creating an instance of the `Orbit` class. At each phase (epoch) `x`, a grid is created underneath the planet which is used to determine the brightness-weighted quantities according to a chosen limb darkening law. The brightness-weighted stellar velocity along the transit chord due to rotation can then be computed by a call to `get_rotational_velocity()`, for a combination of the stellar equatorial velocity `v_eq`, the projected obliquity `ell`, stellar inclination `i_star` and latitudinal differential rotation factor `alpha`. A contribution from convective blueshift can also be

included, which is expressed as a linear or quadratic polynomial function of the brightness-weighted μ. Some examples of the models generated from the below code are shown in Figure 2.12.

```
import numpy as np
import olio
import matplotlib.pyplot as plt

orbit = olio.Orbit(aor=10, ror=0.1, i_pl=89)
ustar = [0.4, 0.3] # quadratic limb darkening coefficients
x = np.linspace(-0.02, 0.02, 100) # orbital phase

# compute velocity model due to rotation
v_rigid_rot = olio.QuadLimbDark(ustar).get_rotational_velocity(
                                    orbit=orbit, x=x, v_eq=3, ell=45
                                    )
v_diff_rot = olio.QuadLimbDark(ustar).get_rotational_velocity(
                                    orbit=orbit, x=x, v_eq=3, ell=45, i_star=60, alpha=0.2
                                    )

# compute convective blueshift
v_cb_lin = olio.QuadLimbDark(ustar).get_convective_velocity(orbit=orbit, x=x, c=[0.3])
v_cb_quad = olio.QuadLimbDark(ustar).get_convective_velocity(orbit=orbit, x=x, c=[0.3, 0.1])

# create plot
ax = plt.figure(figsize=(7.5,4)).subplot_mosaic(
    """
    AB
    """, gridspec_kw={'wspace':0.3}
)

ax['A'].set_title('rotation')
ax['A'].plot(x, v_rigid_rot, ls='solid', c='k', label='rigid-body rotation')
ax['A'].plot(x, v_diff_rot, ls='dashed', c='k', label='differential rotation')
ax['A'].set_ylim(-2, 2.5)

ax['B'].set_title('convective blueshift')
ax['B'].plot(x, v_cb_lin, c='k', ls='dotted', label=r'linear in $\langle \mu \rangle$')
ax['B'].plot(x, v_cb_quad, c='k', ls='dashdot', label=r'quadratic in $\langle \mu \rangle$')
ax['B'].set_ylim(-0.3, 0.2)

m = ~np.isnan(v_rot) # mask out-of-transit data for plot limits
[ax[l].set_xlabel('phase') for l in ax]
[ax[l].set_ylabel('local surface velocity (km/s)') for l in ax]
[ax[l].set_xlim(x[m].min(), x[m].max()) for l in ax]
[ax[l].legend() for l in ax]
```

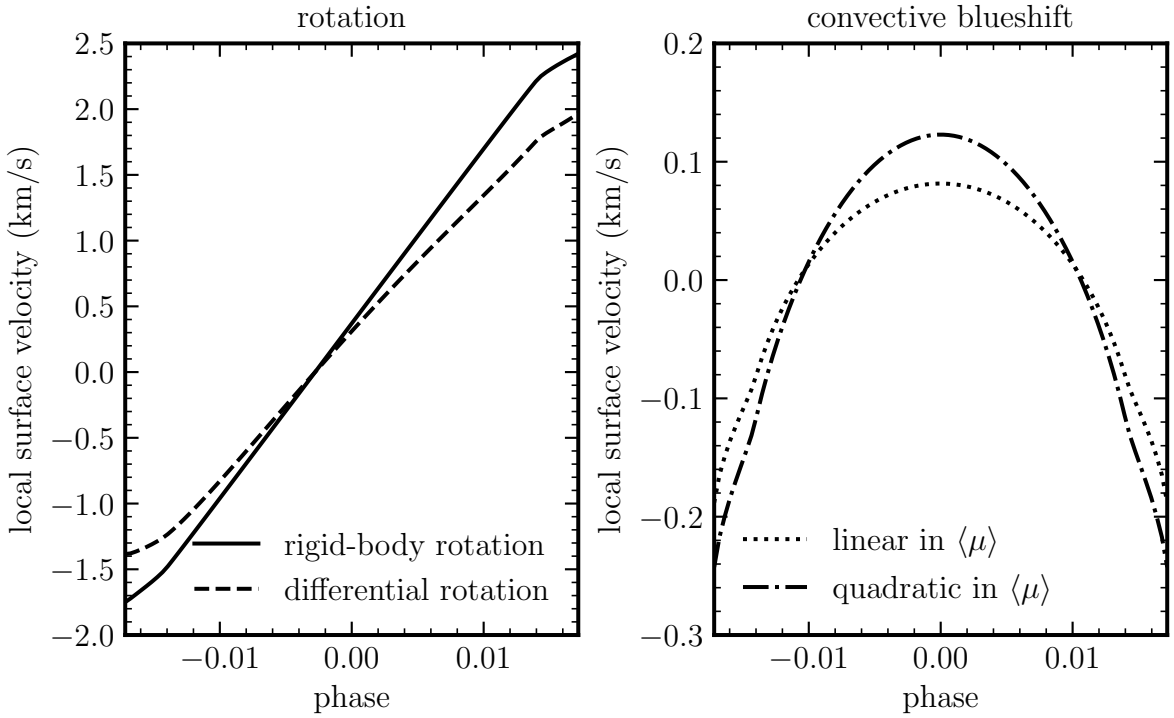


Figure 2.12: Demonstration of surface velocity models computed with OLIO for rotation (*left*) and centre-to-limb convective blueshift variation (*right*). *Left:* The rigid-body model (*solid line*) is computed with $v \sin i_\star = 3\,\mathrm{km\,s^{-1}}$, $\lambda = 45°$. The differential rotation model (*dashed*) is computed with $v_{\mathrm{eq}} = 3\,\mathrm{km\,s^{-1}}$, $i_\star = 60°$, $\lambda = 45°$, and $\alpha = 0.2$. *Right:* The convective blueshift models are expressed as polynomials in the brightness-weighted distance from the stellar centre, $\langle\mu\rangle$, with linear coefficient $300\,\mathrm{m\,s^{-1}}$ for the linear model (*dotted*), and an additional quadratic coefficient of $100\,\mathrm{m\,s^{-1}}$ (*dash-dotted*).

CHAPTER 3

DISCOVERY AND CHARACTERISATION OF NEW EXOPLANETS AND BROWN DWARFS

3.1 An eclipsing substellar binary in a young triple system discovered by SPECULOOS

Parts of the following Sections are taken from my mid-course assessment (MCA) report submitted in October 2018.

3.1.1 An unexpected discovery

The SPECULOOS observatory (Search for habitable Planets EClipsing ULtra-cOOl Stars) comprises four 1 m class telescopes that survey a sample of ~1000 late M dwarf stars and brown dwarfs to search for rocky transiting planets. The facility is located at ESO Paranal Observatory, Chile, and has been fully operational since late 2017 (Burdanov et al. 2018). In July 2017, one of the telescopes was monitoring a brown dwarf during commissioning (hereafter 2M1510 A) known to have a companion on a wide 250 AU orbit (2M1510 B), when it detected a ~4 % V-shaped dip in the brightness of the target lasting about 90 min. A reconnaissance spectrum was obtained with the NIRSPEC instrument on the 10 m Keck telescope revealed line splitting in the spectral lines, as shown in Figure 3.1. The spectrum confirmed that 2M1510 A in fact consists of two near-equal brightness objects, and the 2M1510 system forms a hierarchical triple. Given the signal in the SPECULOOS data, the inner binary was now known to be inclined in such a way that they could eclipse each other. Only one other eclipsing brown dwarf binary system is known to exist, so these objects are extremely rare (Stassun et al. 2006).

Eclipsing binary stars form the cornerstone for verifying stellar evolution models (Torres et al. 2010). The same is true for evolution of substellar objects, though these models are much less observationally

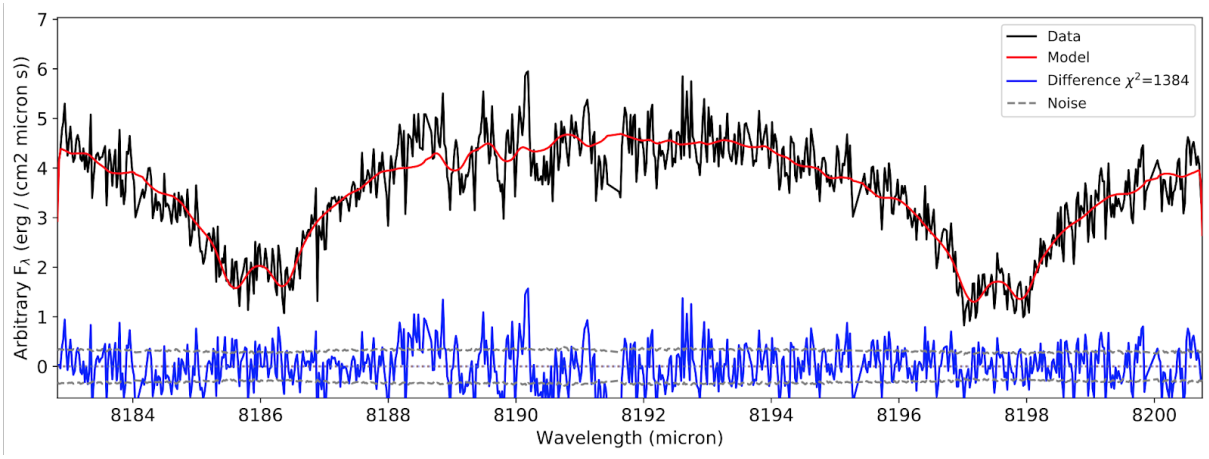


Figure 3.1: A spectrum of 2M1510 A taken with the UVES instrument on the VLT, revealing splitting at the locations of the absorption lines at approximately 8186 Å and 8197.7 Å due to the composite spectrum from both brown dwarfs. Note that there is an error in the wavelength label, the numbers are in units of Å. The black line corresponds to the spectral data, the red line is the forward model, the blue line is the residual of the fit with grey lines corresponding to the 1σ uncertainties on the data. Figure by courtesy of Adam Burgasser.

constrained (Baraffe et al. 2003). Brown dwarfs are hot as they form and contract, but quickly cool down as they thermally radiate their energy away when contraction is stopped due to electron degeneracy pressure in the core (Burrows et al. 1997). As a result the majority of known field brown dwarfs are biased towards young objects. However, their mass and radius are typically obtained from comparing their spectra and brightness to evolutionary models which carries large uncertainties. Eclipses ensure a measurement of the orbital inclination, which enables an absolute determination of its mass and a radius which can be used to calibrate brown dwarf cooling curves (Burrows et al. 1997).

3.1.2 Contribution

I started my PhD at Birmingham in September 2017, just months after the initial discovery of the eclipsing nature of 2M1510 A. Over the past few years prior to this I had started to become increasingly interested in exoplanets, so I was extremely excited to finally start my doctorate and work with Amaury, whom I had met during my master's thesis research. Over several conversations prior to working together he had learned of my excitement about working on exoplanets and my goals. So high was his trust in my abilities, in fact, that in my second week at Birmingham he asked me if I wanted to contribute to the paper on the discovery on 2M1510, which we at the time already suspected could be submitted to a high-impact journal. I maintained a high level of responsibility in this work that taught me an extraordinary amount in my first six months, and I drew upon this experience in my next paper — which I did lead.

My primary role in this article was to obtain the brown dwarf and orbital properties by analysing the eclipse from SPECULOOS and radial velocity data we obtained from the UVES and NIRSPEC spectrographs. This work formed the foundation of the fitting code AMELIE, which is outlined in Chapter 2.4.1. My contribution to the manuscript is outlined in the "Methods" section of the published

article, under the headings *Global analysis of the radial velocity and photometric data*, and *Assumptions for the final orbit fit*. The results from my analysis is shown in Figure 1 in the manuscript below (Figure 3.4 in the thesis), which I created. The radial velocity and eclipse data are consistent with a pair or brown dwarfs with masses $M_1 = 0.0382 \pm 0.0027\,M_\odot$, $M_2 = 0.0375 \pm 0.0029\,M_\odot$ with an orbital period of $P = 20.9022 \pm 0.0058$ d. The orbital solution points to an eccentric system with $e = 0.309 \pm 0.022$, and $\omega = -89.9° \pm 3.3°$.

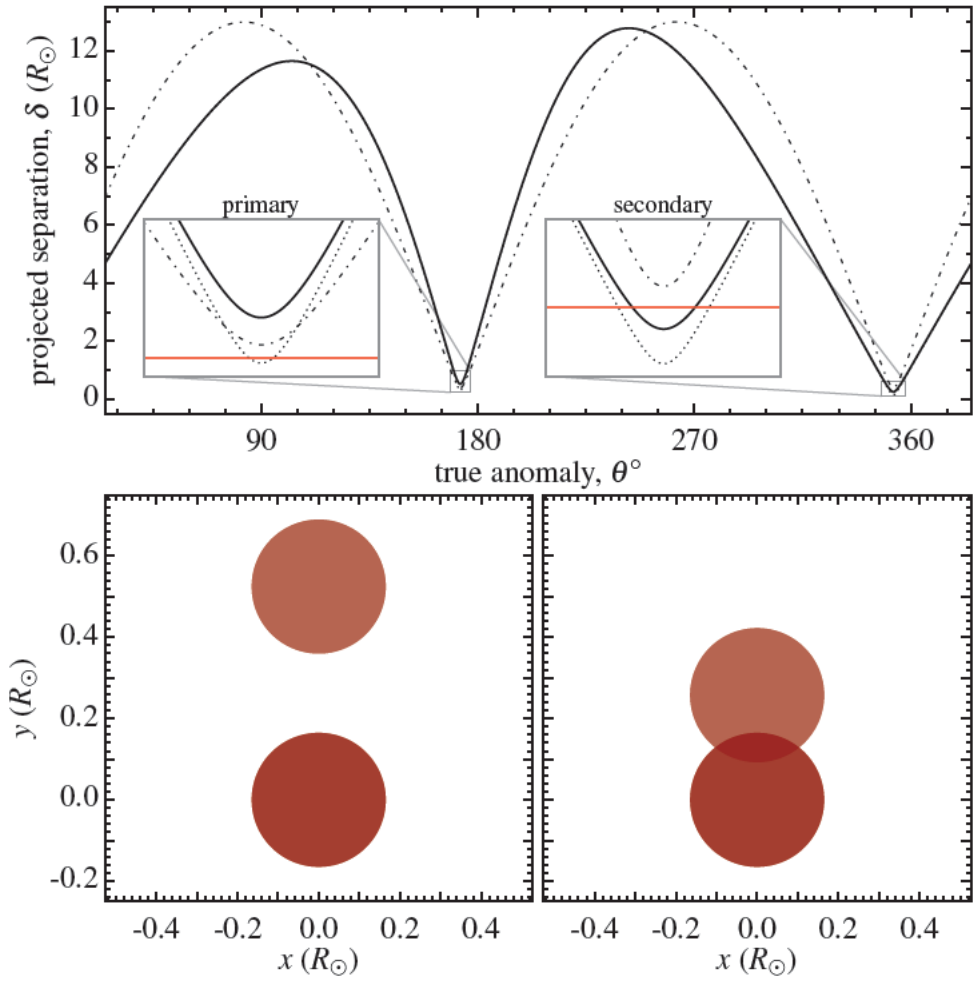


Figure 3.2: *Top:* The projected separation between the two brown dwarfs during their orbit. The dash-dotted line is the equivalent curve if the eccentricity was zero. The dotted line shows the separation curve for the minimum inclination needed for a primary eclipse to occur, which is i=89.1°. The two insets are zoomed in on the expected position where primary eclipse would occur, and where secondary eclipse occurs. The red line in the insets denote the minimum separation needed for there to be an eclipse. *Bottom:* A visual representation of the projected separation at the expected times of primary (*left*) eclipse (inferior conjunction, Chapter 2.1.1) and secondary eclipse (*right*, superior conjunction). The darker object is the primary component.

In addition, I co-led the photometric follow-up campaign with SPECULOOS. My role was to predict next observable eclipses using our model for the initial eclipse and the period constrained from the radial velocity data. Following one orbital period after the eclipse detection, our model (based on follow-up

radial velocity data) predicted another eclipse was narrowly missed with SPECULOOS by a matter of minutes. The radial velocity data can not sufficiently constrain the data, and as a result, two main orbital solutions existed. One was much more likely than the other, as shown in the second panel of Figure 3.3. We carried out numerous photometric monitoring campaigns at predicted eclipse windows in an attempt to detect another eclipse to precisely establish the ephemeris. For this we used SPECULOOS from Chile, but also the MONET/South telescope, located in Sutherland, South Africa. We carried out this campaign over two observing seasons, which ran from April to August of 2018 and 2019. Owing to the long orbital period of the binary (~20 days) there were few observable events from the ground so we did not recover a second eclipse. Despite these non-detections, the flat light curves were still useful as they ruled out certain solutions such that the uncertainty in the ephemeris shrunk. This is reflected in the final parameters listed in Table 2 in the manuscript below.

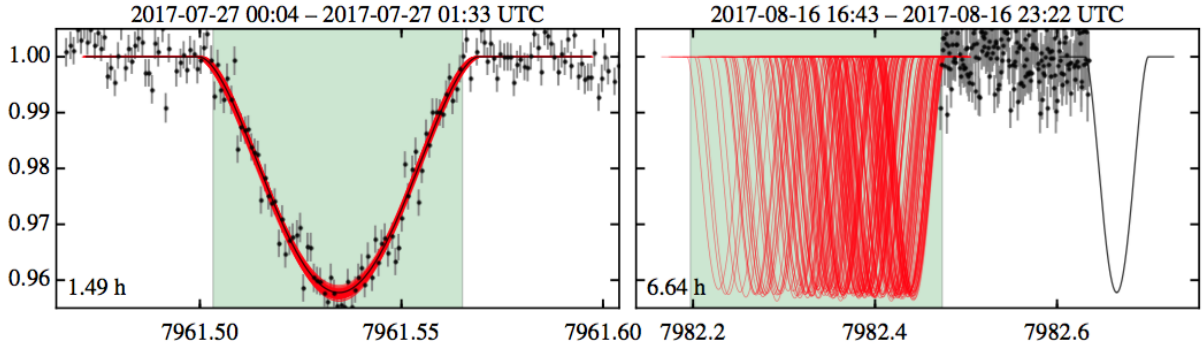


Figure 3.3: The two panels show the brightness of 2M1510 A as a function of time with errors. The green regions are possible orbital solutions within 2σ. The first panel (*left*) shows the detected eclipse, and the second panel (*right*) shows how a second eclipse was narrowly missed, leading to two distinct orbital solutions, placing the eclipse either just before or after the observations.

nature astronomy

LETTERS

https://doi.org/10.1038/s41550-020-1018-2

Check for updates

An eclipsing substellar binary in a young triple system discovered by SPECULOOS

Amaury H. M. J. Triaud[1]✉, Adam J. Burgasser[2]✉, Artem Burdanov[3], Vedad Kunovac Hodžić[1], Roi Alonso[4], Daniella Bardalez Gagliuffi[5], Laetitia Delrez[6], Brice-Olivier Demory[7], Julien de Wit[8], Elsa Ducrot[3], Frederic V. Hessman[9], Tim-Oliver Husser[9], Emmanuël Jehin[10], Peter P. Pedersen[6], Didier Queloz[6], James McCormac[11], Catriona Murray[6], Daniel Sebastian[3], Samantha Thompson[6], Valérie Van Grootel[10] and Michaël Gillon[3]

Mass, radius and age are three of the most fundamental parameters for celestial objects, enabling insight into the evolution and internal physics of stars, brown dwarfs and planets. Brown dwarfs are hydrogen-rich objects that are unable to sustain core fusion reactions but are supported against collapse by electron degeneracy pressure[1]. As they age, brown dwarfs cool, reducing their radius and luminosity. Young exoplanets follow a similar behaviour. Brown dwarf evolutionary models are relied upon to infer the masses, radii and ages of young brown dwarfs[2,3]. Similar models are also used to infer the mass and radius of directly imaged exoplanets[4]. Unfortunately, only sparse empirical mass, radius and age measurements are currently available, and so the models remain mostly unvalidated. Double-line eclipsing binaries provide the most direct route towards the absolute determination of the masses and radii of stars[5–7]. Here we report the discovery by SPECULOOS (Search for habitable Planets EClipsing ULtra-cOOl Stars) of the 2M1510A triple system, consisting of a nearby, eclipsing, double-line brown dwarf binary and a widely separated tertiary brown dwarf companion. We find that the system is a member of Argus, a 45 ± 5 million-year-old moving group[8,9]. The system's age matches those of currently known directly imaged exoplanets so 2M1510A provides an opportunity to benchmark evolutionary models of brown dwarfs and young planets. We find that widely used evolutionary models[3] do reproduce the mass, radius and age of the binary components remarkably well, but overestimate their luminosity by up to 0.65 magnitudes, which could result in underestimations of 20% to 35% of photometric masses for directly imaged exoplanets and young-field brown dwarfs.

There is only one double-line eclipsing substellar binary currently known: 2MASS J05352184-0546085AB (hereafter 2M0535)[10,11]. A member of the 1-Myr-old Orion Nebular Cluster, this system is a unique benchmark for evolutionary models of brown dwarfs, but its youth implies that component parameters could be affected by differential formation age, ongoing accretion, rapid rotation, and structural and surface effects induced by strong magnetic activity. Consequently, its parameters have proved difficult to reconcile with evolutionary models[12]. Masses and radii have also been determined for roughly a dozen brown dwarfs identified in transit around more massive stars[13,14]. Although their ages are relatively mature (>1 Gyr), the substantial scatter of these objects in the mass-radius plane suggests that their evolution may be influenced by their proximity to their host star[13]. Robust tests of substellar evolutionary models necessitate the identification of substellar double-line eclipsing binaries in clusters of various ages. 2M1510, the system we present here, is older than 2M0535, and has smaller radii that are intermediate between those of young and old brown dwarfs.

We have identified a double-line eclipsing binary system within a compact, fully substellar triple system, which is also a member of a nearby stellar association older than Orion. The brown dwarf binary 2MASSW J1510478-281817 (hereafter 2M1510A) and its visual companion 2MASS J15104761-2818234 (hereafter 2M1510B) were first identified in 2MASS data[15] as a resolved (separation 6.8 arcsec), unequal-brightness ($\Delta J = 1.17 \pm 0.04$), M dwarf visual binary[16]. 2M1510A is known to exhibit Hα emission[16] (see Methods). With an average Gaia-measured distance of 36.6 ± 0.3 pc (ref. [17]) the projected separation between 2M1510A and 2M1510B spans 250 astronomical units (AU). 2M1510A has been identified as a kinematic member of the 45 ± 5 Myr Argus moving group[8,9], and we confirm membership for this component and 2M1510B with Gaia data and radial velocity measurements reported here (see Methods). In addition, newly acquired low-resolution near-infrared spectra for both sources exhibit low surface gravity absorption features consistent with 10–100-Myr-old substellar objects (see Methods). Despite their unequal brightness, the near-infrared and red optical spectra of these sources have similar classifications, leading to the early proposition that 2M1510A might itself be "an equal luminosity double"[16]. We name the two components 2M1510Aa and 2M1510Ab, forming a tight inner binary, with 2M1510B as the tertiary member of the system.

Both sources were simultaneously monitored during commissioning observations of the SPECULOOS-South Observatory at

[1]School of Physics and Astronomy, University of Birmingham, Edgbaston, Birmingham, UK. [2]Center for Astrophysics and Space Sciences, University of California, San Diego, La Jolla, CA, USA. [3]Astrobiology Research Unit, Université de Liège, Liège, Belgium. [4]Instituto de Astrofísica de Canarias, La Laguna, Tenerife, Spain. [5]Department of Astrophysics, American Museum of Natural History, New York, NY, USA. [6]Cavendish Laboratory, Cambridge, UK. [7]University of Bern, Center for Space and Habitability, Bern, Switzerland. [8]Department of Earth, Atmospheric and Planetary Sciences, Massachusetts Institute of Technology, Cambridge, MA, USA. [9]Institut für Astrophysik, University of Göttingen, Göttingen, Germany. [10]Space Sciences, Technologies and Astrophysics Research (STAR) Institute, Université de Liège, Liège, Belgium. [11]Department of Physics, University of Warwick, Coventry, UK.
✉e-mail:

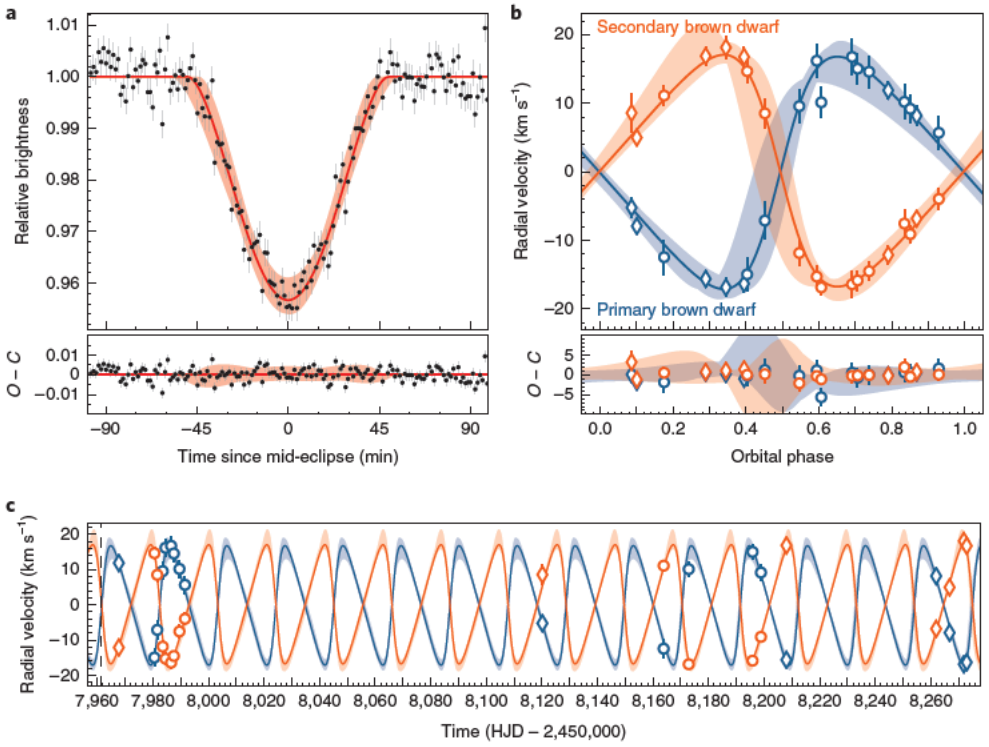


Fig. 1 | Data demonstrating that 2M1510A is a substellar eclipsing binary. a, SPECULOOS photometric data (black points) and their 1σ uncertainties showing the observed 4% grazing eclipse. The red solid line is the best-fit model from the joint global fit with its 2σ confidence region (red shaded region). Below are the residuals of the best fit (O – C). **b**, The phase-folded radial velocity orbit of the brown dwarf primary (blue) and secondary (orange). A systemic velocity of –12.9 km s^{-1} has been subtracted from the values. Individual points are measurements (UVES, circles; NIRSPEC, diamonds) with their 1σ uncertainties. Solid lines indicate the joint global fit with 2σ uncertainty regions shaded. Below are the residuals of the best fit (O – C). **c**, Radial velocity observations and models as in **b**, but shown as a function of time. The vertical dashed line on day 7,961.5 indicates the epoch of the secondary eclipse displayed in **a**. These combined data allow us to measure the masses of the two brown dwarfs and their combined radius.

Cerro Paranal, Chile, which consists of four robotic telescopes, each with a one-metre-diameter primary mirror[18]. The main goal of the SPECULOOS-South Observatory is to identify rocky planets transiting the lowest-mass stars and brown dwarfs, such as those found in the TRAPPIST-1 system[19]. We began monitoring 2M1510A on 2017 July 18. On 2017 July 26, we detected a 4% drop in brightness over a 90-minute duration, with a profile consistent with a grazing eclipse (see Fig. 1a). We promptly obtained high-resolution, near-infrared spectra of both sources using the Near-InfraRed Spectrometer (NIRSPEC[20]) on the Keck II telescope on 2017 August 02. These data (see Methods) revealed 2M1510A to be a double-line spectroscopic binary with component radial velocity separation of 22.9 ± 1.0 km s^{-1}, indicating a relatively short orbital period. In the following months, we obtained twelve high-resolution red optical spectra of 2M1510A using the red arm of the UltraViolet Visual Échelle Spectrometer (UVES[21]) on the Very Large Telescope UT2 (Kueyen), and another six Keck/NIRSPEC near-infrared spectra (Fig. 1b, c). We extracted component radial velocities from these 19 spectra as detailed in the Methods. The velocity components of 2M1510A, which are distinguishable by their slightly unequal relative fluxes, show a clear pattern of oscillation, consistent with two brown dwarfs in close orbit around a common centre of mass.

We jointly fitted the primary and secondary radial velocities of 2M1510A with SPECULOOS photometry to a binary model, assuming Keplerian orbits. Our models are produced with *ellc*[22] and converged using the *emcee* sampler[23], in a tested *python* package named *amelie*[14]. We found a solution and estimated uncertainties using Markov Chain Monte Carlo (MCMC) techniques, as described in the Methods. All orbital and physical parameters are provided in Tables 1 and 2. The data are consistent with a pair of near-equal-mass brown dwarfs: 2M1510Aa, with a mass of $0.0382 \pm 0.0027\ M_\odot$ ($40.0\ M_{\rm Jup}$), and 2M1510Ab, with a mass of $0.0375 \pm 0.0029\ M_\odot$ ($39.3\ M_{\rm Jup}$), where $M_\odot$ is the solar mass and $M_{\rm Jup}$ is the mass of Jupiter. The pair occupies a 20.902 ± 0.006 day orbit, with a non-zero eccentricity $e = 0.31 \pm 0.02$ and an orbital inclination $i = 88.5 \pm 0.1°$. Our orbital solution determines that the observed grazing eclipse occurs when the primary passes in front of the secondary (secondary eclipse) near periastron. The primary eclipse, which occurs close to apoastron, is undetectable owing to the tilt and semi-major axis of the orbit ($a = 0.063 \pm 0.001$ AU). This prevents the measurement of individual component radii, but we can constrain the sum of the radii (see Methods) to be $0.315 \pm 0.016\ R_\odot$ ($3.15\ R_{\rm Jup}$), where $R_\odot$ is the solar radius, and $R_{\rm Jup}$ is the radius of Jupiter. Since both masses are equivalent to within their uncertainties, we assume that each component has a radius equal to half of their sum. We note that the NIRSPEC and UVES spectra indicate a flux ratio $f_2/f_1 = 0.83$–0.88 between both components, which could originate either from a radius ratio of 0.91–0.94 (assuming equal temperatures), a temperature ratio of 0.95–0.97 (assuming equal radii), or a mixture of the two. Since we are unable to differentiate between these cases, we assume equal radii for our subsequent analysis.

We compare our measurements to evolutionary models[3] in Figs. 2 and 3. We find that the masses and radii are independently compatible with the age of the Argus moving group, 45 ± 5 Myr (ref. [9]) to within 1σ. In Fig. 3 we present mass tracks as a function of radius and age (Fig. 3a), and of luminosity and age (Fig. 3b). Those models also predict individual component magnitudes, which we find to be brighter than the observed absolute magnitudes (see Methods). Each

Table 1 | Characteristics of 2M1510A and 2M1510B and of the binary system

Parameter	2M1510A	2M1510B
	2MASS J15104786-2818174[a]	2MASS J15104761-2818234[a]
	Gaia 6212595980928732032[b]	Gaia 6212595980924278144[b]
Right ascension, declination (J2000)	15 h 10 min 47.47 s, −28°18′18.3″	15 h 10 min 47.72 s, −28°18′24.2″
G magnitude	17.487±0.002[b]	18.886±0.004[b]
J magnitude	12.84±0.03[a]	14.01±0.03[a]
H magnitude	12.11±0.03[a]	13.32±0.03[a]
K magnitude	11.69±0.03[a]	12.79±0.03[a]
Parallax π (mas)	27.2±0.3[b]	27.7±0.5[b]
Right ascension projected proper motion $\mu_\alpha \cos\delta$ (mas yr^{-1})	−118.7±0.5[b]	−117.4±0.9[b]
Declination proper motion μ_δ (mas yr^{-1})	−46.9±0.4[b]	−45.7±0.7[b]
RV (km s^{-1})	−12.9±0.4	−12.0±0.3
Spectral type	M8 (red optical)[c]	M9 (red optical)[c]
	M9γ (near-infrared)	M9γ (near-infrared)
	Binary system	
Distance (pc)	36.6±0.3[b]	
$\mu_\alpha \cos\delta$ (mas yr^{-1})	−118.4±0.6	
μ_δ (mas yr^{-1})	−46.6±0.5	
RV (km s^{-1})	−12.3±0.4	
Galactic space velocities U, V, W (km s^{-1})	(−5.3±0.3, 24.7±0.3, −1.3±0.2)	
Age (Myr)	45±5[d]	

References: a:[15] b:[8] c:[16] d:[9]

Table 2 | Orbital and physical parameters for 2M1510 Aab

Orbital period (day)	$20.9022^{+0.0059}_{0.0056}$
Semimajor axis (AU)	0.0627 ± 0.0014
Tsec (HJD − 2450000)	$7961.53441^{+0.00064}_{0.00061}$
Eccentricity	0.309 ± 0.022
Argument of periastron (°)	−89.9 ± 3.3
Inclination (°)	88.5 ± 0.1
Mass ratio	0.981 ± 0.049
Primary's mass, M_1 ($M_\odot$)	$0.0382^{+0.0028}_{0.0026}$
Secondary's mass, M_2 ($M_\odot$)	$0.0375^{+0.0029}_{0.0028}$
Sum of radii, $R_1 + R_2$ ($R_\odot$)	$0.3147^{+0.0159}_{0.0157}$
Flux ratio, f_2 / f_1	0.827 ± 0.013 (819 nm) 0.88 ± 0.07 (2.3 μm)

component of 2M1510A appears fainter by 0.65 ± 0.14, 0.48 ± 0.13, and 0.40 ± 0.13 in the J, H and K magnitudes, respectively, than the model predictions. Our estimate of the bolometric luminosity is similarly below model predictions (Fig. 3). This disagreement is consistent with prior measurements of young brown dwarfs and planetary mass objects. For example, ref. [24] measure a luminosity of β Pic b that is 0.7 dex below the hot-start model predictions for that source's mass and age. Young ultracool dwarfs have been found to be both more and less luminous than models in colour–magnitude diagrams by up to 1 magnitude (or equivalently too blue or too red[25]). Model magnitudes are often used to obtain mass estimates (or detection limits) for directly imaged planets[26]. Should the magnitude differences measured for 2M1510Aab and other young brown dwarfs extend to massive exoplanets, our results suggest that the latter masses could have been systematically underestimated by 20%–35%. Alternatively, if we assume that the dynamical masses and the bolometric luminosity are correct, the models imply that the age of the system is of the order of 70 Myr (see Methods). In this case the measured radii would become 1.09 larger than predicted by the models[3].

The formation of close binaries, particularly those with non-zero eccentricities, remains an area of debate[27,28]. One possible formation mechanism is the dynamic perturbation of a wide tertiary companion in a misaligned orbital plane. If the outer orbit is inclined by more than 40°, the inner pair can experience important variations in eccentricity, approaching unity, through so-called Lidov–Kozai cycles[28–30]. When the inner pair is at periastron, tidal dissipation works to circularize the orbit and reduce its orbital semimajor axis. We investigated whether 2M1510A's parameters are compatible with Lidov–Kozai cycles (see Methods). We conclude that this is unlikely to be the case: 2M1510B's separation is too large, leading to Lidov–Kozai cycles that would greatly exceed the system's current age. The eccentricity we detect is therefore likely to be primordial, and the pair probably formed via another mechanism. Furthermore, the separation between both companions at periastron is 43 stellar radii, implying tides that are relatively weak and unlikely to change the orbital parameters over billions of years. Main-sequence binaries with orbital separation in excess of 10–12 stellar radii show very little signs of tidal evolution post-main-sequence[27].

Our photometric monitoring of the system with SPECULOOS[18] and the MONET/South telescope[31] partially covered four eclipse epochs, and have so far failed to recover a second eclipse, a constraint that is included in our orbit fit. We used all of the photometric data to search for evidence of rotationally modulated variability. While we detect statistically significant 1%–2% photometric variability from both sources, we do not detect significant periodicity (see Methods). We determined rotational $v\sin i$ values of 8.7 ± 1.0 km s^{-1} and 6.8 ± 1.5 km s^{-1} for the primary and secondary

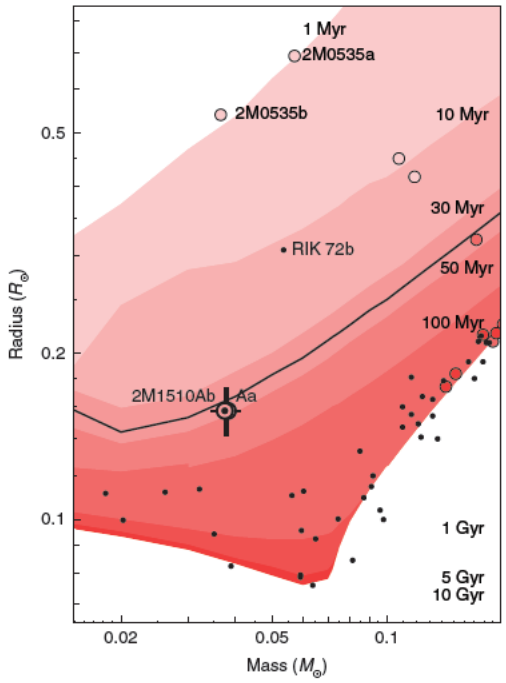


Fig. 2 | Mass–radius diagram showing the position of the 2M1510Aab eclipsing pair (shown in black with their 1σ uncertainties). The red-shaded areas separate the tracks of the Exeter/Lyon evolutionary models[4,3], with ages labelled. Circles delineate mass/radius measurements obtained for previously detected double-line eclipsing binaries, with their colour corresponding to the age estimated for each binary. Dark dots depict mass/radius measurements for interferometric measurements, single-line eclipsing binaries and transiting exoplanets. The young brown dwarfs 2M0535AB[11] and RIK 27b[7] are labelled. 2M1510A's parameters are consistent with the 45±5 Myr age of the Argus moving group, just below a 40-Myr isochrone highlighted in black. 2M1510Aab, our double-line eclipsing system, is in an area of parameter space with no equivalent systems. Literature measurements are reported in Supplementary Tables 5 and 6.

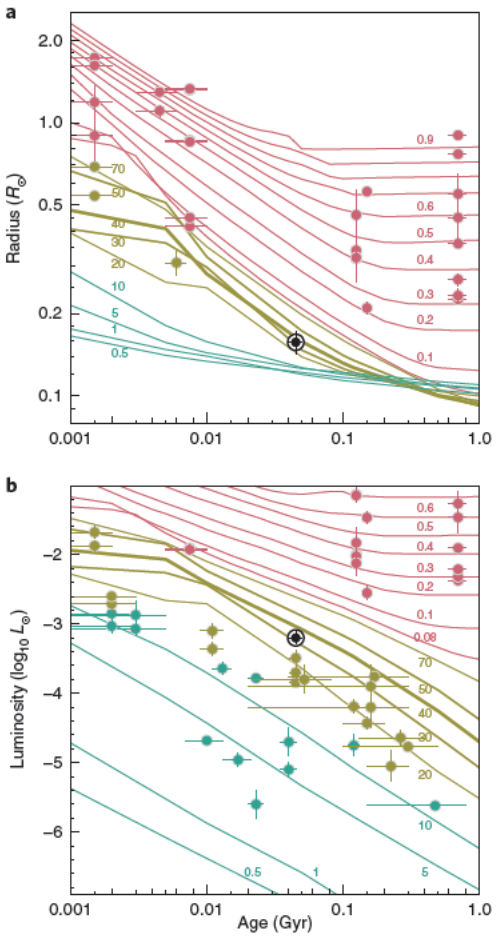


Fig. 3 | Radius and luminosity measurements as a function of system age, for stars, brown dwarfs and giant exoplanets with their 1σ uncertainties. **a**, Radius versus age; **b**, luminosity versus age. Each line corresponds to a model of a given mass[4,3]. Stellar masses (pink lines) are labelled in units of $M_\odot$, whereas brown dwarf (khaki lines) and exoplanet masses (blue lines) are labelled in units of M_{Jup}. Dots following a similar colour scheme are systems reported in the literature[7,32]. We note that directly imaged planetary mass objects do not have measured radii. 2M1510Aa and Ab are represented as a single black point, and along with 2M0535AB[11] and RIK 72b[7] are the smallest and least massive objects with measured masses, radii and age (panel **a**). Together, they form an empirical isochrone for masses close to 40 M_{Jup}. Models for 30 M_{Jup}, 40 M_{Jup} and 50 M_{Jup} are depicted as bolder lines. In panel **b** we note that the bolometric luminosity (and the J, H and K magnitudes) of 2M1510Aab fall under the 0.038 $M_\odot$ (40 M_{Jup}) track as measured from dynamical masses.

of 2M1510A from our UVES data, which for our measured radii imply rotation periods of 20–30 h. This is shorter than the expected convective turnover time for these stars (>2 days) and argues that both the variability and H_α emission arise from magnetic activity.

The 2M1510 system is a young, substellar triple system, fortunately containing an equal-mass eclipsing close binary. Another six young brown dwarf triple systems are known (see Supplementary Table 7). Of these, the 2M1510 system is the only one containing three components of approximately the same mass. In addition, the separation ratio between the inner and outer orbits is the smallest of all young triple brown dwarf systems found so far.

The physical parameters and age of 2M1510A are in excellent agreement with cooling models[2,3,4], providing long-sought empirical verification at an age comparable to those of the currently known directly imaged giant exoplanets[32]. Adjustment of the models to explain the luminosity of 2M1510 will also affect the masses and radii of young directly imaged exoplanets, which are inferred from their luminosity and age using cooling models similar to those used for brown dwarfs.

Methods

Photometric observations and calibration. Photometric data reduction of each observing night was performed using the SPECULOOS pipeline based on PyRAF utilities. After standard pre-reduction procedures (bias, dark and flat-field corrections)[33], the images were aligned with respect to the first image of each individual observing run. Aperture photometry was performed on all identified point sources using DAOPHOT[33]. Aperture photometry was done for eight aperture sizes, with sizes dependent on the average full width at half maximum (FWHM) of the stellar profiles through the observing run. The final set of comparison stars and the aperture size were selected to optimize photometric quality, as evaluated by the standard deviation of the flux of a designated check star, that is, a non-variable star similar in terms of magnitude and colour to the target star. Reduction of data obtained with the MONET/South robotic telescope followed a similar procedure, adapted to account for different charge-coupled device (CCD) detector properties.

Photometric variability of 2M1510. To study variability over several nights, the data were reduced, as will be described in detail (C.M. et al., manuscript in preparation). Briefly, we combine 40 reference stars in the field with similar brightness to build a synthetic time series, which is used as a comparison to our main target, 2M1510A. Similarly, we used 132 reference stars for 2M1510B, a larger number, owing to the fainter magnitude of this source. In addition, we

apply a colour-dependent correction to the photometry, based on the precipitable water vapour column, a value provided by the European Southern Observatory (ESO) at the site where SPECULOOS is located, which allows us to correct for variations in extinction caused by humid ty. We further remove 155 frames where the background exceeds 2,000 counts, an unusually high value, probably caused by light cloud passage. The same procedure is applied for 2M1510A and 2M1510B. Our resulting lightcurves (Supplementary Fig. 1) contain 6,423 measurements and are stable within 3% over 75 days with no discernible frequency. The only feature of note is the eclipse in the lightcurve of 2M1510A. Over a single night, the variability is typically <1%–2%. Larger variations are usually caused by cloudy weather, where our precipitable water vapour correction is no longer effective.

Spectral and gravity classification of 2M1510A and 2M1510B. We obtained and analysed new low-resolution near-infrared spectra for 2M1510A and 2M1510B obtained w th the SpeX spectrograph on the National Aeronautics and Space Administration (NASA) Infrared Telescope Facility[34]. Prism-dispersed spectra spanning 0.8–2.45 μm at a median wavelength resolution of $\lambda/\Delta\lambda = 120$ were obtained on 2015 July 2 (1510A) and 2016 May 28 (1510B) (Principal Investigator D.B.G.), and reduced using the SpeXtool package[35,36] following standard procedures. These data were compared to both 'field' spectral standards[37] and low-surface gravity M and L dwarf standards[38,39]. Supplementary Fig. 2 shows the best matches, which for both components is the M9 γ (very low surface gravity) standard TWA 26[16]. The spectra of both 2M1510 components are slightly bluer, and have a weaker 1.05-μm VO band, than the spectrum of TWA 26, consistent with an older age than this 10-Myr-old standard[40,41]. We also evaluated gravity-sensitive spectral indices[38] for both spectra, and find them to be consistent with an intermediate-gravity (INT-G) classification, which equates to an age of the order of 100 Myr[8,38]. Thus, both components have spectra consistent with young, low-surface-gravity brown dwarfs at an age roughly consistent with the Argus association[9].

Hα emission for 2M1510A was measured in each of the UVES spectra by first flux calibrating each spectrum to the combined-light absolute *i*-band magnitude of this source, $M_i = 14.22 \pm 0.02$, based on photometry from PAN-STARRS and astrometry from Gaia. We used the same magnitude to calibrate each spectrum, and hence ignore any intrinsic variability in the continuum emission. We then directly integrated the Hα profile after subtracting the local continuum to compute the total line flux and Hα luminos ty. We found a mean value of $\log_{10}(L_{H\alpha}/L_{\odot}) = -7.51 \pm 0.19$ for the 12 observations (range -7.90 ± 0.27 to -7.37 ± 0.15), with the scatter consistent with a common mean. Using the combined light luminosity of the pair based on the component luminosities computed below, $\log_{10}(2L_{bol}/L_{\odot}) = -2.90 \pm 0.09$, we infer $\log_{10}(L_{H\alpha}/L_{bol}) = -4.61 \pm 0.20$. If the emission arises from just one component, then $\log_{10}(L_{H\alpha}/L_{bol}) = -4.31 \pm 0.20$. These values are consistent with prior measurements[42]. The Hα line is broader than the velocity difference between the components, with a consistent full width at 10% maximum of 100 ± 10 km s^{-1}, indicative of chromospheric activity. The relative weakness and breadth of the Hα line prevents us from determining which (or both) of the components may be contributing to the emission. If the emission does arise from one component (for example, the secondary), the empirical relations of ref. [12] would predict an effective temperature T_{eff} decrease of 1%–4% and radius increase of up to 6%, corresponding to a flux ratio (0.89–0.97) that roughly reproduces that inferred from the modelled UVES and NIRSPEC observations. However, as we cannot constrain the source of the emission, and as the relations[12] are anchored to early- and mid-type field M stars as opposed to late-M young brown dwarfs, we cannot conclusively determine whether this is the source of the observed flux ratio.

Modelling of VLT/UVES spectra. Thirteen epochs of UVES[21] spectra were obtained between 2017 August 15 and 2018 March 21 (Universal Time, UT) through VLT programs 299.C-5046(A) and 2100.C-5024(A) (Principal Investigator A.H.M.J.T.). The standard UVES configuration was used with a 0″.504′ slit and dispersions centred on 437 nm (blue channel) and 760 nm (red channel) with resolutions $\lambda/\Delta\lambda = 65{,}000$ (blue channel) and $\lambda/\Delta\lambda = 74{,}000$ (red channel). The data were reduced using the ESO UVES pipeline[43]. One of the epochs (2018 February 3) was obtained in poor conditions, and was not included in our analysis; the remaining observations had average signal-to-noise ratios (*S*/*N*) of 6–10 in the red channel and no detection in the blue channel[44,45].

The *S*/*N* of the UVES data only rises above 5 for $\lambda > 800$ nm, and occasionally exceeds 10 in regions centred at 815 nm, 825 nm, 885 nm, 898 nm, 912 nm, 925 nm and 938 nm. The *S*/*N* peaks at these wavelengths owing to the blaze pattern of the échelle. We measured radial velocities at the 819 nm Na I doublet, which is between the first two 'high *S*/*N*' peaks. We note that the *S*/*N* of each spectrum differs owing to variations in observing conditions. In the best spectrum, 30% of the data longward of 800 nm has $S/N > 10$; in the worst spectrum, none of the data rises above this level.

The extracted spectra were forward-modelled using an MCMC algorithm[44,45] that is integrated into the SpeX Prism Library Analysis Toolkit (SPLAT)[46]. The modelling was restricted to the 818–820 nm range, which covers the $2p^6 3p$ ($^2P^0$ J = 1/2, 3/2) → $2p^6 3d$ (^2D J = 3/2, 5/2) Na I doublet. Data were initially shifted to the telluric rest frame by cross-correlating superimposed telluric H_2O absorption features in the neighbouring continuum (815–818 nm) to a telluric transmission spectrum $T_0(\lambda)$[47]. We computed an observed telluric transmission spectrum for each epoch as a function of wavelength λ of the form $T(\lambda) = T_0(\lambda)^{\alpha} \otimes f_G(\Delta\lambda_{res})$, where α is an exponential scaling factor, $\otimes$ denotes convolution, and $f_G(v_{res})$ is a Gaussian broadening kernel with width $\Delta\lambda_{res} = \lambda v_{res}/c$; v_{res} was found to be 5.8 ± 0.4 km s^{-1} in the continuum region. The telluric model was divided out of the data, with the cores of strong telluric absorption lines (transmission <70%) masked. We note that in the four 2018 epochs, the telluric lines overlap with the Na I features; however, the breadth of the stellar features still allowed for robust modelling of the data.

The forward model for the data is described as:

$$[\lambda] = C[\lambda] \times (1 + C_{off}) \times \{M_1([\lambda_1^*], T_{eff,1}, \log_{10}g_1) \otimes f_V(v \sin i_1) + f_2 \times M_2([\lambda_2^*], T_{eff,2}, \log_{10}g_2) \otimes f_V(v \sin i_2)\} \otimes f_G(\Delta\lambda_{res})$$

Here, M_1 and M_2 are BTSettl08 models[48] for the primary and secondary atmospheres with temperatures $T_{eff,1}$ and $T_{eff,2}$ (in kelvin) and log surface grav ties $\log_{10}g_1$ and $\log_{10}g_2$ (in centimetres per second squared), respectively; and $0 < f_2 < 1$ is a scaling factor to account for the relative flux of these models. The model wavelength vectors $\boldsymbol{\lambda}^*_1$ and $\boldsymbol{\lambda}^*_2$ are defined as:

$$\lambda_1^* = \lambda \times \left(1 + \left[RV_1 \quad RV_{bary}(t) + RV_{shift}\right]/c\right)$$

$$\lambda_2^* = \lambda \times \left(1 + \left[RV_2 \quad RV_{bary}(t) + RV_{shift}\right]/c\right)$$

where RV_1 and RV_2 are the heliocentric radial velocities of the primary and secondary, RV_{bary} is the barycentric velocity of the system at the observing epoch (t), and RV_{shift} is a nuisance parameter to adjust for zero-point wavelength shifts, all in units of kilometres per second. The model spectra were each convolved with a rotational broadening kernel $f_V(v\sin i)$ for projected rotational velocities $v\sin i_1$ and $v\sin i_2$ (in kilometres per second) for the primary and secondary, respectively, using a limb darkening parameter $\varepsilon = 0.6$ (ref. [49]). The combined spectrum was convolved with a Gaussian broadening profile $f_G(\Delta\lambda_{res})$ as described above. C_{off} is a nuisance parameter allowing for an additive offset to the flux (for example, owing to residual background emission), while $C(\lambda)$ is a 6th-order polynomial used to match the continuum between model and data.

The full model nominally consists of 20 free parameters; however, the 7 parameters of C[λ] were fitted at each comparison step, RV_{bary} is pre-determined for each observing epoch, and $\Delta\lambda_{res}$ was adopted from the initial fit of telluric absorption in the neighbouring continuum. Furthermore, to improve convergence we varied the parameters f_2, $v\sin i_1$, and $v\sin i_2$ only for data from epochs 2017 August 15, 21 and 22, when the velocity separation of the two components was greatest. These values were consistent with each other and yielded means of $f_2 = 0.827 \pm 0.013$, $v\sin i_1 = 8.7 \pm 0.3$ km s^{-1} and $v\sin i_2 = 6.8 \pm 0.6$ km s^{-1}. For the remaining epochs, we forced these three parameters to be fixed. Furthermore, given the near-unity flux ratio, we imposed the constraint $T_{eff,1} = T_{eff,2}$ and $\log_{10}g_1 = \log_{10}g_2$, and constrained $2{,}000\,K < T_{eff,1} < 3{,}000\,K$ and $3.5 < \log g_1 < 5.5$. The remaining 6 free parameters ($T_{eff,1}$, $\log g_1$, RV_1, RV_2, RV_{shift}, C_{off}) were determined for each spectrum through forward modelling.

After obtaining initial estimates for the model parameters by visual inspection, we deployed a Metropolis–Hastings MCMC algorithm[50,51] with Gibbs sampling[52] and a modified Langevin Rule[53] to optimize the fits and explore the parameter space. Owing to computational restrictions, we used a single MCMC chain of 3,000 steps for each spectrum. At each step, a new value for a single parameter was proposed by drawing from a Gaussian distribution centred on the current parameter value and with a fixed (pre-determined) distribution width. We used the *F*-test cumulative distribution function $F_{CDF}(\chi^2_p/\chi^2_c, DOF, DOF)$ as our test condition, comparing the χ^2 values between the current (χ^2_c) and proposed (χ^2_p) model w th degrees of freedom DOF = 750. The DOF is equal to the number of spectral data points between 818–820 nm (depending on telluric absorption masking) minus the number of fit parameters, which includes the 7 polynomial coefficients of $C[\lambda]$. The proposed parameter set was accepted if $2F_{CDF} - 1 < U(0,1)$, where $U(0,1)$ is a random number drawn from a uniform distribution between 0 and 1. With this criterion, every model with smaller χ^2 was accepted, while higher χ^2 models were accepted based on the degree of deviation from the current model as measured by F_{CDF}. We added an additional criterion to check if the chain was wandering significantly from the current best-f t solution by calculating $F'_{CDF}(\chi^2_c/\chi^2_{min}, DOF, DOF)$ and requiring that $F'_{CDF} < 0.95$; that is, that the chain is no more than 95% (2σ) away from the best-fit model. If this condition was violated, the chain was forced to return to the best-fit parameter set. This algorithm had a high acceptance ratio of 90%, implying that it efficiently explored the parameter space. Tests of shorter chains, as well as the final overall parameter distribution, indicate successful convergence for each parameter. The final parameters were determined as the median and 16% and 84% quantiles of the chain after removing the initial 25% of samples to allow for convergence.

Supplementary Figs. 3 and 4 illustrate the best-f t spectrum and parameter distributions, respectively, for the spectrum obtained on 2017 August 21 (UT). A table summarizing the parameters inferred from each of the UVES epochs is given in Supplementary Table 1. In all fits, the best-fit χ^2 is consistent with

accurate representation of the data given the fit DOFs, while global model variables $T_{\rm eff,1} = 2753 \pm 196$ K and $\log_{10}g_1 = 4.10 \pm 0.24$ are consistent between all 12 epochs. We note that individual epoch uncertainties in these parameters were increased to reflect the scatter in the measurements. There are no strong correlations in the posterior distributions between the inferred atmospheric parameters ($T_{\rm eff,1}$ and $\log_{10}g_1$) and component radial velocities, so these parameters are effectively decoupled.

Acquisition and modelling of Keck/NIRSPEC spectra. Seven epochs of observations of 2M1510A and three epochs of 2M1510B were obtained with Keck/NIRSPEC[20] between 2017 August 2 and 2018 June 3 (UT) (Principal Investigator A. J. B.). The observations were obtained using NIRSPEC's high-resolution mode and N7 filter with e ther the 0″.432′ wide slit (2017 August 2) or 0″.288′ wide slit (all other epochs), providing coverage over 1.99–2.40 μm in 7 orders with average resolutions $\lambda/\Delta\lambda = 25{,}000$ (0″.432′ slit) and $\lambda/\Delta\lambda = 37{,}500$ (0″.288′ slit). Spectral data were extracted using a custom modification of the REDSPEC code[54], which includes spatial and spectral rectification, optimal extraction, and combination of AB pairs. Nearby A0 V stars were observed before or after 2M1510A and 2M1510B for telluric calibration and wavelength calibration (see below).

Our analysis focused on the 2.29–2.32 μm spectral region, which encompasses both strong CO absorption bands intrinsic to the stars and telluric H_2O and CO features used to refine the wavelength calibration. The data for 2M1510A were forward-modelled in the same manner as the UVES data, with the exception that H_2O and CO telluric absorption features were left unmasked in the data, and the forward model included the telluric transmission function. The forward model took the form:

$$D[\lambda] = C[\lambda] \times (1 + C_{\rm off}) \times \left\{ T_0[\lambda]^{\alpha} \times \left[M_1\left([\lambda_1^*], T_{\rm eff,1}, \log_{10}g_1\right) \otimes f_{\rm V}(v \sin i_1) + f_2 \times M_2\left([\lambda_2^*], T_{\rm eff,1}, \log_{10}g_1\right) \otimes f_{\rm V}(v \sin i_2) \right] \right\} \otimes f_{\rm G}(\Delta\lambda_{\rm res})$$

with parameters as described above. Since the data are of too low a resolution to measure $v\sin i$ for either component, we fixed these parameters to the best-fit values from the UVES data, and again assumed common temperatures and surface gravities. Additionally, we only fitted f_2 for data with the maximum veloc ty separations, on 2017 August 2, 2018 March 30 and 2018 June 2 (UT). This resulted in 8 or 9 free parameters ($T_{\rm eff,1}$, $\log_{10}g_1$, f_2, $\rm RV_1$, $\rm RV_2$, α, $\rm RV_{shift}$, $C_{\rm off,}$ $\Delta\lambda_{\rm res}$) for each spectrum that was determined through MCMC forward modelling. As with the UVES data, we used a single MCMC chain with the evaluation metrics described above.

Supplementary Figs. 5 and 6 illustrate the best-fit spectrum and parameter distributions, respectively, for the spectrum of 2M1510A obtained on 2017 August 2 (UT), and Supplementary Table 2 summarizes the parameter determinations for each NIRSPEC epoch. Again, the best-fit χ^2 values were consistent with this model being an accurate representation of the data, and we found mean values of $T_{\rm eff,1} = 2755 \pm 20$ K, $\log_{10}g_1 = 5.17 \pm 0.12$ and $f_2 = 0.88 \pm 0.07$ to be consistent between the seven epochs. Both $T_{\rm eff,1}$ and f_2 are consistent with the UVES observations, but $\log_{10}g_1$ is significantly higher, suggesting that the models may be gravity-insensitive in this wavelength regime. We found no significant correlations between surface gravity and component radial velocities in our analysis.

For 2M1510B, we applied the same analysis using a single component model, which took the form:

$$D[\lambda] = C[\lambda] \times (1 + C_{\rm off}) \times \left\{ T_0[\lambda]^{\alpha} \times M\left([\lambda^*], T_{\rm eff}, \log_{10}g\right) \times f_{\rm V}(v \sin i) \right\} \times f_{\rm G}(\Delta\lambda_{\rm res})$$

In this case, we left $v\sin i$ as a free parameter, resulting in 8 free parameters ($T_{\rm eff}$, $\log_{10}g$, RV, $v\sin i$, α, $\rm RV_{shift}$, $C_{\rm off,}$ $\Delta\lambda_{\rm res}$) determined through MCMC forward modelling. Supplementary Figs. 7 and 8 illustrate the best-fit spectrum and parameter distributions, respectively, for the spectrum of 2M1510B obtained on 2017 August 2 (UT), and Supplementary Table 3 summarizes the parameter determinations for each NIRSPEC epoch and mean values. The average radial velocity inferred for 2M1510B, -12.0 ± 0.3 km s^{-1}, is within 2σ of the systemic velocity of 2M1510A (see below).

Membership in the Argus association. Given the low-surface-gravity features present in the near-infrared spectra of 2M1510A and 2M1510B, and prior analysis indicating membership of 2M1510A in Argus[8], we re-evaluated the spatial and kinematic alignment of these two sources with 29 nearby young associations using the Banyan Σ code[55], updated to account for a new Argus membership analysis[9]. We adopted as systemic values the uncertainty-weighted averages of the radial velocities, and Gaia parallaxes and proper motions of the two components (Tables 1 and 2). This analysis confirmed membership in the Argus association with 89% probability, versus the 11% probability of being a field star contaminant. The roughly 40 members of Argus have a mean distance of 72 pc from the Sun, and a consensus isochronal age of 40–50 Myr[9,56,57,58]. Hence, membership is consistent with the surface gravity classifications of the low-resolution spectra of 2M1510A and B, which are intermediate between VL-G (about 10 Myr) and INT-G (about 100 Myr;[38]); as well as the age inferred from the evolutionary models based on our mass and radius constraints (Fig. 2).

Global analysis of the radial velocity and photometric data. The orbital and physical parameters of the 2M1510A binary were extracted by performing a global analysis of the radial velocities and photometry. We assumed that the motion of the stars followed Keplerian orbits, and considered both the Doppler variation in their radial motions and geometric obscuration during eclipse phases. Posterior probability distributions of the system's parameters were obtained using a global MCMC. The binary lightcurve software *ellc* was used to generate orbital and lightcurve models[22], and we employed the affine-invariant MCMC sampler *emcee* to explore parameter space[23]. We validated our approach[14,59] by re-analysing data from the eclipsing binary system WW Aurigae[60] and found a 1σ agreement with reported values.

The MCMC's f tting parameters were: the orbital period P; the time of secondary eclipse $T_{\rm sec}$; the sum of scaled radii $r_1 + r_2 = (R_1 + R_2)/a$, where R_1 is the primary radius (defined as the most massive of the pair), R_2 is the secondary radius and a is the semimajor axis; the cosine of the orbital inclination cos$i$; the eccentricity parameters $\sqrt{e}\sin\omega$ and $\sqrt{e}\cos\omega$, where ω is the argument of periapsis; and the radial velocity semi-amplitudes K_1 and K_2 for the primary and secondary, respectively. In addition, we used a linear regression at each MCMC step to calculate a normalization factor for each individual lightcurve, and a velocity offset for each component to marginalize over any difference. We also allow an offset for each spectrograph. We did not apply any specific prior to any of our parameters in our initial runs, but identified several simplifications with minimal impact on the results (see Methods section 'Assumptions for the final orbit fit').

An initial MCMC analysis of only the radial velocities provided initial estimates of the orbital period and non-zero eccentricity, and independently confirmed that the observed eclipse happened at superior conjunction near periastron. With these initial constraints, our full MCMC employed 200 walkers of 20,000 steps each, providing a good exploration of parameter space. The convergence of the chain was assessed using the Gelman–Rubin statistic[61]. All our parameters reached the recommended R-hat < 1.1, which is considered converged[62]. We thinned our chains by a factor of 200 due to autocorrelation and were left with 9,000 independent samples for each parameter. Quantiles at 16%, 50% and 84% are reported in Supplementary Table 4. We graphically represent the best solution and ts 2σ confidence region in Fig. 1. We converted our fitting parameters into physical parameters, and report them in Tables 1 and 2 and Supplementary Table 4.

Assumptions for the final orbit fit. We fixed a number of parameters in our final MCMC, after testing that they had no effect on the fit. As suspected from the grazing eclipse, all runs converged to an orbital configuration where the combination of low inclination and high eccentricity implied the absence of a visible primary eclipse. This means we cannot measure the ratio of eclipse depths, and hence the individual radii.

The surface brightness ratio, radius ratio, and limb darkening coefficients of the brown dwarfs remained unconstrained, resulting in flat posterior distributions. We verified this by comparing the Bayesian Information Criterion (BIC[63]), finding no instances where any combination of these parameters was preferred over fixing them (ΔBIC < 6). Consequently, we fixed the brightness ratio $f_2/f_1 = 0.8$, based on the spectroscopic flux ratios obtained from the UVES and NIRSPEC observations. The radius ratio is fixed to $R_2/R_1 = 1$ since the mass ratio is also compatible with unity. Further support for this assumption emerges from the Exeter/Lyon models[3], where brown dwarfs of the age of Argus and within the mass ranges we infer, share the same size (see Fig. 3a). We adopt a quadratic limb-darkening law and determine its limb-darkening coefficients $c1$ and $c2$ with LDTk[64]. These coefficients were calculated using a stellar spectrum library[65], integrating over a red-optical/near-infrared bandpass ($I+z$) attenuated by the quantum efficiency of SPECULOOS's e2V deep-depleted detector, assuming evolutionary model parameters for our 45-Myr-old brown dwarf system: $T_{\rm eff} = 2{,}400$ K, $\log_{10}g = 4.55$, and [M/H] = 0.0. Although the stellar parameters may deviate slightly from these values, the limb-darkening coefficients are relatively insensitive over a wide range of temperature and surface gravity.

Our fit to the photometric data did not include detrending of the lightcurves. We attempted to detrend the photometric data by constructing a baseline model of time, sky background levels, FWHM changes in the PSF, and changes in pixel position x,y, using polynomials of degrees 1–3 for combinations of these parameters. For each baseline model we calculated the BIC, in which the lowest value would be preferred. For all data used in our analysis, we found that no photometric detrending was justified. We allow the f t to rescale our photometric and radial velocity uncertainties.

Bolometric luminosity and absolute JHK magnitudes. Absolute magnitudes M for 2M1510A were computed from apparent magnitudes m and the Gaia parallax distance d using the standard equation $m - M = 5\log_{10}(d/10\,{\rm pc})$. For 2MASS photometry, we infer combined-light absolute magnitudes of $M_{\rm J} = 10.02 \pm 0.05$, $M_{\rm H} = 9.29 \pm 0.04$, and $M_{\rm K} = 8.87 \pm 0.04$. Assuming both components have approximately the same near-infrared brightness, the corresponding component absolute magnitudes are $M_{\rm J} = 10.78 \pm 0.05$, $M_{\rm H} = 10.05 \pm 0.04$, and $M_{\rm K} = 9.63 \pm 0.04$.

To calculate the bolometric luminosity, we used the J-band bolometric correction relations of ref. [66], assuming a spectral type of M8.5 ± 0.5 (the average of VL-G and FLD-G classifications). Using $\rm BC_J = 1.97 \pm 0.16$ and the component

absolute J-band magnitude given above, we find $\log_{10}(L_{bol}/L_{\odot}) = -3.20 \pm 0.07$, again assuming equal-brightness components. To account for a K-band flux ratio of 0.88, we raise the uncertainties to reach the value 3.20 ± 0.09.

Assuming a mass of $0.04\,M_{\odot}$ for both components, evolutionary models[3] predict $M_J = 10.13 \pm 0.12$, $M_H = 9.57 \pm 0.11$ and $M_K = 9.23 \pm 0.11$ at the 45 ± 5 Myr age of Argus. The observed-minus-expected differences are thus $\Delta M_J = 0.65 \pm 0.14$, $\Delta M_H = 0.48 \pm 0.13$ and $\Delta M_K = 0.40 \pm 0.13$, all significantly fainter. The ΔM values were estimated assuming both objects have the same luminosity. However, our spectroscopic fits indicate a flux ratio $f_2/f_1 = 0.83$–0.88. This translates into a 0.07–0.10 magnitude change in the absolute magnitudes, which are smaller than the current uncertainties. If we use the absolute magnitudes to infer mass, the evolutionary models predict 0.025–$0.030\,M_{\odot}$ for each component, 20% to 35% lower than the dynamical masses. Our estimate of bolometric luminosity (based on K magnitudes) leads to photometric masses of $0.31^{+0.04}_{-0.03}\,M_{\odot}$ (Fig. 2). If instead, we assume the bolometric luminosity and dynamical masses are correct, the models would imply that the system has an age of 71^{+15}_{-12} Myr, consistent with an older (but not consensus) age for Argus of 60 Myr[38]. However, the observed sum of radii would now be larger by a factor of 1.09 compared to the models.

Kozai analysis. It has been posited that most binaries with orbital periods below 10 days were formed via the Lidov–Kozai mechanism[29,30]. If inclined by more than 40° to the inner binary, a tertiary can exchange angular momentum with the inner pair. The eccentricity of the inner pair oscillates, and is able to reach values near unity under some circumstances. When the two inner stars are at periastron, tidal friction will circularize the orbit and shrink its semi-major axis. At present, 2M1510Aa and 2M1510Ab are far enough from each another at periastron that tidal forces are irrelevant. Both objects are separated by 43 radii at periastron and tides are mostly ineffective for separations >10–12 radii, as tidal circularization timescales are proportional to R^5 (ref. [67]). However, the system is young enough that it could currently be undergoing Lidov–Kozai oscillations depending on the orb tal elements of the tertiary companion.

We estimate the Lidov–Kozai oscillation timescale[68] for the triple system, defined as:

$$\tau_{LK} = (2\pi/3)^*\left(P_{out}^2/P_{in}\right)^*((M_1 + M_2 + M_3)/M_2)^*\left(1 \quad e_{out}^2\right)^{3/2}$$

where P_{out} and P_{in} are the outer and inner orbital periods, respectively; e_{out} is the outer eccentricity; and M_1 and M_2 are the masses of 2M1510Aa and 2M1510Ab and M_3 is the mass of 2M1510B. We take M_1, M_2 and P_{in} from Table 2, assume $M_3 = M_1$, and assume $e_{out} = 0$. Using Kepler's third law and the projected separation of 2M1510A and 2M1510B (250 au) as the tertiary semi-major axis, we calculate $P_{out} \approx 11{,}500$ years. For these values, the Lidov–Kozai timescale is of the order of 1 Gyr, implying that the outer tertiary is unlikely to be responsible for the elevated eccentric ty of the inner pair. Exploring our assumptions (Supplementary Fig. 7), we find that only for $e_{out} > 0.8$ and 2M1510B currently near apastron would τ_{LK} approach the age of the system. Given the narrow parameter space of this solution, we conclude that the tertiary had no influence on the eccentricity of 2M1510Aa and 2M1510Ab, and that this eccentricity is probably primordial.

In addition, in the absence of a credible Lidov–Kozai path, the 2M1510 pair must have come together via an alternative process, such as disk fragmentation and a subsequent disk migration[69].

Data availability

All reduced photometric timeseries will be made available for download at the CDS, and on request to A.H.M.J.T. Raw SPECULOOS CCD frames will become available through the ESO archive in January 2021; they can be requested from the authors before this date. Eventually the archive will also contain lightcurves for all reference stars in the frames as well. Our UVES spectra are now publicly available on the ESO archive, and can be found by searching the archive for ProgID 299.C-5046 and 2100.C-5024. MONET-South raw images can be made available upon request. NIRSPEC spectra are available at the Keck Observatory Archive, and can be found be searching the archive for Principal Investigator A.J.B. and programmes U009, U010 and U136. SpeX spectra are now available via SPLAT (https://github.com/aburgasser/splat). Requests concerning the data used in this publication can be addressed to A.H.M.J.T. and A.J.B. Figure 1 contains SPECULOOS photometry, as well as UVES and NIRSPEC spectra.

Code availability

The photometric reduction packages use standard public routines such as PyRAF and *astropy*. Radial velocities were extracted from UVES and NIRSpec data from a code built from elements of SPLAT (https://github.com/aburgasser/splat). The *amelie* code combines *ellc* and *emcee* (see text), which are both public codes. *amelie* can be made available upon request, and a stable version is planned to be released on GitHub.

Received: 27 April 2019; Accepted: 16 January 2020;
Published online: 09 March 2020

References

1. Kumar, S. S. On the nature of Van Briesbroeck's star BD +4 4048 B. *Astron. J.* **68**, 283 (1963).
2. Burrows, A. et al. A nongray theory of extrasolar giant planets and brown dwarfs. *Astrophys. J.* **491**, 856 (1997).
3. Baraffe, I. et al. New evolutionary models for pre-main sequence and main sequence low-mass stars down to the hydrogen-burning limit. *Astron. Astrophys.* **577**, A42 (2015).
4. Baraffe, I. et al. Evolutionary models for cool brown dwarfs and extrasolar giant planets. The case of HD 209458. *Astron. Astrophys.* **402**, p701–712 (2003).
5. Hilditch, R. W. *An Introduction to Close Binary Stars* (Cambridge Univ. Press, 2001).
6. Torres, G., Andersen, J. & Giménez, A. Accurate masses and radii of normal stars: modern results and applications. *Astron. Astrophys. Rev.* **18**, 67–127 (2010).
7. David, T. J. et al. Age determination in Upper Scorpius with eclipsing binaries. *Astrophys. J.* **872**, 161 (2019).
8. Gagné, J. et al. BANYAN. VII. A new population of young substellar candidate members of nearby moving groups from the BASS survey. *Astrophys. J. Suppl.* **219**, 33 (2015).
9. Zuckerman, B. The nearby, young, Argus association: membership, age, and dusty debris disks. *Astrophys. J.* **870**, 27 (2019).
10. Stassun, K. G., Mathieu, R. D. & Valenti, J. A. Discovery of two young brown dwarfs in an eclipsing binary. *Nature* **440**, p311–314 (2006).
11. Stassun, K. G. et al. A surprising reversal of temperatures in the brown dwarf eclipsing binary 2MASS J05352184-0546085. *Astrophys. J.* **664**, 1154 (2007).
12. Stassun, K. G. et al. An empirical correction for activity effects on the temperatures, radii, and estimated masses of low-mass stars and brown dwarfs. *Astrophys. J.* **756**, 47 (2012).
13. Triaud, A. H. M. J. et al. The EBLM project. I. Physical and orbital parameters, including spin-orbit angles, of two low-mass eclipsing binaries on opposite sides of the brown dwarf limit. *Astron. Astrophys.* **549**, A19 (2013).
14. Hodžić, V. et al. WASP-128b: a transiting brown dwarf in the dynamical-tide regime. *Mon. Not. R. Astron. Soc.* **481**, 5091–5097 (2018).
15. Cutri, R. M. et al. *VizieR Online Data Catalog: 2MASS All-Sky Catalog of Point Sources* (Centre de Données astronomique de Strasbourg, 2003); http://adsabs.harvard.edu/abs/2003yCat.2246….0C
16. Gizis, J. E. Brown dwarfs and the TW Hydrae association. *Astrophys. J.* **575**, 484–492 (2002).
17. Bailer-Jones, C. A. et al. Estimating distance from parallaxes. IV. Distances to 1.33 billion stars in Gaia Data Release 2. *Astron. J.* **156**, 58 (2018).
18. Delrez, L. et al. SPECULOOS: a network of robotic telescopes to hunt for terrestrial planets around the nearest ultracool dwarfs. *Proc. SPIE* **10700**, 11 (2018).
19. Gillon, M. et al. Seven temperate terrestrial planets around the nearby ultracool dwarf star TRAPPIST-1. *Nature* **542**, 456–460 (2017).
20. McLean, I. S. et al. Design and development of NIRSPEC: a near-infrared echelle spectrograph for the Keck II telescope. *Proc. SPIE* **3354**, 566 (1998).
21. Dekker, H. et al. Design, construction, and performance of UVES, the echelle spectrograph for the UT2 Kueyen Telescope at the ESO Paranal Observatory. *Proc. SPIE* **4008**, 534 (2000).
22. Maxted, P. F. L. *ellc*: A fast, flexible light curve model for detached eclipsing binary stars and transiting exoplanets. *Astron. Astrophys.* **591**, A111 (2016).
23. Foreman-Mackey, D. et al. emcee: the MCMC hammer. *Publ. Astron. Soc. Pacif.* **125**, 306 (2013).
24. Dupuy, T. J., Brandt, T. D., Kratter, K. M. & Bowler, B. P. A model-independent mass and moderate eccentricity for β Pic b. *Astrophys. J. Lett.* **871**, 4 (2019).
25. Liu, M. C., Dupuy, T. & Allers, K. N. The Hawaii Infrared Parallax Program. II. Young ultracool field dwarfs. *Astrophys. J.* **833**, 96 (2016).
26. Lagrange, A.-M. et al. A probable giant planet imaged in the β Pictoris disk. VLT/NaCo deep L'-band imaging. *Astron. Astrophys.* **493**, L21–L25 (2009).
27. Triaud, A. H. M. J. et al. The EBLM Project IV. Spectroscopic orbits of over 100 eclipsing M dwarfs masquerading as transiting hot-Jupiters. *Astron. Astrophys.* **608**, A129 (2017).
28. Moe, M. & Kratter, K. M. Dynamical formation of close binaries during the pre-main-sequence phase. *Astrophys. J.* **854**, 44 (2018).
29. Mazeh, T. & Shaham, J. The orbital evolution of close triple systems—the binary eccentric ty. *Astron. Astrophys.* **77**, 145–151 (1979).
30. Fabrycky, D. & Tremaint, S. Shrinking binary and planetary orbits by Kozai cycles with tidal friction. *Astrophys. J.* **669**, 1298–1315 (2007).
31. Bischoff, K. et al. MONET/North: a very fast 1.2m robotic telescope. *Proc. SPIE* **6270**, id. 62701Q (2006).
32. Bowler, B. P. Imaging extrasolar giant planets. *Publ. Astron. Soc. Pacif.* **128**, 102001 (2016).
33. Tody, D. The IRAF data reduction and analysis system. *Proc. SPIE* **627**, 733 (1986).

34. Rayner, J. T. et al. SpeX: a medium-resolution 0.8-5.5 micron spectrograph and imager for the NASA Infrared Telescope Facility. *Publ. Astron. Soc. Pacif.* **115**, 362 (2003).
35. Vacca, W. D., Cushing, M. C. & Rayner, J. T. A method of correcting near-infrared spectra for telluric absorption. *Publ. Astron. Soc. Pacif.* **115**, 389 (2003).
36. Cushing, M. C., Vacca, W. D. & Rayner, J. T. Spextool: a spectral extraction package for SpeX, a 0.8-5.5 micron cross-dispersed spectrograph. *Publ. Astron. Soc. Pacif.* **116**, 326 (2004).
37. Kirkpatrick, J. D. et al. Discoveries from a near-infrared proper motion survey using multi-epoch Two Micron All-Sky Survey data. *Astrophys. J. Suppl.* **190**, 100 (2010).
38. Allers, K. N. & Liu, M. C. A near-infrared spectroscopic study of young field ultracool dwarfs. *Astrophys. J.* **772**, 79 (2013).
39. Cruz, K. L. et al. Meeting the cool neighbors. XII. An optically anchored analysis of the near-infrared spectra of L dwarfs. *Astron. J.* **155**, 34 (2018).
40. Bell, C. P. M., Mamajek, E. E. & Naylor, T. A self-consistent, absolute isochronal age scale for young moving groups in the solar neighbourhood. *Mon. Not. R. Astron. Soc.* **454**, 593 (2015).
41. Looper, D. L. et al. Discovery of an M9.5 candidate brown dwarf in the TW Hydrae association: DENIS J124514.1-442907. *Astrophys. J. Lett.* **669**, L97 (2007).
42. Burgasser, A. J. et al. The Brown Dwarf Kinematics Project (BDKP). IV. Radial velocities of 85 late-M and L dwarfs with MagE. *Astrophys. J. Suppl.* **220**, 18 (2015).
43. Modigliani, A. & Larsen, J. M. *FLAMES-UVES Pipeline User Manual* VLT-MAN-ESO-19500-3016 (European Southern Observatory, 2018); ftp://ftp.eso.org/pub/dfs/pipelines/uves/uves-fibre-pipeline-manual-18.8.1.pdf
44. Blake, C. H., Charbonneau, D. & White, R. J. The NIRSPEC Ultracool Dwarf Radial Velocity Survey. *Astrophys. J.* **723**, 684 (2010).
45. Burgasser, A. J. et al. The orbit of the L dwarf+T dwarf spectral binary SDSS J080531.84+481233.0. *Astrophys. J.* **827**, 25 (2016).
46. Burgasser, A. J. et al. The SpeX Prism Library Analysis Toolkit (SPLAT): a data curation model. *Astron. Soc. India Conf. Ser.* **14**, 7–12 (2017).
47. Moehler, S. et al. Flux calibration of medium-resolution spectra from 300 nm to 2500 nm: model reference spectra and telluric correction. *Astron. Astrophys.* **568**, A9 (2014).
48. Allard, F., Homeier, D. & Freytag, B. Models of very-low-mass stars, brown dwarfs and exoplanets. *Phil. Trans. R. Soc. A* **370**, 2765–2777 (2012).
49. Gray, D. F. *The Observation And Analysis Of Stellar Photospheres* Vol. 20 (Cambridge Astrophysical Series, 1992); http://adsabs.harvard.edu/abs/1992oasp.book.....G
50. Metropolis, N. et al. Equation of state calculations by fast computing machines. *J. Chem. Phys.* **21**, 1087 (1953).
51. Hastings, W. K. Monte Carlo sampling methods using Markov chains and their applications. *Biometrika* **57**, 97–109 (1970).
52. Geman, S. & Geman, D. Stochastic relaxation, Gibbs distributions, and the Bayesian restoration of images. *IEEE Trans. Pattern Anal. Mach. Intell.* **6**, 721–741 (1984).
53. Roberts, G. & Rosenthal, J. Optimal scaling of discrete approximations to Langevin diffusions. *J. R. Stat. Soc. B* **160**, 255–268 (1998).
54. Kim, S., Prato, L. & McLean, I. S. *REDSPEC: NIRSPEC Data Reduction* (Astrophysical Source Code Library, 2015); http://adsabs.harvard.edu/abs/2015ascl.soft07017K
55. Gagné, J. et al. BANYAN. XI. The BANYAN σ multivariate Bayesian algorithm to identify members of young associations with 150 pc. *Astrophys. J.* **856**, 23 (2018).
56. Zuckerman, B. et al. The Tucana/Horologium, Columba, AB Doradus, and Argus associations: new members and dusty debris disks. *Astrophys. J.* **732**, 61 (2011).
57. Barrado y Navascues, D. et al. Spectroscopy of Very Low Mass Stars and BrownDwarfs in IC 2391: Lithium Depletion and Hα Emission. *Astrophys. J.* **614**, 386 (2004).
58. Torres, C. A., et al. in *Handbook of Star Forming Regions. Volume II: The Southern Sky* Vol. 5 (ed. Reipurth, B) 757 (ASP Monograph Publ, 2008).
59. von Boetticher, A. et al. The EBLM project. III. A Saturn-size low-mass star at the hydrogen-burning limit. *Astron. Astrophys.* **604**, L6 (2017).
60. Southworth et al. Absolute dimensions of detached eclipsing binaries—I. The metallic-lined system WW Aurigae. *Mon. Not. R. Astron. Soc.* **363**, 529–542 (2005).
61. Gelman, A. & Rubin, D. B. Inference from iterative simulation using multiple sequences. *Stat. Sci.* **7**, 4 (1992).
62. Gelman A., Carlin J., Stern H. & Rubin D. *Bayesian Data Analysis* 2nd edn (Chapman & Hall/CRC Texts in Statistical Science, Taylor & Francis, 2003).
63. Schwarz, G. Estimating the dimension of a model. *Ann. Stat.* **6**, 2 (1978).
64. Parviainen, H. & Aigrain, S. LDTK: Limb Darkening Toolkit. *Mon. Not. R. Astron. Soc.* **453**, 3821 (2015).
65. Husser, T.-O. et al. A new extensive library of PHOENIX stellar atmospheres and synthetic spectra. *Astron. Astrophys.* **553**, A6 (2013).
66. Filippazzo, J. C. et al. Fundamental parameters and spectral energy distributions of young and field age objects w th masses spanning the stellar to planetary regime. *Astrophys. J.* **810**, 158 (2015).
67. Hut, P. Tidal evolution in close binary systems. *Astron. Astrophys.* **99**, 126–140 (1981).
68. Kiseleva, L. G. et al. Tidal friction in triple stars. *Mon. Not. R. Astron. Soc.* **300**, 292 (1998).
69. Tokovinin, A. & Moe, M. Formation of close binaries by disc fragmentation andmigration, and its statistical modeling, *Mon. Not. R. Astron. Soc.* 5158–5171 (2020).

Acknowledgements

We thank the personnel of ESO who host SPECULOOS at Paranal Observatory, and who have awarded two Director Discretionary Time (DDT) programmes to confirm this object (Prog ID 099.C-0138 and 2100.C-5024, Principal Investigator A.H M.J.T.). In addition, we thank C. Alvarez, G. Doppman, P. Gomez, H. Hershey and J. Rivera at the Keck Observatory and G. Osterman and E. Volquardsen at the Infra-Red Telescope Facility, for their assistance with the observations reported here. This work also used observations from the Las Cumbres Observatory Global Telescope network, awarded through a DDT programme (PI Alonso). We made use of PyRAF, which is a product of the Space Telescope Science Institute, which is operated by the Association of Universities for Research in Astronomy (AURA) for NASA. PyRAF uses the Image Reduction and Analysis Facility, which is distributed by the National Optical Astronomy Observatory, which is operated by AURA, under cooperative agreement with the National Science Foundation. We used the SIMBAD database, operated at Centre de Données astronomique de Strasbourg, Strasbourg, France; NASA's Astrophysics Data System Bibliographic Services; the M, L, T and Y dwarf compendium housed at DwarfArchives.org; and the SpeX Prism Libraries (http://www.browndwarfs.org/spexprism). We recognize and acknowledge the very significant cultural role and reverence that the summit of Mauna Kea has always had within the indigenous Hawaiian community. We are most fortunate and grateful to have the opportunity to conduct observations from this mountain. This research also made use of Astropy (www.astropy.org), a community-developed core PYTHON package for astronomy as well as the open-source PYTHON packages NUMPY (www.numpy.org), SCIPY (www.scipy.org) and MATPLOTLIB (www.matplotlib.org). A.H.M.J.T. received funding from the European Research Council (ERC) under the European Union's Horizon 2020 research and innovation programme (grant agreement number 803193/BEBOP). A.H.M.J.T. also received funding from the Leverhulme Trust (Research Project Grant number RPG-2018-418) and from the Science, Technology and Facilities Council (grant number ST/S00193X/1). A.J.B. acknowledges funding support from the National Science Foundation (award number AST-1517177). The material is based upon work supported by NASA (grant number NNX15AI75G). B.-O.D. acknowledges support from the Swiss National Science Foundation (PP00P2-163967). M.G. received funding from the ERC (FP/2007-2013 grant agreement number 336480/SPECULOOS), from an ARC grant for Concerted Research Actions, financed by the Wallonia-Brussels Federation, from the Simons Foundation, and from the MERAC foundation. M.G. and E.J. are Senior Research Associates at the Fonds de la Recherche Scientifique–Fond National de la Recherche Scientifique. L.D. acknowledges support from the Gruber Foundation Fellowship. V.K.H. is supported by a generous Birmingham Doctoral Scholarship and by a studentship from Birmingham's School of Physics and Astronomy.

Author contributions

A.H.M.J.T. led the data acquisition, obtained UVES data, and organised the analysis and interpretation of this system. A.J.B. obtained the NIRSPEC data, extracted radial velocities from NIRSPEC and UVES data, produced early parameters of the system, and performed the spectral typing and assessment of Argus membership. A.B. and V.K.H. led the photometric follow-up. A.B., E.D., C.M., P.P.P., L.D. and M.G. reduced the photometric data. V.K.H. produced the global analysis. M.G., E.J., D.S., B.-O.D., D.Q., L.D., C.M., P.P.P., J.d.W., A.H.M.J.T., E.D., A.B. and S.T. participated with the preparation, construction and running of the SPECULOOS facility/survey. J MC. provided the DONUTS software used for guiding. D.B.G. provided the SpeX data while R.A., F.H. and T.-O.H. participated in the photometric follow-up. V.V.G. calculated stellar models. All authors assisted in writing the manuscript.

Competing interests

The authors declare no competing interests.

Additional information

Supplementary information is available for this paper at https://doi.org/10.1038/s41550-020-1018-2.

Correspondence and requests for materials should be addressed to A.H.M.J.T. or A.J.B.

Peer review information *Nature Astronomy* thanks Víctor Béjar, Keivan Stassun and the other, anonymous, reviewer(s) for their contribution to the peer review of this work.

Reprints and permissions information is available at www.nature.com/reprints.

Publisher's note Springer Nature remains neutral with regard to jurisdictional claims in published maps and institutional affiliations.

© The Author(s), under exclusive licence to Springer Nature Limited 2020

3.1.5 Further developments and future work

Following the write-up of the article we pursued additional follow-up observations to capture a second eclipse and reduce the uncertainty on the ephemeris further. We obtained photometric observations with the LCOGT network from Siding Springs, Australia, as well as additional radial velocity data from UVES. One of the LCOGT light curves show a signal with duration and depth consistent with the egress of the eclipse, though the sequence was interrupted due to weather and therefore has little out-of-transit coverage. Moreover, 2M1510 was observed in long-cadence mode with *TESS* in Cycle 1 during a predicted eclipse. Although the eclipse is relatively short (~90 min) compared to the long-cadence data (30 min), there is a signal consistent with the expected depth (accounting for time-averaging) in the vicinity of the orbital solution. The analysis of these data as well as new *TESS* photometry from Cycle 3 will be the subject of a future paper.

3.2 WASP-128 b: a transiting brown dwarf in the dynamical-tide regime

The following published work is my first lead-author paper, and is the culmination of a project I started working on in March/April 2018. Following my initial work on the brown dwarf binary 2M1510 A (see below, Section 3.1), my code AMELIE (Chapter 2.4.1) only needed slight modification to be able to fit a single-line binary system such as a brown dwarf or exoplanet orbiting a star. All the experience gained from my work on 2M1510 could now be applied to this new discovery. The system in question is WASP-128, which was observed by the WASP survey that monitored the sky in search of transiting hot Jupiters (Pollacco et al. 2006). Using a Box-Least-Squares (BLS) algorithm (Collier Cameron et al. 2006), the team identified a flat dip in the light curve consistent with a transit depth of ~7 ppt, repeating with a period of 2.208 days. Follow-up spectra with CORALIE quickly revealed a radial velocity semi-amplitude of ~5 km s^{-1}, which is far in excess of what is expected for a planetary companion. From this the team determined the object is a brown dwarf (Burrows et al. 1997). This was only the second transiting brown dwarf to be discovered by WASP (Anderson et al. 2011), and roughly a dozen other transiting brown dwarfs had been found altogether (e.g. Bayliss et al. 2017 and references therein). WASP-128 b was therefore a rare find, much more so than exoplanets. To this date this short paper remains my most cited work with 26 citations on ADS[a], most of which is due to an increase in brown dwarf discoveries that came after it (e.g. Carmichael et al. 2020, 2021, and references therein). This publicity led to serving as a referee for MNRAS and A&A on two occasions concerning new brown dwarf discoveries.

Two years after our paper was published, Smith et al. (2020) investigated *TESS* photometry of WASP-128 and found that the original ephemeris published in Hodžić et al. (2018) was erroneous (by 14σ) and could not be reconciled with the timing of the *TESS* transits. The original code used in the analysis in Hodžić et al. (2018) had been changed significantly by this time, which prevented an investigation into where the error came from. The values reported in Table 1 of Hodžić et al. (2018) (Section 3.2.5 in this thesis) were written by hand, thus a typographical error could be a likely explanation. In every work

[a] https://ui.adsabs.harvard.edu/, 28 September 2021

since then I have created tables using software routines instead of writing the values by hand in order to prevent similar mistakes.

Monthly Notices of the ROYAL ASTRONOMICAL SOCIETY

MNRAS 00, 1 (2018) doi:10.1093/mnras/sty2512
Advance Access publication 2018 September 14

WASP-128b: a transiting brown dwarf in the dynamical-tide regime

Vedad Hodžić,[1]★ Amaury H. M. J. Triaud,[1] David R. Anderson,[2] François Bouchy,[3] Andrew Collier Cameron,[4] Laetitia Delrez,[5] Michaël Gillon,[6] Coel Hellier,[2] Emmanuël Jehin,[6] Monika Lendl,[7,3] Pierre F. L. Maxted,[2] Francesco Pepe,[3] Don Pollacco,[8] Didier Queloz,[5,3] Damien Ségransan,[3] Barry Smalley,[2] Stéphane Udry,[3] and Richard West[8]

[1]*School of Physics and Astronomy, University of Birmingham, Edgbaston, Birmingham B15 2TT, UK*
[2]*Astrophysics Group, Keele University, Staffordshire ST5 5BG, UK*
[3]*Observatoire de Genève, Université de Genève, Chemin des Maillettes 51, CH-1290 Sauverny, Switzerland*
[4]*Centre for Exoplanet Science, SUPA School of Physics and Astronomy, University of St. Andrews, North Haugh, Fife KY16 9SS, UK*
[5]*Cavendish Laboratory, J J Thomson Avenue, Cambridge CB3 0HE, UK*
[6]*Institut d'Astrophysique et de Géophysique, Université de Liège, Allée du 6 Août, 17, Bat. B5C, Liège 1, Belgium*
[7]*Space Research Institute, Austrian Academy of Sciences, Schmiedlstr. 6, A-8042 Graz, Austria*
[8]*Department of Physics, University of Warwick, Gibbet Hill Road, Coventry CV4 7AL, UK*

Accepted 2018 August 28. Received 2018 August 27; in original form 2018 July 16

ABSTRACT

Massive companions in close orbits around G dwarfs are thought to undergo rapid orbital decay due to runaway tidal dissipation. We report here the discovery of WASP-128b, a brown dwarf discovered by the WASP survey transiting a G0V host on a 2.2 d orbit, where the measured stellar rotation rate places the companion in a regime where tidal interaction is dominated by dynamical tides. Under the assumption of dynamical equilibrium, we derive a value of the stellar tidal quality factor $\log Q'_\star = 6.96 \pm 0.19$. A combined analysis of ground-based photometry and high-resolution spectroscopy reveals a mass and radius of the host, $M_\star = 1.16 \pm 0.04\,\mathrm{M}_\odot$, $R_\star = 1.16 \pm 0.02\,\mathrm{R}_\odot$, and for the companion, $M_\mathrm{b} = 37.5 \pm 0.8\,M_\mathrm{J}$, $R_\mathrm{b} = 0.94 \pm 0.02\,R_\mathrm{J}$, placing WASP-128b in the driest parts of the brown dwarf desert, and suggesting a mild inflation for its age. We estimate a remaining lifetime for WASP-128b similar to that of some ultra-short period massive hot Jupiters, and note it may be a propitious candidate for measuring orbital decay and testing tidal theories.

Key words: methods: data analysis – planets and satellites: dynamical evolution and stability – binaries: eclipsing – brown dwarfs.

1 INTRODUCTION

Brown dwarfs are substellar objects that occupy the mass range ∼13–80 Jupiter masses, (M_J), thought to form via gravitational instability or molecular cloud fragmentation (Chabrier et al. 2014). Despite their abundance, however, very little is known about brown dwarfs. Most are found to be solitary, show complex spectral features that are difficult to model, and their masses are typically hard to estimate because the models are degenerate with their age, radius, and metallicity. Brown dwarf companions orbiting Sun-like stars offer a chance to study these objects in more detail as the stellar ages can be tied to the orbiting brown dwarf. Moreover, transit light curves can lift the inclination angle degeneracy to yield an unambiguous mass from radial velocity measurements, providing precise physical parameters that are crucial for testing substellar evolutionary models.

Despite being fully sensitive throughout the brown dwarf mass range, early Doppler surveys reported that brown dwarf companions are found in fewer numbers than their free-floating counterparts, termed the *brown dwarf desert* (Marcy & Butler 2000; Sahlmann et al. 2011; Ma & Ge 2014). When comparing the same sample of host stars, up to 16 per cent of Sun-like stars have companions more massive than Jupiter, of which <1 per cent are brown dwarfs (Grether & Lineweaver 2006). Only 12 transiting brown dwarfs have been found to date (Bayliss et al. 2017 and references therein, Cañas et al. 2018), where just three have been detected from the ground, possibly due to a detection bias (Csizmadia et al. 2015). Only one other brown dwarf has been discovered by

★ E-mail:

© 2018 The Author(s)
Published by Oxford University Press on behalf of the Royal Astronomical Society

the WASP survey (WASP-30b; Anderson et al. 2011; Triaud et al. 2013).

Most massive substellar companions on close orbits have been found around F-type stars, and very few around G dwarfs, which has been interpreted as being due to rapid engulfment of massive planets and brown dwarfs around G dwarfs due to strong tidal coupling (Bouchy et al. 2011; Guillot et al. 2014; Damiani & Díaz 2016). Stars generally spin down as they age due to magnetic braking, where stellar winds carry highly ionized material that couples to the magnetic field lines and gets carried away from the star, leading to angular momentum loss. G dwarfs are typically more efficient at magnetic braking due to their deeper outer convective layer. However, companions on close orbits can transfer angular momentum from the orbit to the stellar spin, thereby draining angular momentum from the system via magnetic braking, leading to orbital decay until the companion is engulfed by the host. The rate of the companion's orbital decay is predicted to increase by up to three orders of magnitude in the dynamical-tide regime (Ogilvie & Lin 2007), with observational evidence on hot Jupiter hosts supporting stronger tidal coupling than for equilibrium tides (Collier Cameron & Jardine 2018). The strong dynamical tides from the companion excite inertial gravity waves (g-modes) in the convective layer that, in G dwarfs, break and dissipate in the radiative core, resulting in a spin-up the star from the inside (Barker & Ogilvie 2010; Essick & Weinberg 2016). Thus, in systems where the host stars can be spun up by a massive companion such as a brown dwarf, the strong tidal coupling is expected to lead to runaway orbital decay of the companion on to the central star on short time-scales compared to the lifetime of the star (Barker & Ogilvie 2010).

In this context, we report the discovery of WASP-128b, a new transiting brown dwarf discovered by the WASP survey, orbiting a G0V host on a close orbit, where the measured stellar rotation rate places the system well-within the dynamical-tide regime, suggesting strong tidal coupling between the pair.

2 OBSERVATIONS

2.1 Photometry

WASP-128 is a moderately bright ($V = 12.5$) G0V star at a distance of 422 ± 5 pc. The WASP survey (Pollacco et al. 2006) obtained 31 543 images of WASP-128 between 2006 May 04 and 2012 Dec. 19, identifying a periodic 2.208 d transit signal in the photometry (Collier Cameron et al. 2006). Consequently, we initiated photometric and spectroscopic follow-up observations.

Five transits of WASP-128b were obtained using the 0.6 m TRAPPIST robotic telescope (Gillon et al. 2011; Jehin et al. 2011), located at ESO La Silla Observatory (Chile). The first of these transit observations is partial, covering only the second half of the transit. All five transits were observed through a 'blue-blocking' filter. The images are calibrated using standard procedures (bias, dark, and flat-field correction) and photometry is extracted using the IRAF/DAOPHOT[1] aperture photometry software (Stetson 1987), as described by Gillon et al. (2013). For each transit observation, a careful selection of both the photometric aperture size and stable comparison stars is performed manually to obtain the most accurate differential light curve of WASP-128. Some light curves are affected by a meridian flip; that is, the 180° rotation that TRAPPIST's equatorial mount has to undergo when the meridian is reached. We account for any potential photometric offset in our baseline model, see Section 3.2.

We observed three transits of WASP-128b using the EulerCam instrument installed at the 1.2 m *Euler* telescope also located at the La Silla site. The observations were carried out through an r'-Gunn filter and the telescope was slightly defocused to improve PSF sampling and observation efficiency. Each transit light curve is obtained using relative aperture photometry while optimizing reference star selection and extraction apertures to minimize the residual light curve rms. The instrument and the associated data reduction is described in more detail in Lendl et al. (2012). Some of the images of WASP-128 leading up to and during the ingress of the second transit were saturated, and as such, we discarded a handful of observations in our analysis that had count levels above 50 000 ADU.

2.2 Spectroscopy

We collected 48 spectra from the CORALIE spectrograph on the *Euler* telescope between 2013-06-06 and 2016-11-24, as well as 23 HARPS spectra on the ESO 3.6 m telescope between 2015 April 02 and 2018 March 22. Both sets of data are reduced using similar data reduction softwares. Their resulting spectra are correlated with a numerical mask matching a G2V star (Baranne et al. 1996; Pepe et al. 2002). These procedures have been demonstrated to reach high precision and high accuracy (e.g. Mayor et al. 2009; López-Morales et al. 2014). We perform a single 3σ-clip on each radial velocity set using the line full width at half-maximum (FWHM) and bisector inverse slope span (BIS). One HARPS observation is discarded due to a highly discrepant BIS value, and one CORALIE observation was discarded due to the FWHM clip. Those outliers are highlighted in Appendix A.

3 DATA ANALYSIS

3.1 Spectral analysis

Using methods similar to those described by Doyle et al. (2013), we used the co-added HARPS spectrum to determine values for stellar effective temperature $T_{\rm eff}$, surface gravity $\log g_\star$, metallicity [Fe/H], and projected stellar rotational velocity $v \sin i_\star$. In determining $v \sin i$ we assumed a macroturbulent velocity of 4.4 ± 0.7 km s^{-1}, based on the asteroseismic calibration of Doyle et al. (2014). Using MKCLASS (Gray & Corbally 2014), we obtain a spectral-type G0V for WASP-128, which is consistent with the temperature derived from the spectral analysis. The Lithium abundance $\log A(\mathrm{Li}) = 2.62 \pm 0.09$ suggests a relatively young age of 1–2 Gyr.

3.2 Global modelling

The combined data are analysed using AMELIE, a novel software package that jointly models the photometric and radial velocity data in a standard Bayesian framework. The code is essentially a PYTHON wrapper on the `ellc` binary star light-curve model (Maxted 2016) for computing exoplanet and eclipsing binary light curves and their radial velocity orbits, and the EMCEE affine-invariant Markov chain Monte Carlo (MCMC) sampler (Goodman & Weare 2010;

[1] IRAF is distributed by the National Optical Astronomy Observatory, which is operated by the Association of Universities for Research in Astronomy, Inc., under cooperative agreement with the National Science Foundation.

Foreman-Mackey et al. 2013) for exploring the posterior parameter space.

We adopt a quadratic limb darkening law to model the intensity distribution of the stellar disc, using the LDTKpackage (Husser et al. 2013; Parviainen & Aigrain 2015) to sample band-specific limb darkening coefficients for the *Euler* and TRAPPIST data sets, following the triangular parametrization described in Kipping (2013). No priors are imposed on the limb darkening parameters, rather, we fit the intensity profile of the disc using the built-in likelihood function, allowing uncertainties in the spectral parameters to be propagated to our final result. In addition, we sample the following parameters for our transit and radial velocity model: Period, P; mid-transit reference time, T_0; transit depth, D; transit width (time from first to fourth contact), W; impact parameter, b; and radial velocity semi-amplitude, K. Moreover, for our eccentric model we also sample the parameters $\sqrt{e}\sin\omega$ and $\sqrt{e}\cos\omega$, and in our orbital decay model we further sample $\dot{P} = \mathrm{d}P/\mathrm{d}t$. In all cases we use non-informative priors that are either physically bounded (e.g. $0 < b < 1$) or sensibly bounded to a wide enough region (e.g. $0 < K < 50\,\mathrm{km\,s^{-1}}$), where the transit mid-point is bounded by the light curves on 2014 March 03.

For each sampled set of parameters we further compute photometric and radial velocity baseline models. Our photometric baseline model consists of a normalization factor with a second-order polynomial in time for each light curve to allow for airmass and seeing effects. Moreover, we experimented with additional photometric detrending using sky background levels, FWHM changes in the PSF, and changes in the target pixel position on the CCD. Using the Bayesian Information Criterion (BIC; Schwarz 1978) to compare model complexity, we find that an additional first-order polynomial using sky background levels is strongly preferred for the *Euler* light curve on 2014 March 25. On the nights of 2014 Feb. 11, 2014 March 03, and 2015 May 10, the TRAPPIST telescope peformed a meridian flip, for which we account for any potential offsets by allowing an additional normalization factor before the flip. The radial velocity baseline model consists of a constant systemic velocity for each instrument. The CORALIE data are partitioned into two data sets due to an upgrade of the instrument that could affect the velocity zero-point (Triaud et al. 2017). We compare the constant velocity model with models allowing a first- and second-order drift term, but find that any higher order terms are unjustified. The baseline model parameters are computed using a least-squares algorithm for every proposed parameter set in the MCMC sampling. Finally, we also sample additional errors on our photometry and radial velocity data to account for underestimated errors due to instrumental effects and stellar activity.

The mean stellar density can be estimated independently from a transit light curve and can be used with other observables to constrain the mass and age of a star from stellar evolution models (Seager & Mallén-Ornelas 2003; Triaud et al. 2013). We use BAGEMASS (Maxted, Serenelli & Southworth 2015) to estimate the age and mass of the host star, using our estimates of $T_{\rm eff}$ and [Fe/H] from the spectral modelling in Section 3.1, luminosity from *Gaia* DR2 (Andrae et al. 2018), and the mean stellar density from the transit light curves as inputs to the code. The mass is then used as input to our Keplerian model.

We initiate 256 walkers at positions normally dispersed close to the solution, and run each walker for 30 000 steps, chosen such that each walker is run for a few tens of autocorrelation lengths after discarding the first 15 000 steps as burn-in. The independent chains were thinned by a factor 100 due to autocorrelation, leaving each parameter with 38 400 independent samples, before computing the $\hat{R}$ statistic (Gelman et al. 2003), and mixing the chains. All parameters reach the recommended $\hat{R} < 1.1$, indicating overall convergence.

4 RESULTS

Using BAGEMASS we find an age of 2.3 ± 0.9 Gyr and mass of $M_\star = 1.16 \pm 0.04\,\mathrm{M_\odot}$ for WASP-128. From this we derive a radius of the star of $R_\star = 1.16 \pm 0.02\,\mathrm{R_\odot}$, and mass and radius of $M_\mathrm{b} = 37.5 \pm 0.8\,M_\mathrm{J}$ and $R_\mathrm{b} = 0.94 \pm 0.02\,R_\mathrm{J}$, for the companion, placing it securely in the brown dwarf regime. The best-fitting models with the photometric data are shown in Fig. 1, and in Fig. 2 for the radial velocity data. The results from our MCMC and derived parameters are shown in Table 1 with their 68 per cent confidence interval.

Eccentric model. Given the close proximity to the host star, it is expected that the orbit of WASP-128b has been tidally circularized due to tidal dissipation in the brown dwarf as this would happen on a time-scale of $\leq$1 Gyr (Barker & Ogilvie 2009). Nevertheless, when including eccentricity in our model, we derive a value of $e = 0.003^{+0.003}_{-0.002}$. Observational errors can lead to the detection of a small, non-zero, but spurious eccentricity (Lucy & Sweeney 1971). The BIC strongly disfavours an eccentric model compared to a circular fit. We apply the revised Lucy-Sweeney test (Lucy 2013) to put an upper limit of $e < 0.007$ on the eccentricity using their uniform prior. The results of the other parameters between the two models are consistent with each other, and as such we present the results from the circular fit in Table 1, with our upper limit on the eccentricity.

Orbital decay model. A periodic signal of 2.93 ± 0.03 d was found in the photometric data (Maxted et al. 2011), which is consistent with the derived rotation period of $P_\star = 2.93 \pm 0.18$ d for WASP-128, using the observed $v \sin i_\star$ and $R_\star$. The fast rotation for an early G dwarf could indicate a tidal spin-up due to its massive companion. Given the expected strong tidal coupling in this system, we attempted to directly measure an orbital decay in the radial velocity data by including a period time-derivative, $\dot{P}$ in our model. We find that $\dot{P} = 1.05^{+1.13}_{-1.14}\,\mathrm{s\,yr^{-1}}$, and note that, although not significant, we would not expect a positive $\dot{P}$ in our case where $P_\mathrm{orb} < P_\star$.

5 DISCUSSION

5.1 Tidal evolution

The orbital decay of the companion is significantly affected by magnetic braking as long as the total angular momentum of the system can remain above the critical limit (Damiani & Lanza 2015; Damiani & Díaz 2016),

$$L_\mathrm{crit} = 4\left(\frac{G^2}{27}\frac{M_\star^3 M_\mathrm{b}^3}{M_\star + M_\mathrm{b}}(\beta(t) I_\star + I_\mathrm{b})\right)^{\frac{1}{4}},$$

where $I = \alpha M R^2$ is the moment of inertia of the two objects, defined by their effective squared radii of gyration, α. The inclusion of $\beta(t)$ extends the original work by Hut (1980) to include the effects of orbital evolution due to magnetic braking, where $\beta = \Omega/n$ is the ratio of the stellar rotation rate to the orbital frequency, with $n^2 = G(M_\star + M_\mathrm{b})/a^3$. When $L > L_\mathrm{crit}$, the system can enter a pseudo-equilibrium state which is stable if the orbital angular momentum

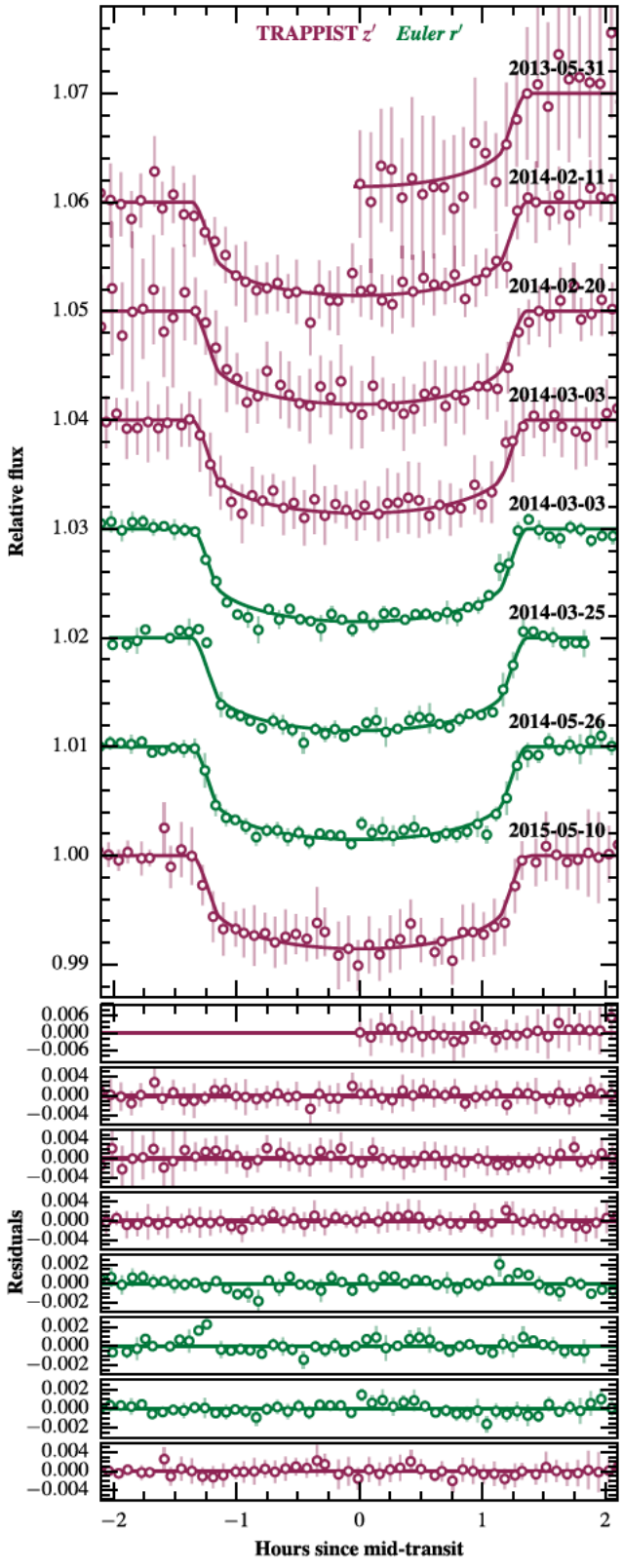


Figure 1. Transits of WASP-128 taken with the *Euler* (*green*) and TRAPPIST (*vermillion*) telescopes. The points correspond to detrended data binned to 5 min, and the coloured lines are the best-fitting models. The residuals of the fit are shown in the lower panel.

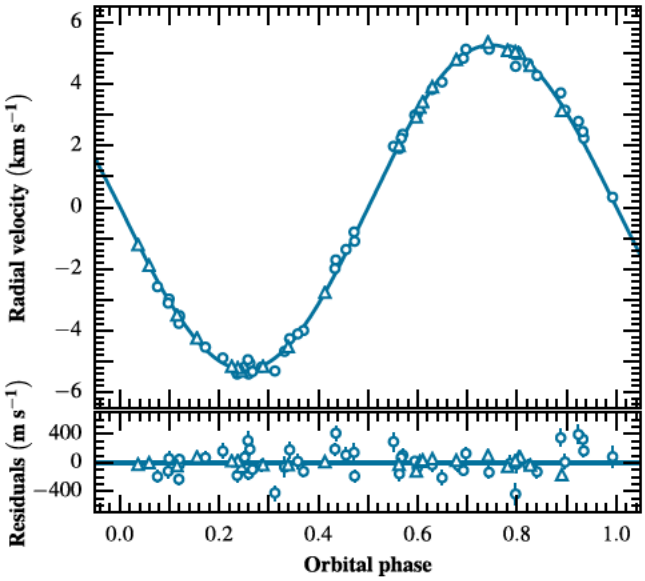


Figure 2. The radial velocity motion of WASP-128 due to its brown dwarf companion, folded on the best-fitting period. The blue points correspond to RV measurements taken with CORALIE (*circles*) and HARPS (*triangles*). The solid line is the best-fitting model. The residuals of the fit are shown in the lower panel.

Table 1. WASP-128 system information and results. Numbers in brackets denote uncertainties on the last two digits from the 16th and 84th percentiles. ⋆ and 'b' subscripts denote the host star and companion, respectively.

WASP-128					
$11^h31^m26^s.10$ $-41°41'22''.3$					
2MASS J11312609-4141222					
Gaia 5382697351745548416					
Parameter	Value	Unit	Parameter	Value	Unit
Spectral and system parameters					
$T_{\rm eff}$	5950 ± 50	K	d	422 ± 6	pc
$\log g_\star$	4.1 ± 0.1	cgs	$\tau_\star$	2.2 ± 0.9	Gyr
[Fe/H]	0.01 ± 0.12	dex	$G_{\rm mag}$	12.3	
$v \sin i_\star$	20.0 ± 1.2	km s^{-1}	Sp. type	G0V	
Sampled parameters					
P	$2.208524\,(^{+21}_{-20})$	d	K	$5.272\,(^{+16}_{-16})$	km s^{-1}
T_0	$2456720.68369\,(^{+19}_{-19})$	$\rm BJD_{UTC}$	$q_1(r')$	$0.3679\,(^{+12}_{-12})$	
D	$0.00699\,(^{+15}_{-15})$		$q_2(r')$	$0.39437\,(^{+92}_{-92})$	
W	$0.11290\,(^{+48}_{-44})$	d	$q_1(z')$	$0.3805\,(^{+12}_{-12})$	
b	$0.11\,(^{+10}_{-07})$	$R_\star$	$q_2(z')$	$0.39827\,(^{+89}_{-89})$	
Derived parameters					
$M_\star$	$1.155\,(^{+39}_{-39})$	$M_\odot$	$M_{\rm b}$	$37.19\,(^{+83}_{-85})$	$M_{\rm J}$
$R_\star$	$1.152\,(^{+21}_{-16})$	$R_\odot$	$R_{\rm b}$	$0.937\,(^{+22}_{-18})$	$R_{\rm J}$
$R_\star/a$	$0.1489\,(^{+24}_{-09})$		$R_{\rm b}/a$	$0.01246\,(^{+27}_{-18})$	
$\rho_\star$	$0.807\,(^{+16}_{-38})$	$\rho_\odot$	$\rho_{\rm b}$	$55.9^{+2.6}_{-3.5}$	g cm^{-3}
$\log g_\star$	$4.396\,(^{+08}_{-14})$	cgs	$\log g_{\rm b}$	$5.040\,(^{+13}_{-18})$	cgs
a	$0.03590\,(^{+38}_{-40})$	AU	i	$89.10\,(^{+63}_{-91})$	°
$M_{\rm b}/M_\star$	$0.03074\,(^{+37}_{-35})$		$f(m)$	$0.0000316\,(^{+03}_{-03})$	$M_\odot$
$R_{\rm b}/R_\star$	$0.08359\,(^{+89}_{-88})$		e	<0.007	

$L_{\rm orb}$ satisfies

$$L_{\rm orb} > (4 - \beta(t))(I_\star + I_{\rm b})n.$$

The companion satisfies both these criteria, so is thus either evolving towards the dynamically stable state, or is already in synchronization. Under the assumption of the latter, we can derive the stellar tidal dissipation parameter $Q'_\star$ that is needed to balance the tidal torque with the wind braking torque using relations in e.g. Brown et al. (2011) and Damiani & Díaz (2016), finding $\log Q'_\star = 6.96 \pm 0.19$. Recently, Collier Cameron & Jardine (2018) presented a study of the hot Jupiter population that yielded a value of $\log Q'_\star = 8.26 \pm 0.14$. In the regime where $0.5 < P/P_\star < 2$, dynamical tide become important (Ogilvie & Lin 2007). For a subset of hot Jupiters that fall into this range, the tidal dissipation parameter was found to be an order of magnitude smaller, where $\log Q'_\star = 7.31 \pm 0.39$, which is consistent with our estimate. In fact, using the above estimate for $Q'_\star$, we derive that the spin period of the star needed for a dynamically stable state is $2.80^{+0.44}_{-0.26}$ d, which increases confidence in our assumption about spin-orbit synchronization. While in the dynamically stable state, the infall time of WASP-128b is given by the magnetic braking time-scale, and we derive a remaining lifetime of 267^{+145}_{-67} Myr. In reality this is a lower limit, as the infall time will not be driven by magnetic braking once the companion is below the critical orbital period needed to stay in the dynamically stable state. Thereafter, the infall will proceed more slowly, but will still reach the Roche limit within a few tens of Myr (fig. 3, Damiani & Díaz 2016).

More generally, lifetime estimates depend on the structural and rotational evolution of stars (Bolmont & Mathis 2016; Gallet et al. 2017). Using $\log Q'_\star = 6$ and implementing a dynamical model that includes tidal interactions between the star and companion, stellar evolution, magnetic braking, and tidal dissipation by gravity waves, Guillot et al. (2014) predicts a survival time of 50–60 per cent of the host's main-sequence lifetime for a companion at the mass of WASP-128b initially at a 3 d orbit. The main-sequence lifetime of WASP-128 with a mass of about 1.16 $M_\odot$ is ∼6.9 Gyr, which corresponds to a lifetime of 3.5–4.2 Gyr for WASP-128b. The age estimated from BAGEMASS could thus be consistent with the companion's survival, although a thorough calculation of the companion's evolutionary history is needed to estimate its initial location (Brown et al. 2011).

5.2 Inflation

In Fig. 3, we place WASP-128b in a mass–radius diagram with the other known transiting brown dwarfs. WASP-128b sits in the driest part of the brown dwarf desert, $35 < m \sin i < 55$ $M_{\rm J}$ (Sahlmann et al. 2011; Ma & Ge 2014), coinciding with the ∼45 $M_{\rm J}$ mass minimum found in Grether & Lineweaver (2006). It has been suggested that this minimum separates two brown dwarf populations differing by their formation mechanisms: The first formed in the protoplanetary disc via gravitational instability, and the second through molecular cloud fragmentation (Ma & Ge 2014). In this context, WASP-128b clearly belongs to the low-mass population of brown dwarfs.

Using our mass and age estimates for WASP-128b, the COND03 evolutionary models (Baraffe et al. 2003) predict a radius of 0.90 $R_{\rm J}$, which suggests a mild inflation compared to the measured radius. Irradiation effects should have little impact in inflating brown dwarfs, thus it is more likely due to some other mechanism that deposits energy in the brown dwarf interior (Bouchy et al. 2011).

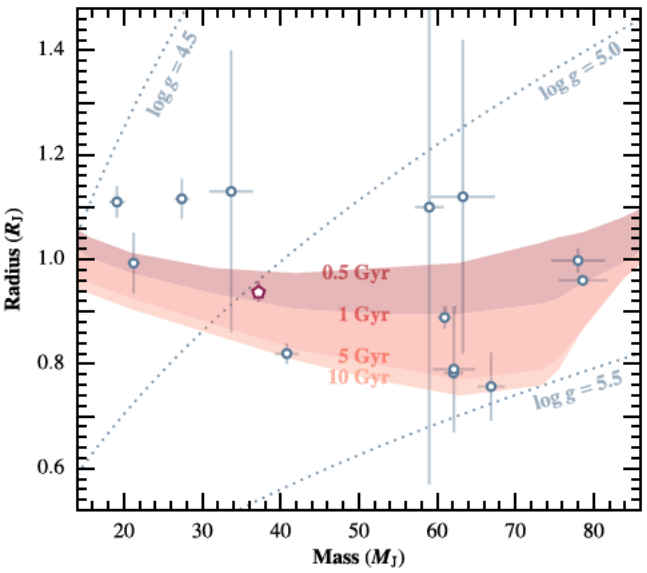


Figure 3. Mass–radius diagram placing WASP-128b (*vermillion*) in the context of the other known transiting brown dwarfs. Objects are from Bayliss et al. (2017) and references therein, including the recent discovery of Kepler-503b (Cañas et al. 2018). The shaded area outlines isochrones for substellar objects from the COND03 models (Baraffe et al. 2003).

6 CONCLUSION

We have discovered WASP-128b, a transiting brown dwarf from the WASP survey on a 2.2 d orbit around a G dwarf. Dynamical-tide theory predicts very few such objects should exist due to rapid orbital decay from strong stellar tidal coupling. Using radial velocity data collected over ∼5 yr, we rule out any significant orbital decay, and we derive a value of the stellar tidal quality factor based on an assumption of dynamical stability. The derived age, mass, and size of WASP-128b suggest a mild inflation, although we cannot rule out a young age.

ACKNOWLEDGEMENTS

The authors are grateful to the anonymous referee for providing useful comments. This study was carried out using data collected at ESO's La Silla Observatory, Chile: HARPS on the ESO 3.6m (Prog IDs 095.C-0105 & 097.C-0434), the Swiss *Euler* telescope, and TRAPPIST. The data are publicly available at CDS, and on demand to the main author. We would like to thank the kind attention of the ESO staff at La Silla, and the many observers who collected data with CORALIE and HARPS along the years. VH is supported by the School of Physics & Astronomy at the University of Birmingham, as well a generous grant through the Postgraduate Research Scholarship Fund at the University of Birmingham. This work has made use of data from the European Space Agency (ESA) mission *Gaia* (https://www.cosmos.esa.int/gaia), processed by the *Gaia* Data Processing and Analysis Consortium (DPAC, https://www.cosmos.esa.int/web/gaia/dpac/consortium). Funding for the DPAC has been provided by national institutions, in particular the institutions participating in the *Gaia* Multilateral Agreement. This research also made use of Astropy, a community-developed core PYTHON package for Astronomy (The Astropy Collaboration 2018), as well as the open-source PYTHON packages NUMPY (Walt, Colbert & Varoquaux 2011), SCIPY (Jones et al. 2001), and MATPLOTLIB (Hunter 2007).

REFERENCES

Anderson D. R. et al., 2011, ApJ, 726, L19
Andrae R. et al., 2018, A&A, 616, A8
Baraffe I., Chabrier G., Barman T. S., Allard F., Hauschildt P. H., 2003, A&A, 402, 701
Baranne A. et al., 1996, A&AS, 119, 373
Barker A. J., Ogilvie G. I., 2009, MNRAS, 395, 2268
Barker A. J., Ogilvie G. I., 2010, MNRAS, 404, 1849
Bayliss D. et al., 2017, AJ, 153, 15
Bolmont E., Mathis S., 2016, Celest. Mech. Dyn. Astron., 126, 275
Bouchy F. et al., 2011, A&A, 525, A68
Brown D. J. A., Collier Cameron A., Hall C., Hebb L., Smalley B., 2011, MNRAS, 415, 605
Cañas C. I. et al., 2018, ApJ, 861, L4
Chabrier G., Johansen A., Janson M., Rafikov R., 2014, Protostars and Planets VI, University of Arizona Press, Tucson, p. 619
Collier Cameron A., Jardine M., 2018, MNRAS, 476, 2542
Collier Cameron A. et al., 2006, MNRAS, 373, 799
Csizmadia S. et al., 2015, A&A, 584, A13
Damiani C., Díaz R. F., 2016, A&A, 589, A55
Damiani C., Lanza A. F., 2015, A&A, 574, A39
Doyle A. P. et al., 2013, MNRAS, 428, 3164
Doyle A. P, Davies G. R., Smalley B., Chaplin W. J., Elsworth Y., 2014, MNRAS, 444, 3592
Essick R., Weinberg N. N., 2016, ApJ, 816, 18
Foreman-Mackey D., Hogg D. W., Lang D., Goodman J., 2013, PASP, 125, 306
Gallet F., Bolmont E., Mathis S., Charbonnel C., Amard L., 2017, A&A, 604, A112
Gelman A., Carlin J., Stern H., Rubin D., 2003, Bayesian Data Analysis, 2nd edn. Chapman & Hall/CRC Texts in Statistical Science, Taylor & Francis
Gillon M., Jehin E., Magain P., Chantry V., Hutsemékers D., Manfroid J., Queloz D., Udry S., 2011, EPJ Web Conf. p. 06002
Gillon M. et al., 2013, A&A, 552, A82
Goodman J., Weare J., 2010, Commun. Appl. Math. Comput. Sci., 5, 65
Gray R. O., Corbally C. J., 2014, AJ, 147, 80
Grether D., Lineweaver C. H., 2006, ApJ, 640, 1051
Guillot T., Lin D. N. C., Morel P., Havel M., Parmentier V., 2014, EAS Publ. Ser. Vol. 65, Evolution of Exoplanets and Their Parent Stars. Cambridge Univ. Press, Cambridge, p. 327
Hunter J. D., 2007, Comput. Sci. Eng., 9, 90
Husser T.-O., Wende-von Berg S., Dreizler S., Homeier D., Reiners A., Barman T., Hauschildt P. H., 2013, A&A, 553, A6
Hut P., 1980, A&A, 92, 167
Jehin E. et al., 2011, Messenger, 145, 2
Jones E. , Oliphant T., Peterson P. et al., 2001, SciPy: Open Source Scientific Tools for Python. http://www.scipy.org/
Kipping D. M., 2013, MNRAS, 435, 2152
Lendl M. et al., 2012, A&A, 544, A72
López-Morales M. et al., 2014, ApJ, 792, L31
Lucy L. B., 2013, A&A, 551, A47
Lucy L. B., Sweeney M. A., 1971, AJ, 76, 544
Ma B., Ge J., 2014, MNRAS, 439, 2781
Marcy G. W., Butler R. P., 2000, PASP, 112, 137
Maxted P. F. L., 2016, A&A, 591, A111
Maxted P. F. L. et al., 2011, PASP, 123, 547
Maxted P. F. L., Serenelli A. M., Southworth J., 2015, A&A, 575, A36
Mayor M. et al., 2009, A&A, 493, 639
Ogilvie G. I., Lin D. N. C., 2007, ApJ, 661, 1180
Parviainen H., Aigrain S., 2015, MNRAS, 453, 3821
Pepe F. et al., 2002, Messenger, 110, 9
Pollacco D. L. et al., 2006, PASP, 118, 1407
Sahlmann J. et al., 2011, A&A, 525, A95
Schwarz G., 1978, Ann. Stat., 6, 461
Seager S., Mallén-Ornelas G., 2003, ApJ, 585, 1038
Stetson P. B., 1987, PASP, 99, 191
The Astropy Collaboration, 2018, AJ, 156, A33
Triaud A. H. M. J. et al., 2013, A&A, 549, A18
Triaud A. H. M. J. et al., 2017, MNRAS, 467, 1714
Walt S. v. d., Colbert S. C., Varoquaux G., 2011, Comput. Sci. Eng., 13, 22

APPENDIX A: RADIAL VELOCITIES

Table A1. HARPS radial velocity data set. Machine readable format is available online at CDS.

BJD_{UTC}	RV ($km\,s^{-1}$)	σ ($km\,s^{-1}$)	FWHM ($km\,s^{-1}$)	BIS ($km\,s^{-1}$)
57114.604490	10.19886	0.03857	28.02641	0.65954
57114.767777	11.96217	0.03481	28.04199	0.49807
57115.580569	19.81497	0.03248	28.21436	−0.43354
57115.821461	17.86571	0.03447	28.53128	−0.25040
57116.701126	9.56556	0.03357	27.96543	0.04673
57135.560277[a]	19.32195	0.04225	28.00931	−212.09835
57137.581652	20.08288	0.03328	28.06999	−0.14360
57138.694412	9.41227	0.03810	27.94346	−0.07837
57139.649675	19.51470	0.03889	27.97368	−0.00470
57141.695657	17.97551	0.03256	28.06352	−0.23932
57157.596595	19.73995	0.03206	27.75519	−0.30482
57158.556607	9.51614	0.02926	27.90052	−0.15205
57181.510526	18.63475	0.03266	27.77245	−0.24299
57182.583973	11.22922	0.03476	27.98556	−0.23481
57183.570990	16.72535	0.03284	27.84478	−0.14822
57184.619044	13.51188	0.03994	28.02373	0.01529
57199.571858	19.70855	0.04228	27.54479	−0.61449
57202.552044	10.48449	0.03984	28.13346	−0.40772
57203.556020	18.14702	0.04130	27.74655	−0.40814
57204.548030	12.83536	0.03205	28.24409	−0.43471
57486.697998	19.76909	0.03492	27.99402	−0.27572
57487.645330	9.56572	0.03248	28.20436	−0.32989
58198.758018	9.99469	0.03287	27.88726	0.24160
58199.708869	17.65346	0.03003	27.82458	0.08529

[a]Marks data that were excluded from the fit.

Table A2. CORALIE (1) radial velocity data set. Machine readable format is available online at CDS.

BJD_{UTC}	RV ($km\,s^{-1}$)	σ ($km\,s^{-1}$)	FWHM ($km\,s^{-1}$)	BIS ($km\,s^{-1}$)
56449.553799	9.66479	0.07635	27.71726	0.39581
56684.776572	19.97341	0.08458	28.16283	− 0.18934
56687.719393	12.26985	0.08186	27.55700	− 0.23831
56690.804858	13.74564	0.08728	28.12772	0.13317
56692.786749	10.85002	0.07247	27.75353	− 0.01915
56693.785368	19.51221	0.07121	27.96600	− 0.04120
56694.751460	9.43889	0.07732	27.92017	− 0.20278
56696.650910	11.26911	0.07950	28.07056	− 0.37291
56697.709981	17.87517	0.07976	27.92011	− 0.31469
56714.747621	9.53700	0.10260	27.63444	− 0.81799
56718.738063	11.08132	0.07096	28.14193	− 0.27901
56722.748140	17.08727	0.07493	28.02565	− 0.30170
56726.607359	19.62246	0.08759	28.05893	0.27405
56739.667157	17.83755	0.06912	28.30868	− 0.37087
56740.828853	11.33148	0.08085	28.03725	0.18074
56743.729435	12.86017	0.08500	27.87329	− 0.47992
56748.718570	19.68182	0.07960	28.05396	0.58332
56773.547138	17.30455	0.09400	27.93314	− 0.50840
56809.616019	9.78716	0.08697	27.88691	− 0.28205
56810.576861	19.97365	0.09314	27.82375	0.03207
56811.626760	10.30808	0.08987	27.63040	− 0.42166
56833.553624	11.87092	0.08970	27.65532	− 0.32040
56837.523574	17.99888	0.10351	28.34447	0.25509
56878.471921	13.13879	0.10648	28.82110	− 0.02549
56879.472253	18.55910	0.11714	27.56328	0.27840
56880.475420[a]	10.58605	0.10760	29.58610	0.46275

[a]Marks data that was excluded from the fit.

Table A3. CORALIE (2) radial velocity data set. Machine readable format is available online at CDS.

BJD_{UTC}	RV ($km\,s^{-1}$)	σ ($km\,s^{-1}$)	FWHM ($km\,s^{-1}$)	BIS ($km\,s^{-1}$)
56998.827826	17.47009	0.12933	27.08932	− 0.39700
57010.832418	10.57601	0.09756	28.24718	− 0.27460
57015.847897	18.50726	0.08972	28.09100	− 0.49615
57023.751810	9.79495	0.10472	28.25546	0.04621
57026.761266	17.05405	0.09548	27.88570	− 0.35298
57068.721936	16.92315	0.08204	27.84734	− 0.23294
57079.758041	16.58560	0.09324	27.88199	− 0.24752
57081.729334	13.31412	0.09905	27.79138	− 0.20482
57119.490788	16.66207	0.12742	27.87915	− 0.93028
57121.524136	13.88072	0.12961	27.91771	− 0.24793
57138.722837	9.73737	0.11964	28.15435	− 0.85951
57188.507306	19.25630	0.14644	28.72389	− 0.47192
57370.812711	10.00891	0.13534	28.44965	0.13814
57371.843190	19.65781	0.12413	28.39575	− 0.22403
57422.738422	18.95753	0.09442	28.50348	− 0.36238
57423.721681	9.50032	0.08920	27.99541	− 0.06870
57458.648308	11.57403	0.09403	28.15161	− 0.40348
57477.536707	18.74728	0.10241	28.08040	0.08369
57560.561020	9.27320	0.09932	28.36695	0.08509
57569.464267	9.35399	0.11077	28.10119	0.12780
57590.489717	19.78442	0.10282	27.71082	0.09967
57716.848800	15.01008	0.14879	27.54259	− 1.16172

APPENDIX B: PHOTOMETRIC INFORMATION

Table B1. Light-curve information for WASP-128.MF denotes an additional constant offset for the meridian flip.

Date	Instrument	Filter	t_{exp} s	N_{exp}	Baseline function
2013 May 31	TRAPPIST	Sloan z'	8	705	$p(t^2)$
2014 Feb 11	TRAPPIST	Sloan z'	11	832	$p(t^2)$ + MF
2014 Feb 20	TRAPPIST	Sloan z'	11	1014	$p(t^2)$
2014 Mar 03	TRAPPIST	Sloan z'	11	860	$p(t^2)$
2014 Mar 03	*Euler*	Gunn r'	60	215	$p(t^2)$ + MF
2014 Mar 25	*Euler*	Gunn r'	75	136	$p(t^2 + \mathrm{sky}^1)$
2014 May 26	*Euler*	Gunn r'	60	203	$p(t^2)$
2015 May 10	TRAPPIST	Sloan z'	8	969	$p(t^2)$ + MF

This paper has been typeset from a TEX/LATEX file prepared by the author.

3.3 TOI-1259 Ab: a gas giant transiting a K dwarf with a white dwarf companion

3.3.1 Contribution

In February 2020 I attended the *TESS* Ninja 3 meeting which was hosted at the University of Sydney in Sydney, Australia. During this week two other participants, David Martin and Kareem El-Badry, had a look at a candidate planet transiting TOI-1259 A with an orbital period of 3.478 days. TOI-1259 A itself is a K dwarf, and this system had featured in some of Kareem's earlier work because of the known white dwarf companion in this system, TOI-1259 B. After the meeting ended, David proposed to lead a paper on the discovery of this system, and I offered to do the global analysis of the photometry and radial velocity data. We acquired radial velocity data using the SOPHIE spectrograph at Observatoire de Haute-Provence (OHP) near Marseille, France. The radial velocity variation revealed a planetary nature for the companion, $M_\mathrm{p} = 0.441 \pm 0.048\,M_\mathrm{Jup}$, thus TOI-1259 Ab was amongst the deepest transiting hot Jupiters given the small size of the host star.

My role in this paper was therefore similar to that in 2M1510 (Section 3.1). I modelled the *TESS* data (Figures 7 and 8 in the paper below, or Figures 3.16 and 3.17 in the thesis), ground-based light curves from various telescopes (Figure 9 in the manuscript, or Figure 3.18 in the thesis) and the SOPHIE radial velocities (Figure 11, Figure 3.20 in the thesis). This time, however, I used the EXOPLANET code (Foreman-Mackey 2019). TOI-1259 A is close to the JWST continuous viewing zone and had therefore been observed in nine *TESS* sectors at the time. The EXOPLANET model and the MCMC sampler in PYMC3 are both faster and more efficient than those implemented in AMELIE, thus saving considerable computing time. In addition, EXOPLANET includes an implementation of Gaussian process models with CELERITE (Foreman-Mackey et al. 2017), which can deal with the out-of-transit variation and complex correlated signals visible in some of the ground-based light curves (Figure 3.18). Given the large amount of data from various sources (which increases model complexity), the dynamical model-building framework of PYMC3 is a big advantage.

Monthly Notices of the ROYAL ASTRONOMICAL SOCIETY

MNRAS **507**, 4132–4148 (2021)
Advance Access publication 2021 July 27

https://doi.org/10.1093/mnras/stab2129

TOI-1259Ab – a gas giant planet with 2.7 per cent deep transits and a bound white dwarf companion

David V. Martin [1]★† Kareem El-Badry [2] Vedad Kunovac Hodžić [3]‡ Amaury H. M. J. Triaud [3] Ruth Angus [4,5] Jessica Birky [6] Daniel Foreman-Mackey [5] Christina Hedges [7,8] Benjamin T. Montet [9] Simon J. Murphy [10] Alexandre Santerne [11] Keivan G. Stassun [12] Alexander P. Stephan [1,13] Ji Wang [1] Paul Benni [14] Vadim Krushinsky [15] Nikita Chazov [16] Nikolay Mishevskiy [17] Carl Ziegler [18] Abderahmane Soubkiou [19] Zouhair Benkhaldoun [19] Isabelle Boisse [11] Matthew Battley [20,21] Nicola J. Miller [21] Douglas A. Caldwell [8,22] Karen Collins [22] Christopher E. Henze [8] Natalia M. Guerrero [23] Jon M. Jenkins [8] David W. Latham [24] Adam Levine [23] Scott McDermott [25] Susan E. Mullally [26] George Ricker [23] Sara Seager [23,27,28] Avi Shporer [23] Andrew Vanderburg [29] Roland Vanderspek [23] and Joshua N. Winn [30]

Affiliations are listed at the end of the paper

Accepted 2021 June 21. Received 2021 June 10; in original form 2020 December 30

ABSTRACT

We present TOI-1259Ab, a $1.0R_{\rm Jup}$ gas giant planet transiting a $0.71R_{\odot}$ K-dwarf on a 3.48 d orbit. The system also contains a bound white dwarf companion TOI-1259B with a projected distance of ∼1600 au from the planet host. Transits are observed in nine *TESS* sectors and are 2.7 per cent deep – among the deepest known – making TOI-1259Ab a promising target for atmospheric characterization. Our follow-up radial velocity measurements indicate a variability of semiamplitude $K = 71\,{\rm m\,s^{-1}}$, implying a planet mass of $0.44M_{\rm Jup}$. By fitting the spectral energy distribution of the white dwarf, we derive a total age of $4.08^{+1.21}_{-0.53}$ Gyr for the system. The K dwarf's light curve reveals rotational variability with a period of 28 d, which implies a gyrochronology age broadly consistent with the white dwarf's total age.

Key words: planets and satellites: formation – binaries: eclipsing – stars: individual (TOI-1259) – stars: low-mass – stars: rotation.

1 INTRODUCTION

We know that roughly half of the stars in the galaxy exist in multiples (Duquennoy & Mayor 1991; Tokovinin 2014), but the vast majority of exoplanet discoveries have been in single star systems. The presence of a stellar companion will affect exoplanet populations. It may restrict the regions where planets may orbit stably (Dvorak 1984; Holman & Wiegert 1999; Mardling & Aarseth 2001), reduce the lifetime of protoplanetary discs (Kraus et al. 2012; Daemgen et al. 2015; Cheetham et al. 2015), inhibit planetesimal formation (Thébault, Marzari & Scholl 2008; Xie, Zhou & Ge 2009) and induce high-eccentricity dynamics (Mazeh & Shaham 1979; Eggleton & Kisseleva-Eggleton 2006; Fabrycky & Tremaine 2007). Early exoplanet searches avoided close stellar multiples, whereas more distant binary companions were often undetected. Now, the vast *Gaia* astrometry survey is revealing thousands of wide binaries (El-Badry & Rix 2018; Hartman & Lépine 2020; Mugrauer & Michel 2020), many of which contain confirmed or candidate planets.

An even less studied aspect of exoplanet populations is the effect of stellar evolution, with most planets being discovered around main-sequence stars. As stars evolve they will expand, lose mass and, in most cases, leave behind a degenerate white dwarf (WD). A surprising discovery is that up to roughly 50 per cent of WDs have atmospheres polluted with heavy elements (Debes, Walsh & Stark 2012; Farihi 2016; Wilson et al. 2019), despite the fact that the high gravity should cause such elements to settle out of the atmosphere in a short time. This is seen as evidence that circumstellar planetary material occasionally accretes on to WDs, replenishing the heavy elements.

However, it is tricky to actually find planets around WDs. A lack of sharp spectral features prevents precise radial velocity (RV) monitoring (Maxted, Marsh & Moran 2000). A small radius, similar to that of the Earth, significantly reduces transit probabilities and durations (Farmer & Agol 2003; Faedi et al. 2010). A typically faint apparent magnitude leads to noisy light curves. Astrometric planet detection with *Gaia* is promising, but will still be challenging because of the faintness of the objects (Silvotti et al. 2014). Evidence for circumbinary planets has been presented for some binaries containing at least one WD (e.g. Qian et al. 2009), but the validity of the

* E-mail:
† Fellow of the Swiss National Science Foundation.
‡ Fulbright Fellow.

© 2021 The Author(s)
Published by Oxford University Press on behalf of Royal Astronomical Society

Downloaded from https://academic.oup.com/mnras/article/507/3/4132/6329054 by University of Birmingham user on 24 September 2021

Table 1. Summary of the TOI-1259 system. Host star parameters derived from SED fits (Section 3.1). White dwarf parameters are detailed in Table 4, and we only show parameters from the first model in that table here. Full planet parameters are shown in Table 5. Coordinates and distances are from the *TESS* Input Catalog v8.1.

Parameter	Description	Value
Host star – TOI-1259A		
TIC	*TESS* Input Catalog	288735205
Gaia	ID	2294170838587572736
α	Right ascension	282.100297136879° ($18^h48^m24\overset{s}{.}07$)
δ	Declination	79.2560447193138° ($79°15'21\overset{''}{.}76$)
$V_{\rm mag}$	Apparent V magnitude	12.08
d	Distance (pc)	118.11 ± 0.37
$M_\star$	Mass ($M_\odot$)	$0.68^{+0.10}_{-0.01}$
$R_\star$	Radius ($R_\odot$)	0.739 ± 0.031
$T_{\rm eff,\star}$	Effective temperature (K)	4775 ± 100
$[{\rm Fe/H}]_\star$	Metallicity	-0.5 ± 0.5
$\log g_\star$	Surface gravity (cgs)	4.5 ± 0.5
Transiting planet – TOI-1259Ab		
$M_{\rm pl}$	Mass ($M_{\rm Jup}$)	$0.441^{+0.049}_{-0.047}$
$R_{\rm pl}$	Radius ($R_{\rm Jup}$)	$1.022^{+0.030}_{-0.027}$
$P_{\rm pl}$	Orbital period (d)	$3.4779780^{+0.0000019}_{-0.0000017}$
$a_{\rm pl}$	Semimajor axis (au)	$0.04070^{+0.00114}_{-0.00110}$
$e_{\rm pl}$	Eccentricity	0
Bound white dwarf companion – TOI-1259B		
TIC	*TESS* Input Catalog	1718312312
GAIA	ID	2294170834291960832
α	Right ascension	282.11052432749° ($18^h48^m26\overset{s}{.}53$)
δ	Declination	79.2594025546024° ($79°15'33\overset{''}{.}85$)
$V_{\rm mag}$	Apparent V magnitude	19.23
d	Distance (pc)	120.6 ± 4.6
$M_{\rm WD}$	Mass ($M_\odot$)	0.561 ± 0.021
$R_{\rm WD}$	Radius ($R_\odot$)	0.0131 ± 0.0003
$\rm sep_{WD}$	Projected current separation (au)	1648
$T_{\rm eff,\,WD}$	Effective temperature (K)	6300^{80}_{-70}

evidence has been repeatedly questioned (Wittenmyer, Horner & Marshall 2013; Zorotovic & Schreiber 2013; Bear & Soker 2014). Only recently did Vanderburg et al. (2020) discover the first bona fide planet transiting a WD: WD 1856 + 534 (see also Alonso et al. 2021). There have also been discoveries of transiting planetary debris (Vanderburg et al. 2015; Manser et al. 2019; Guidry et al. 2020; Vanderbosch et al. 2020) and accretion on to a WD attributed to the evaporating atmosphere of a giant planet (Gänsicke et al. 2019).

In this paper, we present TOI-1259Ab, a planet that is relevant to questions at the intersection of stellar evolution and stellar multiplicity. It is a transiting Jupiter-sized planet on a 3.48 d orbit around a K-dwarf, with a WD companion at a projected separation of ≈1600 au. The WD was already known to be bound based on its *Gaia* parallax and common proper motion (El-Badry & Rix 2018). The transits were discovered by the *TESS* Science Processing Operations Center (SPOC; Jenkins et al. 2016) and the community was alerted by the *TESS* Science Office on 17 October 2019 (Guerrero 2020), but the unusually deep transits of 2.7 per cent raised concerns that the signal is actually due to an eclipsing binary. Through our RV follow-up, we confirm that the signal is due to a planet, with a mass of $0.44 M_{\rm Jup}$. We summarize the key aspects of the TOI-1259 system in Table 1.

Only a few bona fide planets have been discovered with degenerate outer companions (Table 2), the first being Gliese-86b (Queloz et al. 2000; Els et al. 2001; Lagrange et al. 2006). Mugrauer (2019) found 204 binary companions in a sample of roughly 1300 exoplanet hosts, of which eight of the companions were WDs. Mugrauer & Michel (2020) found five WD companions to *TESS* Objects of Interest, including TOI-1259, but without RV data to confirm the TOIs as planets. Some of these planets were also in the El-Badry & Rix (2018) catalogue.

Even when a planet host star is still on the main sequence, the evolution of an outer companion still has implications for the planet's dynamics and survival (Kratter & Perets 2012; Stephan et al. 2020). Heavy element pollution in any of these WDs may be caused by its stellar binary companion (Veras et al. 2011, 2013; Bonsor & Veras 2015; Hamers, Perets & Portegies Zwart 2016; Stephan, Naoz & Zuckerman 2017), and would also suggest both stars in the binary host (or once hosted) planets, of which only two systems are presently known (WASP-94, Neveu-VanMalle et al. 2014 and XO-2, Desidera et al. 2014). The presence of a WD companion also makes it possible to calculate the system's age independently of other methods such as gyrochronology and isochrone fitting (Barnes 2003; Jørgensen & Lindegren 2005; Angus et al. 2019).

WD aside, the planet TOI-1259Ab has some beneficial properties for future atmospheric follow-up with *James Webb Space Telescope (JWST)*. The planet has 2.7 per cent deep transits on its 0.71 $R_\odot$ K-dwarf host, which are amongst the deepest known (Fig. 1). The 0.71 $R_\odot$ K-dwarf host star has a J magnitude of 10.226, and is located on the sky with an ecliptic latitude of 76.878°, placing it near the *TESS* and *JWST* continuous viewing zones. A measurement of the planet's atmospheric composition or other properties would also complement any measurement of pollution in the WD atmosphere, as we try to better understand the formation and survival of planets in multistellar systems.

Our paper is structured as follows. Section 2 details the *TESS* photometry, SOPHIE RVs, and *Gaia* astrometry. In Section 3, we present a combined analysis of these data and thereby characterize the planet, its host star, and the companion WD. We conclude by discussing some implications for this system and potential future work in Section 4.

2 OBSERVATIONS

2.1 *TESS* photometry

The *TESS* mission observed TOI-1259 in 2 min cadence mode for a total of 240 d, covering nine sectors (14, 17–21, 24–26) between 2019 July 18 and 2020 July 4. The *TESS* Science Processing Operations Center pipeline (Jenkins et al. 2016) identified a ∼2.5 per cent transit signal lasting ∼2.2 h, repeating with a period of 3.48 d. The flat-bottomed shape and deep transit – combined with the K dwarf host – is consistent with a giant planet, substellar object, or very low-mass star. There were 58 transit events in the *TESS* data.

The *TESS* spacecraft fires its thrusters to unload angular momentum from its reaction wheels every few days, which may cause the images obtained in the timestamps to appear disjoint. To make sure the momentum dumps do not affect our further analysis, we identify the times of these events from the Data Quality Flags in the FITS files, and exclude the data obtained within four hours on either side of the thruster events.

Downloaded from https://academic.oup.com/mnras/article/507/3/4132/6329054 by University of Birmingham user on 24 September 2021

Table 2. Known extra-solar planets around a main-sequence star with a bound white dwarf companion, ordered by the current projected separation of the white dwarf (sep_{WD}). Of the TOIs (*TESS* Objects of Interest) with white dwarf companions in the catalogues of El-Badry & Rix (2018) and Mugrauer & Michel (2020), only TOI-1259Ab is confirmed to be a planet. CTOI-53309262 was only seen to transit once by *TESS* and so its period and semimajor axis are to be determined (TBD).

Name	a_{pl} (au)	Sep_{WD} (au)	Planet reference	White dwarf reference
HD 13445 (Gliese-86)	0.1143	21	Queloz et al. (2000)	Els et al. (2001) Lagrange et al. (2006)
HD 27442 (Epsilon Reticuli)	1.271	236	Butler et al. (2001)	Chauvin et al. (2006) Mugrauer, M. et al. (2007)
HIP 116454	0.098	524	Vanderburg et al. (2015)	Vanderburg et al. (2015)
HD 8535	2.45	560	Naef et al. (2010)	Mugrauer (2019)
CTOI-53309262	TBD	625	Unconfirmed Community TOI (Single Transit Only)	El-Badry & Rix (2018) Mugrauer & Michel (2020)
Kepler-779	0.0558	1105	Morton et al. (2016)	Mugrauer (2019)
TOI-1703	0.0223	1302	Unconfirmed TOI	Mugrauer & Michel (2020)
TOI-1259	0.0416	1648	This Paper	El-Badry & Rix (2018) Mugrauer & Michel (2020)
HD 107148	0.269	1790	Butler et al. (2006)	Mugrauer & Dinçel (2016)
TOI-249	0.0564	2615	Unconfirmed TOI	El-Badry & Rix (2018) Mugrauer & Michel (2020)
WASP-98	0.0453	3500	Hellier et al. (2014)	Mugrauer (2019) Southworth et al. (2020)
HD 118904	1.7	3948	Jeong et al. (2018)	Mugrauer (2019)
TOI-1624	0.0688	4965	Unconfirmed TOI	Mugrauer & Michel (2020)
HD 147513 (62 G. Scorpii)	1.32	5360	Mayor et al. (2004)	Alexander & Lourens (1969)

Table 3. Stellar radius and mass measurements based on four different methods. In all cases, we use a fit to the SED combined with *Gaia* DR2 parallaxes. In methods 1 and 2 we follow the procedure of Stassun & Torres (2016) and Stassun et al. (2017, 2018) to derive the radius and the mass comes from the SED measurement of the surface gravity $\log g$ (1) and the Torres et al. (2010) mass–radius relationship (2). In methods 3 and 4, we use ExoFASTv2 (Eastman et al. 2019) to fit the SED and two different isochrones. We use method 2 (in bold) as the nominal value.

Method	Radius ($R_\odot$)	Mass ($M_\odot$)
1. SED + $\log g$	0.739 ± 0.031	0.79 ± 0.14
2. SED + Torres et al. (2010) M-R	0.739 ± 0.031	0.68 ± 0.08
3. SED + MIST isochrones	0.733 ± 0.022	$0.777^{+0.037}_{-0.038}$
4. SED + PARSEC isochrones	0.729 ± 0.020	$0.777^{+0.034}_{-0.031}$

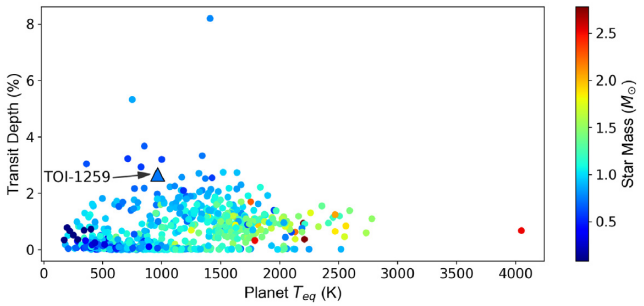


Figure 1. Transit depths of all confirmed transiting exoplanets as a function of the planet's equilibrium temperature (where such a value has been calculated). The colour indicates the mass of the host star in solar masses. The triangle demarcates TOI-1259 with 2.7 per cent deep transits.

2.2 Ground based follow-up photometry

We acquired ground-based time-series follow-up photometry of TOI-1259A as part of the *TESS* Follow-up Observing Program.[1] A full transit was observed on UTC 2019 October 10 using an unfiltered diffuser and again on UTC 2019 October 17 in g'-band from the Deep Sky West 0.5-m telescope near Rowe, New Mexico, USA. An egress was observed on UTC 2019 October 6 in *R* and *V* band using two 0.4-m telescopes at Kourovka observatory of Ural Federal University near Yekaterinburg, Russia. A full transit was observed on UTC 2019 October 24 in z' band from the 0.36-m telescope at Acton Sky Portal private observatory in Acton, MA, USA. A full transit was observed on UTC 2019 December 4 in *R* band from the 0.25-m telescope at Ananjev L33 private observatory near Ananjev, Ukraine. All observations detected on-time transits with depths consistent with *TESS* using apertures that were not blended with any known TICv8 or *Gaia* DR2 neighbouring stars, except the diffuser observation was partially contaminated with a star that is too faint to cause the transit detection. Although *TESS* observed 58 transits of TOI-1259 b in Cycle 2, we also include all available ground-based light curves in our analysis, with the exception of the *R*- and *V*-band observations at Kourovka Observatory on 2019 October 6 which only observed the egress. The reduced data of all ground-based photometry are available at ExoFOP-*TESS*.[2]

2.3 SOPHIE radial velocities

To measure the mass of TOI-1259Ab we used SOPHIE, which is a high resolution[3] échelle spectrograph used to find extra-solar planets

[1] https://⟨0:italic ⟩TESS⟨/0:italic⟩.mit.edu/followup
[2] https://exofop.ipac.caltech.edu/⟨0:italic ⟩TESS⟨/0:italic⟩
[3] We used the 'high-efficiency mode', which has a resolution of $R = 39\,000$ and is typically used for stars fainter than 10th magnitude.

Downloaded from https://academic.oup.com/mnras/article/507/3/4132/6329054 by University of Birmingham user on 24 September 2021

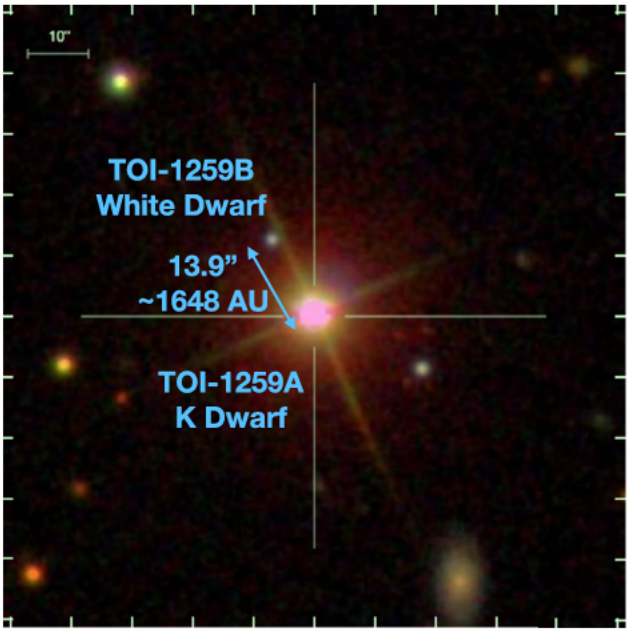


Figure 2. SDSS image of the planet host TOI-1259A and its bound white dwarf companion TOI-1259B. The image is centred on TOI-1259A at RA $18^{h}48^{m}24\overset{s}{.}07$, Dec $79°15'21\overset{''}{.}76$.

with high-precision RVs (Perruchot et al. 2008; Bouchy et al. 2009). It is installed on the 1.93-m telescope at Observatoire de Haute Provence, France.

We obtained 19 RV measurements of TOI-1259Ab between 2020 June 10 and 2020 July 16 using the SOPHIE spectrograph. All RVs were calculated using the standard SOPHIE pipeline, where a cross-correlation function is calculated between the data and a K5 mask. Each observation yielded an RV with a precision of roughly 20 m s^{-1}.

We note that our spectra are not contaminated by the bound WD, since it is both too faint (19.23 mag compared with 12.08 for the host star) and too far away (13.9 arcsec separation compared with 3 arcsec diameter SOPHIE fibres) to contribute any light.

2.4 *Gaia* astrometry

TOI-1259A and its WD companion (TOI-1259B) were identified as a candidate wide binary by El-Badry & Rix (2018), who searched *Gaia* DR2 for pairs of stars with positions, parallaxes, and proper motions consistent with bound Keplerian orbits.[4] Fig. 2 shows an SDSS image of the system, with both the K-dwarf primary and WD companion clearly visible. The projected angular (physical) separation of the pair is 13.9 arcsec (1648 au). The plane-of-the-sky absolute velocity difference between the WD and K dwarf is $\Delta V_{\perp} = 0.47^{+0.59}_{-0.25}$ km s^{-1}. For comparison, we can calculate the Keplerian orbital velocity of a circular orbit separated by 1648 au, with masses 0.68 and 0.561 $M_{\odot}$ (see Table 1):

$$V = \sqrt{\frac{G\,(M_{\star} + M_{\rm WD})}{\rm sep_{WD}}}, \qquad (1)$$

where $G = 6.67384 \times 10^{-11}$. The value $V = 0.82$km s^{-1} is consistent with the *Gaia* measurement, within the precision of the measurements which are limited by the *Gaia* proper motion uncertainties. The semimajor axis of the WD–K dwarf orbit and the 3D separation of the two stars are not currently measurable. However, for randomly oriented orbits and a plausible eccentricity distribution, the projected semimajor axis is almost always within a factor of two of the true semimajor axis (see El-Badry & Rix 2018, their fig. B1). The WD companion was later independently identified by Mugrauer & Michel (2020).

Because orbital accelerations are not easy to measure in long-period binaries, distinguishing gravitationally bound wide binaries from chance alignments depends on statistical arguments about the probability of chance alignments. The chance alignment probability for a given separation, data quality, and background source density can be estimated empirically (e.g. Lépine & Bongiorno 2007; El-Badry et al. 2019; Tian et al. 2020). We follow the approach described in Tian et al. (2020) to estimate the chance-alignment probability. In brief, we repeat the binary search after artificially shifting each star in *Gaia* DR2 by ∼1°, searching for companions around its new position. This procedure removes genuine binaries, but preserves chance alignment statistics (see Lépine & Bongiorno 2007). Comparing the number of binary candidates found so far to the number found in *Gaia* DR2 at similar separation, we estimate a chance-alignment probability of $\sim 1 \times 10^{-4}$ for TOI-1259A and its companion. That is, there is little doubt that the planet host and WD are physically associated.

3 ANALYSIS AND RESULTS

3.1 Host star parameters

We performed an analysis of the broad-band spectral energy distribution (SED) of the star together with the *Gaia* DR2 parallaxes (adjusted by +0.08 mas to account for the systematic offset reported by Stassun & Torres 2018), in order to determine an empirical measurement of the stellar radius, following the procedures described in Stassun & Torres (2016), Stassun, Collins & Gaudi (2017), and Stassun et al. (2018). We pulled the *BVgri* magnitudes from *APASS*, the JHK_S magnitudes from *2MASS*, the *W1–W4* magnitudes from *WISE*, the $GG_{\rm BP}G_{\rm RP}$ magnitudes from *Gaia*, and the NUV magnitude from *GALEX*. Together, the available photometry spans the full stellar SED over the wavelength range 0.2–22 μm (see Fig. 3).

We performed a fit to the SED using Kurucz (1979) stellar atmosphere models, with the effective temperature ($T_{\rm eff}$), metallicity ([Fe/H]), surface gravity ($\log g$) as free parameters. The only additional free parameter is the extinction (A_V), which we restricted to the maximum line-of-sight value from the dust maps of Schlegel, Finkbeiner & Davis (1998). The resulting fit is very good (Fig. 3) with a reduced χ^2 of 1.7 and best-fitting $A_V = 0.20 \pm 0.07$, $T_{\rm eff} = 4775 \pm 100$ K, $\log g = 4.5 \pm 0.5$, and [Fe/H] $= -0.5 \pm 0.5$. Integrating the (unreddened) model SED gives the bolometric flux at Earth, $F_{\rm bol} = 5.94 \pm 0.14 \times 10^{-10}$ erg s^{-1} cm^{-2}. Taking the $F_{\rm bol}$ and $T_{\rm eff}$ together with the *Gaia* DR2 parallax, gives the stellar radius, $R_{\star} = 0.739 \pm 0.031$ $R_{\odot}$.

The stellar mass can be obtained from the SED analysis in two ways. First, we can use the $R_{\star}$ together with $\log g$ to obtain a mass estimate of $M_{\star} = 0.79 \pm 0.14$ $M_{\odot}$. Alternatively, we can apply the Torres, Andersen & Giménez (2010) empirical mass–radius relations to get a value $M_{\star} = 0.68 \pm 0.08$ $M_{\odot}$.

As an independent test of our stellar parameters, we ran EXOFASTv2 (Eastman et al. 2019) to create a joint fit of the SED and two different types of isochrones: MIST (Choi et al. 2016; Dotter 2016) and PARSEC (Bressan et al. 2012). With MIST we obtain

[4]Orbital motion means that even bound orbits may have slightly different proper motions, but we require that this difference is less than the expected maximum orbital velocity at this separation.

Downloaded from https://academic.oup.com/mnras/article/507/3/4132/6329054 by University of Birmingham user on 24 September 2021

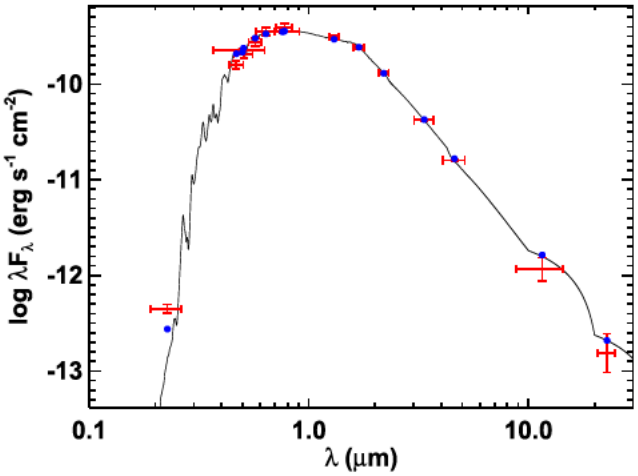


Figure 3. Spectral energy distribution of TOI-1259A. The red symbols represent the observed photometric measurements, where the horizontal bars represent the effective width of the passband. The blue symbols are the model fluxes from the best-fit Kurucz (1979) atmosphere model (black).

$R_\star = 0.733 \pm 0.022$ and $M_\star = 0.777^{+0.037}_{-0.038}$ and with PARSEC we obtain similar values of $R_\star = 0.729 \pm 0.020$ and $M_\star = 0.777^{+0.034}_{-0.031}$.

Throughout this paper, we will use the $R_\star = 0.739\,R_\odot$ and $M_\star = 0.68\,M_\odot$ values calculated using the empirical SED and Torres et al. (2010) relation, respectively. These are the priors that will be used in the global analysis to determine the planet parameters in Section 3.6. In Table 3 we list our four different pairs of derived values for the primary star mass and radius.

3.2 Host star rotation

We use a Systematics-insensitive Periodogram (SIP) to build a periodogram whilst simultaneously detrending *TESS* instrument systematics from scattered background, following the method first described in Angus, Foreman-Mackey & Johnson (2016) and more recently implemented for *TESS* data in Hedges et al. (2020). For this we use the Simple Aperture Photometry (SAP) light curves, since the PDCSAP light curves tend to have the rotation period removed, or at least made harder to identify. The SIP power amplitude is shown in Fig. 4. The SIP shows the most significant power at a period of $P_{rot} = 28$ d and a secondary peak at $P_{rot} \approx 40$ d. We adopt the more significant peak at $P_{rot} = 28$ d as the true rotation rate of TOI-1259. The signal at $P_{rot} \approx 40$ d is possibly an alias of the rotation period.

The rotation period of $P_{rot} = 28$ d is close to the orbital period of *TESS* (27 d). We conduct two tests of the validity of this rotation rate. First, We construct SIPs for the targets neighbouring TOI-1259 and find no evidence of a similar peak in near-by targets. Secondly, we create a SIP for all 'background' pixels outside of the *TESS* pipeline aperture in the *TESS* Target Pixel File for TOI-1259. This background SIP, shown as a blue line in Fig. 4, has no power at 28 d. This suggests that the 28 d signal is intrinsic to the target, and not an artefact of, for example, the sampling frequency of *TESS*.

3.3 Host star age

When estimating the ages of K dwarfs using gyrochronology, it is essential to account for 'stalled magnetic braking'. Recent observations have revealed that rotational evolution is inhibited for middle-aged K dwarfs (Curtis et al. 2019; Angus et al. 2020). This stalled rotational evolution is thought to be caused by an internal

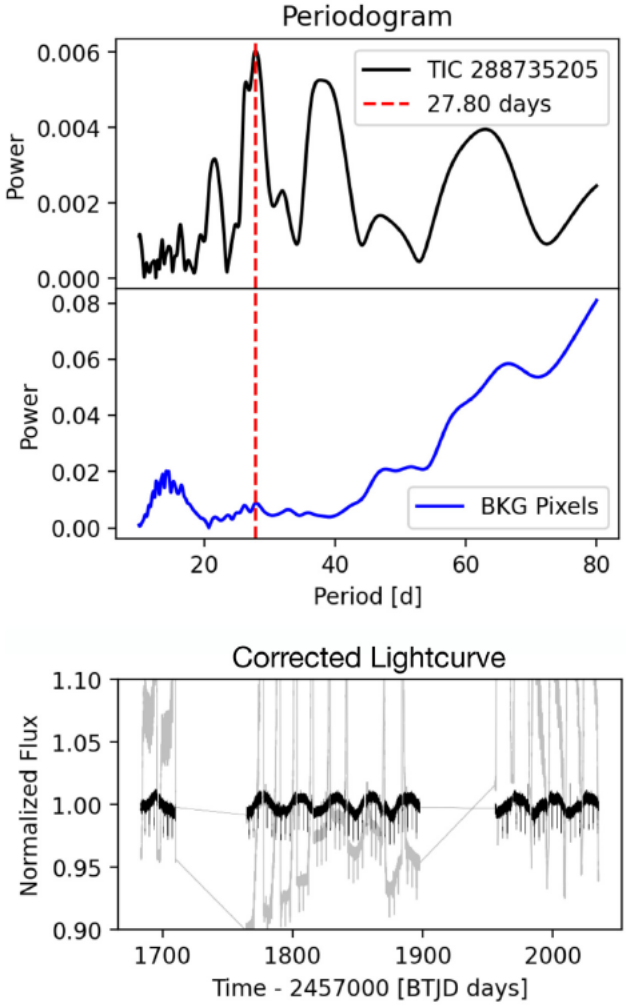


Figure 4. Top: Systematics-Insensitive Periodogram (SIP) for TOI-1259b. The periodogram is calculated for both the corrected light curve (the black line) and the background (BKG) pixels (the blue line). There is a strong peak in the SIP at 28 d, which is attributed to the rotation of the planet host and denoted by a red-dashed line. The background pixels show no evidence of any periodicity, suggesting that the 28 d signal is both real and intrinsic to the target. Note that these periodograms are not normalized by the measurement errors. Bottom: The light curve for TOI-1259. The grey points show the raw data *TESS* data, and the black points show the data corrected using `TESS-sip`, showing a clear periodicity.

redistribution of angular momentum (Spada & Lanzafame 2020). Unless this phenomenon is taken into account, the ages of K dwarfs could be underestimated by more than 2 Gyr.

We estimated an age for this star using a new gyrochronology model that accounts for stalled magnetic braking (Angus et al., in preparation). This model was calibrated by fitting a Gaussian process (GP), a semiparametric model that is flexible enough to capture the complex nature of stellar spin-down, to a number of asteroseismic stars and open clusters, including NGC 6811 where many member stars exhibit stalled magnetic braking (Curtis et al. 2019). We also used kinematic ages of *Kepler* field stars to calibrate this model for old K and early M dwarfs, where there is a dearth of suitable open cluster calibration stars. These kinematic ages also reflect the stalled magnetic braking behaviour seen in open clusters (Angus et al. 2020).

Using this model, we infer an age of $4.8^{+0.7}_{-0.8}$ Gyr for this star. The quoted age uncertainty is the formal uncertainty that results from the

Downloaded from https://academic.oup.com/mnras/article/507/3/4132/6329054 by University of Birmingham user on 24 September 2021

Table 4. Parameters of the WD. We compare constraints derived assuming a hydrogen versus helium atmosphere and constraints that assume two different IFMRs.

Parameter	H atm; El-Badry + 18 IFMR	H atm; Williams + 09 IFMR	He atm; El-Badry + 18 IFMR	He atm; Williams + 09 IFMR
Total age (Gyr)	$4.08^{+1.21}_{-0.53}$	$3.73^{+0.56}_{-0.31}$	$4.67^{+1.70}_{-0.94}$	$3.94^{+0.81}_{-0.44}$
Cooling age (Gyr)	$1.88^{+0.07}_{-0.06}$	$1.88^{+0.07}_{-0.06}$	$1.78^{+0.06}_{-0.05}$	$1.78^{+0.06}_{-0.05}$
Pre-WD age (Gyr)	$2.18^{+1.2733}_{-0.5597}$	$1.84^{+0.61}_{-0.35}$	$2.87^{+1.73}_{-1.00}$	$2.14^{+0.86}_{-0.47}$
Radius ($R_\odot$)	$0.0131^{+0.0003}_{-0.0003}$	$0.0131^{+0.0003}_{-0.0003}$	$0.0129^{+0.0003}_{-0.0003}$	$0.0129^{+0.0003}_{-0.0003}$
Mass ($M_\odot$)	$0.561^{+0.021}_{-0.021}$	$0.561^{+0.021}_{-0.021}$	$0.548^{+0.021}_{-0.019}$	$0.548^{+0.021}_{-0.019}$
Initial mass ($M_\odot$)	$1.59^{+0.22}_{-0.22}$	$1.72^{+0.17}_{-0.17}$	$1.45^{+0.22}_{-0.20}$	$1.61^{+0.17}_{-0.17}$
$T_{\rm eff}$ (K)	6300^{+80}_{-70}	6300^{+80}_{-70}	6330^{+80}_{-70}	6330^{+80}_{-70}
A_V (mag)	$0.019^{+0.018}_{-0.013}$	$0.019^{+0.018}_{-0.013}$	$0.019^{+0.017}_{-0.013}$	$0.019^{+0.017}_{-0.013}$

uncertainty on the star's rotation period, and does not account for uncertainty in the model. Quantifying the magnitude of the model uncertainty is beyond the scope of this paper, however, a 20 per cent uncertainty of around 1 Gyr may be a more reasonable estimate of the true age uncertainty. This estimated age for the planet host is consistent with that of the total age of the WD (Section 3.4).

3.4 White dwarf age

WDs steadily cool as they age. A WD's cooling age – that is, the time since it became a WD – can therefore be constrained from its temperature and luminosity. If the WD's mass is known, the initial mass of its progenitor star can be inferred through the initial–final mass relation (IFMR), and this initial mass constrains the pre-WD age of the WD progenitor. Therfore, if we have a well-constrained distance to the WD then its total age, i.e. the sum of its main sequence lifetime and its cooling age, can be robustly measured from its SED. Under the reasonable ansatz that the WD and K dwarf formed at the same time, we can then measure the total system age from the WD.

We use `BASE-9` (von Hippel et al. 2006; De Gennaro et al. 2008; Stein et al. 2013; Stenning et al. 2016) to fit the SDSS *ugriz* photometry of the the WD. `BASE-9` combines evolutionary models for WDs (Althaus & Benvenuto 1998; Montgomery et al. 1999), WD atmospheric models (Bergeron, Wesemael & Beauchamp 1995; Holberg & Bergeron 2006), PARSEC evolutionary models (Bressan et al. 2012), and semiempirical IFMRs to predict the SED of a WD with a given age, initial mass and metallicity, distance, extinction, and spectral type. It then uses MCMC methods to constrain these parameters from the SED of an observed WD.

We use the *Gaia* parallax of the brighter K dwarf companion as a prior. For the initial [Fe/H], we assume a Gaussian prior with a mean of −0.2 and a standard deviation of 0.3, appropriate for a disc star in the solar neighbourhood (e.g. Hayden et al. 2015). The spectral type of the WD is not known. Although we expect extinction to be almost negligible for such a nearby WD, we fit the extinction A_V as a free parameter, with a Gaussian prior with a mean of 0.01 and a standard deviation of 0.02, based on the 3D dust map of Green et al. (2019). For context, the SFD reddening (which quantifies the total dust column to infinity, including dust behind the WD) at the WD's position is $E(B-V) = 0.085$ (Schlegel et al. 1998). We use a flat prior between 0 and 12 Gyr for total age. Our fiducial fit assumes the WD has a hydrogen atmosphere, which is true for ∼75 per cent of WDs with its temperature and mass. We also show how the constraints would change if the WD has a helium atmosphere in Table 4.

A systematic uncertainty in modeling the WD's evolution is the IFMR. Because most published IFMRs are discrete, analytic fitting functions, this uncertainty is difficult to marginalize over gracefully. To estimate the magnitude of this uncertainty, we compare constraints that assume two different IFMRs: the IFMR measured by Williams, Bolte & Koester (2009) from bound clusters, and the IFRM measured by El-Badry, Rix & Weisz (2018) from the *Gaia* colour–magnitude diagram of nearby field WDs.

Fig. 5 shows the resulting constraints on parameters of the WD, assuming a hydrogen atmosphere. Values are also reported in Table 4. The temperature and radius of the WD are well constrained by the SED. Because the radius of a WD is determined primarily by its mass, this also constrains the WD's mass, which in turn constrains the initial mass of the WD progenitor. The cooling age of the WD is reasonably well constrained to be between 1.7 and 2 Gyr. The pre-WD age is more uncertain, because a modest uncertainty in initial mass leads to a significant uncertainty in main-sequence lifetime. This is the primary cause of the differences in the constraints obtained for the two different IFMRs. The two relations are actually quite similar at the relevant WD mass (see El-Badry et al. 2018, their fig. 3), but the El-Badry et al. (2018) relation is somewhat shallower. This means that a larger range of initial masses could produce the observed WD mass, and thus, that there is a larger range of allowed pre-WD ages. The pre-WD lifetime of a $2\,M_\odot$ star is ≈1.3 Gyr, while that of a $1.2\,M_\odot$ star is ≈6 Gyr, so the resulting uncertainty is non-negligible. A tighter constraint on the WD mass – which is potentially achievable via gravitational redshift, e.g. Reid 1996 – could improve the statistical uncertainty on total age. However, the constraint is already tight enough that systematic uncertainty due to the IFMR is comparable to the statistical uncertainty, so the IFMR uncertainty would likely dominate the age uncertainty even with significantly better data.

Table 4 also shows how constraints on the WD's parameters would change if it had a helium atmosphere rather than a hydrogen atmosphere. Changing the atmosphere slightly changes the WD's colours and the mass–radius relation, such that the implied mass of the WD is lower. The difference is, however, relatively modest. Obtaining a spectrum of the WD would remove this source of uncertainty, since a WD with a hydrogen atmosphere and $T_{\rm eff} > 6000$ K would have detectable Balmer lines.

Our derived total age for TOI-1259B is consistent with the $4.8^{+0.7}_{-0.8}$ Gyr age derived for the planet host TOI-1259A based on gyrochronology (Section 3.3).

3.5 Radial velocity modelling

To confirm the planet we conduct two independent analyses. First, in this section we detect solely the RV signal, using the genetic algorithm YORBIT (Ségransan et al. 2010). Secondly, in Section 3.6 we do a combined fit of both the photometry and RV, with a completely different code.

Downloaded from https://academic.oup.com/mnras/article/507/3/4132/6329054 by University of Birmingham user on 24 September 2021

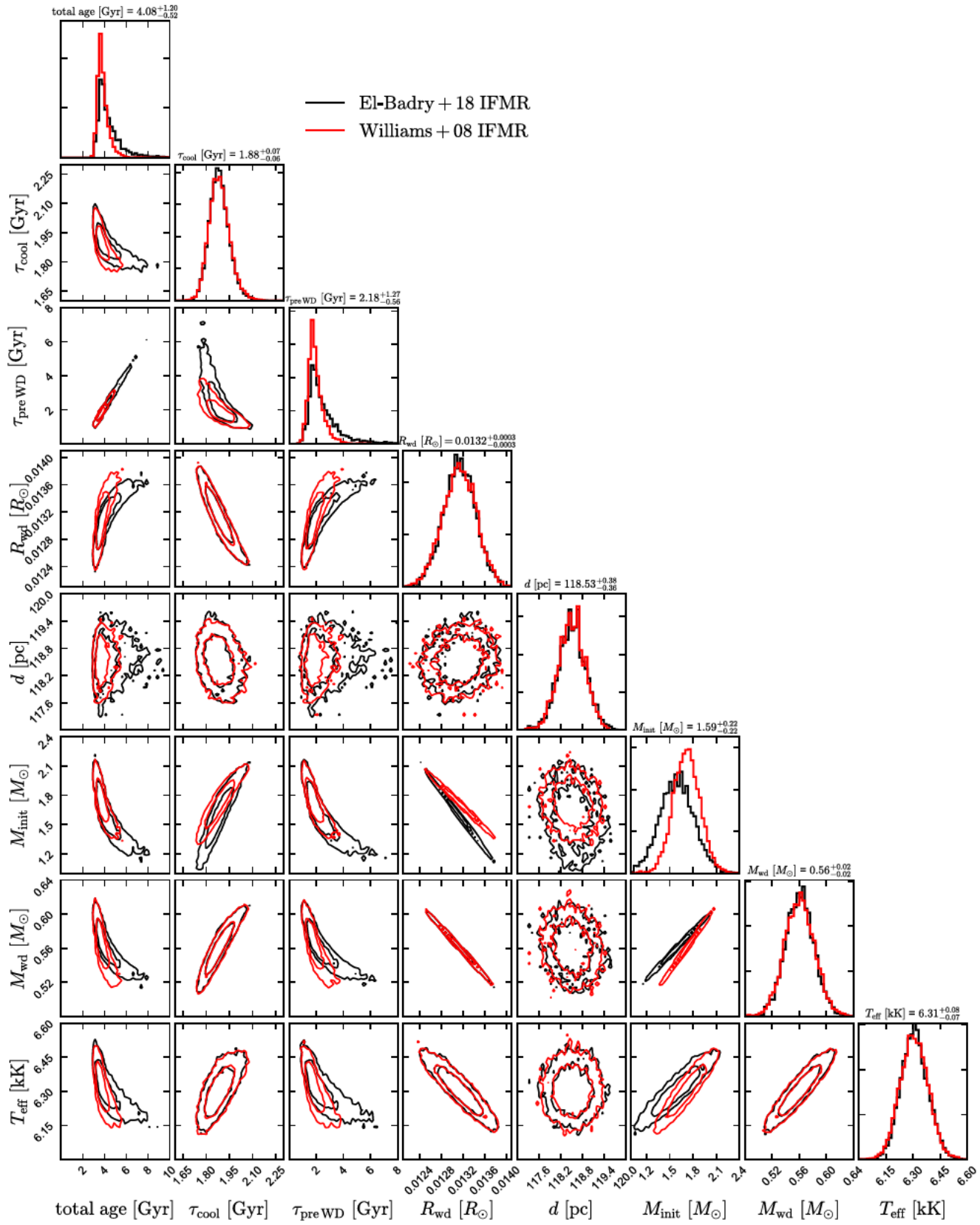


Figure 5. Parameters of the WD and its progenitor, obtained from fitting the SED. We compare constraints obtained when assuming the initial–final mass relations (IFMR) from El-Badry et al. (2018) and Williams et al. (2009). For this figure we assume a hydrogen atmosphere, but in Table 4 we also show results for a potential helium atmosphere. Values listed on the diagonal are based on the El-Badry et al. (2018) IFMR. Contours enclose 68 and 95 per cent probability. The total age of the WD – and thus, presumably, the age of the system – is at least 3 Gyr. The age uncertainty is dominated by uncertainty in the mass and pre-WD age of the progenitor.

Downloaded from https://academic.oup.com/mnras/article/507/3/4132/6329054 by University of Birmingham user on 24 September 2021

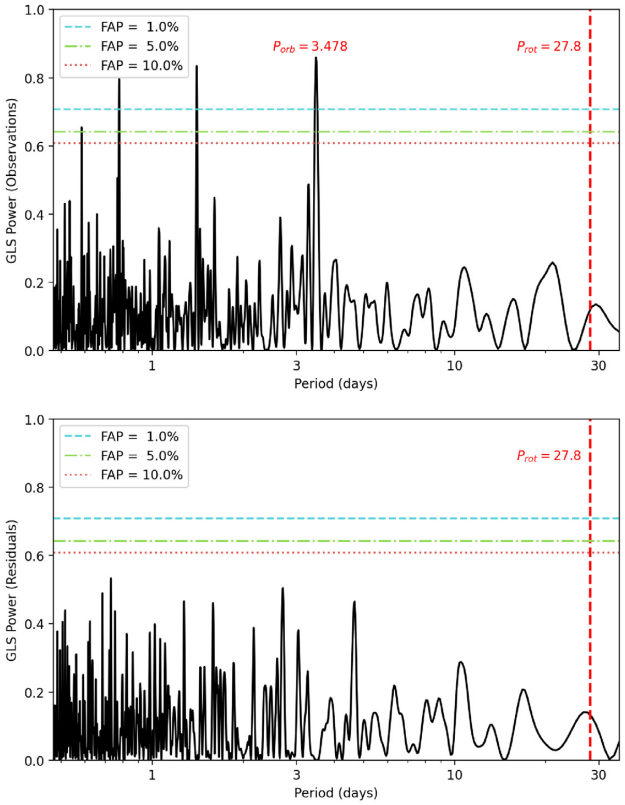


Figure 6. Generalized Lomb–Scargle (GLS) periodogram of the 19 SOPHIE RV points (top) and the residuals to the circular Keplerian fit (bottom). The highest peak for the observations corresponds to the transiting planet orbital period at 3.45 d. There are also harmonics at integer fractions of this period. Note that these periodogram does not include any information from the photometry. The RV detection alone is significant, above a 1 per cent false alarm propbability (FAP). For reference, we show the 27.8 d rotation period of the host star with a red-dashed line, at which there is no power in the GLS. The GLS periodogram of the residuals shows no significant peak above a 10 per cent FAP.

In Fig. 6 we show a generalized Lomb–Scargle periodogram derived solely from the SOPHIE RVs. The 3.478 d period from the TOI catalogue is denoted by a red-dashed line. This corresponds to the highest peak in the periodogram, demonstrating that the RV signal is produced by the same body that produces the *TESS* transit signals. We note that our spectra are not contaminated by the bound WD, since it is both too faint (19.23 mag compared with 12.08 for the host star) and too far away (13.9 arcsec separation compared with 3 arcsec diameter SOPHIE fibres) to contribute any light.

We then run the YORBIT genetic algorithm, allowing it to fit a single Keplerian model with a period between 3 and 4 d, which is roughly centred on the highest peak of the periodogram. The best-fitting model of the RVs alone has a period of $P_{\rm pl} = 3.42 \pm 0.06$ d, and a best-fitting transit mid-point of 2037.96 ± 0.14 ($\rm BJD_{UTC}$ - 2 457 000), both of which match the *TESS* photometry. The best-fitting model also has an eccentricity of $e_{\rm pl} = 0.178$, which would be surprisingly high for such a short period planet.

To test if the planet signal (and its potential eccentricity) is significant, we calculate the Bayesian information criterion (BIC) by

$$BIC = n \ln\left(\frac{RSS}{n}\right) + k \ln n_{\rm obs}, \quad (2)$$

where k is the number of model parameters, *RSS* is the sum of the squares of the model residuals (in *m/s*) and $n_{\rm obs} = 13$ is the number of observations. We calculate the BIC for a flat line ($k = 1$), the best-fitting eccentric model from YORBIT ($k = 6$) and a forced circular model with the same period ($k = 4$). The flat, eccentric, and circular *BIC* values are 157.8, 136.2, and 133.6, respectively. The circular planet model has the lowest *BIC*, making it the favoured model. For one model to be significantly better than another though, a *BIC* reduction of more than 6 is considered 'strong evidence'. This means that the circular model is not significantly better than the eccentric model, but both are significantly better than the flat model. Otherwise said, the RVs alone provide strong evidence that the planet exists, but we cannot constrain its eccentricity.

3.6 Global modelling of the photometry and radial velocity

We model the combined light curves (*TESS* and ground-based) and RV data using EXOPLANET (Foreman-Mackey et al. 2020). The EXOPLANET software uses STARRY (Luger et al. 2019; Agol, Luger & Foreman-Mackey 2020) to rapidly compute analytical limb darkened light curves, and is also integrated with CELERITE for scalable GP computations. Since the models (and their gradients) within EXOPLANET are analytical, the software is built on the THEANO (Theano Development Team 2016) engine and therefore allows the use of PYMC3 (Salvatier, Wiecki & Fonnesbeck 2016), which offers fast and effective convergence using gradient-based sampling algorithms.

The SAP light curve from *TESS* shows a clear rotational signal of the host star (Fig. 4). While we could take advantage of the rotational signal in our transit modelling, we derive a rotation period in Section 3.2 using the SIP. We therefore opt to use the PDCSAP flux (Smith et al. 2012; Stumpe et al. 2012, 2014; Jenkins et al. 2016). in our transit analysis, which is corrected for spacecraft systematics and the rotation signal since the derived rotation period is on a similar time-scale to a *TESS* sector.

The *TESS* spacecraft fires its thrusters to unload angular momentum from its reaction wheels every few days, which may cause the images obtained in the timestamps to appear disjoint. To make sure the momentum dumps do not affect our further analysis, we identify the times of these events from the Data Quality Flags in the FITS files, and exclude the data obtained within four hours on either side of the thruster events.

We model the out-of-transit variability using GPs. We use the SHOTERM model in `celerite` (Foreman-Mackey et al. 2017; Foreman-Mackey 2018), fixing the quality factor $Q = 1/\sqrt{2}$ so that the covariance function becomes

$$k(\tau) = S_0\,\omega_0\,\exp\left(-\frac{1}{\sqrt{2}}\omega_0\tau\right)\cos\left(\frac{\omega_0\,\tau}{\sqrt{2}} - \frac{\pi}{4}\right).$$

We fit for the natural logarithms of the amplitude and frequency, S_0 and ω_0. Since each *TESS* sector may have systematics on different time-scales and amplitudes, we model each sector and ground-based light curve with individual GPs, and also assign individual flux scaling terms and white noise terms.

We fit the *TESS* and ground-based photometry using our GP model combined with a transit model, as well as a Keplerian model for the RV data. We place Gaussian priors on the stellar mass and radius using values from the SED analysis in Section 3.1, $M_\star = 0.68 \pm 0.08\,\rm M_\odot$, $R_\star = 0.739 \pm 0.031\,\rm R_\odot$. Further, we vary the impact parameter b, as well as the natural logarithms of the period P, mid-transit time T_0, planet radius $R_{\rm pl}$, and planet mass $M_{\rm pl}$. The limb darkening of the star is described by a quadratic formula,

Downloaded from https://academic.oup.com/mnras/article/507/3/4132/6329054 by University of Birmingham user on 24 September 2021

Table 5. Derived parameters from the joint modelling of *TESS* photometric and SOPHIE RV data.

Parameter	Description	Value *circular model (adopted)*	Value *eccentric model*
Derived stellar parameters			
$M_\star$ ($M_\odot$)	Stellar mass[a]	$0.744^{+0.064}_{-0.059}$	$0.743^{+0.066}_{-0.064}$
$R_\star$ ($R_\odot$)	Stellar radius[b]	$0.711^{+0.020}_{-0.019}$	$0.711^{+0.024}_{-0.024}$
$\rho_\star$ (g cm^{-3})	Stellar density	$2.92^{+0.03}_{-0.04}$	$2.91^{+0.26}_{-0.25}$
$\log g_\star$ (cgs)	Stellar surface gravity	$4.605^{+0.013}_{-0.013}$	$4.581^{+0.044}_{-0.045}$
Derived planet parameters			
P (d)	Orbital period	$3.4779780^{+0.0000019}_{-0.0000017}$	$3.4779779^{+0.0000018}_{-0.0000016}$
T_0 (BJD$_{\rm UTC}$ - 2 457 000)	Transit mid-point	$1686.700531^{+0.000097}_{-0.000104}$	$1686.700536^{+0.000099}_{-0.000100}$
$M_{\rm pl}$ ($M_{\rm Jup}$)	Planet mass	$0.441^{+0.049}_{-0.047}$	$0.440^{+0.051}_{-0.047}$
$R_{\rm pl}$ ($R_{\rm Jup}$)	Planet radius	$1.022^{+0.030}_{-0.027}$	$1.021^{+0.034}_{-0.034}$
$\rho_{\rm pl}$ (g cm^{-3})	Planet density	$0.513^{+0.051}_{-0.048}$	$0.513^{+0.071}_{-0.066}$
$\log g_{\rm pl}$ (cgs)	Planet surface gravity	$3.019^{+0.040}_{-0.040}$	$3.019^{+0.050}_{-0.053}$
$M_{\rm pl}/M_\star$	Mass ratio	$0.000567^{+0.000056}_{-0.000055}$	$0.000568^{+0.000052}_{-0.000051}$
$R_{\rm pl}/R_\star$	Planet-to-star radius ratio	$0.14762^{+0.00035}_{-0.00030}$	$0.14764^{+0.00032}_{-0.00031}$
$a/R_\star$	Scaled separation	$12.314^{+0.036}_{-0.056}$	$12.301^{+0.352}_{-0.358}$
$R_\star/a$	Scaled stellar radius	$0.08121^{+0.00037}_{-0.00023}$	$0.08130^{+0.00244}_{-0.00226}$
$R_{\rm pl}/a$	Scaled planet radius	$0.011981^{+0.000077}_{-0.000033}$	$0.012002^{+0.000371}_{-0.000348}$
$T_{\rm eq}$ (K)	Planet equilibrium temperature[c]	963^{+21}_{-21}	963^{+25}_{-25}
b ($R_\star$)	Impact parameter	$0.065^{+0.055}_{-0.044}$	$0.064^{+0.055}_{-0.045}$
$i_{\rm p}$ (°)	Orbital inclination	$89.70^{+0.20}_{-0.26}$	$89.70^{+0.21}_{-0.26}$
a (AU)	Semimajor axis	$0.04070^{+0.00114}_{-0.00110}$	$0.04069^{+0.00116}_{-0.00120}$
D_{T_0}	Transit depth at T_0	$0.026759^{+0.000099}_{-0.000100}$	$0.026756^{+0.000097}_{-0.000095}$
T_{14} (d)	Transit duration between 1$^{\rm st}$ and 4$^{\rm th}$ contacts	$0.10314^{+0.00020}_{-0.00020}$	$0.10313^{+0.00020}_{-0.00019}$
K (m s^{-1})	RV semiamplitude	$72.0^{+6.8}_{-6.4}$	$72.2^{+6.4}_{-6.4}$
e	Eccentricity	0	$0.030^{+0.034}_{-0.022}$
ω (°)	Argument of periastron	–	5^{+132}_{-138}
$\sqrt{e}\cos\omega$	Unit eccentricity parameter	–	$-0.038^{+0.142}_{-0.127}$
$\sqrt{e}\sin\omega$	Unit eccentricity parameter	–	$0.005^{+0.144}_{-0.156}$
$u_{\rm TESS}$	Limb darkening coefficient, *TESS* band	$0.5241^{+0.0066}_{-0.0064}$	$0.5232^{+0.0067}_{-0.0068}$
$v_{\rm TESS}$	Limb darkening coefficient, *TESS* band	$0.088^{+0.016}_{-0.017}$	$0.088^{+0.015}_{-0.015}$
u_R	Limb darkening coefficient, *R* band	$0.5328^{+0.0103}_{-0.0097}$	$0.5333^{+0.0099}_{-0.0098}$
v_R	Limb darkening coefficient, *R* band	$0.171^{+0.020}_{-0.020}$	$0.172^{+0.020}_{-0.020}$
$u_{z'}$	Limb darkening coefficient, z' band	$0.3689^{+0.0102}_{-0.0097}$	$0.3687^{+0.0100}_{-0.0096}$
$v_{z'}$	Limb darkening coefficient, z' band	$0.209^{+0.020}_{-0.020}$	$0.209^{+0.021}_{-0.020}$
$u_{g'}$	Limb darkening coefficient, g' band	$0.8026^{+0.0098}_{-0.0101}$	$0.8024^{+0.0100}_{-0.0098}$
$v_{g'}$	Limb darkening coefficient, g' band	$0.030^{+0.020}_{-0.021}$	$0.029^{+0.021}_{-0.020}$
$u_{\rm white}$	Limb darkening coefficient, white light	$0.6640^{+0.0098}_{-0.0100}$	$0.6627^{+0.0105}_{-0.0104}$
$v_{\rm white}$	Limb darkening coefficient, white light	$0.059^{+0.019}_{-0.019}$	$0.062^{+0.021}_{-0.020}$

Notes. [a]Controlled by Gaussian prior, $\mathcal{N}(0.68, 0.05)$.
[b]Controlled by Gaussian prior, $\mathcal{N}(0.739, 0.031)$.
[c]Assuming zero albedo.

with coefficients and uncertainties within the *TESS*, *R*, z', g', and white light bands determined using PYLDTK (Parviainen & Aigrain 2015) and EXOFAST online tool.[5] PYLDTK and EXOFAST interpolate the Husser et al. (2013) and Claret & Bloemen (2011) atmospheric models, respectively, where we used stellar parameters from Table 3. We vary the limb darkening coefficients with a Gaussian prior centred on the computed values, with standard deviation of 0.01 and 0.02 for c_1 and c_2, respectively. These uncertainties roughly correspond to twice the computed error, which we inflated to account for uncertainties in the stellar atmospheric models. The SOPHIE RV data is further described by the semiamplitude K, eccentricity parameters $\sqrt{e}\cos\omega$ and $\sqrt{e}\sin\omega$, and additional nuisance parameters that model the offset and a white noise term that is added in quadrature to the SOPHIE uncertainties.

We first perform a maximum-likelihood fit, followed by MCMC sampling using the NUTS sampler within PYMC3 to obtain credible

[5]http://astroutils.astronomy.ohio-state.edu/exofast/limbdark.shtml (Eastman, Gaudi & Agol 2013).

Downloaded from https://academic.oup.com/mnras/article/507/3/4132/6329054 by University of Birmingham user on 24 September 2021

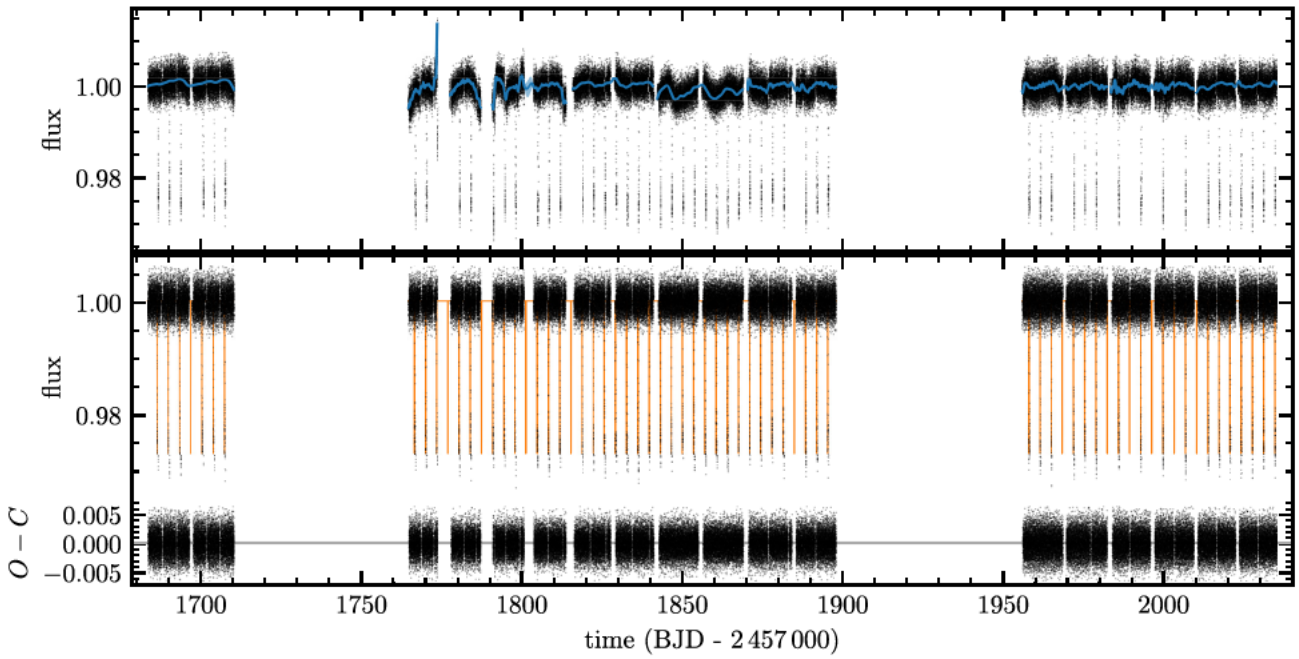


Figure 7. *Upper panel:* Nine sectors of *TESS* PDCSAP photometry of TOI-1259. The blue model is the Gaussian process model. *Middle panel:* The light curve after removing the Gaussian process model, showing transits only, with the transit model overlaid in orange. *Bottom panel:* Residuals from the best-fitting full model.

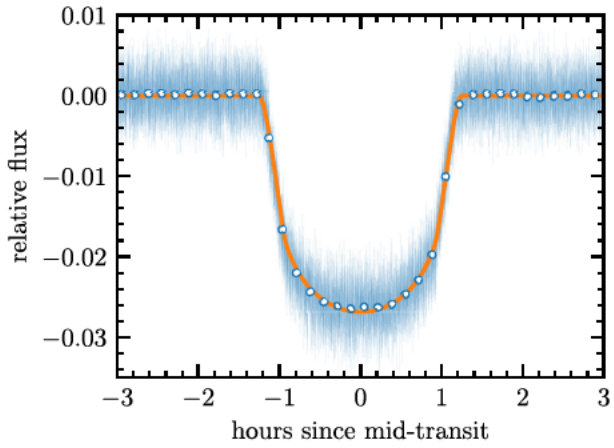


Figure 8. Phase folded and detrended light curve of the primary transit after removing the Gaussian process model. We show the unbinned data in blue, and the data averaged in 10 min bins in blue/white points. The orange line is the best-fitting transit model, with a maximum depth of 2.7 per cent.

intervals on our parameters. We launch two independent chains that are run for 4000 tuning steps and 2000 production steps. We confirmed that the sampler converged by checking the Gelman–Rubin criterion, $\hat{R} < 1.01$, and all parameters have >200 effective samples. We report the values and 15.8 and 84.2 percentiles for the stellar, planet and orbital parameters in Table 5, and similarly for the nuisance parameters in Table A1. The fits to the transit photometry is shown in Figs 7, 8, 9 and the RV fit in Fig. 11. Our RV measurements are all published online.

The combined fit to the *TESS* light curves and SOPHIE RVs reveals that TOI-1259 b is a giant planet with mass $M_{\rm pl} = 0.441^{+0.049}_{-0.047}\,M_{\rm Jup}$, and radius $R_{\rm pl} = 1.022^{+0.030}_{-0.027}\,R_{\rm Jup}$. The RV data constrains the eccentricity to be <0.13 (99 per cent credible interval). Using the approximate tidal circularization time-scale in section 6 of Barker & Ogilvie (2009) with their example tidal parameters, we find that TOI-1259 b might have circularized after ∼2 Gyr, which is shorter than the estimated age of the host star (∼5 Gyr). As in Section 3.5, the eccentricity measurement from our global analysis is not statistically signficant. The BIC prefers a circular model over the eccentric model, with $\Delta{\rm BIC} = {\rm BIC_{circ}} - {\rm BIC_{ecc}} = -23.8$. We therefore adopt the circular model, but report results from both analyses in Table 5.

We visually searched for a secondary eclipse in the binned residuals of the phase-folded *TESS* photometry, shown in Fig. 10. The residuals close to phase 0.5 (where a secondary eclipse would be for a circular orbit) show no signs of a planet occultation. There may be a tentative signal of a ∼100 ppm secondary eclipse at phase ∼0.64. However, this implies an eccentricity of roughly 0.2–0.3. Such high eccentricities are not supported by the current RV data. We estimate the secondary eclipse depth to be 63 ppm, using the simple approximation $\approx 0.5(R_{\rm pl}/a_{\rm pl})^2$, where we assume a geometric albedo of 0.5 and ignore thermal emission. An eclipse of this depth would be consistent with the small dip seen at phase 0.64, but more observations, potentially including those from an extended *TESS* mission, would be needed to confirm that this feature is a secondary eclipse.

4 DISCUSSION

We have confirmed that the *TESS* transiting candidate TOI-1259Ab is a $0.441 M_{\rm Jup}$ transiting exoplanet on a 3.48 d orbit, through our RV and ground-based photometric follow-up. Furthermore, by combining with the existing *Gaia* binaries catalog of El-Badry & Rix (2018), we show that this planet exists in a binary star system, where its primary star is a 0.68 $M_\odot$ K-dwarf and the secondary star is a 0.56 $M_\odot$ WD on a bound orbit. The current projected separation is roughly 1648 au. All of the key parameters of this system are summarized in Table 1.

Downloaded from https://academic.oup.com/mnras/article/507/3/4132/6329054 by University of Birmingham user on 24 September 2021

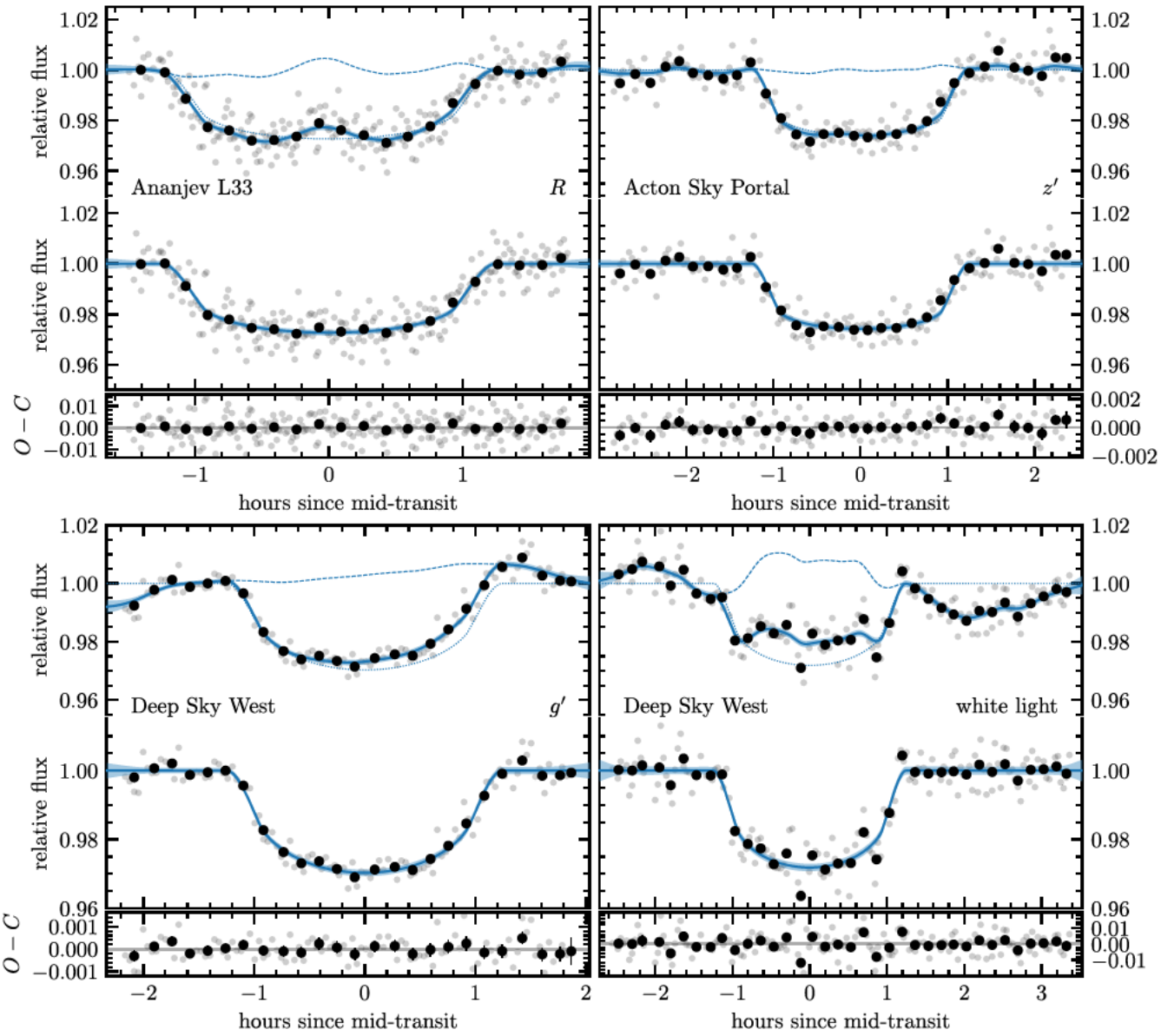


Figure 9. Transit light curves of TOI-1259 b followed up with small (< 50 cm) ground-based telescopes with various filters. For each light curve, we show the raw data in the top panel (*grey*) overlaid with data binned in 10 min intervals (*black*). The best-fitting model is shown as a solid blue line, which consists of a Gaussian process (GP) model (*dashed*) and transit model (*dotted*). The 1σ uncertainty of the GP model is indicated by the shaded region. The middle panels are 'cleaned' light curves after removing the GP model, and the bottom panels are residuals from the best-fitting model.

4.1 Comparison with Mugrauer & Michel (2020)

Mugrauer & Michel (2020) independently characterized the WD companion to TOI-1259. They also concluded that it was a bound companion, and determined a projected separation of roughly 1600 au, which is the same as in El-Badry & Rix (2018). Their derived WD effective temperature of $T_{\rm eff} = 6473^{+672}_{-419}$ K agrees with our calculations of $T_{\rm eff} = 6300^{+80}_{-70}$ K.

4.2 Dynamical history

Wang et al. (2014) determined that the planet frequency in binary systems was lower than that around single stars for binary separations up to 1500 au. Some other studies suggest that the influence of a binary is less far-reaching, with only 100–200 au and tighter binaries affecting planet populations (Kraus et al. 2016; Moe & Kratter 2019; Ziegler et al. 2021). With a mass of 0.56 $M_\odot$ at a distance of about 1600 au, our WD is presently at a separation not predicted to impact planet formation. However, during its main-sequence lifetime, the WD's progenitor would have been both more massive (~1.59 $M_\odot$) and much closer (~900 au, assuming adiabatic mass-loss). At this point secular effects such as Kozai–Lidov (Kozai 1962; Lidov 1962; Mazeh & Shaham 1979) may have been relevant to the planet. Indeed, the Kozai–Lidov effect may have brought the planet to its current orbital configuration, by inducing high-eccentricity tidal migration (Fabrycky & Tremaine 2007; Naoz, Farr & Rasie 2012; Naoz 2016), if the planet started out at a wider orbit, as would be expected for a gas giant. Given the estimated pre-WD age of the system (2 Gyr), a large range of orbital parameters could have led to the observed orbit of the planet TOI-1259Ab. In such a case,

Downloaded from https://academic.oup.com/mnras/article/507/3/4132/6329054 by University of Birmingham user on 24 September 2021

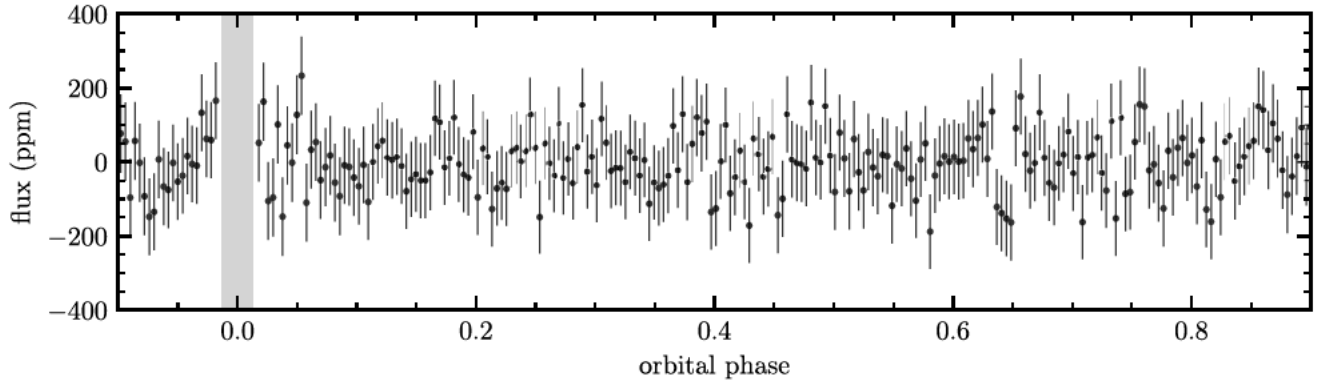


Figure 10. *Top:* The light curve folded on the phase of the planet orbit, with data points binned in 20 min intervals. The grey highlighted area is the transit duration. The expected secondary eclipse depth is 63 ppm, which is comparable to the noise. There is no apparent signal at $\phi = 0.5$, where one could expect a secondary eclipse for a circular orbit. There is a tentative signal centred on $\phi = 0.64$ with a duration that is consistent with a secondary eclipse, however, this implies an eccentricity of roughly 0.2–0.3 that is incompatible with the RV data.

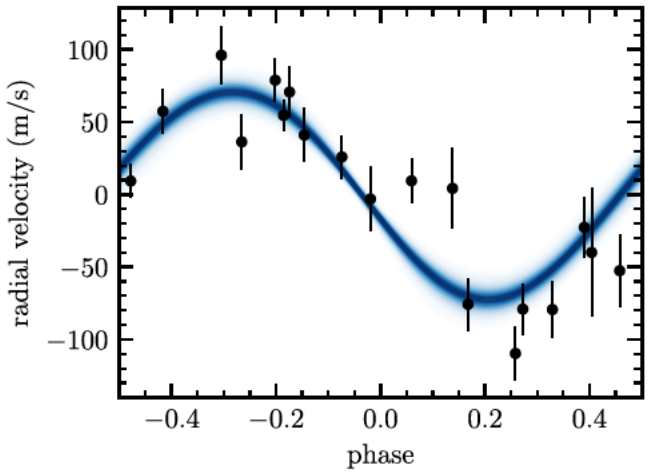


Figure 11. SOPHIE RV (*black*) with the 99th percentile models from a joint fit with the *TESS* photometry encapsulated in the blue region. The RV are indicative of a $0.44 M_{\rm Jup}$ planet, and are in phase with the transits observed by *TESS*.

the companion star evolving into a WD may have also acted as a natural 'shut-off' for such secular effects (Dawson & Johnson 2018).

We also note here that our combined photometry and RV fit favours a circular solution for the planetary orbit. The planet may have had a higher eccentricity (e.g. due to Kozai–Lidov) in the past but with a semimajor axis of only 0.04 au it likely would have been circularized by tidal interactions within the age of the system. Higher precision photometric follow-up that is able to reveal the secondary transit of the planet would most likely be the best means of detecting any potential small but non-zero eccentricity.

Any planets that orbited the WD progenitor may have experienced the opposite effect; the evolution of their host into a WD may have acted to 'turn-on' secular effects (Shappee & Thompson 2013; Stephan et al. 2017; Stephan, Naoz & Gaudi 2018; Stephan, Naoz & Gaudi 2020). This could cause the destruction of its planets. TOI-1259A's WD companion would therefore be a worthwhile target for finding signatures of heavy element pollution by planetary debris. In any case, more detailed studies of the dynamical history of TOI-1259 and of Gliese-86b, which has a WD companion at a projected separation of just 21 au (Queloz et al. 2000; Els et al. 2001; Lagrange et al. 2006), are warranted and will be part of a future work.

4.3 Future spectroscopic characterization of the white dwarf companion

There is a propensity for WDs to have atmospheres contaminated by heavy elements (Debes et al. 2012; Farihi 2016; Wilson et al. 2019), despite an expectation that such elements would quickly settle towards the core due to the high gravity. This has been measured in WDs without any known exoplanet companions, but the pollution itself has been attributed to the accretion of surrounding planetary material. It would be interesting to know if WD such as TOI-1259B, which do have a known associated planet, are more likely to be polluted than 'lonely' WDs. Southworth et al. (2020) most recently tested this for WASP-98,[6] but their spectroscopy of the WD revealed a featureless spectrum and hence no evidence of pollution could be ascertained. It will ultimately be beneficial to conduct such spectroscopy on not only TOI-1259B, but indeed all of the similar systems listed in Table 2.

Follow-up spectroscopy will also hopefully inform us if the atmosphere is hydrogen or helium dominated. Breaking this degeneracy would allow a more accurate constraint on the WD parameters since we could choose the appropriate model from Table 4.

4.4 Future *JWST* observations

Kempton et al. (2018) derived a Transmission Spectroscopy Metric (TSM). It is a means of prioritizing exoplanets for future atmospheric characterization, in particular using the *JWST*, and is proportional to the expected signal-to-noise ratio for the planet's transmission spectrum. Their analytic expression is

$$\mathrm{TSM} = S \times \frac{R_{\rm pl}^3 T_{\rm eq}}{M_{\rm pl} R_\star^2} \times 10^{-m_J/5}, \quad (3)$$

where m_J is the magnitude of the host star in the J band and S is a an empirical scale factor derived by Kempton et al. (2018) to make their simple analytic expression match the more detailed simulations of Louie et al. (2018). The factor S depends on the radius of the

[6] A similar configuration to TOI-1259, but with a wider binary separated by ∼3500 au.

Downloaded from https://academic.oup.com/mnras/article/507/3/4132/6329054 by University of Birmingham user on 24 September 2021

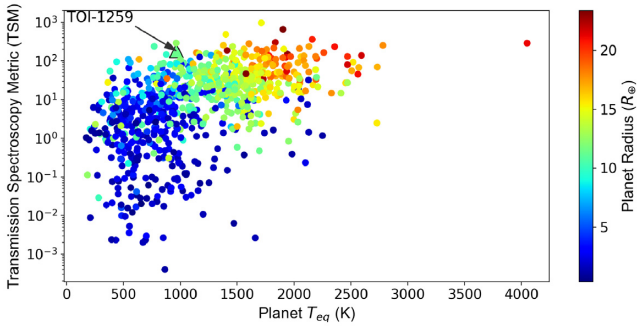


Figure 12. Transit Spectroscopy Metric (TSM) from Kempton et al. (2018) for all confirmed transiting exoplanets as a function of their equilibrium temperature (where such a value has been calculated). The TSM is calculated using equation (3). The colour scale is the planet radius. TOI-1259Ab has a TSM of 180, making it ideal for atmospheric follow-up. In particular, it has one of the highest TSM values for a planet cooler than 1000 K and of Jupiter-size or less.

transiting planet: $S = 0.19$ for $R_{\rm pl} < 1.5R_\oplus$; $S = 1.26$ for $1.5 < R_{\rm pl} < 2.75R_\oplus$; $S = 1.28$ for $2.75 < R_{\rm lp} < 4.0R_\oplus$ and $S = 1.15$ for $R_{\rm pl} > 4.0R_\oplus$.[7]

For TOI-1259Ab we calculate a value of TSM =180, which places it in the top 3 per cent of all confirmed transiting exoplanets. We demonstrate this in Fig. 12. TOI-1259Ab has a scaled separation $a/R_\star = 12.314^{+0.036}_{-0.056}$ and an equilibrium temperature $T_{\rm eq} = 963 \pm 21$ K. Most of the planets with a higher TSM value are hotter and larger. There are only two objects cooler than 1000 K with a higher TSM: WASP-69b and WASP-107b. These two planets have already received considerable attention with respect to their atmospheres. WASP-69b (Anderson et al. 2014) has a confirmed presence of helium in its atmosphere from ground-based observations (Nortmann et al. 2018). WASP-107b (Anderson et al. 2017) is a so-called 'super-puff', based on a $0.12M_{\rm Jup}$ mass and a $0.94R_{\rm Jup}$ radius, and *Hubble Space Telescope* observations have revealed the presence of both helium (Spake et al. 2018) and water (Kreidberg et al. 2018).

With an ecliptic latitude of 76.878°, TOI-1259Ab is near the *JWST* continuous viewing zone and is observable for typically 227 d per year, which will assist future atmospheric characterization.

ACKNOWLEDGEMENTS

This project began at the Expanding the Science of *TESS* meeting, which took place in 2020 February the University of Sydney, back when meeting people in large groups was still a thing. The RV observations were partly conducted while OHP was in 'remote observing' mode, a special mode produced as a response the unique COVID-19 situation. We are extremely grateful for the dedication of the staff at OHP that allowed observations to resume. We thank Markus Mugrauer for looking at a draft version of this paper. Finally, we thank a referee for providing a thorough review that undoubtedly improved the quality of the paper.

The observations were obtained under an OHP DDT programme (PI Triaud). This work was in part funded by the U.S.–Norway Fulbright Foundation and a NASA *TESS* GI grant G022253 (PI: Martin). DVM received funding from the Swiss National Science Foundation (grant P 400P2 186735). AHMJT received funding from the European Research Council (ERC) under the European Union's Horizon 2020 research and innovation programme (grant 803193/BEBOP). VKH is also supported by a Birmingham Doctoral Scholarship, and by a studentship from Birmingham's School of Physics & Astronomy. SG has been supported by STFC through consolidated grants ST/L000733/1 and ST/P000495/1. SJM was supported by the Australian Research Council through DECRA DE180101104. VK has been supported by the Ministry of science and Higher Education of the Russian Federation , topic № FEUZ-2020-0038.

We acknowledge the use of public *TESS* Alert data from pipelines at the *TESS* Science Office and at the *TESS* SPOC. Some of the data presented in this paper were obtained from the Mikulski Archive for Space Telescopes (MAST). Resources supporting this work were provided by the NASA High-End Computing (HEC) Program through the NASA Advanced Supercomputing (NAS) Division at Ames Research Center for the production of the SPOC data products.

This research has used `AstroPy`,[8] a community-developed core PYTHON package for Astronomy (Astropy Collaboration 2013, 2018).

Based in part on observations made at Observatoire de Haute Provence (CNRS), France.

DATA AVAILABILITY

All *TESS* data are publicaly available and can be downloaded using LIGHTKURVE (Lightkurve Collaboration 2018) or other tools. The SOPHIE RVs are published as supplementary data. Any other data/models in this article will be shared on reasonable request to the corresponding author.

REFERENCES

Agol E., Luger R., Foreman-Mackey D., 2020, AJ, 159, 123
Alonso R. et al., 2021, A&A, 649, A131
Althaus L. G., Benvenuto O. G., 1998, MNRAS, 296, 206
Anderson D. R. et al., 2014, MNRAS, 445, 1114
Anderson D. R. et al., 2017, A&A, 604, A110
Angus R. et al , 2019, AJ, 158, 173
Angus R. et al , 2020, AJ, 160, 90
Angus R., Foreman-Mackey D., Johnson J. A., 2016, ApJ, 818, 109
Astropy Collaboration, 2013, A&A, 558, A33
Astropy Collaboration, 2018, AJ, 156, 123
Barker A. J., Ogilvie G. I., 2009, MNRAS, 395, 2268
Barnes S. A., 2003, ApJ, 586, 464
Bear E., Soker N., 2014, MNRAS, 444, 1698
Bergeron P., Wesemael F., Beauchamp A., 1995, PASP, 107, 1047
Bonsor A., Veras D., 2015, MNRAS, 454, 53
Bouchy F. et al., 2009, A&A, 505, 853
Bressan A., Marigo P., Girardi L., Salasnich B., Dal Cero C., Rubele S., Nanni A., 2012, MNRAS, 427, 127
Butler R. P. et al., 2006, ApJ, 646, 505
Butler R. P., Tinney C. G., Marcy G. W., Jones H. R. A., Penny A. J., Apps K., 2001, ApJ, 555, 410
Chauvin G., Lagrange A.-M., Udry S., Fusco T., Galland F., Naef D., Beuzit J.-L., Mayor M., 2006, A&A, 456, 1165
Cheetham A. C., Kraus A. L., Ireland M. J., Cieza L., Rizzuto A. C., Tuthill P. G., 2015, ApJ, 813, 83
Choi J., Dotter A., Conroy C., Cantiello M., Paxton B., Johnson B. D., 2016, ApJ, 823, 102

[7]Whilst we use this final scale factor for all planets above $4R_\oplus$, Kempton et al. (2018) only define it for 4 to $10R_\oplus$ and do not give a scale factor for larger planets.

[8]http://www.astropy.org

Downloaded from https://academic.oup.com/mnras/article/507/3/4132/6329054 by University of Birmingham user on 24 September 2021

Claret A., Bloemen S., 2011, A&A, 529, A75
Curtis J. L., Agüeros M. A., Douglas S. T., Meibom S., 2019, ApJ, 879, 49
Daemgen S., Bonavita M., Jayawardhana R., Lafrenière D., Janson M., 2015, ApJ, 799, 155
Dawson R. I., Johnson J. A., 2018, ARA&A, 56, 175
De Gennaro S., von Hippel T., Winget D. E., Kepler S. O., Nitta A., Koester D., Althaus L., 2008, AJ, 135, 1
Debes J. H., Walsh K. J., Stark C., 2012, ApJ, 747, 148
Desidera S. et al., 2014, A&A, 567, L6
Dotter A., 2016, ApJS, 222, 8
Duquennoy A., Mayor M., 1991, A&A, 500, 337
Dvorak R., 1984, Celest. Mech., 34, 369
Eastman J. D. et al., 2019, preprint (arXiv:1907.09480)
Eastman J., Gaudi B. S., Agol E., 2013, PASP, 125, 83
Eggleton P. P., Kisseleva-Eggleton L., 2006, Ap&SS, 304, 75
El-Badry K., Rix H.-W., 2018, MNRAS, 480, 4884
El-Badry K., Rix H.-W., Tian H., Duchêne G., Moe M., 2019, MNRAS, 489, 5822
El-Badry K., Rix H.-W., Weisz D. R., 2018, ApJ, 860, L17
Els S. G., Sterzik M. F., Marchis F., Pantin E., Endl M., Kürster M., 2001, A&A, 370, L1
Fabrycky D., Tremaine S., 2007, ApJ, 669, 1298
Faedi F., West R. G., Burleigh M. R., Goad M. R., Hebb L., 2010, MNRAS, 410, 899
Farihi J., 2016, New Astron. Rev., 71, 9
Farmer A. J., Agol E., 2003, ApJ, 592, 1151
Foreman-Mackey D., 2018, Res. Notes Am. Astron. Soc., 2, 31
Foreman-Mackey D., Agol E., Ambikasaran S., Angus R., 2017, AJ, 154, 220
Foreman-Mackey D., Luger R., Czekala I., Agol E., Price-Whelan A., Brandt T. D., Barclay T., Bouma L., 2020, exoplanet-dev/exoplanet v0.4.0.
Gänsicke B. T., Schreiber M. R., Toloza O., Gentile Fusillo N. P., Koester D., Manser C. J., 2019, Nature, 576, 61
Green G. M., Schlafly E., Zucker C., Speagle J. S., Finkbeiner D., 2019, ApJ, 887, 93
Guidry J. A. et al., 2020, ApJ, 912, 125
Hamers A. S., Perets H. B., Portegies Zwart S. F., 2016, MNRAS, 455, 3180
Hartman Z. D., Lépine S., 2020, ApJS, 247, 66
Hayden M. R. et al., 2015, ApJ, 808, 132
Hedges C., Angus R., Barentsen G., Saunders N., Montet B. T., Gully-Santiago M., 2020, Res. Notes AAS, 4, 220
Hellier C. et al., 2014, MNRAS, 440, 1982
Holberg J. B., Bergeron P., 2006, AJ, 132, 1221
Holman M. J., Wiegert P. A., 1999, AJ, 117, 621
Husser T.-O., Wende-von Berg S., Dreizler S., Homeier D., Reiners A., Barman T., Hauschildt P. H., 2013, A&A, 553, A6
Jenkins J. M. et al., 2016, in Proc. SPIE Conf. Ser., Vol. 99133, Software and Cyberinfrastructure for Astronomy IV. SPIE, Bellingham, p. 99133E
Jeong G., Han I., Park M.-G., Hatzes A. P., Bang T.-Y., Gu S., Bai J., Lee B.-C., 2018, AJ, 156, 64
Jørgensen B. R., Lindegren L., 2005, A&A, 436, 127
Kempton E. M.-R. et al., 2018, PASP, 130, 114401
Kozai Y., 1962, AJ, 67, 591
Kratter K. M., Perets H. B., 2012, ApJ, 753, 91
Kraus A. L., Ireland M. J., Hillenbrand L. A., Martinache F., 2012, ApJ, 745, 19
Kraus A. L., Ireland M. J., Huber D., Mann A. W., Dupuy T. J., 2016, AJ, 152, 8
Kreidberg L., Line M. R., Thorngren D., Morley C. V., Stevenson K. B., 2018, ApJ, 858, L6
Kurucz R. L., 1979, ApJS, 40, 1
Lagrange A. -M., Beust H.,Udry S.,Chauvin G.,Mayor M.,2006, A&A, 459, 955
Lépine S., Bongiorno B., 2007, AJ, 133, 889
Lidov M. L., 1962, Planet. Space Sci., 9, 719
Lightkurve Collaboration, 2018, Astrophysics Source Code Library, record ascl: 1812.013
Louie D. R., Deming D., Albert L., Bouma L. G., Bean J., Lopez-Morales M., 2018, PASP, 130, 044401
Lourens A., 1969, Mon. Notes Astron. Soc. South. Afr., 28, 95
Luger R., Agol E., Foreman-Mackey D., Fleming D. P., Lustig-Yaeger J., Deitrick R., 2019, AJ, 157, 64
Manser C. J. et al., 2019, Science, 364, 66
Mardling R. A., Aarseth S. J., 2001, MNRAS, 321, 398
Maxted P. F. L., Marsh T. R., Moran C. K. J., 2000, MNRAS, 319, 305
Mayor M., Udry S., Naef D., Pepe F., Queloz D., Santos N. C., Burnet M., 2004, A&A, 415, 391
Mazeh T., Shaham J., 1979, A&A, 77, 145
Moe M., Kratter K. M., 2019, preprint (arXiv:1912.01699)
Montgomery M. H., Klumpe E. W., Winget D. E., Wood M. A., 1999, ApJ, 525, 482
Morton T. D., Bryson S. T., Coughlin J. L., Rowe J. F., Ravichandran G., Petigura E. A., Haas M. R., Batalha N. M., 2016, ApJ, 822, 86
Mugrauer M., 2019, MNRAS, 490, 5088
Mugrauer M., Dinçel B., 2016, Astron. Nachr., 337, 627
Mugrauer M., Michel K. U., 2020, Astron. Nachr., 341, 996
Mugrauer M., Neuhäuser R., Mazeh T., 2007, A&A, 469, 755
Naef D. et al., 2010, A&A, 523, A15
Naoz S., 2016, ARA&A, 54, 441
Naoz S., Farr W. M., Rasie F. A., 2012, ApJ, 754, L36
Neveu-VanMalle M. et al., 2014, A&A, 572, A49
Nortmann L. et al., 2018, Science, 362, 1388
Parviainen H., Aigrain S., 2015, MNRAS, 453, 3821
Perruchot S. et al., 2008, in Proc. SPIE Conf. Ser. Vol. 7014, Ground-based and Airborne Instrumentation for Astronomy II. SPIE, Bellingham, p. 70140J
Qian S.-B., Dai Z.-B., Liao W.-P., Zhu L.-Y., Liu L., Zhao E. G., 2009, ApJ, 706, L96
Queloz D. et al., 2000, A&A, 354, 99
Reid I. N., 1996, AJ, 111, 2000
Salvatier J., Wiecki T. V., Fonnesbeck C., 2016, PeerJ. Comput. Sci., 2, e55
Schlegel D. J., Finkbeiner D. P., Davis M., 1998, ApJ, 500, 525
Ségransan D. et al., 2010, A&A, 511, A45
Shappee B. J., Thompson T. A., 2013, ApJ, 766, 64
Silvotti R., Sozzetti A., Lattanzi M., Morbidelli R., 2014, Detectability of Substellar Companions Around White Dwarfs with Gaia. preprint (arXiv:1412.3307)
Smith J. C. et al., 2012, PASP, 124, 1000
Southworth J., Tremblay P.-E., Gänsicke B. T., Evans D., Močnik T., 2020, MNRAS, 497, 4416
Spada F., Lanzafame A. C., 2020, A&A, 636, A76
Spake J. J. et al., 2018, Nature, 557, 68
Stassun K. G., Collins K. A., Gaudi B. S., 2017, AJ, 153, 136
Stassun K. G., Corsaro E., Pepper J. A., Gaudi B. S., 2018, AJ, 155, 22
Stassun K. G., Torres G., 2016, AJ, 152, 180
Stassun K. G., Torres G., 2018, ApJ, 862, 61
Stein N. M., van Dyk D. A., von Hippel T., DeGennaro S., Jeffery E. J., Jefferys W. H., 2013, Stat. Anal. Data Mining: ASA Data Sci. J., 9, 34
Stenning D. C., Wagner-Kaiser R., Robinson E., van Dyk D. A., von Hippel T., Sarajedini A., Stein N., 2016, ApJ, 826, 41
Stephan A. P., Naoz S., Gaudi B. S., 2018, AJ, 156, 128
Stephan A. P., Naoz S., Gaudi B. S., 2020, Giant Planets, Tiny Stars: Producing Short-Period Planets around White Dwarfs with the Eccentric Kozai-Lidov Mechanism. preprint (arXiv:2010.10534)
Stephan A. P., Naoz S., Gaudi B. S., Salas J. M., 2020, ApJ, 889, 45
Stephan A. P., Naoz S., Zuckerman B., 2017, ApJ, 844, L16
Stumpe M. C. et al., 2012, PASP, 124, 985
Stumpe M. C., Smith J. C., Catanzarite J. H., Van Cleve J. E., Jenkins J. M., Twicken J. D., Girouard F. R., 2014, PASP, 126, 100
Theano Development Team, 2016, preprint (abs/1605.02688)
Thébault P., Marzari F., Scholl H., 2008, MNRAS, 388, 1528
Tian H.-J., El-Badry K., Rix H.-W., Gould A., 2020, ApJS, 246, 4
Tokovinin A., 2014, AJ, 147, 87
Torres G., Andersen J., Giménez A., 2010, A&AR, 18, 67
Vanderbosch Z. et al., 2020, ApJ, 897, 171

Downloaded from https://academic.oup.com/mnras/article/507/3/4132/6329054 by University of Birmingham user on 24 September 2021

Vanderburg A. et al., 2015, ApJ, 800, 59
Vanderburg A. et al., 2015, Nature, 526, 546
Vanderburg A. et al., 2020, Nature, 585, 363
Veras D., Mustill A. J., Bonsor A., Wyatt M. C., 2013, MNRAS, 431, 1686
Veras D., Wyatt M. C., Mustill A. J., Bonsor A., Eldridge J. J., 2011, MNRAS, 417, 2104
von Hippel T., Jefferys W. H., Scott J., Stein N., Winget D. E., De Gennaro S., Dam A., Jeffery E., 2006, ApJ, 645, 1436
Wang J., Fischer D. A., Xie J.-W., Ciardi D. R., 2014, ApJ, 791, 111
Williams K. A., Bolte M., Koester D., 2009, ApJ, 693, 355
Wilson T. G., Farihi J., Gänsicke B. T., Swan A., 2019, MNRAS, 487, 133
Wittenmyer R. A., Horner J., Marshall J. P., 2013, MNRAS, 431, 2150
Xie J.-W., Zhou J.-L., Ge J., 2009, ApJ, 708, 1566
Ziegler C., Tokovinin A., Latiolais M., Briceno C., Law N., Mann A. W., 2021, preprint (arXiv:2103.12076)
Zorotovic M., Schreiber M. R., 2013, A&A, 549, A95

SUPPORTING INFORMATION

Supplementary data are available at *MNRAS* online.

TOI-1259_OHP.rdb

Please note: Oxford University Press is not responsible for the content or functionality of any supporting materials supplied by the authors. Any queries (other than missing material) should be directed to the corresponding author for the article.

APPENDIX A: NUISANCE PARAMETERS FROM THE GLOBAL ANALYSIS

Table A1. Fitted Gaussian process (GP) and radial velocity nuisance parameters from the joint modelling of the photometric and radial velocity data. Only the parameters for the circular orbital model are given, as the differences from the eccentric model are negligible.

Parameter	Description	Value	Prior
Sector 14			
$\log S_0\omega_0^4$	GP amplitude	$-15.77^{+0.59}_{-0.51}$	$\mathcal{N}(\log \mathrm{var(flux)}, 5^2)$
$\log \omega_0$ (s^{-1})	GP frequency	$-0.90^{+0.56}_{-1.20}$	$\mathcal{N}(\log 2\pi/5, 5^2)$
$\log \sigma^2$	White noise term	$-24.52^{+3.16}_{-5.73}$	$\mathcal{N}(\log \mathrm{var(flux)}, 10^2)$
$\mathcal{F}$	Flux scaling factor	$0.99949^{+0.00053}_{-0.00446}$	$\mathcal{N}(\mathrm{median(flux)}, 5^2)$
Sector 17			
$\log S_0\omega_0^4$	GP amplitude	$-8.71^{+0.28}_{-0.27}$	$\mathcal{N}(\log \mathrm{var(flux)}, 5^2)$
$\log \omega_0$ (s^{-1})	GP frequency	$0.28^{+0.32}_{-0.38}$	$\mathcal{N}(\log 2\pi/5, 5^2)$
$\log \sigma^2$	White noise term	$-24.52^{+3.29}_{-5.28}$	$\mathcal{N}(\log \mathrm{var(flux)}, 10^2)$
$\mathcal{F}$	Flux scaling factor	$1.00051^{+0.00206}_{-0.00247}$	$\mathcal{N}(\mathrm{median(flux)}, 5^2)$
Sector 18			
$\log S_0\omega_0^4$	GP amplitude	$-10.19^{+0.33}_{-0.31}$	$\mathcal{N}(\log \mathrm{var(flux)}, 5^2)$
$\log \omega_0$ (s^{-1})	GP frequency	$0.75^{+0.16}_{-0.17}$	$\mathcal{N}(\log 2\pi/5, 5^2)$
$\log \sigma^2$	White noise term	$-24.86^{+3.47}_{-6.10}$	$\mathcal{N}(\log \mathrm{var(flux)}, 10^2)$
$\mathcal{F}$	Flux scaling factor	$0.99975^{+0.00041}_{-0.00044}$	$\mathcal{N}(\mathrm{median(flux)}, 5^2)$
Sector 19			
$\log S_0\omega_0^4$	GP amplitude	$-14.68^{+0.50}_{-0.52}$	$\mathcal{N}(\log \mathrm{var(flux)}, 5^2)$
$\log \omega_0$ (s^{-1})	GP frequency	$-0.01^{+0.25}_{-0.29}$	$\mathcal{N}(\log 2\pi/5, 5^2)$
$\log \sigma^2$	White noise term	$-24.74^{+3.25}_{-5.49}$	$\mathcal{N}(\log \mathrm{var(flux)}, 10^2)$
$\mathcal{F}$	Flux scaling factor	$1.00004^{+0.00019}_{-0.00019}$	$\mathcal{N}(\mathrm{median(flux)}, 5^2)$
Sector 20			
$\log S_0\omega_0^4$	GP amplitude	$-14.21^{+0.39}_{-0.37}$	$\mathcal{N}(\log \mathrm{var(flux)}, 5^2)$
$\log \omega_0$ (s^{-1})	GP frequency	$-0.37^{+0.24}_{-0.35}$	$\mathcal{N}(\log 2\pi/5, 5^2)$
$\log \sigma^2$	White noise term	$-24.89^{+3.19}_{-5.37}$	$\mathcal{N}(\log \mathrm{var(flux)}, 10^2)$
$\mathcal{F}$	Flux scaling factor	$0.99995^{+0.00044}_{-0.00061}$	$\mathcal{N}(\mathrm{median(flux)}, 5^2)$
Sector 21			
$\log S_0\omega_0^4$	GP amplitude	$-11.36^{+0.38}_{-0.40}$	$\mathcal{N}(\log \mathrm{var(flux)}, 5^2)$
$\log \omega_0$ (s^{-1})	GP frequency	$1.04^{+0.15}_{-0.16}$	$\mathcal{N}(\log 2\pi/5, 5^2)$
$\log \sigma^2$	White noise term	$-24.77^{+3.13}_{-5.82}$	$\mathcal{N}(\log \mathrm{var(flux)}, 10^2)$
$\mathcal{F}$	Flux scaling factor	$1.00006^{+0.00012}_{-0.00013}$	$\mathcal{N}(\mathrm{median(flux)}, 5^2)$
Sector 24			
$\log S_0\omega_0^4$	GP amplitude	$-11.28^{+0.42}_{-0.44}$	$\mathcal{N}(\log \mathrm{var(flux)}, 5^2)$
$\log \omega_0$ (s^{-1})	GP frequency	$1.14^{+0.16}_{-0.17}$	$\mathcal{N}(\log 2\pi/5, 5^2)$
$\log \sigma^2$	White noise term	$-24.71^{+3.26}_{-5.39}$	$\mathcal{N}(\log \mathrm{var(flux)}, 10^2)$
$\mathcal{F}$	Flux scaling factor	$1.00007^{+0.00010}_{-0.00011}$	$\mathcal{N}(\mathrm{median(flux)}, 5^2)$

Downloaded from https://academic.oup.com/mnras/article/507/3/4132/6329054 by University of Birmingham user on 24 September 2021

Table A1 *– continued*

Parameter	Description	Value	Prior
Sector 25			
$\log S_0\omega_0^4$	GP amplitude	$-9.83^{+0.34}_{-0.32}$	$\mathcal{N}(\log \mathrm{var(flux)}, 5^2)$
$\log \omega_0$ (s^{-1})	GP frequency	$1.51^{+0.13}_{-0.13}$	$\mathcal{N}(\log 2\pi/5, 5^2)$
$\log \sigma^2$	White noise term	$-24.64^{+3.34}_{-5.93}$	$\mathcal{N}(\log \mathrm{var(flux)}, 10^2)$
$\mathcal{F}$	Flux scaling factor	$1.00006^{+0.00010}_{-0.00010}$	$\mathcal{N}(\mathrm{median(flux)}, 5^2)$
Sector 26			
$\log S_0\omega_0^4$	GP amplitude	$-13.37^{+0.63}_{-0.61}$	$\mathcal{N}(\log \mathrm{var(flux)}, 5^2)$
$\log \omega_0$ (s^{-1})	GP frequency	$0.44^{+0.24}_{-0.28}$	$\mathcal{N}(\log 2\pi/5, 5^2)$
$\log \sigma^2$	White noise term	$-24.67^{+3.33}_{-5.35}$	$\mathcal{N}(\log \mathrm{var(flux)}, 10^2)$
$\mathcal{F}$	Flux scaling factor	$1.00005^{+0.00015}_{-0.00015}$	$\mathcal{N}(\mathrm{median(flux)}, 5^2)$
R band			
$\log S_0\omega_0^4$	GP amplitude	$2.87^{+1.82}_{-2.48}$	$\mathcal{N}(-1, 10^2)$
$\log \omega_0$ (s^{-1})	GP frequency	$5.10^{+2.29}_{-0.57}$	$\mathcal{N}(\log 2\pi/0.04, 10^2)$
$\log \sigma^2$	White noise term	$-10.98^{+0.25}_{-0.29}$	$\mathcal{N}(\log \mathrm{var(flux)}, 10^2)$
$\mathcal{F}$	Flux scaling factor	$0.89563^{+0.00080}_{-0.00069}$	$\mathcal{N}(\mathrm{median(flux)}, 5^2)$
z' *band*			
$\log S_0\omega_0^4$	GP amplitude	$-8.89^{+8.50}_{-3.46}$	$\mathcal{N}(-1, 10^2)$
$\log \omega_0$ (s^{-1})	GP frequency	$2.34^{+10.24}_{-2.53}$	$\mathcal{N}(\log 2\pi/0.04, 10^2)$
$\log \sigma^2$	White noise term	$-18.14^{+4.86}_{-7.64}$	$\mathcal{N}(\log \mathrm{var(flux)}, 10^2)$
$\mathcal{F}$	Flux scaling factor	$0.14724^{+0.00132}_{-0.00026}$	$\mathcal{N}(\mathrm{median(flux)}, 5^2)$
g' *band*			
$\log S_0\omega_0^4$	GP amplitude	$-3.14^{+1.27}_{-1.23}$	$\mathcal{N}(-1, 10^2)$
$\log \omega_0$ (s^{-1})	GP frequency	$2.84^{+0.93}_{-1.20}$	$\mathcal{N}(\log 2\pi/0.04, 10^2)$
$\log \sigma^2$	White noise term	$-19.04^{+4.66}_{-7.50}$	$\mathcal{N}(\log \mathrm{var(flux)}, 10^2)$
$\mathcal{F}$	Flux scaling factor	$0.16291^{+0.00197}_{-0.00266}$	$\mathcal{N}(\mathrm{median(flux)}, 5^2)$
White light			
$\log S_0\omega_0^4$	GP amplitude	$3.10^{+1.11}_{-1.03}$	$\mathcal{N}(-1, 10^2)$
$\log \omega_0$ (s^{-1})	GP frequency	$3.97^{+0.42}_{-0.48}$	$\mathcal{N}(\log 2\pi/0.04, 10^2)$
$\log \sigma^2$	White noise term	$-10.90^{+0.21}_{-0.21}$	$\mathcal{N}(\log \mathrm{var(flux)}, 10^2)$
$\mathcal{F}$	Flux scaling factor	$1.36259^{+0.00500}_{-0.00481}$	$\mathcal{N}(\mathrm{median(flux)}, 5^2)$
SOPHIE			
$\log \sigma$ ($\mathrm{km\,s}^{-1}$)	White noise term	$-5.44^{+1.34}_{-4.40}$	$\mathcal{N}(\log \mathrm{median(RV)}, 5^2)$
γ ($\mathrm{km\,s}^{-1}$)	Systemic velocity	$-40.8197^{+0.0046}_{-0.0047}$	$\mathcal{N}(\mathrm{median(RV)}, 0.5^2)$

[1]*Department of Astronomy, The Ohio State University, Columbus, OH 43210, USA*
[2]*Department of Astronomy and Theoretical Astrophysics Center, University of California Berkley, Berkley, CA 94720, USA*
[3]*School of Physics and Astronomy, University of Birmingham, Edgbaston, Birmingham B15 2TT, UK*
[4]*American Museum of National History, New York, NY 10024, USA*
[5]*Center for Computational Astrophysics, Flatiron Institute, New York, NY 10010, USA*
[6]*Department of Astronomy, University of Washington, Seattle, WA 98105, USA*
[7]*Bay Area Environmental Research Institute, PO Box 25, Moffett Field, CA, USA*
[8]*NASA Ames Research Center, MS 244-30, Moffett Field, CA 94035, USA*
[9]*School of Physics, University of New South Wales, Sydney, NSW 2052, Australia*
[10]*Sydney Institute for Astronomy (SIfA), School of Physics, University of Sydney, NSW 2006, Australia*
[11]*CNRS, CNES, LAM, Aix Marseille Univ, Marseille, 13388, France*
[12]*Department of Physics & Astronomy, Vanderbilt University, Nashville, TN 37235, USA*
[13]*Center for Cosmology and AstroParticle Physics, The Ohio State University, Columbus, OH 43210, USA*
[14]*Acton Sky Portal Private Observatory , Acton, MA 01720, USA*
[15]*Laboratory of Astrochemical Research, Ural Federal University, Ekaterinburg, Russia, ul. Mira d. 19, Yekaterinburg 620002, Russia*
[16]*Astronomical department, Ural Federal University , Yekaterinburg 620002, Russia*
[17]*Private Astronomical Observatory, Ananjev, Odessa Region UA-66400, Ukraine*
[18]*Department of Physics, Engineering and Astronomy, Stephen F. Austin State University, TX 75962, USA*
[19]*Oukaimeden Observatory, High Energy Physics and Astrophysics Laboratory, Cadi Ayyad University, Marrakech, 644M+C9G, Oukaimeden, Morocco*
[20]*Astrophysics Group, Keele University, Keele, Staffordshire ST5 5BG, UK*
[21]*Centre for Exoplanets and Habitability, University of Warwick, Gibbet Hill Road, Coventry CV4 7AL, UK*
[22]*SETI Institute, 189 Bernardo Ave, Suite 200, Mountain View, CA 94043, USA*
[23]*Department of Physics and Kavli Institute for Astrophysics and Space Research, Massachusetts Institute of Technology, Cambridge, MA 02139, USA*

Downloaded from https://academic.oup.com/mnras/article/507/3/4132/6329054 by University of Birmingham user on 24 September 2021

[24]*Harvard-Smithsonian Center for Astrophysics, 60 Garden St, Cambridge, MA 02138, USA*
[25]*Proto-Logic LLC, 1718 Euclid Street NW, Washington, DC 20009, USA*
[26]*Space Telescope Science Institute, 3700 San Martin Drive, Baltimore, MD 21218, USA*
[27]*Department of Earth, Atmospheric and Planetary Sciences, Massachusetts Institute of Technology, Cambridge, MA 02139, USA*
[28]*Department of Aeronautics and Astronautics, Massachusetts Institute of Technology, Cambridge, MA 02139, USA*
[29]*Department of Astronomy, The University of Wisconsin-Madison, Madison, WI 53706, USA*
[30]*Department of Astrophysical Sciences, 4 Ivy Lane, Princeton University, Princeton, NJ 08544, USA*

This paper has been typeset from a TEX/LATEX file prepared by the author.

Downloaded from https://academic.oup.com/mnras/article/507/3/4132/6329054 by University of Birmingham user on 24 September 2021

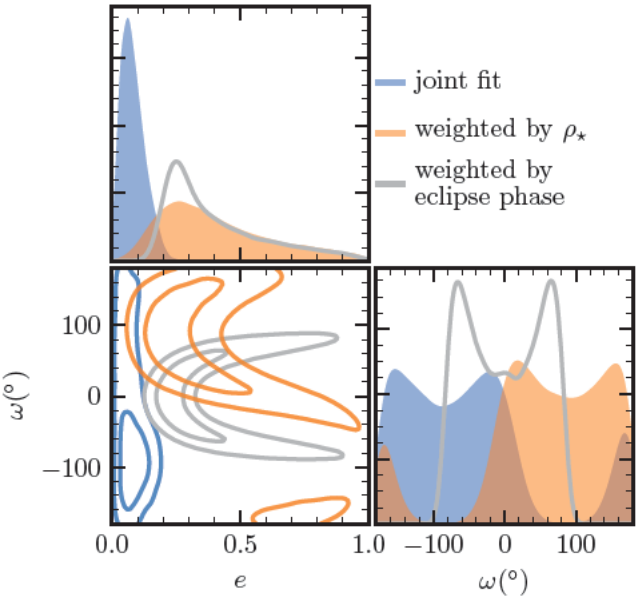


Figure 3.22: Posteriors for the e and ω using constraints from various sources. *Blue:* Constrained by the radial velocity data (joint fit with photometry). *Orange:* Constraint from comparing the stellar density derived from two different sources. *Gray:* Constraint from approximate location and duration of the candidate secondary eclipse in Figure 11 (Section 3.3.5).

3.3.6 Additional analysis

During my work on TOI-1259 Ab I spent a bit of time studying the "blip" at orbital phase $\phi = 0.64$ shown in Figure 11 of the paper (Section 3.3.5). I wondered whether this was due to a secondary eclipse, in which case the planet would be eccentric since it is offset from $\phi = 0.5$ (recall Chapter 2.1.3). To investigate this further I compared the stellar density constraints I got from the transit modelling with that listed in the Tess Input Catalog (TIC, Stassun et al. 2018) using the method outlined in Dawson & Johnson (2012). The basic principle of the method is that the first-order effect of eccentricity on a transit light curve is a change to its duration, which measures the stellar density (Equation 2.8). The stellar density measured from the transit duration can then be compared to that obtained from different means, e.g. based on the stellar mass and radius listed in the TIC (see Stassun et al. 2018), which constrains the eccentricity.

The results are shown as the orange curve in Figure 3.22. Though fairly unconstrained, the eccentricity seemed to be significantly different from zero using this method, and appeared to match the constraint from the putative secondary eclipse. This motivated us to pursue additional radial velocity data. Ultimately, however, the final radial velocity data did not favour a significant eccentricity (*blue curve*), so we adopted a circular model in the paper.

As can be seen in Figure 4 in the paper (Section 3.3.4), the star exhibits a photometric signal due to spot(s) carried around by stellar rotation, which determined the rotation period of the star is ~28 days. Upon closer inspection of the Simple Aperture Photometry (SAP) flux from *TESS* (which is the uncorrected flux), some transits appear to occult spots, which causes a characteristic brightening in

the transit light curve (Sanchis-Ojeda et al. 2011). This is shown in Figure 3.23 for TOI-1259 Ab. The top panel shows the spot-induced rotational signal apparent in the un-corrected light curve. The middle panel is a zoom-in on the first available sector of *TESS* data, with the locations of two neighbouring transits highlighted in blue and orange. This panel also shows that the brightess of the star is close to a minimum, which means the spot(s) is facing us. The bottom panels show these two transits up close. The blue transit occurs first and encounters a spot in the last half of its transit. One orbital period later the planet transits once more and occults a spot again, but this time earlier than before. If these two spot occultations are due to the *same* spot, then the orbit is retrograde to the rotation of the star. To confirm this, I wrote a proposal to observe two transits of TOI-1259 Ab using the HARPS-N spectrograph on the TNG telescope located at Observatorio del Roque de los Muchachos in La Palma, Spain. The proposal was unfortunately not accepted, however, in future work I wish to revisit this system to analyse the spot-crossing events in more detail, which in itself can constrain the spin-orbit angle (Chapter 1.4.1, Sanchis-Ojeda et al. 2012).

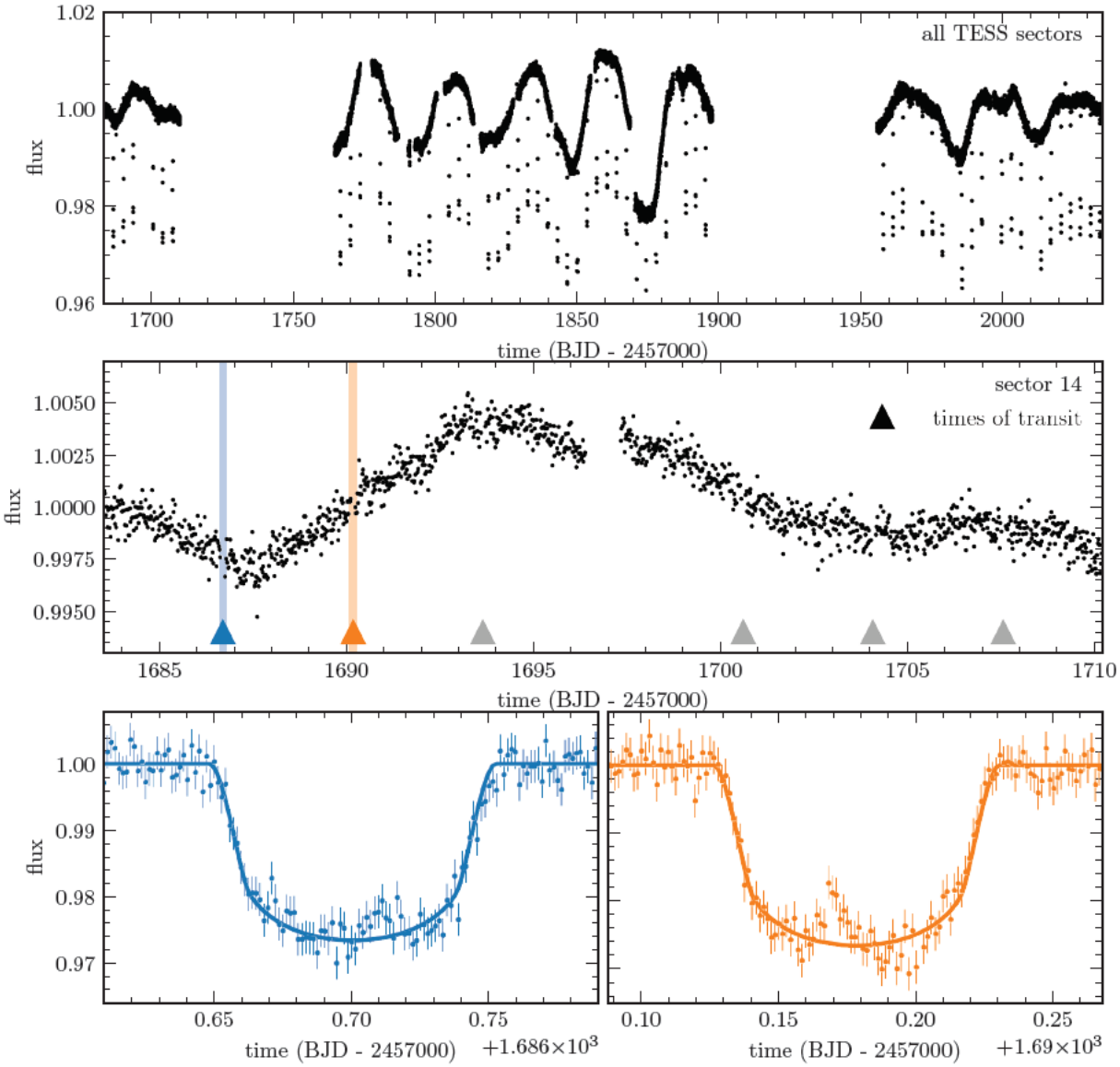


Figure 3.23: Transit spot-crossing events for TOI-1259 Ab. *Top:* A view of the SAP flux from *TESS* of TOI-1259 A. *Middle:* A closer look on the first sector of *TESS* data, highlighting the locations of two adjacent transits in blue and orange. *Bottom:* A closer look at each transit. The first transit (*blue*) occurs first, and encounters a spot in the second half of the transit. The second transit (*orange*) encounters a spot earlier than the previous transit.

CHAPTER 4

STELLAR OBLIQUITIES IN EARTH AND SUPER-EARTH SYSTEMS

By August 2018 my stint on working on brown dwarfs was mostly over, and I was ready for new challenges. The experience I gained from working on Chapter 3.1 and 3.2 was indispensable. I had become comfortable modelling exoplanet data, using MCMC, writing code, scheduling observations, and had learned plenty of science; all of which were key skills in my next two projects.

As discussed in Chapter 1.5, one of the next frontiers in studies of spin-orbit misalignments is to work towards systems hosting small planets and multiple planets (e.g. Sanchis-Ojeda et al. 2012; Bourrier et al. 2018; Hjorth et al. 2021). This is extremely challenging since the Rossiter-McLaughlin effect induced by a typical sub-Neptune sized planet transiting a Sun-like star with similar rotation is $\sim$1 m s^{-1} (Equation 1.4). This level of precision is approaching the limit of current spectrographs (Fischer et al. 2016). As we see from Equation 1.4, if we want to study small planets we can boost the Rossiter-McLaughlin amplitude by also selecting small stars. Then the radius ratio between the star and a planet is similar to a hot Jupiter system and would produce Rossiter-McLaughlin amplitudes of order tens of m s^{-1} for reasonable values of $v \sin i_\star$. Alternatively, we can study stars with high $v \sin i_\star$, though this also has the effect of degrading the radial velocity precision due to enhanced rotational broadening of the absorption lines. A third alternative is the "brute force" approach, where we study *bright* Sun-like stars with the best currently available high-resolution spectrographs on Earth, allowing us to reach radial velocity precision down to a few tens of cm s^{-1} (Pepe et al. 2020).

In this Chapter I present two studies on small-planet systems, one is a Rossiter-McLaughlin campaign on the Earth-sized planets in TRAPPIST-1 using the CARMENES spectrograph, and the other is a measurement of the Rossiter-McLaughlin effect of the super-Earth π Men c using the *ESPRESSO* spectrograph (Kunovac Hodžić et al. 2021).

4.1 Rossiter-McLaughlin campaigns on TRAPPIST-1 observed with CARMENES

The discovery of multiple planets orbiting the ultracool dwarf TRAPPIST-1 were announced in Gillon et al. (2016, 2017). This time coincided with the CARMENES spectrograph coming online, which was amongst the first radial velocity spectrographs that had a near-infrared arm dedicated to searching for planets orbiting M dwarfs (Quirrenbach et al. 2016, 2018). My supervisor, Amaury, obtained time on CARMENES to observe the Rossiter-McLaughlin effect in TRAPPIST-1. The scientific priority of these observations was and continues to be very high. Planetary systems with seven discovered planets and more are incredibly rare, yet they are most like the solar system (Shallue & Vanderburg 2018). In addition, this was the lowest-mass star around which planets had been discovered, which challenged planet formation theories. All of the planets are similar in size to the Earth, several of which orbit within the habitable zone of TRAPPIST-1, where liquid water can exist on the surface of the planets (Gillon et al. 2017). Naturally, measuring the obliquity of the star could tell us something about how such a system came to be.

TRAPPIST-1 is an incredibly challenging target to observe for several reasons. The star is an ultracool dwarf of spectral type M8.5 (Burgasser & Mamajek 2017). Although it is only 12 pc from the Sun (Costa et al. 2006), the star is incredibly faint at optical wavelengths ($V = 18.8$ mag) which is where most radial velocity spectrographs operate. However, at the time of discovery the rotation of the star had been measured to $v \sin i_\star = 6 \pm 2\,\mathrm{km\,s^{-1}}$ (Barnes et al. 2014). If this is the case, this would yield a Rossiter-McLaughlin amplitude of $\sim 50\,\mathrm{m\,s^{-1}}$, which would make it higher than the expected Doppler signal due to the orbit of the planets ($\sim 10\,\mathrm{m\,s^{-1}}$). Such a signal would be detectable with CARMENES. CARMENES consists of two spectrographs. The visible spectrograph ranges from 0.52–0.96 µm with $R = 93\,400$, and the near-infrared spectrograph covers 0.96–1.71 µm with $R = 81\,800$ (Quirrenbach et al. 2016). At the time of our observations there were complications with the data in the near-infrared arm, so only data from the visible arm is currently available. The following is some work I did in the early autumn of 2018.

4.1.1 Observations

We took 176 spectra at 10 min exposures of TRAPPIST-1 in the CARMENES visible arm between 2016-06-01 and 2016-11-19, of which 161 were part of spectroscopic transit sequences. Ten transits were obtained of TRAPPIST-1 b; five of TRAPPIST-1 c, and one partial transit of TRAPPIST-1 g. Two of the sequences contained two transits immediately following one another; one with TRAPPIST-1 b followed by a partial transit of TRAPPIST-1 g on Julian Date 2 457 603, and the other of TRAPPIST-1 c followed by TRAPPIST-1 b on Julian Date 2 457 665. These events were treated with the same offset, see Section 4.1.2. The average RV uncertainty for the entire dataset is $35.5\,\mathrm{m\,s^{-1}}$. The observations are summarised in Table 4.1.

Table 4.1: Summary of observations.

	t_{exp} (min)	N_{obs}	$N_{transits}$	$\langle\sigma\rangle$ (m s^{-1})
TRAPPIST-1 b	-	108	10	36.3
TRAPPIST-1 c	-	48	5	34.6
TRAPPIST-1 g	-	5	1	37.0
Total	10	176	16	35.5

4.1.2 Rossiter-McLaughlin modelling

We modelled the spectroscopic transit with the `ellc` eclipsing binary model, and used the `emcee` Markov chain Monte Carlo algorithm to obtain credible intervals marginalised over other parameters. We used normal priors on the period, P; transit midpoint, T_0; transit depth, D; transit width, W; impact parameter, b, for each planet we had full (TRAPPIST-1 b,c) or partial (TRAPPIST-1 g) spectroscopic transits for, based on the paper by Delrez et al. (2018). The radial velocity semi-amplitude, K, was fixed based on the values of inclination, planet mass, and semi-major axis from the same paper and Grimm et al. (2018) for each planet. The signal of the combined radial velocity variation from the remaining planets is negligible compared to our RV precision, we thus fit individual offsets for each R-M sequence, but no slope due to the short duration of the transits (36.19 min, 42.31 min, and 68.53 min). This choice was also justified by comparing the Bayesian Information Criterion between the two configurations. We used limb darkening parameters from Delrez et al. (2018), based on the Spitzer 4.5 µm channel, which is expected to be different from the CARMENES visible arm, but is unlikely to impact our result given the precision of our data. Repeated follow-up transit observations of the TRAPPIST planets have uncovered transit-timing variations (Grimm et al. 2018). For the two innermost planets, the amplitude of this effect is 2–3 min. However, inspecting the dynamical models in Grimm et al. (2018) backpropagated in time shows that our observations fall in a range where the amplitude of the TTVs at most is 1 min, which is negligible given our current errors and 10 min cadence. While variations in transit timing for TRAPPIST-1 g are larger, its single partial transit does not contribute much to the fit and its effect is thus negligible.

We performed various fits, experimenting with no $v \sin i_\star$ prior, fixing $\lambda = 0$ (aligned), using $v \sin i_\star = 6 \pm 2$ km s^{-1} prior from Barnes et al. (2014), and $v \sin i_\star = 1.855 \pm 0.095$ km s^{-1} based on the $P_{rot} = 3.30 \pm 0.14$ days periodic signal from Luger et al. (2017) and Vida et al. (2017) found in the *K2* data, combined with the radius of TRAPPIST-1 from Van Grootel et al. (2018). Finally, we also perform a fit with no Rossiter-McLaughlin effect for reference.

The runs were performed with 128 "walkers" dispersed close to the maximum likelihood solution, each running for a total of 5000 steps, where half were discarded as burn-in. All parameters reached the $\hat{R} < 1.1$ convergence criterion (Gelman et al. 2003). The final posterior samples were thinned by a factor 10 due to autocorrelation, before merging the chains to compute the 68 % credible intervals.

Table 4.2: Results from the different runs using various priors on $v \sin i_\star$ and without.

$v \sin i_\star$ prior (km s^{-1})	$v \sin i_\star$ (km s^{-1})	λ (deg)	$\sigma_{\rm residual}$ (m s^{-1})	χ^2	BIC
$\mathcal{N}(6, 2)$	$5.2^{+1.8}_{-1.7}$	60^{+13}_{-26}	25.0	94.3	-857.4
$\mathcal{N}(1.855, 0.095)$	$1.9^{+0.1}_{-0.1}$	22^{+35}_{-52}	25.5	94.6	-856.8
$\mathcal{U}(0, 20)$	$4.24^{+3.49}_{-2.14}$	57^{+18}_{-52}	25.0	93.9	-857.8
$\mathcal{U}(0, 20)$	$2.03^{+1.03}_{-1.06}$	0	25.5	96.6	-860.2
-	0	0	25.6	92.8	-869.1

4.1.3 Results

Overall, the χ^2 does not vary much between the runs, thus most of the differences in the Bayesian Information Criterion that favours one model over another comes from the different number of effective model parameters. As a consequence, our reference run where we do not fit the Rossiter-McLaughlin effect (i.e. we fit a straight line) is greatly preferred by the BIC, with a difference of at least $|\Delta\text{BIC}| = 9$ from the second lowest, where we assume alignment and fit freely for $v \sin i_\star$. However, the latter is not greatly preferred over the other runs with a $|\Delta\text{BIC}|$ of only 3–4. The comparison between the different runs is summarised in Table 4.2 and Figure 4.1, where we show the posterior distributions for $v \sin i_\star$ and λ. In the runs with a prior on $v \sin i_\star$ it seems to recover the prior as the prior and posterior distributions overlap.

The posterior distributions for the sky-projected spin-orbit angle λ is consistently skewed away from alignment where we fit for it. However, for our runs when using a prior on $v \sin i_\star = 1.885 \pm 0.095$ km s^{-1} and without a prior, we retrieve $\lambda = 22^{\circ+35}_{-52}$, and $\lambda = 57^{\circ+18}_{-52}$, respectively, which is consistent with alignment within the 68 % credible interval. The run with using a prior on $v \sin i_\star = 6 \pm 2$ km s^{-1} from rotational line broadening yields $\lambda = 60^{\circ+13}_{-26}$, where misalignment is favoured at 2σ, although the BIC from this run is not particularly favoured.

Conversely, if we assume aligment and fix $\lambda = 0^\circ$ to constrain $v \sin i_\star$, we obtain $v \sin i_\star = 2.03^{+1.03}_{-1.06}$ km s^{-1}; a 2σ detection on the rotation. Interestingly, *a priori* we expect the system to be aligned in such a close-packed system due to dynamical arguments, and if true, places a 3σ upper limit of $v \sin i_\star < 5$ km s^{-1}.

Finally, for our most conservative approach, fitting $v \sin i_\star$ and λ freely, we plot the data and the best-fit Rossiter-McLaughlin models and their 95 % credible intervals in Figure 4.2. Astonishingly, the data may hint at a signal at the expected time, but with the current data, it is not possible to say with high certainty.

4.1.4 Further observations

The current dataset comprises 15 full spectroscopic transits. The current best solution based on the Bayesian Information Criterion, aside from the non-detection reference, has a $n_\sigma = 2.03/1.06 \approx 1.9\sigma$

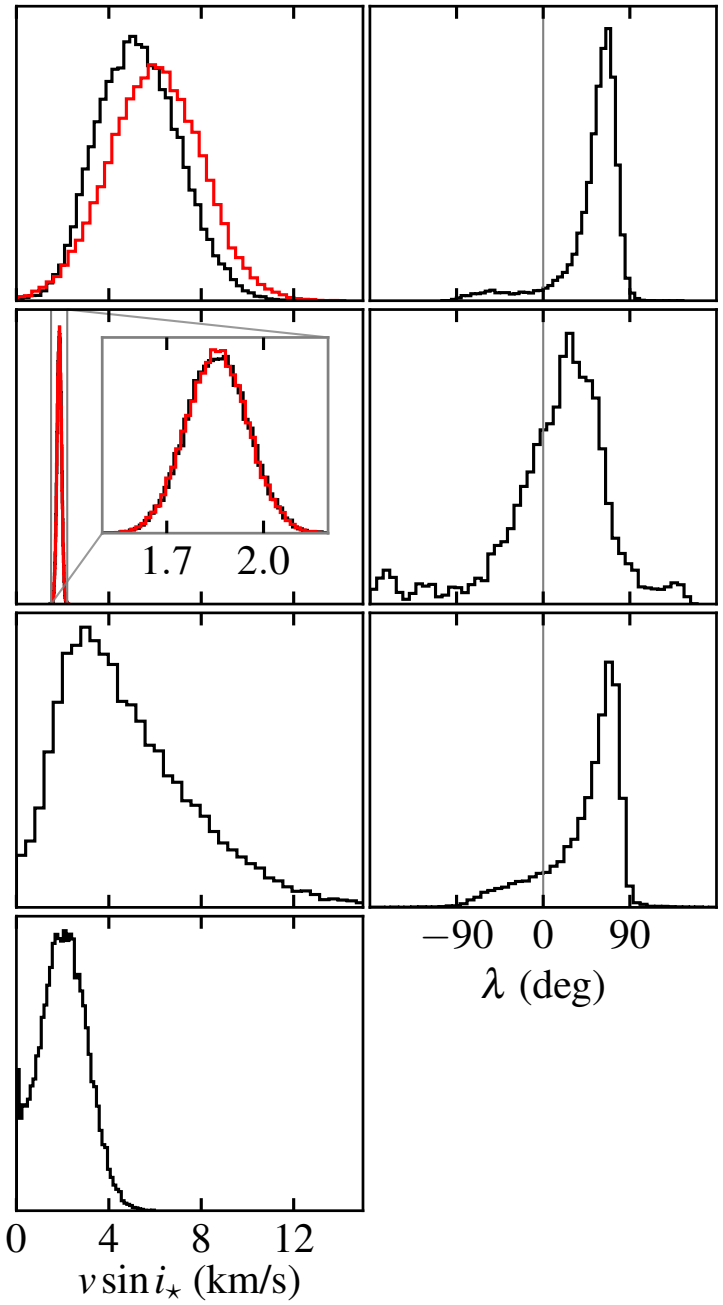


Figure 4.1: Posterior distributions (*black*) for $v \sin i_\star$ and λ from our four runs where either was fit, with prior distribution (*red*) where applicable. *Top:* Prior on $v \sin i_\star = 6 \pm 2\,\mathrm{km\,s^{-1}}$ from spectroscopic line broadening (Barnes et al. 2014). *Upper middle:* Prior on $v \sin i_\star = 1.855 \pm 0.095\,\mathrm{km\,s^{-1}}$ from *K2* periodic signal interpreted as rotation (Luger et al. 2017; Vida et al. 2017). *Lower middle:* No prior. *Bottom:* No prior, fix $\lambda = 0°$ (alignment).

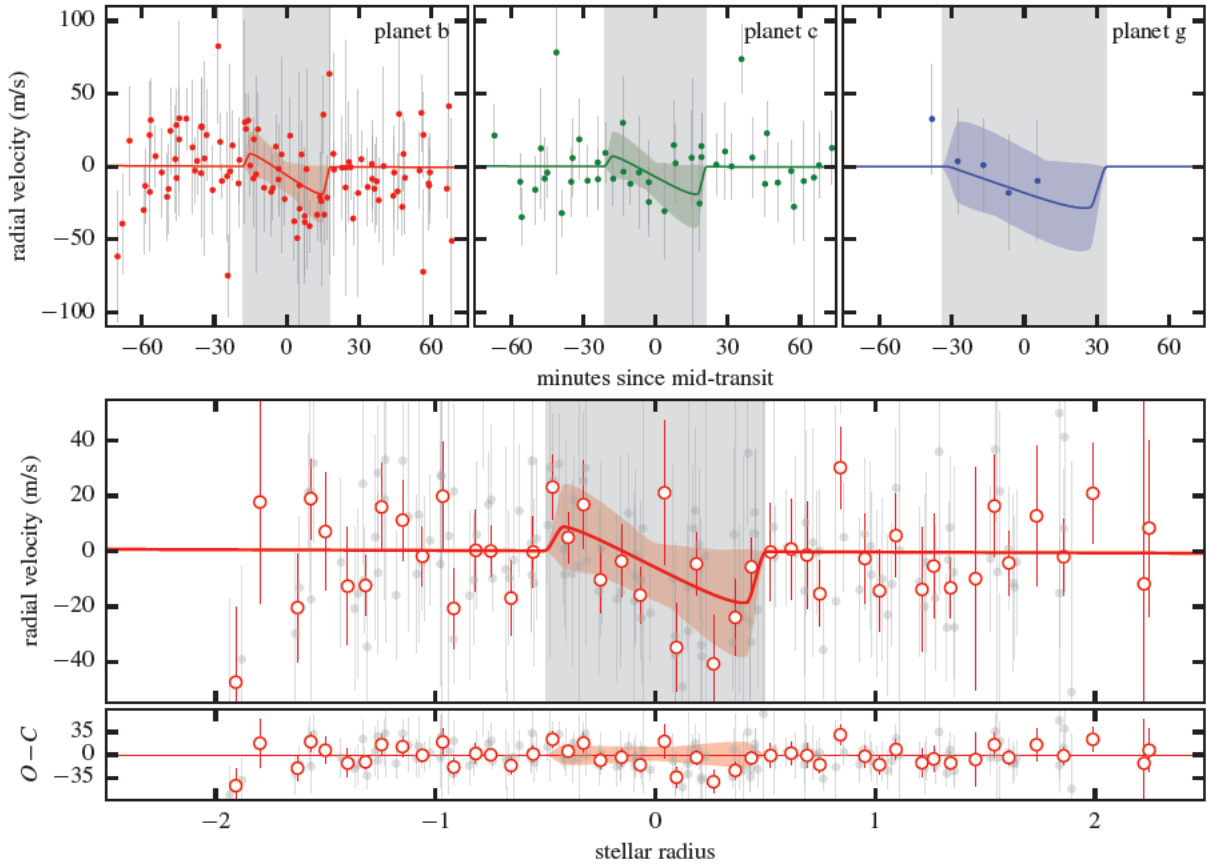


Figure 4.2: The data and their best Rossiter-McLaughlin fits. *Top:* From left to right we show individual fits for TRAPPIST-1 b,c,g. The data are given as coloured dots, with best-fit models in the same colour, and errorbars in gray. The 2σ credible interval is given as a coloured shaded area, while the transit duration is shaded in gray. *Bottom:* The data and models normalised to the stellar disc, allowing us to stack observations in the same frame. Gray dots and errors are the individual data, with binned data and errors in red, binning the stellar disc into 12 equidistant points. The residuals of the fit are shown in the bottom panel.

detection. Assuming only white noise, and that any new data will have roughly the same precision as our current dataset, we can estimate how many more events need to be observed to claim a $>3\sigma$ detection. Adding double the number of observed events to our current dataset, the significance would increase to $1.9\sigma \times \sqrt{3} = 3.3\sigma$. Assuming 2 h per event means an observing programme of roughly $2\,\mathrm{h} \times 2 \times 15 = 60\,\mathrm{h} \approx 7.5$ nights, assuming 8 h observing per night. However, if the data reduction pipeline has improved since the current dataset was reduced it would be lowered. Observing transits of TRAPPIST-1 g would allow longer exposures due to its longer transit, thus increasing the SNR. However, with a ~12 d period, observable transits from the ground are rare.

4.1.5 Conclusion and further developments

- Comparing various runs by the Bayesian Information Criterion, we find that the data is most compatible with no Rossiter-McLaughlin detection.

- Assuming alignment, we recover $v \sin i_\star = 2.03^{+1.03}_{-1.06}$ with 95 % confidence, and $v \sin i_\star < 5\,\mathrm{km\,s^{-1}}$ at 99.7 % confidence.
- Achieving a 3σ detection on $v \sin i_\star$, and constraining the sky-projected spin-orbit angle λ further, would require an observing programme of about 60 h, or 7.5 nights.

The most important result from this work is that the rotation of the star is significantly lower than previously thought, and indeed it appeared to match reported signals that had been attributed to rotation in *K2* data (Luger et al. 2017; Vida et al. 2017). As a result the Rossiter-McLaughlin amplitude is much lower than anticipated and therefore not detected. We estimated we need an additional 60 h of observations on CARMENES to claim a 3σ detection and found that this was not feasible.

Instead, we pursued additional observations in other ways. On two occasions I submitted proposals to *ESPRESSO* to observe the Rossiter-McLaughlin effect in TRAPPIST-1, showing that we could claim a detection in 22 hours of observations. These were unfortunately rejected on both occasions. As a result my supervisor and I reached out to the SPIRou team and started a collaboration. Led by a PhD student at the University of Montreal, they submitted proposals on several occasions to observe the Rossiter-McLaughlin effect of TRAPPIST-1 b. In this collaboration I am providing an analysis of the CCFs with the reloaded Rossiter-McLaughlin method. Recently, we also obtained CCFs from our original CARMENES data — made possible by the work presented in Lafarga et al. (2020) — thus a new analysis may be able to provide further constraints on this data as well.

In the meantime, Hirano et al. (2020) observed transits of TRAPPIST-1 b, e and f over the course of one night. They obtained near-infrared radial velocities during transit using the IRD spectrograph on the 8.2-m Gemini-N telescope at Mauna Kea, Hawaii, and constrained the spin-orbit angle to $\lambda = 1^\circ \pm 28^\circ$ and $\lambda = 19^{\circ\,+13^\circ}_{-15^\circ}$, by analysing the radial velocities and deformation of the spectral lines, respectively (Hirano et al. 2020). They too, find a low value for $v \sin i_\star = 1.50 \pm 0.37\,\mathrm{km\,s^{-1}}$, which is agreement with our value from the CARMENES data by assuming $\lambda = 0^\circ$ (Bottom panel, Figure 4.2).

Table 4.3: Table of priors used in the analysis. $\mathcal{N}$ denotes the normal distribution with the given mean and standard deviation in brackets, while $\mathcal{U}$ denotes a uniform distribution with lower and upper limits in brackets. *References:* [1]Barnes et al. (2014); [2]Luger et al. (2017), Vida et al. (2017); [2]Delrez et al. (2018).

Parameter	Prior	Unit
TRAPPIST-1		
$v \sin i_\star$	$\mathcal{N}(6, 2)$[1]	km s^{-1}
$v \sin i_\star$	$\mathcal{N}(1.855, 0.095)$[2]	km s^{-1}
TRAPPIST-1 b		
P	$\mathcal{N}(1.51087637, 0.00000039)$[3]	day
T_0	$\mathcal{N}(7322.51654, 0.00012)$[3]	day
b	$\mathcal{N}(0.157, 0.075)$[3]	$R_\star$
W	$\mathcal{N}(0.025132, 0.000083)$[3]	day
D	$\mathcal{N}(0.007277, 0.000075)$[3]	
TRAPPIST-1 c		
P	$\mathcal{N}(2.42180746, 0.00000091)$[3]	day
T_0	$\mathcal{N}(7282.80879, 0.00018)$[3]	day
b	$\mathcal{N}(0.148, 0.088)$[3]	$R_\star$
W	$\mathcal{N}(0.029381, 0.000097)$[3]	day
D	$\mathcal{N}(0.006940, 0.000068)$[3]	
TRAPPIST-1 g		
P	$\mathcal{N}(12.354473, 0.000018)$[3]	day
T_0	$\mathcal{N}(7665.35084, 0.00020)$[3]	day
b	$\mathcal{N}(0.406, 0.03)$[3]	$R_\star$
W	$\mathcal{N}(0.04759, 0.00026)$[3]	day
D	$\mathcal{N}(0.00764, 0.00011)$[3]	

4.2 Orbital misalignment of the super-Earth π Men c with the spin of its star

4.2.1 An opportune moment for jumping onto the *TESS* bandwagon

We have arrived at what is perhaps the most important scientific contribution in my PhD, but what has also undeniably been the most challenging work. As I was concluding my work on TRAPPIST-1 the *TESS* spacecraft announced its first discovery: a super-Earth orbiting the naked-eye star π Men c (Huang et al. 2018; Gandolfi et al. 2018). The system was already home to a Doppler planet/brown dwarf on a wide eccentric orbit (Jones et al. 2002), and therefore formed a type of hierarchical triple system. Observational constraints on the formation on super-Earths are scarce, and this system provided a particularly interesting target to test disc-free migration scenarios given the existence of its outer companion.

I calculated that the Rossiter-McLaughlin amplitude in this system would be $\sim$60 cm s^{-1}. This would have been very difficult to do with HARPS, which has a precision limit of about 50 m s^{-1} and has been the premier exoplanet high-resolution spectrograph since 2003 (Mayor et al. 2003). However, on 1 October 2018 the European Southern Observatory's new generation exoplanet spectrograph, *ESPRESSO*, finished its commissioning (Pepe et al. 2020). *ESPRESSO* boasts a limit of 10 cm s^{-1}, and measuring a $\sim$60 cm s^{-1} signal would then be within the realm of possibility. I brought up these thoughts to Amaury and he strongly encouraged me to write a proposal to ask for Director's Discretionary Time (DDT) to observe the transit of π Men c. There were only two fully visible transits remaining that year before the star had set, on November 3 and December 17, so time was of the essence. I wrote the proposal with some help from Amaury, and I asked ESO to observe both transits. The proposal got accepted within about two weeks, just in time to schedule observations for the transits, and was some of the first science data taken with *ESPRESSO*. However, ESO initially only accepted the first transit event, and asked for a report of the analysis of this data to justify the need for a second transit. I therefore only had a few weeks to analyse the data and write the report before the 17 December transit event. On the evening of 2 November 2018, the night of the first transit — and the night before my 27th birthday — I stayed up late obsessively checking the weather in Paranal. Immediately upon waking up the next morning I logged into my account on ESO to check the nightly report — we had data!

ESPRESSO was so new that the data reduction pipeline was not yet available when we observed the first transit. Instead, Gaspare Lo Curto at ESO kindly provided us the radial velocities using the not-yet public pipeline. Loading in the data to plot it was a moment of great excitement, and even more so when I saw there was structure within the timeseries. Then, I looked at the scale of the radial velocity axis. The radial velocity sequence from the first transit can be seen in the top panel of Figure 4.4 (Figure 2 in the published paper). The $\sim$3 m s^{-1} variation seen in the data far exceeded the expected $\sim$0.5 m s^{-1} signal. The most dominant signal in the radial velocity timeseries is the $\sim$6 min variation due to stellar oscillations, which occur due to the excitation and damping of pressure modes near the turbulent convective surface regions of stars (Basu & Chaplin 2017). A second signal is longer in timescale — a few hours — and I wondered whether this was the Rossiter-McLaughlin signal. It was clear that by

looking at the data that just modelling the Rossiter-McLaughlin effect on its own would not suffice, I had to come up with a method of dealing with the oscillations.

At the time I had seen Gaussian process (GP) regression being increasingly used in modelling correlated signals in transit light curves and radial velocity timeseries (e.g. Haywood et al. 2014; Gillen et al. 2017; Farr et al. 2018). A relatively new open-source GP code had recently been published by Foreman-Mackey et al. (2017), which employed a kernel function which had the functional form of a simple harmonic oscillator that could lend itself well to modelling stellar oscillations. Over the next week I worked intensely on learning about CELERITE and implementing it in AMELIE to model the oscillations with the Rossiter-McLaughlin model. The GP model was a success as shown in Figure 4.4. The issue was the longer timescale signal. This could either be due to the Rossiter-McLaughlin effect, or due to an additional signal of unknown origin. The conclusion was clear, in any case: we had to observe a second transit to be sure of what we were seeing.

Our results from the GP modelling showed that the frequency of the oscillations had two solutions. This ambiguity was due to our data sampling. The exposure time in the first transit sequence was set to 120 s, with the CCD read-out time being 45 s, so the cadence of our data was 165 s. The Nyquist frequency of our data was therefore close to the frequency of oscillation. Our second run was accepted given the findings of my report, and this time — after some discussion with co-authors Bill Chaplin and Guy Davies — we decided to lower the exposure time to 80 s. This would ensure we could unambiguously find the right frequency, but also get enough photons to reach sufficient precision on individual measurements for the Rossiter-McLaughlin effect. The second transit sequence is shown to the right in Figure 4.4. The signal seen in the first sequence now seems to have disappeared, which validated our decision to ask for another transit.

The road from acquiring the data to publishing the paper took about two years. First, I had to do an analysis of transit photometry from *TESS* to nail down the orbital period, which was needed for the analysis of the *ESPRESSO* data. The discovery papers from Huang et al. (2018) and Gandolfi et al. (2018) were based on one sector of *TESS* data only, and the uncertainty on the orbital period was about 7 min at the time of the 3 November transit. By the time we had acquired the *ESPRESSO* data π Men had been observed in two more *TESS* sectors. I worked on understanding and analysing this data more or less full-time over the next six months after acquiring the data. Some time went into learning how to use the data reduction pipeline for *ESPRESSO*. Some more time went into investigating the CCFs order-by-order to see if there was any colour-dependence in the radial velocities, though no firm conclusions could be drawn. Once I felt I could not get any more information out of modelling the radial velocity timeseries I took a break from this work for my own sanity. I started to work on a new project for my upcoming research visit at The University of Chicago, which ran from September 2019 – March 2020. During my time in the US I started slowly poking at the data again, but this time working on a CCF analysis using the reloaded Rossiter-McLaughlin method. The analysis of the CCFs appeared to favour a somewhat misaligned system, but I did not feel confident enough to say for certain since I was not yet very familiar with the reloaded technique (Section 2.2.4). I decided I needed to get more experience by working on

another easier system first to learn gain more experience. That system was J0608-59/TOI-1338, which is outlined in Chapter 6. That work taught me a lot about working on CCFs and the reloaded Rossiter-McLaughlin method. After concluding that work, I returned to analysing the π Men data with more confidence, re-doing all analysis, and started to write the paper. Indeed, all my analysis pointed towards a misaligned configuration which was a big result. Finally, after further delays in productivity due to the COVID pandemic, I submitted the paper in the summer of 2020. Shortly prior to this, a potential explanation for the misalignment came with the discovery of a mutual inclination between the π Men c and the outer planet b (Damasso et al. 2020; De Rosa et al. 2020; Xuan & Wyatt 2020). The paper was accepted in January 2021, and is outlined below.

Monthly Notices of the ROYAL ASTRONOMICAL SOCIETY

MNRAS **502,** 2893–2911 (2021) doi:10.1093/mnras/stab237
Advance Access publication 2021 January 29

Orbital misalignment of the super-Earth π Men c with the spin of its star

Vedad Kunovac Hodžić [1]★ Amaury H. M. J. Triaud [1] Heather M. Cegla [2,3]† William J. Chaplin[1,4] and Guy R. Davies[1,4]

[1]*School of Physics and Astronomy, University of Birmingham, Edgbaston, Birmingham B15 2TT, UK*
[2]*Department of Physics, University of Warwick, Gibbet Hill Road, Coventry CV4 7AL, UK*
[3]*Observatoire de Genève, Université de Genève, Chemin des Maillettes 51, CH-1290 Sauverny, Switzerland*
[4]*Stellar Astrophysics Centre (SAC), Department of Physics and Astronomy, Aarhus University, Ny Munkegade 120, DK-8000 Aarhus C, Denmark*

Accepted 2021 January 22. Received 2021 January 22; in original form 2020 July 22

ABSTRACT

Planet–planet scattering events can leave an observable trace of a planet's migration history in the form of orbital misalignment with respect to the stellar spin axis, which is measurable from spectroscopic time-series taken during transit. We present high-resolution spectroscopic transits observed with *ESPRESSO* of the close-in super-Earth π Men c. The system also contains an outer giant planet on a wide, eccentric orbit, recently found to be inclined with respect to the inner planetary orbit. These characteristics are reminiscent of past dynamical interactions. We successfully retrieve the planet-occulted light during transit, and find evidence that the orbit of π Men c is moderately misaligned with the stellar spin axis with $\lambda = -24\overset{\circ}{.}0 \pm 4\overset{\circ}{.}1$ ($\psi = 26\overset{\circ}{.}9^{+5\overset{\circ}{.}8}_{-4\overset{\circ}{.}7}$). This is consistent with the super-Earth π Men c having followed a high-eccentricity migration followed by tidal circularization, and hints that super-Earths can form at large distances from their star. We also detect clear signatures of solar-like oscillations within our *ESPRESSO* radial velocity time series, where we reach a radial velocity precision of $\sim$20 cm s^{-1}. We model the oscillations using Gaussian processes (GPs) and retrieve a frequency of maximum oscillation, $\nu_{\rm max} = 2771^{+65}_{-60}$ μHz. These oscillations make it challenging to detect the Rossiter–McLaughlin effect using traditional methods. We are, however, successful using the *reloaded* Rossiter–McLaughlin approach. Finally, in the appendix, we also present physical parameters and ephemerides for π Men c from a GP transit analysis of the full *Transiting Exoplanet Survey Satellite* Cycle 1 data.

Key words: asteroseismology – techniques: radial velocity – techniques: spectroscopic – binaries: eclipsing.

1 INTRODUCTION

Perhaps one of the most surprising results from two decades of exoplanet research is that planet sizes between those of Earth and Neptune (1.5–2 $R_\oplus$) are the most likely outcome of planet formation (e.g. Borucki et al. 2010; Batalha et al. 2013), even when such planets are completely absent from our own Solar system. Dubbed *super-Earths* (see Schlichting 2018 for a review), these planets orbit 50 per cent of Sun-like (FGK) stars (Howard et al. 2010; Mayor et al. 2011; Fressin et al. 2013), and rise to 75 per cent when including M dwarfs (Bonfils et al. 2013; Dressing & Charbonneau 2015; Gaidos et al. 2016; Hardegree-Ullman et al. 2019). The currently operating *Transiting Exoplanet Survey Satellite* (*TESS*) survey (Ricker et al. 2015) is expected to find $\sim$1000 additional super-Earths and mini-Neptunes in its 2-yr nominal mission lifetime (Barclay, Pepper & Quintana 2018; Huang et al. 2018a).

Yet for their abundance, there have been few observational constraints on their formation and dynamical evolution. In general, super-Earth formation consists of core formation followed by gas accretion on to the assembled core (Pollack et al. 1996; Chabrier et al. 2014). In the context of *in situ* formation, the inner protoplanetary disc does not have enough solid material in close-in feeding zones, such that any embryo will reach an isolation (maximum) mass well below that of super-Earths (Armitage 2013). Core accretion until isolation mass followed by a giant impact phase is also unlikely to produce the observed super-Earth population (Hansen & Murray 2012; Schlichting 2014; Dawson, Lee & Chiang 2016), which points to another likely mechanism at work to explain the close-in super-Earths. Several super-Earths have been detected in circumbinary configurations (e.g. Orosz et al. 2019; Kostov et al. 2020). Due to strong gravitational perturbations produced by the binary orbital motion on to protoplanetary discs, planet formation is thought to only be possible at several au from the central binaries (e.g. Paardekooper et al. 2012; Pierens, McNally & Nelson 2020) implying that the detected systems had to migrate in (Martin 2018; Pierens et al. 2020).

Close-in planet formation may be aided by an influx of solids in the form of pebbles (Johansen & Lambrechts 2017; Lambrechts et al. 2019), planetesimals, or even fully formed cores from a mass reservoir at several au, where the isolation mass is higher. In either scenario, *in situ* formation or inward gas disc migration (see Baruteau et al. 2014 for a review), planets would remain aligned with the stellar equator, even in the event of interactions in multiplanet systems (Bitsch et al. 2013).

This is not the case for high-eccentricity migration, which can deliver fully formed super-Earths (or even hot Jupiters) to close-in, *inclined* orbits from beyond the snowline. In this two-step process,

★ E-mail:
†CHEOPS Fellow, SNSF NCCR-PlanetS.

© 2021 The Author(s)
Published by Oxford University Press on behalf of Royal Astronomical Society

Downloaded from https://academic.oup.com/mnras/article/502/2/2893/6123888 by University of Birmingham user on 09 March 2021

an outer giant planet will scatter the super-Earth to a highly elliptical orbit. At each periastron passage, the super-Earth will pass very close to the star (a few hundredths of au) and cause tidal dissipation in the planet, which acts to reduce the orbital energy and circularize the orbit to its present-day location. The initial scattering event produces a broad distribution of orbital inclinations (Fabrycky & Tremaine 2007; Chatterjee et al. 2008; Naoz et al. 2011), unlike the aforementioned disc migration pathways that result in co-planar systems.

One of the most promising ways of distinguishing different migration pathways is through the Rossiter–McLaughlin effect (McLaughlin 1924; Rossiter 1924), which measures the projected spinorbit angle between the orbital plane and stellar spin axis, λ. Rossiter–McLaughlin measurements have all but become routine observables for hot Jupiters, and a trend has emerged in which stars above the Kraft break ($T_{\rm eff} \gtrsim 6200$ K) tend to host misaligned massive planets, while stars below (cold stars) tend to have co-planar planets (see Triaud 2018 for a review, and references therein). In general, this can be explained by hot Jupiters being massive enough to realign the stellar spin axis from tidal coupling to their thick convective envelopes, and spin-down due to magnetic breaking, while more massive stars have thinner – or non-existent – convective envelopes and remain fast rotators (Winn et al. 2010b; Dawson 2014). These considerations muddle our interpretation of the dynamical histories of exoplanets, and thus inferring the migration pathways and formation mechanisms of close-in massive planets from spin–orbit angle measurements remains difficult. Smaller planets, however – such as super-Earths – are not massive enough to realign the star within the tidal decay time-scale or lifetime of the star (Dawson 2014), and will therefore keep their orbital inclinations, allowing us to robustly infer their migration pathways from their present-day orbital obliquities. However, Rossiter–McLaughlin observations have thus far largely eluded the super-Earths. The expected radial velocity semi-amplitudes are often at or below the m s^{-1} level, which is at the precision limit of our best spectrographs on the brightest stars, and where phenomena such as stellar oscillations and near-surface convection begin to dominate the signal. Nevertheless, successful Rossiter–McLaughlin campaigns have been carried out on small planets, such as the misaligned Neptune-mass exoplanets HAT-P-11 b (Winn et al. 2010a; Hirano et al. 2011), GJ 436 b (Bourrier et al. 2018), the somewhat contentious result on the super-Earth 55 Cnc e (Bourrier & Hébrard 2014; López-Morales et al. 2014), and most recently on the 22-Myr Neptune-sized planet au Mic b (Addison et al. 2020; Hirano et al. 2020; Palle et al. 2020).

Here, we present a detection of the planetary shadow of a close-in super-Earth, known to host a giant planet companion on a wide, eccentric orbit. We find that the orbit is misaligned with the stellar spin axis, pointing to an origin beyond the snowline, and may show evidence of high-eccentricity migration following dynamical interaction with the outer companion in the system's youth. We present spectroscopic transits obtained with the *ESPRESSO* spectrograph (Pepe et al. 2014), as one of the first science observations after completing its commissioning, and demonstrate its capabilities for providing observational constraints on planet formation of the most common population of exoplanets.

The paper is organized as follows: In Section 2, we present our analyses of the *ESPRESSO* data that include (i) modelling of the Rossiter–McLaughlin anomaly combined with a Gaussian process (GP) model for the asteroseismic activity and (ii) an independent analysis using the reloaded Rossiter–McLaughlin method. In addition, in Appendix A we include our transit analysis using the full *TESS* Cycle 1 data to inform our Rossiter–McLaughlin modelling. In Section 3, we present our updated transit parameters, and new asteroseismic parameters and obliquity measurements. We discuss our results in the context of planet formation in Section 4, and conclude in Section 5. In Appendix A, we present our analysis on *TESS* photometric data to constrain the transit ephemerides and parameters for the Rossiter–McLaughlin analysis.

2 *ESPRESSO* DATA ANALYSIS

2.1 Observations and data reduction

Two transits of π Men c were observed on the nights of 2018 November 2 (run A) and 2018 December 16 (run B) using the *ESPRESSO* spectrograph (Pepe et al. 2014) mounted on the Very Large Telescope at ESO Paranal Observatory (DDT 2102.C-5008, PI: Hodžić). The transit in run A was observed concurrently with *TESS* Sector 4 observations. *ESPRESSO* observations were carried out under very good conditions (seeing ∼0.5 arcsec) in the high-resolution mode using 1 × 1 binning. Integration times were fixed at 120 and 80 s for runs A and B, respectively, with 44 s dead time per observation due to read-out, reaching median signal-to-noise ratio (SNR) per pixel of 272 and 200 at 550 nm for each run. The two runs cover, respectively, 5 and 6 h uninterrupted sequences that cover the full transit duration and additional baselines of 2–3 h before and after the transits. The observations are summarised in Table 1.

The spectra were reduced with version 2.0 of the *ESPRESSO* data reduction pipeline,[1] using a G2 binary mask to create cross-correlation functions (CCFs) that are fitted with Gaussian profiles. From the Gaussian fits, we derive the depth (contrast), width [full width at half-maximum (FWHM)], and mean (radial velocity). The first sequence shows some variation in the derived contrast and SNR throughout the night, which may be due to passing thin clouds . In Section 2.4.1, we describe a way of mitigating its impact on our result. The second sequence is stable with the contrast normally dispersed around the mean, but with a slope as the SNR increases throughout the night. The resulting median uncertainties on the integrated radial velocities are 24 and 35 cm s^{-1} for the first and second sequences, respectively.

The choice of exposure time for run B was informed by a preliminary analysis of run A, which showed two possible solutions for the frequency of maximum oscillation. We therefore opted for faster sampling rate in run B while still making sure to reach the required radial velocity precision for the Rossiter–McLaughlin effect.

2.2 Detection of solar-like oscillations in *ESPRESSO* data

Our initial approach to obtain the spin–orbit angle of π Men c is to fit the Rossiter–McLaughlin effect from the *ESPRESSO* radial velocity time series. The expected amplitude of the Rossiter–McLaughlin effect for this system (assuming $\lambda \sim 0^\circ$) is ~ 50 cm s^{-1}. In this section, we shall see that the radial velocity time series is dominated by variability due to oscillations with amplitudes of a few m s^{-1}, which makes it challenging to extract the signal of the Rossiter–McLaughlin effect. Before attempting to detect the transiting planet, we first need to characterize the oscillation signal

Fig. 1 shows the frequency power spectrum of the *ESPRESSO* radial velocity residuals. Here, we joined the two segments of

[1] ftp://ftp.eso.org/pub/dfs/pipelines/espresso/espdr-reflex-tutorial-1.0.0.pdf

Downloaded from https://academic.oup.com/mnras/article/502/2/2893/6123888 by University of Birmingham user on 09 March 2021

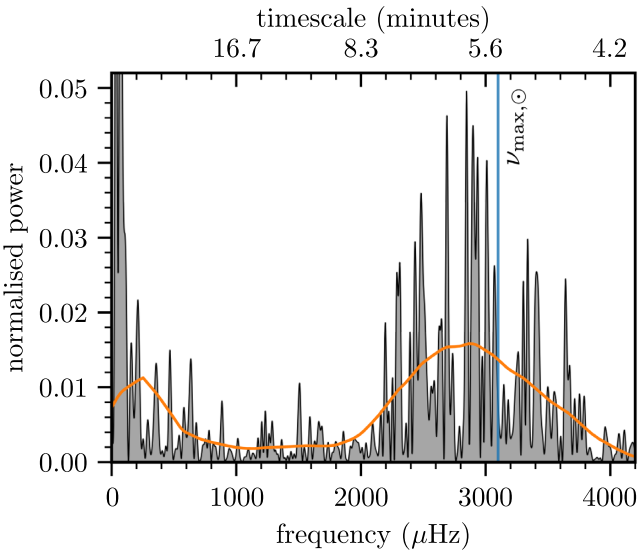


Figure 1. Lomb–Scargle periodogram of the combined *ESPRESSO* radial velocity data. The orange curve shows the heavily smoothed spectrum and reveals an estimate of $\nu_{\max} \simeq 2900$ μHz. In blue, we denote the frequency of maximum oscillation for the Sun for comparison.

data together, and then computed the spectrum using a Lomb–Scargle periodogram (Press & Rybicki 1989), sampled at a frequency resolution that corresponds to the inverse of the length of the combined data set. The spectrum shows a clear excess of power due to solar-like oscillations (*p* modes), centred around a frequency of maximum oscillations power of $\nu_{\max} \simeq 2800$ μHz. Note that the approach of joining together the two Doppler time series does not affect the detectability of the oscillations, because the damping times of the detectable modes are much shorter (of the order of a few days) than the gap between the two sets of data.

Owing to the very short duration of the combined data set, it is not possible to resolve the individual overtones of the oscillation spectrum. The excess power due to the oscillations may as such be modelled to first order in these data as a Gaussian or Lorentzian in frequency (here we choose the latter; see e.g. Farr et al. 2018). Note the orange line in Fig. 1 shows the result of smoothing the spectrum with a double-boxcar filter of width 735 μHz.

We also searched the combined *TESS* residual light curve (after removing the transit and GP signal) for solar-like oscillations, but were unable to uncover evidence of detectable modes. However, as we shall see in the next section, the high-S/N *ESPRESSO* data do show clearly detectable oscillations in Doppler velocity.

2.3 Gaussian process modelling of asteroseismic signal and Rossiter–McLaughlin effect

In this section, we build on our analysis from Kunovac-Hodzic & Triaud (2019) to try to recover the 'classical', or velocimetric, Rossiter–McLaughlin effect. As is evident from Fig. 1, our data show clear signals from oscillations due to *p* modes and possibly other lower frequency stellar activity. In recent years, GPs have been shown to be robust models to describe correlated noise, stellar rotation, or other activity at various time-scales (e.g. Haywood et al. 2014; Grunblatt, Howard & Haywood 2015; Gillen et al. 2017; Angus et al. 2018). Recently, there have also been examples of applying CARMA models (Farr et al. 2018) or GPs (Foreman-Mackey et al. 2017) to asteroseismic analyses in the time-domain. This allows for simultaneous transit or Keplerian modelling, whereas it has traditionally been done in frequency space. Following Foreman-Mackey et al. (2017), the oscillations may be modelled as a sum of stochastically driven damped simple harmonic oscillators (SHO), with power spectrum $S(\omega)$ given by

$$S(\omega) = \sqrt{\frac{2}{\pi}} \frac{S_0\,\omega_0^4}{\left(\omega^2 - \omega_0^2\right)^2 + \omega_0^2\omega^2/Q^2}, \quad (1)$$

ω_0 is the peak angular frequency, S_0 is the maximum power, Q is the quality factor that describes the damping time-scale. For large Q, equation (1) approaches a single-peaked Lorentzian function, and for modelling oscillations from different modes, Q would describe their damping time-scale. From Section 2.2, we determined our data set is too short to resolve individual overtones of the power spectrum, thus we only use a single SHO term (whose power spectrum is described by equation 1) to capture the overall shape of the *p* mode power excess, and in this case Q will effectively describe the width of the power envelope. Similar assumptions have been made in e.g. Farr et al. (2018). The covariance function of equation (1) is a type of quasi-periodic function, given by

$$k(\tau) = S_0\,\omega_0\,Q\,\exp\left(-\frac{\omega_0\tau}{2Q}\right)\cos\left(\eta\,\omega_0\,\tau\right) + \frac{1}{2\eta Q}\sin\left(\eta\,\omega_0\,\tau\right), \quad (2)$$

where τ is the lag between two measurements in time, and $\eta = \sqrt{|1 - 1/4Q^2|}$.

In addition to the oscillations, the data show an additional lower frequency variability component. The variability does not appear to be periodic, but has characteristics of correlated (red) noise which may originate from stellar surface convection or instrumental/environmental effects. In the case of run A, the background component may be dominated by changes in SNR due to varying observing conditions, see Fig. B1. Hereafter we refer to this as the 'background' component, and let it encapsulate any variability that is not constrained by the oscillations model or the Rossiter–McLaughlin signal. A similar model to equation (1) can be used to describe the background term by fixing $Q = 1/\sqrt{2}$. In this case, the power spectral density given in equation (1) simplifies to

$$S(\omega) = \sqrt{\frac{2}{\pi}} \frac{S_0}{(\omega/\omega_0)^4 + 1}, \quad (3)$$

which describes a Harvey-like model commonly used to describe the background power due to surface convection (granulation) in asteroseismic and helioseismic analyses (Harvey 1985), but has also been used to model correlated signals in both radial velocity data and photometry (Foreman-Mackey et al. 2017). The covariance function for the background model simplifies to

$$k(\tau) = S_0\,\omega_0 \exp\left(-\frac{\omega_0\tau}{\sqrt{2}}\right)\cos\left(\frac{\omega_0\tau}{\sqrt{2}} - \frac{\pi}{4}\right). \quad (4)$$

We use the CELERITE GPs software (Foreman-Mackey et al. 2017) to model the stellar signals together with a Rossiter–McLaughlin model. We use the simple harmonic oscillator (SHO) kernel within CELERITE, which is a type of quasi-periodic kernel whose power spectral density and covariance function are described by equations (1) and (2). We fit for the frequency of maximum oscillation power, $\nu_{\max} = \omega_{\max}/2\pi$, logarithm of the amplitude $\ln S_{\rm osc}$, and power-excess width, $\ln Q_{\rm osc}$ to fit the high-frequency variations in our data, which was clearly favoured by the Bayesian Information Criterion (BIC). We include an additional SHO term with PSD given by equation (3) and covariance function by equation (4) for the low frequency background component, where Q is fixed to $1/\sqrt{2}$, and is also clearly favoured by the BIC. Here, we fit

Downloaded from https://academic.oup.com/mnras/article/502/2/2893/6123888 by University of Birmingham user on 09 March 2021

for the logarithm of the amplitude $\ln S_{\rm bkg}$, and angular frequency $\ln \omega_{\rm bkg}$. We attempted to also include a second background term, but found no support for a second signal from a comparison of the BIC.

The oscillation time-scale is only a few times that of our cadence, which can potentially introduce smearing of the oscillation signal. To account for this, we use integrated versions of the CELERITE kernels that we introduced above (Dan Foreman-Mackey, private communication). However, we found that this effect did not make a noticeable different on our result. Moreover, inspecting the data in Fig. 2, the noise properties of the two sequences appear qualitatively different. We therefore model the two *ESPRESSO* time series with individual GP kernels since their covariance properties are expected to differ, but share the hyperparameters between them. The priors on the hyperparameters are shown in Table 2.

Our orbital model is computed using ELLC, where the Rossiter–McLaughlin effect is computed as the flux-weighted radial velocity, as included in the package. We vary the transit parameters with Gaussian priors based on the posterior distribution obtained from our *TESS* photometric analysis (Appendix A), which are listed in Table 4. The radial velocity semi-amplitude is also varied with a Gaussian prior $K = 1.5 \pm 0.2\,{\rm m\,s^{-1}}$, according to the most recent radial velocity orbit analysis in Damasso et al. (2020), which is in agreement with Huang et al. (2018b) and Gandolfi et al. (2018). For the Rossiter–McLaughlin effect, we fit for the projected rotation, $v_{\rm eq}\sin i_\star$, of the star, and the spin–orbit angle, λ, and restrict their values to $v_{\rm eq}\sin i_\star \sim \mathcal{U}(0, 20)\,{\rm km\,s^{-1}}$, $\lambda \sim \mathcal{U}(-180^\circ, 180^\circ)$.

The free parameters in our joint GP and Rossiter–McLaughlin model are sampled using the EMCEE package (Foreman-Mackey et al. 2013). Given the relatively large number of parameters, we launch 400 'walkers' that we run for ∼50 times the estimated autocorrelation length of the parameters. We discard the samples associated with a burn-in phase, which we determined visually, and then checked for convergence by verifying that all parameters reached $\hat{R} < 1.1$ (Gelman et al. 2003). The chains were further thinned by their estimated autocorrelation length before merging them, resulting in >1000 effective samples per parameter.

As we shall see in Section 3, the detection of the Rossiter–McLaughlin effect is uncertain using the velocimetric method outlined in this section. Therefore, as a next step, we attempt to directly analyse the line profile distortion due to the planet in the next section.

2.4 Rossiter–McLaughlin reloaded

2.4.1 Retrieving the occulted light

A relatively recent method termed the reloaded Rossiter–McLaughlin method (Cegla et al. 2016; Bourrier et al. 2017, 2018; Ehrenreich et al. 2020; Kunovac Hodžić et al. 2020) uses the CCF to retrieve the light on the stellar disc that is occulted by the planet during transit, and has been shown to address some issues that may bias measurements of λ in 'classical' Rossiter–McLaughlin analyses, such as the method presented in Section 2.3. In summary, the in-transit CCFs ($\rm CCF_{in}$) are subtracted from a reference out-of-transit CCF ($\rm CCF_{out}$) to retrieve the local stellar CCF behind the planet. We refer the reader to Cegla et al. (2016) for more details, and also similar, pioneering methods in Albrecht et al. (2007) and Collier Cameron et al. (2010). In the following, we will use the abbreviation 'DI' to refer to 'disc-integrated' CCFs, to make clear the distinction from the 'local' CCFs. Local CCF refers to the retrieved stellar light behind the planet, i.e. Doppler shadow.

The continuum levels of *ESPRESSO* CCFs are arbitrary due to not being flux-calibrated. We therefore start by normalizing the DI CCFs by their individual continuum values. Moreover, we also scale them by a quadratic limb darkened transit model computed from the parameters derived in Appendix A, using the same limb darkening coefficients as in the *TESS* transit analysis. The DI CCFs are then shifted to the stellar rest frame by removing the Keplerian motion of the star due to planet c, using the semi-amplitude as derived from Huang et al. (2018b) and Gandolfi et al. (2018). The reflex motion of the star due to planet b is smaller – about 10 and 20 $\rm cm\,s^{-1}$ over the transit duration for each run, respectively – and is therefore a negligible effect. Moreover, we further shift the out-of-transit data to a common systemic velocity at each night, γ, determined from a weighted average of the out-of-transit disc-integrated radial velocities. The latter step is done in order to build as close to a true, intrinsic line profile of the star as possible, without being affected by the smearing due to the potential large radial velocity variation outside of transit, as can be seen in Fig. 2.

The signal that we are trying to extract is a very subtle distortion of the DI line profiles, which is expected to cause a shift in radial velocity of just ∼50 $\rm cm\,s^{-1}$, or put another way; a change in the CCF shape due to the missing flux that is comparable to the transit depth of ∼250 ppm. In order to reach this precision, we are required to bin the in-transit DI CCFs to enhance the SNR of the occulted light. An additional benefit of the binning is to reduce the impact of stellar oscillations. We show in Fig. 3, the radial velocity scatter for a range of bin widths, demonstrating that the oscillations are effectively binned down as white noise for specific integration times (Chaplin et al. 2019). This is particularly clear when the observing conditions are more stable, such as for run B (Fig. B1).

While binning the DI CCFs equates to longer exposure time and thus higher SNR, it may also have detrimental effects on the signal we are trying to extract. The reloaded Rossiter–McLaughlin effect relies on isolating the differences in the DI CCF shape between in-transit and out-of-transit observations. The contrast (depth) of the DI CCF seems correlated with the SNR, as a lower SNR means fewer stellar absorption lines are resolved when cross-correlating the spectrum with the stellar template. Therefore if the contrast (or FWHM) of the in-transit DI CCFs differ from the out-of-transit DI CCFs at a comparable level to the expected missing light, the residual CCFs (that is the Doppler shadow) may be affected by this difference and thus bias the measurement of its measured radial velocity. This is particularly an issue for run A, where in Fig. B1, we show that the contrast during transit varies over a range of ∼500 ppm, which is twice the expected signal of the Doppler shadow. In order to attempt to reduce the impact of this effect, we found it best to choose a bin width large enough to effectively reduce the stellar oscillations (Fig. 3) and obtain a high enough SNR, but such that it still bins together DI CCFs with similar contrast. We found that a bin width of 15 min was a good compromise taking the above considerations into account, while retaining sampling.

Given the variation in contrast, we found it best to also create master out-of-transit DI CCFs that have characteristics that are as close as possible to the values of the binned in-transit DI CCFs to isolate the Doppler shadow. For each *ESPRESSO* sequence, we create three master out-of-transit CCFs that we refer to as *top*, *middle*, and *bottom*. The top and bottom master CCFs are weighted averages of a combination of the lowest and highest SNR DI CCFs, respectively. The middle master CCF is created from a combination of DI CCFs such that it falls close to the middle of the two. For each binned

Downloaded from https://academic.oup.com/mnras/article/502/2/2893/6123888 by University of Birmingham user on 09 March 2021

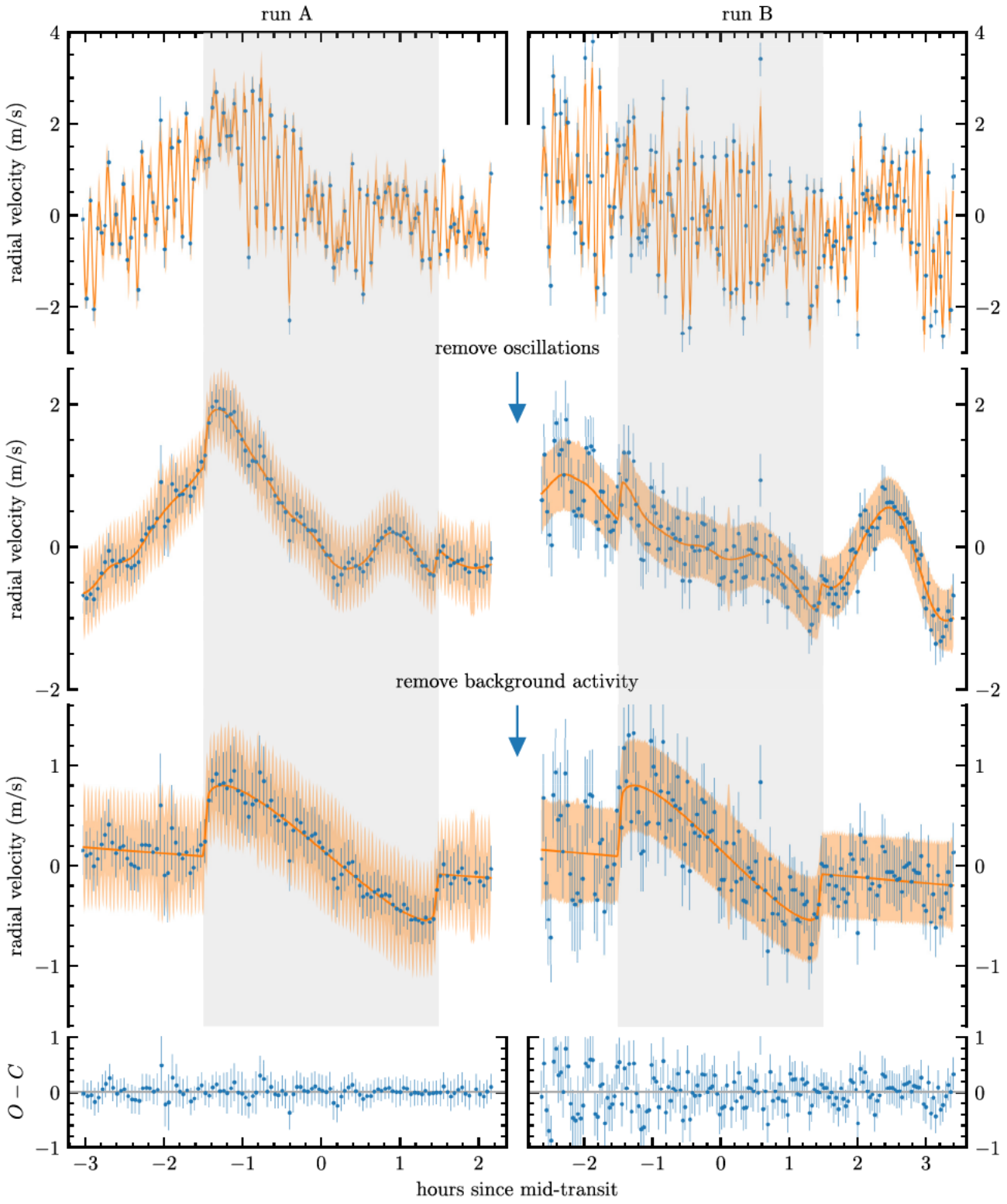


Figure 2. *Top: ESPRESSO* data from run A (*left*) and run B (*right*). The orange line is the best fit from our combined Rossiter–McLaughlin model and GP model (oscillations and 'background' variability). The shaded area is the 68 per cent (1σ) credible interval of the fit. *Upper middle:* The data after removing the contribution from oscillations in our GP model. *Lower middle:* The data after further removing the contribution from the longer-term variability in our GP model. *Bottom:* Residuals of the fit. The grey, shaded regions denote the transit duration.

in-transit DI CCF, we compare its contrast with that of the three master CCFs to determine which one it is closest to. From the selected master CCF, we subtract the binned in-transit DI CCF to retrieve the planet-occulted residual CCFs (Doppler shadow). The residual profiles are shown in Fig. 4, where the Doppler shadow is visible in both runs. The planet appears to be progressively moving from the blueshifted hemisphere to the redshifted hemisphere, indicative of a prograde orbit.

Downloaded from https://academic.oup.com/mnras/article/502/2/2893/6123888 by University of Birmingham user on 09 March 2021

Table 1. Summary of *ESPRESSO* and *TESS* data used in this work.

ESO ID	Run	Night	N_{obs}	t_{exp} (s)	⟨SNR⟩	⟨σ_{RV}⟩ (cm s^{-1})
ESPRESSO (Section 2)						
2012.C-5008(A)	A	2018-11-02	111	120	272	24
2012.C-5008(B)	B	2018-12-16	171	80	200	35
TESS (Appendix A)						
Sector		Date	N_{obs}	t_{exp} (s)		$\sigma_{residual}$ (ppm)
1		2018 July–25 August 22	18 054	120		124
4		2018 October 18–15 November 15	15 768	120		114
8		2019 February 2–28	13 395	120		133
11		2019 April 22–21 May 21	15 299	120		120
12		2019 May 21–June 19	19 071	120		137
13		2019 June–19 July 18	19 562	120		110

Table 2. Priors on the GP hyperparameters for the radial velocity modelling.

Parameter	Prior
rule ln S_{osc} (km^2 s^{-2})	$\mathcal{U}(-35, 15)$
ln Q_{osc}	$\mathcal{U}(0, 4)$
ν_{max} (μHz)	$\mathcal{U}(2100, 4000)$
ln S_{bkg} (km^2 s^{-2})	$\mathcal{U}(-35, -10)$
ln ω_{bkg} (d^{-1})	$\mathcal{U}(3, 5.75)$
ln σ_A (km s^{-1})	$\mathcal{U}(-15, -4)$
ln σ_B (km s^{-1})	$\mathcal{U}(-15, -4)$

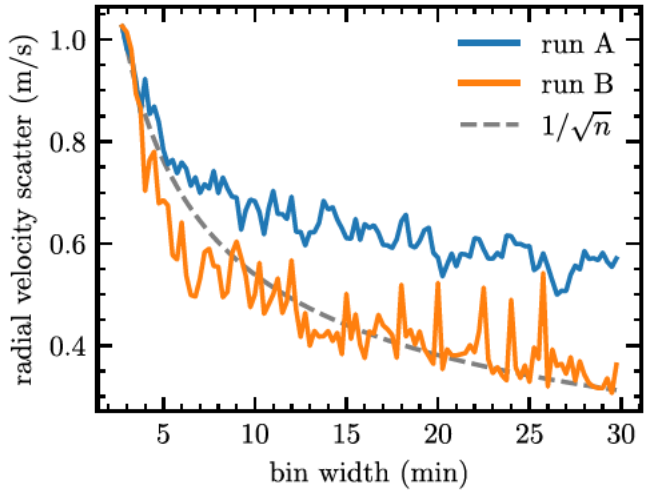


Figure 3. Radial velocity scatter as function of bin width for run A (*blue*) and run B (*orange*). The black dashed line denotes the expectation from white noise scaling.

2.4.2 *Retrieving the surface velocities*

We fit Gaussian profiles to the residual line profiles to determine the radial velocity of the surface of the star where it is occulted by the planet. In order to obtain realistic uncertainities and avoid fitting spurious signals, we use a MCMC sampling method to explore the full posterior distribution and propagate uncertainties in the nuisance parameters to the final radial velocity. We create our Gaussian model using PYMC3 (Salvatier, Wiecki & Fonnesbeck 2016), and vary the line centre, μ; width, σ; contrast, A; and continuum level, c. Additionally, we also freely fit for the CCF error, ϵ. We use the No-U-Turn (NUTS) sampler (Hoffman & Gelman 2014) to sample the parameters from their posterior distribution. Following

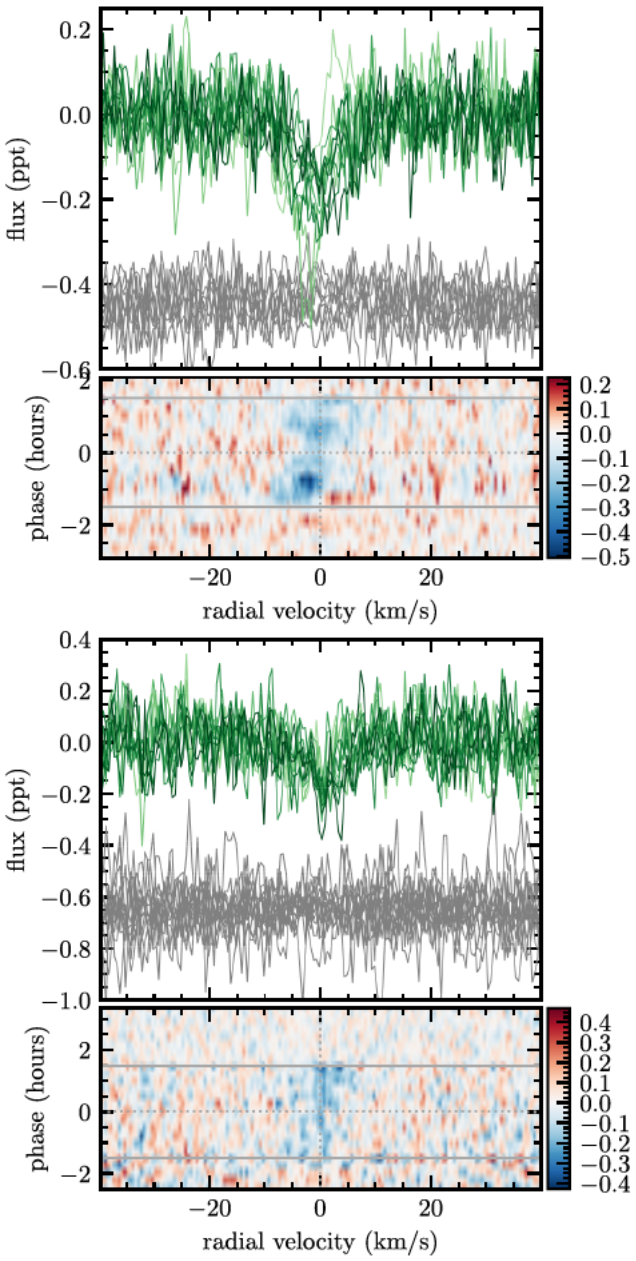


Figure 4. CCF residuals and planet traces for run A (*top*) and run B (*bottom*). In each figure, the upper panel shows the residual profiles obtained from subtracting the binned CCFs from the out of transit reference CCF (CCF$_{out}$). The green colours denote in-transit data, getting darker with time. The grey residuals are binned CCFs outside of transit. In the lower panels, the trace of the planet across the stellar disc is shown, where the grey solid lines denote the transit ingress and egress, while the white dotted lines denote the stellar rest velocity and transit mid-point.

the procedure in Kunovac Hodžić et al. (2020), we use wide priors on our parameters related (typically related to the radial velocity grid or flux range range considered), aimed at returning a conservative estimate of the radial velocity in case the local line centre is poorly resolved. We use a half-normal prior on A, σ, and ϵ as they are restricted to positive values, and a normal prior on μ and c. The priors are shown in Table 3.

From rotational broadening of high-resolution spectra, the projected rotation of π Men is estimated to be ∼3 km s^{-1} (Valenti &

Downloaded from https://academic.oup.com/mnras/article/502/2/2893/6123888 by University of Birmingham user on 09 March 2021

Table 3. Priors on the Gaussian model parameters for modelling the residual CCFs. y refers to the residual CCF flux.

Parameter	Prior
A	$\mathcal{N}(0, \text{range } y)$
σ (km s^{-1})	$\mathcal{N}(0, 10)$
ϵ	$\mathcal{N}(0, \text{sd. } y)$
μ (km s^{-1})	$\mathcal{N}(0, 40)$
c	$\mathcal{N}(0, \text{sd. } y)$

Fischer 2005). For physical reasons, we therefore further restrict the value of μ to $[-5, 5]$ km s^{-1} to avoid fitting spurious correlations that are sometime seen outside the line core. For each residual CCF, we run two individual chains for 5000 tuning steps and 1000 production steps. This typically results in >500 effective samples per parameter that are well mixed, with $\hat{R} < 1.001$ for all parameters. The fits to the individual residual line profiles are shown in Figs C1–C6, and the derived radial velocities are shown in Fig. 5. Moreover, we show how the derived residual CCF contrast and FWHM compare between the two sequences in Fig. C7.

2.4.3 *Local surface velocity modelling*

We model the surface velocities following the semi-analytical model in Cegla et al. (2016). We create a 51 × 51 grid that spans the size of the planet, co-moving with its centre. At every observation, we compute the brightness-weighted rotational velocity by summing the cells on the stellar disc that are occulted by the planet. We assume the star follows a quadratic limb darkening law with coefficients as reported in the *TESS* analysis. We further assume the star follows rigid body rotation, as the precision of our data is not good enough to pick up latitudinal differential rotation. Similarly, we also neglect velocity contributions due to centre-to-limb convective effects. In this case, the theoretical surface velocity depends on the projected rotational velocity, $v_{\rm eq}\sin i_\star$; projected spin–orbit angle, λ; the stellar radius scaled by the planet distance, $R_\star/a$; and orbital inclination, $i_{\rm p}$. We vary $R_\star/a$ and $i_{\rm p}$ within their Gaussian uncertainties determined from the *TESS* transit analysis (Appendix A, Table 4). We let $v_{\rm eq}\sin i_\star \sim \mathcal{U}(0, 10)$ km s^{-1}, and $\lambda \sim \mathcal{U}(-180^\circ, 180^\circ)$. We sample these four parameters using the MCMC sampler as implemented in EMCEE (Foreman-Mackey et al. 2013), running 200 'walkers' for ∼50 times the estimated autocorrelation length of the parameters. The burn-in phase is discarded by visual inspection of the time series of the chains, and we check that we have reached the target posterior distribution by verifying that $\hat{R} < 1.1$ for our parameters (Gelman et al. 2003). We further thin the chains by the estimated autocorrelation length, and reach >1000 effective samples per parameter. The 50th to 99th percentile of the models conditioned on the data are shown in Fig. 5. The Gaussian fit to the first residual CCF in run A (Appendix C) shows signs of a bad comparison with its out-of-transit master CCF due to the rise in flux redwards of the line centre. The line centre is measured at −4.8 km s^{-1}, which is off the scale in Fig. 5. We therefore remove the first data point from run A from our fit to being an outlier. We do, however, verify that our results do not change with its inclusion.

3 RESULTS

We summarize our findings from the *TESS* transit analysis, *ESPRESSO* radial velocity modelling, and reloaded Rossiter–McLaughlin analysis in Table 4. We also report the fitted values for the various Gaussian process nuisance parameters from the photometric and radial velocity analysis in Table D1. In the following, we report our main findings from the analyses presented in this paper.

3.1 Updated planet radius

We show the GP-'detrended' π Men c transit light curve in Fig. 6, which is based on a combined fit of the six available *TESS* sectors in Cycle 1. In Fig. 7, we show the transit depths from fits to individual *TESS* sectors, as well as the combined fit in grey. For comparison, we include the transit depth posteriors from Damasso et al. (2020), who also modelled the full *TESS* Cycle 1 data. Our results are consistent with the discovery papers of Huang et al. (2018b) and Gandolfi et al. (2018), and roughly consistent (1σ to 2σ) to Damasso et al. (2020). The individual sectors show some spread in their distributions, and although most sectors agree to about 1σ, Sectors 11 and 8 are 2σ to 3σ discrepant from Sector 12. We attribute these differences to different time-scales of correlated noise that is fit to each sector. In presence of both high- and low-frequency variation in the light curve, the GP will tend to fit the high-frequency component, which may be on a similar time-scale as the transit duration, and in turn affect the derived transit depth. Given the new transit depth, we obtain a radius of π Men c, $R_{\rm p} = 2.0189^{+0.047}_{-0.045}\,R_\oplus$.

3.2 Contraints on asteroseismology and the 'classical' Rossiter–McLaughlin effect from radial velocity

Our GP model for stellar oscillations, variability, and Rossiter–McLaughlin effect yields a frequency of maximum oscillation power, $\nu_{\rm max} = 2771^{+65}_{-60}$ μHz, which translates to an oscillation period of ∼6 min. The longer time-scale variability, $\omega_{\rm bkg}$, is found to be ∼2.5 h. From Fig. 1, we estimated $\nu_{\rm max} \simeq 2900$ μHz, but note that the visual estimate is skewed towards higher frequencies since the Nyquist frequency of run A is ∼3000 μHz and will thus have increased power close to this frequency. The Nyquist frequency for run B is however ∼4000 μHz and is thus sampled at a fast enough rate to resolve the true frequency.

Although we do not detect $\Delta\nu$ from the *ESPRESSO* analysis, an estimate of the surface gravity can be obtained from $\nu_{\rm max}$ alone through the scaling relation (see Chaplin et al. 2011 and references therein)

$$\nu_{\rm max} \sim 3090\,\mu{\rm Hz}\,\frac{g}{g_\odot}\sqrt{\frac{T_{\rm eff,\odot}}{T_{\rm eff}}}. \quad (5)$$

This gives $\log g = 4.4018 \pm 0.0093$ and is consistent within 1σ to reported values in the discovery papers as obtained from spectral analysis in Ghezzi et al. (2010), but more than a factor 3 improvement on the uncertainty.

The posterior distribution of $v_{\rm eq}\sin i_\star$ shows a 2–3σ detection relative to 0, and a spin–orbit angle that suggests misalignment at 1σ. Based on the Bayesian information criterion (BIC), the Rossiter–McLaughlin model is not necessarily favoured, as the GP asteroseismic model can easily account for the expected ∼50 cm s^{-1} variation. We test this by re-fitting the data without a Rossiter–McLaughlin model. We therefore turned to the reloaded Rossiter–McLaughlin method, where we can analyse the line profile distortions directly to detect the spectroscopic transit and measure λ.

3.3 Detection of the Doppler shadow of π Men c

The stellar surface velocities over the transit duration are plotted in Fig. 5. The two sequences follow the same overall trend, namely a

Downloaded from https://academic.oup.com/mnras/article/502/2/2893/6123888 by University of Birmingham user on 09 March 2021

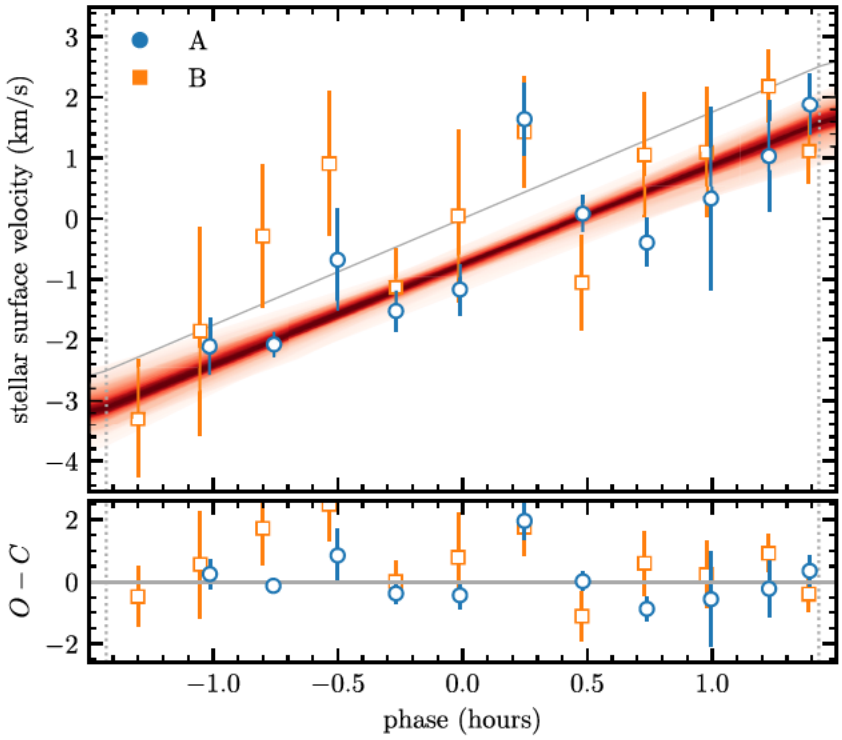


Figure 5. *Upper panel:* The local surface velocities obtained from fitting Gaussian profiles to the in-transit residual CCFs, shown as blue circles and orange squares for runs A and B, respectively. The red shaded area denote the 50th–99th percentiles of the models generated from the posterior distribution of the fit. As a reference, the grey line denotes the $\lambda = 0°$ line, which shows that alignment is firmly rejected. *Lower panel:* The residuals from the best-fitting model.

positive slope for the duration of the transit as the planet moves from blueshifted to redshifted areas on the disc of the rotating star. This signature is expected for a prograde orbit, indicating the Rossiter–McLaughlin effect is detected. The combined fit to both sequences give a projected rotational velocity $v_{\rm eq} \sin i_\star = 3.16 \pm 0.27\,{\rm km\,s^{-1}}$. This value is consistent with the measurements obtained from spectroscopic line broadening in other works (Damasso et al. 2020). The offset of the model from the velocity zero-point at mid-transit determines the projected spin–orbit angle, λ. We find that the orbit is misaligned $-24\overset{\circ}{.}0 \pm 4\overset{\circ}{.}1$ with the stellar spin axis. The reduced χ^2 (χ^2_ν) is 1.73 for the joint data set.

We also fit the two sequences separately to check their consistency. For run A, we obtain $v_{\rm eq} \sin i_\star = 3.13^{+0.31}_{-0.32}\,{\rm km\,s^{-1}}$, $\lambda = -27.2^{+4.8}_{-5.3}$ deg ($\chi^2_\nu = 2.19$); and for run B, we get $v_{\rm eq} \sin i_\star = 2.53^{+0.68}_{-0.78}\,{\rm km\,s^{-1}}$, $\lambda = -8.0^{+12.9}_{-11.6}$ deg ($\chi^2_\nu = 1.53$). The joint fit is primarily driven by run A due to its higher SNR data, but $v_{\rm eq} \sin i_\star$ for run B is consistent with A to 1σ, and λ to within 2σ. The lower value of λ for run B is driven by the first four points (in particular the 3rd and 4th), which are observed at low SNR compared to the second half of the transit. Fitting run B without these data gives $v_{\rm eq} \sin i_\star = 3.3 \pm 0.8\,{\rm km\,s^{-1}}$ and $\lambda = -17° \pm 8°$, which is more in line with run A. In Section 4.1, we discuss how the choice of master CCF may affect the parameter retrieval.

Using *Hipparcos* data of π Men, Zurlo et al. (2018) found a 18.3 ± 1.0 d periodic signal from a periodogram analysis that they interpreted as stellar rotation. Indeed, the *TESS* Sector 1 light curve show some signs of an ~20 d signal, which seem to have disappeared in the three month gap until π Men was observed in the next sector. We can combine the measurement of $P_{\rm rot}$ with $R_\star$ to derive the rotational velocity, $v = 2\pi R_\star / P_{\rm rot}$. We can then randomly sample from the distribution of v, and the stellar inclination, $\sin i_\star$, whose product can be compared to the measured $v_{\rm eq} \sin i_\star$ value from the Rossiter–McLaughlin analysis to retrieve the probability distribution of $i_\star$ (Masuda & Winn 2020). We carry out this exercise, but instead sample uniformly in $\cos i_\star$, and find that $i_\star = 90\overset{\circ}{.}1 \pm 17\overset{\circ}{.}3$. In turn, this allows us to derive the true obliquity, $\psi = 26.9^{+5.8}_{-4.7}$ deg.

4 DISCUSSION

4.1 Robustness of $v_{\rm eq} \sin i_\star$ and λ

We test the robustness of our results using a number of procedures. First, we check whether our results are driven by a few points from run A that have low uncertainties, in particular the points at −1.0 and −0.75 h and +0.5 h, whose errors might be underestimated considering some of these have a low SNR disc-integrated cross-correlation function (DI CCF). We repeat our fitting procedure by excluding these three points and find $v_{\rm eq} \sin i_\star = 2.92 \pm 0.45\,{\rm km\,s^{-1}}$, $\lambda = -23° \pm 5°$, which is consistent to our previous analysis.

Next, we test the sensitivity of $v_{\rm eq} \sin i_\star$ and λ to our choice of fitting the residual CCF uncertainty, ϵ, to make sure the CCF uncertainties are not underestimated. We re-analyse the Gaussian fits to the residual CCFs from both runs, but this time fix the residual CCF uncertainties to the values provided by the *ESPRESSO* data products. Here, we also retrieve consistent results, $v_{\rm eq} \sin i_\star = 2.92 \pm 0.15\,{\rm km\,s^{-1}}$, $\lambda = -19° \pm 2°$, albeit with smaller uncertainties because the fixed *ESPRESSO* CCF uncertainties are up to 30 per cent smaller than our fitted uncertainty, ϵ. We therefore opted for the more conservative approach of fitting ϵ.

We also test how sensitive our results are to the uncertainty in the centre of the line profile. A Gaussian fit to the averaged out-of-transit disc-integrated CCFs gives an uncertainty in the radial velocity centre of $\sim 3\,{\rm cm\,s^{-1}}$, which is below the $10\,{\rm cm\,s^{-1}}$ instrumental precision of *ESPRESSO*. Never the less, we repeat

Downloaded from https://academic.oup.com/mnras/article/502/2/2893/6123888 by University of Birmingham user on 09 March 2021

Table 4. System parameters for π Men (HD 39091) and derived planet parameters from the *ESPRESSO* and *TESS* analysis.

Parameter	Description	Value	Reference/data
System information and stellar parameters			
Gaia DR2 ID	–	4623036865373793408	Simbad
TIC	*TESS* Input Catalogue ID	261136679	MAST
α	Right ascension	$5^h37^m09^s.89$	Simbad
δ	Declination	$-80°28'08''.8$	Simbad
V (mag)	Apparent magnitude	5.67	Simbad
Distance (pc)	Parallax distance	18.27 ± 0.02	Gaia Collaboration et al. (2018)
$T_{\rm eff}$ (K)	Effective temperature	5998 ± 62	Damasso et al. (2020)
log g (cgs)	Stellar surface gravity	4.43 ± 0.1	Damasso et al. (2020)
[Fe/H] (dex)	Stellar metallicity	0.09 ± 0.04	Damasso et al. (2020)
$v_{\rm eq}\sin i_\star$ (km s^{-1})	Projected rotational velocity	3.34 ± 0.07^a	Damasso et al. (2020)
$M_\star$ ($M_\odot$)	Stellar mass	1.07 ± 0.04	Damasso et al. (2020)
$R_\star$ ($R_\odot$)	Stellar radius	1.17 ± 0.02	Damasso et al. (2020)
$L_\star$ ($L_\odot$)	Stellar luminosiity	1.44 ± 0.02	Huang et al. (2018b)
$\tau_\star$ (Gyr)	Stellar age	$2.98^{+1.4}_{-1.3}$	Huang et al. (2018b)
$P_{\rm rot}$ (d)	Photometric rotation period	18.3 ± 1.0	Zurlo et al. (2018)
Transit parameters			
P (days)	Orbital period	6.2678399 ± 0.000011	*TESS*
T_0 (BJD$_{\rm UTC}$ − 2450000)	Transit mid-point	$8425.789204^{+0.000279}_{-0.000280}$	*TESS*
$R_{\rm p}$ ($R_\oplus$)	Planet radius	$2.0189^{+0.0465}_{-0.0448}$	*TESS*
$R_{\rm p}/R_\star$	Planet-to-star radius ratio	$0.015844^{+0.000139}_{-0.000136}$	*TESS*
D_{T_0} (ppm)	Transit depth at T_0	$267.59^{+4.16}_{-3.89}$	*TESS*
$R_\star/a$	Scaled separation	$0.07978^{+0.00175}_{-0.00172}$	*TESS*
b ($R_\star$)	Impact parameter	$0.6465^{+0.0191}_{-0.0210}$	*TESS*
$i_{\rm p}$ (°)	Orbital inclination	$87.045^{+0.157}_{-0.156}$	*TESS*
T_{14} (d)	Transit duration between 1st and 4th contacts	$0.125001^{+0.000484}_{-0.000464}$	*TESS*
e	Eccentricity	0^b	*TESS*
ω (°)	Argument of periastron	0^b	*TESS*
'Classical' Rossiter–McLaughlin and asteroseismology			
$v_{\rm eq}\sin i_\star$ (km s^{-1})	Projected rotation velocity	$4.29^{+1.57}_{-1.58}$	*ESPRESSO* RVs
λ (°)	Spin–orbit angle	$-20.4^{+26.4}_{-24.6}$	*ESPRESSO* RVs
$\nu_{\rm max}$ (μHz)	Frequency of maximum oscillation	$2771.2^{+65.3}_{-59.9}$	*ESPRESSO* RVs
log g (cgs)	Stellar surface gravity^c	4.4018 ± 0.0093	*ESPRESSO* RVs
Reloaded Rossiter–McLaughlin			
$v_{\rm eq}\sin i_\star$ (km s^{-1})	Projected rotational velocity (runs A, B)	3.16 ± 0.27	*ESPRESSO* CCFs
λ (°)	Projected spin–orbit angle (runs A, B)	-24.0 ± 4.1	*ESPRESSO* CCFs
$i_\star$ (°)	Stellar inclination^d	90.1 ± 17.3	$P_{\rm rot}$, $R_\star$, $v_{\rm eq}\sin i_\star$
ψ (°)	3D spin–orbit angle^d	$26.9^{+5.8}_{-4.7}$	λ, $i_{\rm p}$, $i_\star$

[a]Determined from spectral broadening.
[b]Fixed.
[c]Derived from $\nu_{\rm max}$ using equation (5).
[d]Derived from the combination of $P_{\rm rot}$, $R_\star$, and $v_{\rm eq}\sin i_\star$.

our analysis by perturbing the line centre velocity by $\pm 3\,{\rm cm\,s^{-1}}$, and find that our results are not very sensitive to the line centre uncertainty, $v_{\rm eq}\sin i_\star = 3.06 \pm 0.25\,{\rm km\,s^{-1}}$, $\lambda = -19° \pm 4°$ and $v_{\rm eq}\sin i_\star = 3.06 \pm 0.25\,{\rm km\,s^{-1}}$, $\lambda = -24° \pm 4°$ (by adding and subtracting, respectively). The reduced χ^2 does, however, slightly increase from 1.7 to 2.3, which indicates our original solution is optimized.

It is reasonable to assume that the particular selection of spectra to build the master out-of-transit CCF in the reloaded Rossiter–McLaughlin method can impact the results. Indeed, we experimented with several ways of building the reference CCFs. Run A was particularly sensitive to this choice due to the variation in CCF shape during transit from variable observing conditions. Doing the standard approach, i.e. averaging all out-of-transit CCFs into one master CCF that is applied equally to all the binned in-transit points led to significant correlations of the retrieved surface velocities with the DI CCF contrasts. Typically the retrieved parameters using this approach would be $v_{\rm eq}\sin i_\star \sim 5\,{\rm km\,s^{-1}}$ and $\lambda \sim -50°$ for $\chi^2_\nu >> 1$. Besides the poor fit, the $v_{\rm eq}\sin i_\star$ measurement was inconsistent with that determined from rotational broadening, and neither parameter was supported by the retrieved values for run B. We also attempted to build custom master CCFs for each binned in-transit CCF by selecting out-of-transit CCFs that has similar depths, within a pre-determined range. However, this approach led to the in-transit CCFs at the lowest and highest SNR/contrast (beginning and end of transit, Fig. B1) to have very few matches, which led to a low SNR master

Downloaded from https://academic.oup.com/mnras/article/502/2/2893/6123888 by University of Birmingham user on 09 March 2021

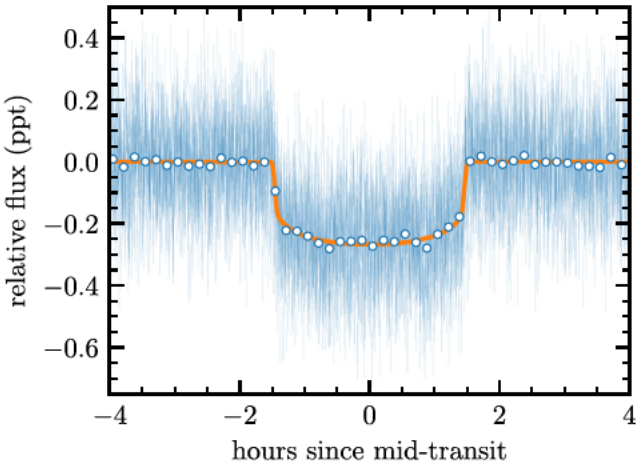


Figure 6. *TESS* data folded on the transit period after removing the best-fitting GP model (*blue points*), and binned to 10 min averages (*blue/white points*). We also show the best-fitting transit model (*orange line*).

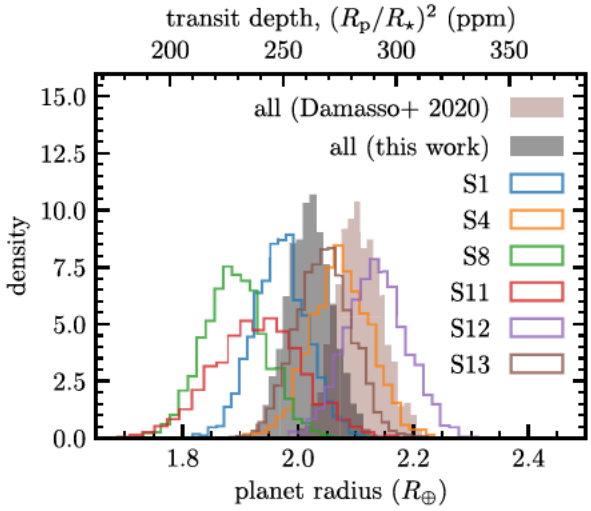


Figure 7. Comparison of the transit depth and planet radius posterior distributions from the MCMC sampling from each sector, and the full combined fit using all sectors (*grey, filled*) using a transit and GP model. We also show the posterior distribution from Damasso et al. (2020) (*pink, filled*) for comparison. These results are consistent with the previously reported values from Huang et al. (2018b) and Gandolfi et al. (2018).

CCF. This again lead to some correlations in the retrieved surface velocities, and a solution that is inconsistent with the priors we placed on $R_\star/a$ and i_p. Out of the many methods we experimented with, the method we outlined in Section 2.4.1 was the only one that led to few correlations in the surface velocities, gave $v_{eq} \sin i_\star$ consistent with the expectation from spectroscopic broadening, and overall less complex.

While the SNR of run B is overall lower than that of run A due to faster sampling and thus more time spent reading the CCD, the observing conditions on that night are much more stable, and gradually improve for the entire duration of the transit. This leads to a slope in the DI CCF contrast of the in-transit data that is easier to deal with. Ultimately, we chose the same strategy for creating master CCFs as for run A for consistency. Overall, we found that the retrieved $v_{eq} \sin i_\star$ and λ for run B are less sensitive to the choice of master CCF. For example, the DI CCFs after the transit of run B have higher SNR than the pre-transit data. A more conservative – and less complex – approach for run B would be to use all the post-transit CCFs as reference. This gives $v_{eq} \sin i_\star \approx 3.5\,\mathrm{km\,s^{-1}}$, $\lambda \approx -30°$. This is more consistent with the result from run A. However, due to lower SNR at the beginning of transit, this method leads to three of the residual profiles being flat. Similarly, we can also create custom master CCFs for each binned in-transit CCF as we outlined for run A in the previous paragraph. This method produces similar $v_{eq} \sin i_\star$, $\lambda \approx -17°$.

Ultimately, the method of creating master CCFs should be determined based on the specific characteristics of each data set, which we have shown is different between runs A and B. Adopting a less complex and conservative approach for run B (but sacrificing consistency), we obtain fully consistent results with run A, namely that the orbit of π Men c is misaligned with the stellar spin by about $-30°$.

4.2 Dynamical history

The formation of super-Earth and sub-Neptune multiplanetary systems is a subject of intense debate (Lee, Chiang & Ormel 2014; Mohanty et al. 2018; Raymond et al. 2018; Coleman et al. 2019; Schoonenberg et al. 2019; Wu 2019). To this day, it remains unclear whether super-Earths and sub-Neptunes form within the water iceline, or whether they can form beyond. Either or both might be true. Detections of super-Earths in circumbinary configurations (e.g. Orosz et al. 2019; Kostov et al. 2020) point out that super-Earths can likely form at large distances before migrating inwards (Martin 2018; Pierens et al. 2020).

When proposing the observations reported here for DDT, we had initially speculated that the architecture of the π Men system was reminiscent of past dynamical interactions, and wanted to verify this with Rossiter–McLaughlin time series. These suspicions are now confirmed by the inclined orbital plane of the inner planet π Men c, but also thanks to three recent analyses that appeared while we were finalizing our own paper. Xuan & Wyatt (2020), Damasso et al. (2020), and De Rosa, Dawson & Nielsen (2020) combined radial velocities with *Gaia* and *Hipparcos* astrometry, and measured that π Men b is inclined with $i_b = 45°.8^{+1°.4}_{-1°.1}$ (Damasso et al. 2020), which also shows a large mutual inclination between π Men b and π Men c.

Together this provides evidence that super-Earths can likely form beyond the iceline around single stars. On its own, the inclination of π Men b did not imply much for π Men c. However, a natural cause for π Men c's own orbital inclination is an exchange of angular momentum between the outer and inner planetary orbits (e.g. Matsumura et al. 2010; Wu & Lithwick 2011). Currently, the two planets are likely too distant from one another to allow such an exchange. To allow raised inclinations, planets b and c would have needed to be closer. Due to their mass and angular momentum ratios, it is more likely that planet c moved inwards than for planet b to move outwards; this would imply that planet c might have formed near or beyond the iceline. Detailed *N*-body numerical simulations will be necessary to explore this scenario further.

5 CONCLUSION

In this paper, we have presented two high-resolution spectroscopic transits of the super-Earth π Men c that we observed with *ESPRESSO*. The two time series show a rich concoction of signals of various origins. We perform an asteroseismic analysis on the radial-velocity time series using GPs and clearly detect the frequency of

Downloaded from https://academic.oup.com/mnras/article/502/2/2893/6123888 by University of Birmingham user on 09 March 2021

maximum oscillation, $\nu_{\rm max}$. We are not sensitive to the measurement of the large frequency separation, $\Delta\nu$, and can therefore not directly measure the stellar mass and radius, but are able to obtain a much tighter constraint on $\log g$ than from spectroscopy.

We performed a transit analysis on all the available data of π Men from *TESS* Cycle 1: a total of six sectors. We revise the transit parameters for π Men c and find a radius of $R_{\rm p} = 2.019^{+0.047}_{-0.045}\,{\rm R}_{\oplus}$, which is roughly consistent with previous analyses in Damasso et al. (2020), Gandolfi et al. (2018), and Huang et al. (2018b).

We attempted to fit the *ESPRESSO* radial velocity time series to isolate 'classical', i.e. velocimetric, Rossiter–McLaughlin effect, but the radial velocity signal was thwarted by asteroseismic *p* modes and a longer term variation that we attribute to a form of stellar granulation. Instead, we turned to the reloaded Rossiter–McLaughlin method to detect the Doppler shadow. Using this method, we were able to detect the transit of π Men c in spectroscopy using *ESPRESSO*, and found that its orbit is misaligned by $-24\overset{\circ}{.}0 \pm 4\overset{\circ}{.}1$ with the stellar spin axis. This makes π Men c the smallest mass-ratio planet measured with the Rossiter–McLaughlin effect. Combining our results with the recent detection of the inclination of the external planet (Damasso et al. 2020; De Rosa et al. 2020; Xuan & Wyatt 2020), we speculate that π Men c likely formed at a large distance from the star. There it gravitationally interacted with π Men b, an interaction that is still evident from their mutual inclinations, π Men c's own inclination with respect to the stellar spin axis, and the high eccentricity of π Men b.

This work stands as a testament to a new avenue of scientific investigation, namely the origins of super-Earth and sub-Neptune planets, which is now made possible by the extreme precision of *ESPRESSO*.

ACKNOWLEDGEMENTS

We would like to thank the referee for their thorough and constructive comments that substantially improved the paper. Parts of this work were carried out during a Fulbright Fellowship at the University of Chicago, funded by the U.S.–Norway Fulbright Foundation. VKH would like to thank Daniel Fabrycky and David Martin for kindly hosting him at the University of Chicago, and for useful discussions on this work. We would also like to thank Dan Foreman-Mackey for help on integrated CELERITE kernels and separation of kernel predictions, and Vincent Bourrier for discussions on strategies for mitigating stellar oscillations. VKH is supported by a Birmingham Doctoral Scholarship, and by a studentship from Birmingham's School of Physics and Astronomy. This research received funding from the European Research Council (ERC) under the European Union's Horizon 2020 research and innovation programme (grant agreement no. 803193/BEBOP and 804752/CartographY). HMC acknowledges the financial support of the National Centre for Competence in Research PlanetS supported by the Swiss National Science Foundation (SNSF), and the UK Research Innovation Future Leaders Fellowship (MR/S035214/1). This paper includes data collected by the TESS mission. Funding for the TESS mission is provided by the NASA's Science Mission Directorate. This research made use of EXOPLANET (Foreman-Mackey 2019) and its dependences (Astropy Collaboration 2013, 2018; Salvatier et al. 2016; The Theano Development Team 2016; Foreman-Mackey et al. 2017; Foreman-Mackey 2018; Luger et al. 2019; Agol, Luger & Foreman-Mackey 2020). This research also made use of the the open-source PYTHON packages EMCEE (Foreman-Mackey et al. 2013), ELLC (Maxted 2016), NUMPY (van der Walt, Colbert & Varoquaux 2011), SCIPY (Jones et al. 2002), and MATPLOTLIB (Hunter 2007).

DATA AVAILABILITY

The spectroscopic data underlying this article are available from the public ESO archive.[2] The photometric data are publicly available from the Mikulski Archive for Space Telescopes (MAST) portal.[3]

REFERENCES

Addison B. C. et al., 2020, preprint (arXiv:2006.13675)
Agol E., Luger R., Foreman-Mackey D., 2020, AJ, 159, 123
Albrecht S., Reffert S., Snellen I., Quirrenbach A., Mitchell D. S., 2007, A&A, 474, 565
Angus R., Morton T., Aigrain S., Foreman-Mackey D., Rajpaul V., 2018, MNRAS, 474, 2094
Armitage P. J., 2013, Astrophysics of Planet Formation. Cambridge University Press, Cambridge
Astropy Collaboration, 2013, A&A, 558, A33
Astropy Collaboration, 2018, AJ, 156, 123
Barclay T., Pepper J., Quintana E. V., 2018, ApJS, 239, 2
Baruteau C. et al., 2014, Protostars and Planets VI. University of Arizona Press, Tucson, p. 667
Batalha N. M. et al., 2013, ApJS, 204, 24
Bitsch B., Crida A., Libert A.-S., Lega E., 2013, A&A, 555, A124
Bonfils X. et al., 2013, A&A, 549, A109
Borucki W. J. et al., 2010, Science, 327, 977
Bourrier V., Hébrard G., 2014, A&A, 569, A65
Bourrier V., Cegla H. M., Lovis C., Wyttenbach A., 2017, A&A, 599, A33
Bourrier V. et al., 2018, Nature, 553, 477
Cegla H. M., Lovis C., Bourrier V., Beeck B., Watson C. A., Pepe F., 2016, A&A, 588, A127
Chabrier G., Johansen A., Janson M., Rafikov R., 2014, Protostars and Planets VI. University of Arizona Press, Tucson, p. 619
Chaplin W. J. et al., 2011, ApJ, 732, 54
Chaplin W. J., Cegla H. M., Watson C. A., Davies G. R., Ball W. H., 2019, AJ, 157, 163
Chatterjee S., Ford E. B., Matsumura S., Rasio F. A., 2008, ApJ, 686, 580
Coleman G. A. L., Leleu A., Alibert Y., Benz W., 2019, A&A, 631, A7
Collier Cameron A., Bruce V. A., Miller G. R. M., Triaud A. H. M. J., Queloz D., 2010, MNRAS, 403, 151
Damasso M. et al., 2020, A&A, 642, A31
Dawson R. I., 2014, ApJ, 790, L31
Dawson R. I., Lee E. J., Chiang E., 2016, ApJ, 822, 54
De Rosa R. J., Dawson R., Nielsen E. L., 2020, A&A, 640, A73
Dressing C. D., Charbonneau D., 2015, ApJ, 807, 45
Ehrenreich D. et al., 2020, Nature, 580, 597
Fabrycky D., Tremaine S., 2007, ApJ, 669, 1298
Farr W. M. et al., 2018, ApJ, 865, L20
Foreman-Mackey D., 2018, Res. Notes Am. Astron. Soc., 2, 31
Foreman-Mackey D , 2019, Astrophysics Source Code Library, record ascl:1910.005
Foreman-Mackey D., Hogg D. W., Lang D., Goodman J., 2013, PASP, 125, 306
Foreman-Mackey D., Agol E., Ambikasaran S., Angus R., 2017, AJ, 154, 220
Fressin F. et al., 2013, ApJ, 766, 81
Gaia Collaboration, 2018, A&A, 616, A1
Gaidos E., Mann A. W., Kraus A. L., Ireland M., 2016, MNRAS, 457, 2877
Gandolfi D. et al., 2018, A&A, 619, L10

[2] www.archive.eso.org
[3] https://mast.stsci.edu/portal/Mashup/Clients/Mast/Portal.html

Downloaded from https://academic.oup.com/mnras/article/502/2/2893/6123888 by University of Birmingham user on 09 March 2021

Gelman A., Carlin J. B., Stern H. S., Rubin D. B., 2003, Bayesian Data Analysis. 2nd edn., CRC Press, Boca Raton, London, New York, Washington, D.C.
Ghezzi L., Cunha K., Smith V. V., de Araújo F. X , Schuler S. C., de la Reza R., 2010, ApJ, 720, 1290
Gillen E., Hillenbrand L. A., David T. J., Aigrain S., Rebull L., Stauffer J., Cody A. M., Queloz D., 2017, ApJ, 849, 11
Grunblatt S. K., Howard A. W., Haywood R. D., 2015, ApJ, 808, 127
Hansen B. M. S., Murray N., 2012, ApJ, 751, 158
Hardegree-Ullman K. K., Cushing M. C., Muirhead P. S., Christiansen J. L., 2019, AJ, 158, 75
Harvey J., 1985, in Rolfe E., Battrick B., eds, ESA Special Publication, Vol. 235, Future Missions in Solar, Heliospheric & Space Plasma Physics. ESA Scientific & Technical Publications Branch, Noordwijk, The Netherlands, p. 199
Haywood R. D. et al., 2014, MNRAS, 443, 2517
Hirano T., Narita N., Shporer A., Sato B., Aoki W., Tamura M., 2011, PASJ, 63, 531
Hirano T. et al., 2020, ApJ, 899, L13
Hoffman M. D., Gelman A., 2014, J. Mach. Learn. Res., 15, 1593
Howard A. W. et al., 2010, Science, 330, 653
Huang C. X. et al., 2018a, ApJL, 868, L39
Huang C. X. et al., 2018b, ApJ, 868, L39
Hunter J. D., 2007, Comput. Sci. Eng., 9, 90
Johansen A., Lambrechts M., 2017, Ann. Rev. Earth Planet. Sci , 45, 359
Jones H. R. A., Paul Butler R., Tinney C. G., Marcy G. W., Penny A. J., McCarthy C., Carter B. D., Pourbaix D., 2002, MNRAS, 333, 871
Kipping D. M., 2013, MNRAS, 434, L51
Kostov V. B. et al., 2020, AJ, 159, 253
Kunovac-Hodzic V., Triaud A., 2019, AAS – Extreme Solar Systems IV, Vol. 51. Bulletin of the American Astronomical Sciety, p. 308.01
Kunovac Hodžić V. et al., 2020, MNRAS, 497, 1627
Lambrechts M., Morbidelli A., Jacobson S. A., Johansen A., Bitsch B., Izidoro A., Raymond S. N., 2019, A&A, 627, A83
Lee E. J., Chiang E., Ormel C. W., 2014, ApJ, 797, 95
Lightkurve Collaboration, 2018, Astrophysics Source Code Library, record ascl:1812.013
López-Morales M. et al., 2014, ApJ, 792, L31
Luger R., Agol E., Foreman-Mackey D., Fleming D. P., Lustig-Yaeger J., Deitrick R., 2019, AJ, 157, 64
Martin D. V., 2018, Handbook of Exoplanets. Springer International Publishing, Cham, p. 156
Masuda K., Winn J. N., 2020, AJ, 159, 81
Matsumura S., Thommes E. W., Chatterjee S., Rasio F. A., 2010, ApJ, 714, 194
Maxted P. F. L., 2016, A&A, 591, A111
Mayor M. et al., 2011, preprint (arXiv:1109.2497)
McLaughlin D. B., 1924, ApJ, 60, 22
Mohanty S., Jankovic M. R., Tan J. C., Owen J. E., 2018, ApJ, 861, 144
Naoz S., Farr W. M., Lithwick Y., Rasio F. A., Teyssandier J., 2011, Nature, 473, 187
Orosz J. A. et al., 2019, AJ, 157, 174
Paardekooper S.-J., Leinhardt Z. M., Thébault P., Baruteau C., 2012, ApJ, 754, L16
Palle E. et al., 2020, A&A, 643, A25
Pepe F. et al., 2014, Astron. Nachr., 335, 8
Pierens A., McNally C. P., Nelson R. P., 2020, MNRAS, 496, 2849
Pollack J. B., Hubickyj O., Bodenheimer P., Lissauer J. J., Podolak M., Greenzweig Y., 1996, Icarus, 124, 62
Press W. H., Rybicki G. B., 1989, ApJ, 338, 277
Raymond S. N., Boulet T., Izidoro A., Esteves L., Bitsch B., 2018, MNRAS, 479, L81
Ricker G. R. et al., 2015, J. Astron. Telesc. Instrum. Syst., 1, 014003
Rossiter R. A., 1924, ApJ, 60, 15
Salvatier J., Wiecki T. V., Fonnesbeck C., 2016, PeerJ Comput. Sci., 2, e55
Schlichting H. E., 2014, ApJ, 795, L15
Schlichting H. E., 2018, Handbook of Exoplanets. Springer International Publishing, Cham , preprint (astro-ph/1802.03090)
Schoonenberg D., Liu B., Ormel C. W., Dorn C., 2019, A&A, 627, A149
The Theano Development Team, 2016, preprint (arXiv:1605.02688)
Triaud A. H. M. J., 2018, Handbook of Exoplanets. Springer International Publishing, Cham, p. 2
Valenti J. A., Fischer D. A., 2005, ApJS, 159, 141
van der Walt S., Colbert S. C., Varoquaux G., 2011, Comput. Sci. Eng., 13, 22
Winn J. N. et al., 2010a, ApJ, 718, 575
Winn J. N., Fabrycky D., Albrecht S., Johnson J. A., 2010b, ApJ, 718, L145
Wu Y., 2019, ApJ, 874, 91
Wu Y., Lithwick Y., 2011, ApJ, 735, 109
Xuan J. W., Wyatt M. C., 2020, MNRAS, 497, 2096
Zurlo A. et al., 2018, MNRAS, 480, 35

APPENDIX A: *TESS* PHOTOMETRIC ANALYSIS

The most recent published orbital parameters for π Men c are based on an analysis of *TESS* Sector 1 data (Gandolfi et al. 2018; Huang et al. 2018b), with, respectively, 5- and 7-min uncertainties on the ephemerides at the time of our spectroscopic transits. Moreover, the initial analyses did not take into account correlated noise in their modelling, which may lead to underestimated errors on the reported transit parameters and can impact our Rossiter–McLaughlin modelling. The light curve from Sector 1 may also show evidence of rotational modulation from a spot on the stellar surface, which may bias the measurement of the transit depth to higher values and thus overestimate the Rossiter–McLaughlin amplitude.

π Men is in a region of the sky that is being overlapped by several *TESS* sectors while the spacecraft surveyed the Southern hemisphere in Cycle 1, which has since completed. π Men has been observed in Sectors 1 (2018 July 25–2018 August 22); 4 (2018 October 18–2018 November 15); 8 (2019 February 2–28), 11 (2019 April 22–2019 May 21), 12 (2019 May 21–2019 June 19); and 13 (2019 June 10–2019 July 18). In this section, we outline our light-curve modelling including the five remaining *TESS* sectors that were not yet available in the discovery papers, and take into account correlated noise using a GP model coupled to a transit model.

A1 Flux extraction and pixel-level decorrelation

The *TESS* 2-min cadence target pixel files (TPF) for sectors 1, 4, 8, 11, 12, and 13 were downloaded using the LIGHTKURVE package (Lightkurve Collaboration 2018). We performed simple aperture photometry using the optimal aperture as determined by the *TESS* Science Processing Operations Center (SPOC). Using this aperture, the relative contribution from contaminant flux in our target aperture is of the order 0.3 ppt, which has a negligible impact ($\sim$10 ppm) on the transit signals.

The raw light curves have systematic effects from the instrument and telescope motion, in particular at the beginning and ends of each *TESS* orbit. In order to remove these effects we applied pixel-level decorrelation (PLD) on the raw light curves using the first-order PLD basis and the top principal components from the second-order basis. In this work, we opted for an implementation as detailed in the documentation for the EXOPLANET[4] package (Foreman-Mackey 2019), but a similar more flexible version can be found in the LIGHTKURVE[5] package as well.

[4] exoplanet.dfm.io
[5] http://docs.lightkurve.org

Downloaded from https://academic.oup.com/mnras/article/502/2/2893/6123888 by University of Birmingham user on 09 March 2021

Table A1. Priors on the parameters for the photometric transit modelling. *N* refers to individual sectors.

Parameter	Prior
$M_\star$ ($M_\odot$)	$\mathcal{N}(1.07, 0.04)$
$R_\star$ ($R_\odot$)	$\mathcal{N}(1.17, 0.02)$
$\ln r_p$ ($R_\odot$)	$\mathcal{N}(-4.05, 1)$
$\ln P$ (d)	$\mathcal{N}(1.84, 1)$
T_0 (BJD-2 450 000)	$\mathcal{N}(8425.7892, 1)$
b	$\mathcal{B}^a$
$\ln \sigma_N$	$\mathcal{N}(\ln \mathrm{var}\, y_N, 10)$
$\ln \rho_N$	$\mathcal{N}(0, 10)$
$\ln s_N^2$	$\mathcal{N}(\ln \mathrm{var}\, y_N, 10)$
Δf_N	$\mathcal{N}(1, 0.1)$

[a]Impact parameter prior (beta distribution) from Kipping (2013).

A2 Transit light curve modelling of *TESS* sectors 1, 4, 8, 11, 12, and 13

We used the EXOPLANET software package (Foreman-Mackey 2019) to model the *TESS* transit signals, including a correlated noise model using GP regression with CELERITE (Foreman-Mackey et al. 2017). We assumed the star follows a quadratic limb darkening law and held the limb darkening parameters $c_1 = 0.28$, $c_2 = 0.27$ fixed for the *TESS* band, following (Huang et al. 2018b). We fit for the orbital period, P; transit mid-point, T_0; impact parameter, b; and planet radius, $\ln r_p$, while also sampling the stellar radius and mass with normal priors $R_\star = 1.17 \pm 0.02\,R_\odot$ and $M_\star = 1.07 \pm 0.04\,M_\odot$ from the analysis in Damasso et al. (2020).

For our GP model, we used a kernel with covariance function given by

$$k(\tau) = \sigma^2 \left[(1 - 1/\epsilon) \exp\left(-\frac{1-\epsilon}{\rho}\sqrt{3}\tau \right) \times (1 - 1/\epsilon) \exp\left(-\frac{1+\epsilon}{\rho}\sqrt{3}\tau \right) \right],$$

where σ describes the amplitude of the signal, and ρ is a characteristic time-scale. In the limit $\epsilon \to 0$, the above function becomes the Matérn-3/2 function, which can flexibly fit instrument systematics related to the *TESS* pointing as well as some astrophysical variability, although the light curves seem to be dominated by the former. We use the default setting in CELERITE to approximate the Matérn-3/2 function ($\epsilon = 0.01$), and fit for the logarithm of the amplitude, $\ln \sigma$, and logarithm of the time-scale, $\ln \rho$. Finally, we also fit for the logarithm of a white noise term for our photometric uncertainties, $\ln s^2$, as well as a photometric offset, Δf. Since each *TESS* sector has different noise properties, we fit each of the above nuisance parameters separately for each sector, while the transit parameters are shared between the full data set. The full set of priors used in the analysis is shown in Table A1.

We found that the measurement of a consistent transit depth between *TESS* sectors is very sensitive to the time-scale of the baseline model being fit. Even after the PLD correction, some data show somewhat disjoint 2.5-d segments from 'momentum dumps' as thrusters are fired to reorient the *TESS* spacecraft, pointing drifts at the start and/or end of each *TESS* orbit, and other show time-scale variation that is most likely related to the spacecraft pointing. In an otherwise smoothly varying light curve, these 'rapid' changes drive the time-scale of the GP kernel lower values to be able to fit both high- and low-frequency variation, which will affect the transit depth. In order to avoid biasing, the measurement of the transit depth, we remove some out-of-transit segments of data associated with rapid changes in the light curve, which range from a few hours to a few days. In addition, one transit from Sector 11 is removed due to a momentum dump during transit that is not sufficiently corrected from the PLD.

We first fit the data using a least-squares algorithm to find the maximum likelihood, and performed a single 5σ-clip on the residuals from the best-fitting model to remove outliers. We then sampled the free parameters of our model with MCMC using the No-U-Turn (NUTS) sampler (Hoffman & Gelman 2014) as implemented in PYMC3 (Salvatier et al. 2016) and EXOPLANET. We launched four independent chains, discarded the first 2000 tuning steps, and finally sampled 1000 additional steps, resulting in >1000 effective samples per parameter. All parameters reached the recommended $\hat{R} < 1.1$ (typically <1.001) convergence criterion (Gelman et al. 2003). We performed the MCMC sampling individually for each *TESS* sector, and also using the full combined data set. The baseline-corrected, phase-folded transit light curve is shown in Fig. 6, and the full transit and GP fit to the data is shown in Fig. A1 with residual rms scatter of 123 ppm.

We also searched for transit timing variations (TTVs) by fitting individual transit times, but found no significant signal. Finally, we also searched the combined *TESS* residual light curve for solar-like oscillations, but were unable to uncover evidence of detectable modes. However, as we report in Section 2, the high S/N *ESPRESSO* data do show clearly detectable oscillations in Doppler velocity.

Downloaded from https://academic.oup.com/mnras/article/502/2/2893/6123888 by University of Birmingham user on 09 March 2021

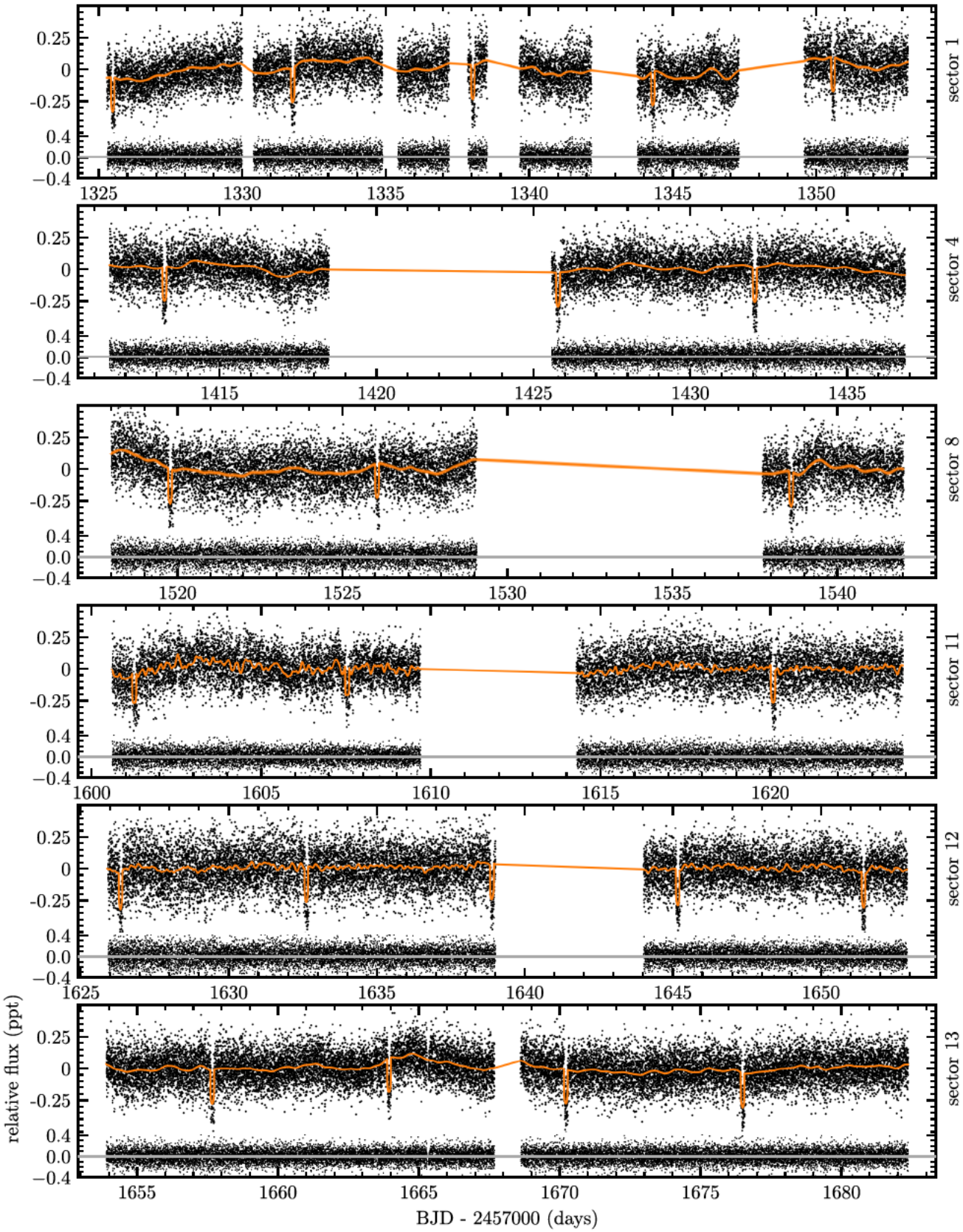


Figure A1. *TESS* data (*black points*) from sectors 1, 4, 8, 11, 12, and 13 fitted with the GP model and transit model (*orange line*) described in Section A. In the lower panel of each sector, we show the residuals from the best fit.

Downloaded from https://academic.oup.com/mnras/article/502/2/2893/6123888 by University of Birmingham user on 09 March 2021

APPENDIX B: *ESPRESSO* OBSERVABLES

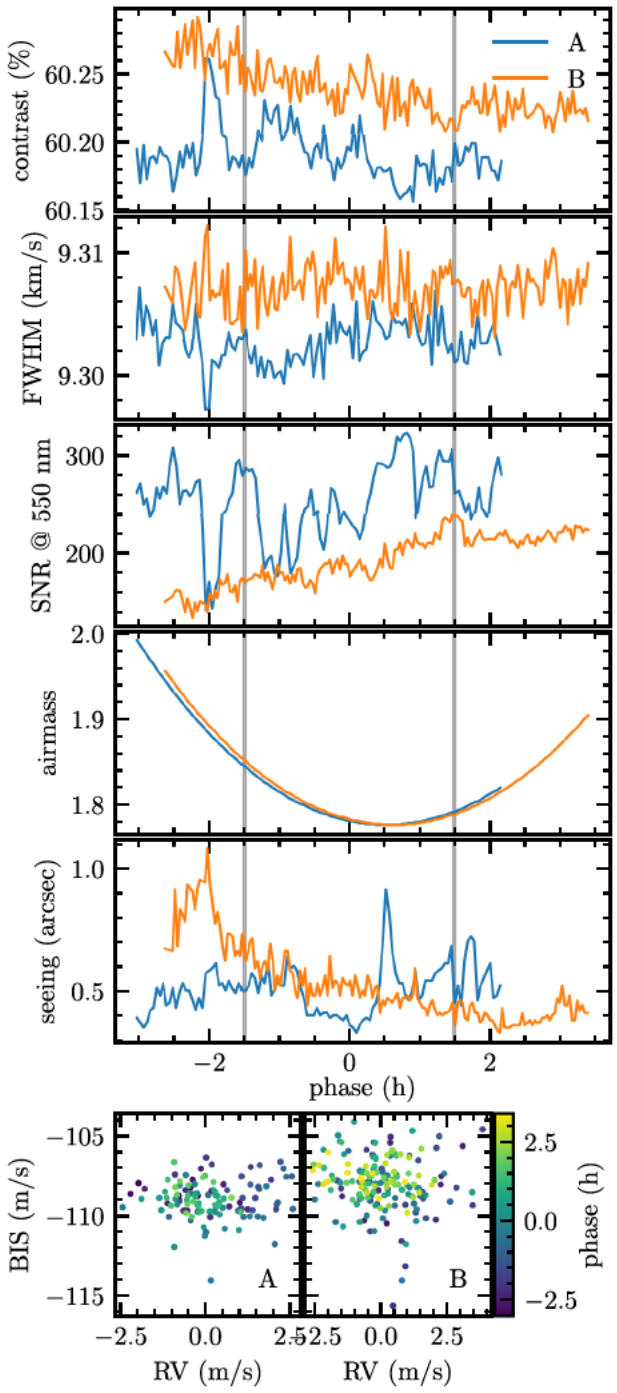


Figure B1. Observing conditions and CCF observables for *ESPRESSO* run A (*blue*) and run B (*orange*). From top to bottom: CCF contrast, CCF FWHM, SNR at 550 nm, airmass, seeing, and bisector inverse slope (BIS). The grey vertical lines denote the transit ingress and egress.

APPENDIX C: RESIDUAL CCF PROFILES

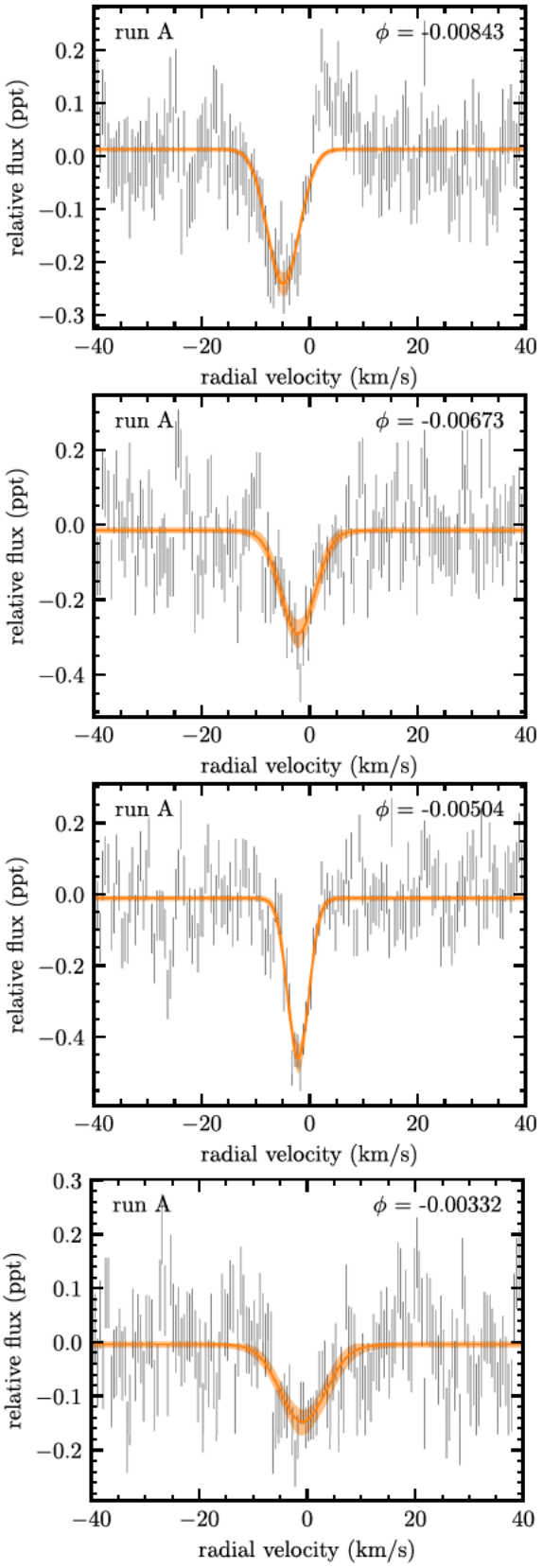


Figure C1. Gaussian fits to the 15 min binned residual line profiles from run A. The orange shading denotes the 1σ uncertainty of the model.

Downloaded from https://academic.oup.com/mnras/article/502/2/2893/6123888 by University of Birmingham user on 09 March 2021

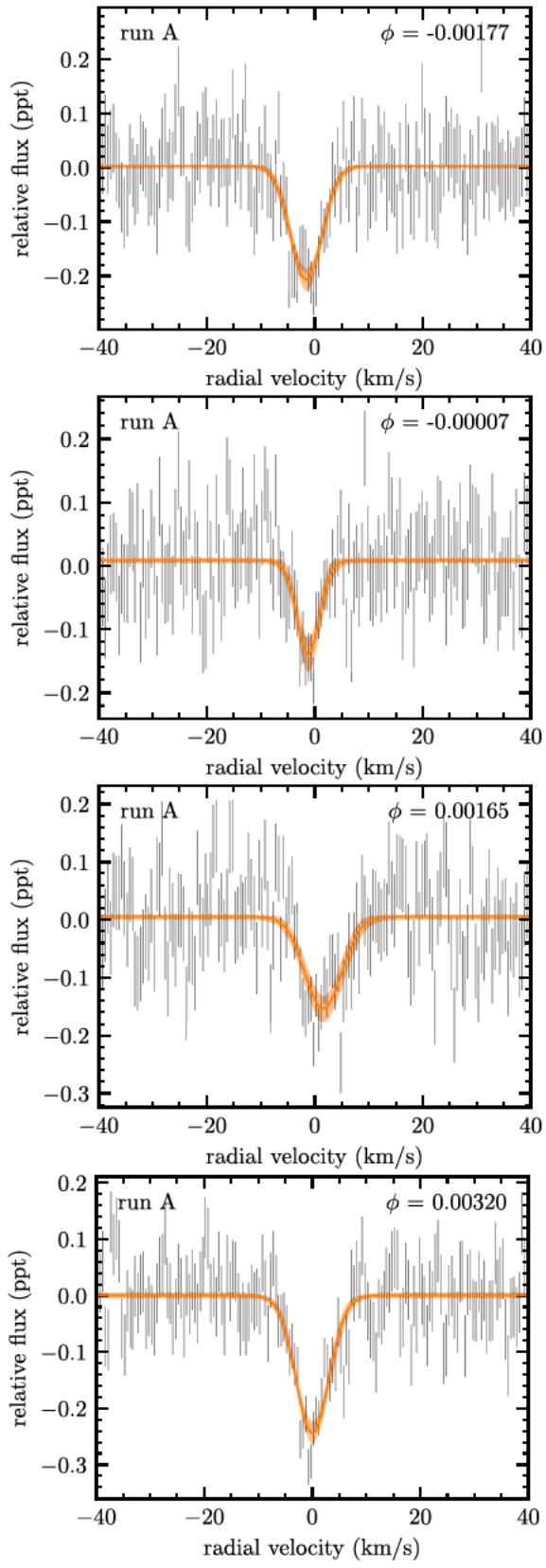


Figure C2. Gaussian fits to the 15 min binned residual line profiles from run A. The orange shading denotes the 1σ uncertainty of the model.

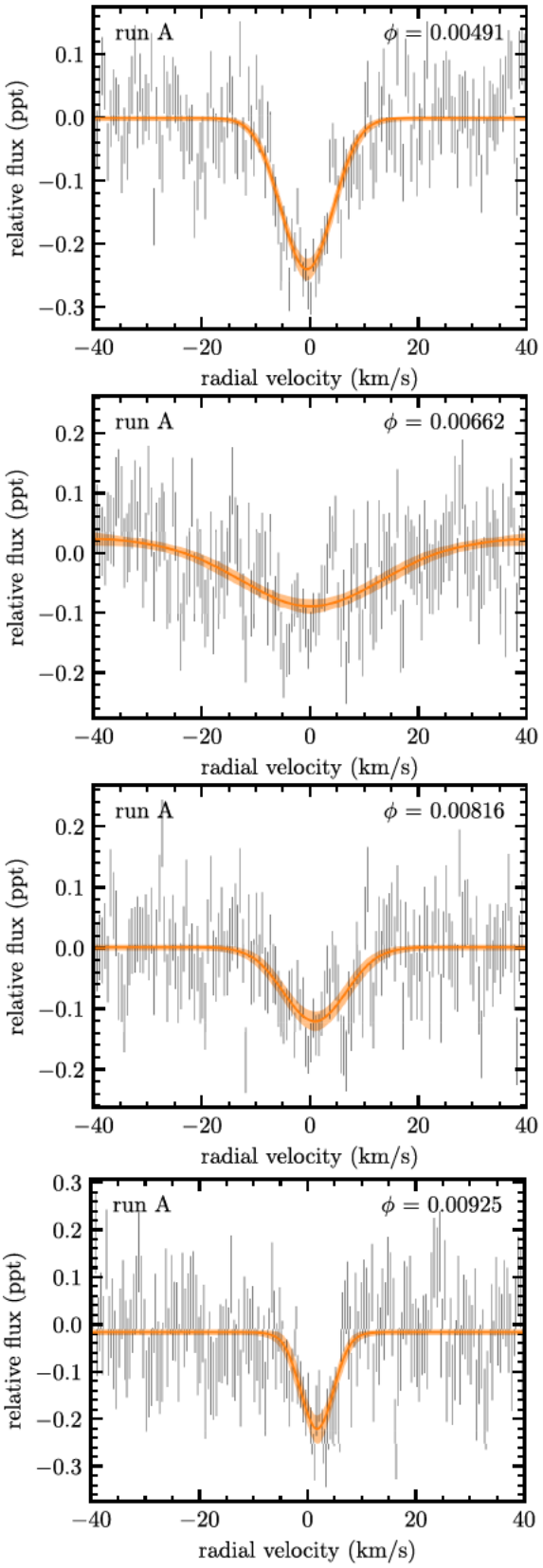


Figure C3. Gaussian fits to the 15 min binned residual line profiles from run A. The orange shading denotes the 1σ uncertainty of the model.

Downloaded from https://academic.oup.com/mnras/article/502/2/2893/6123888 by University of Birmingham user on 09 March 2021

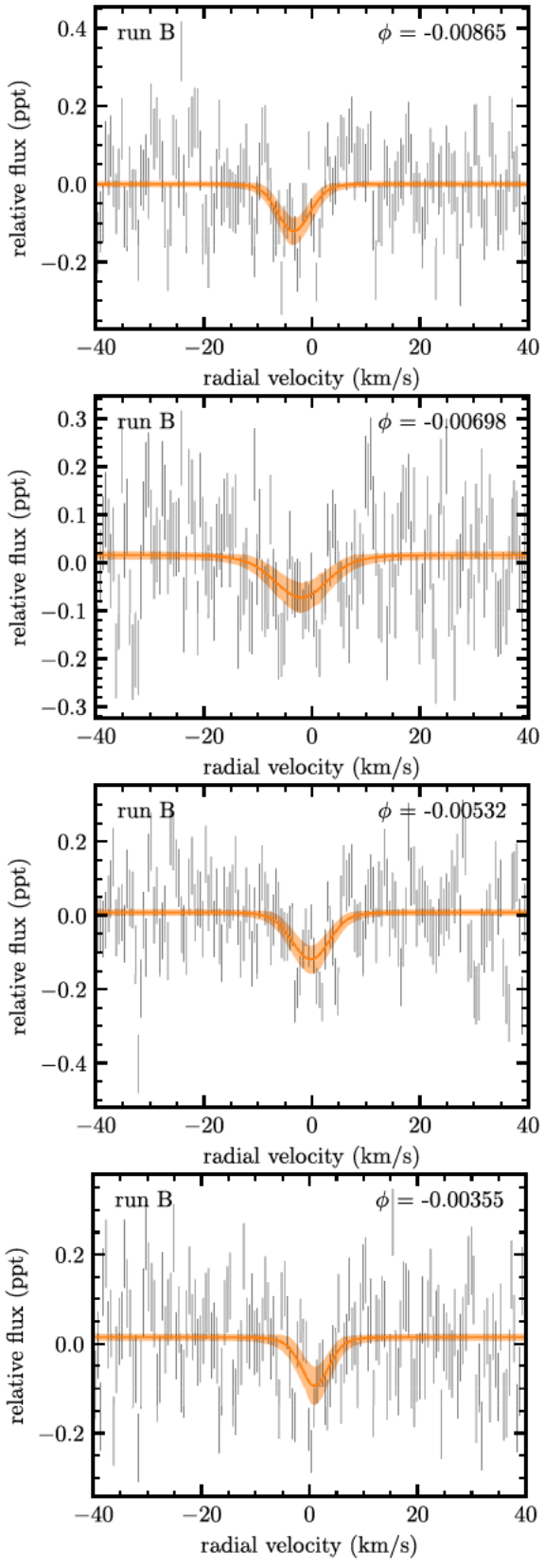


Figure C4. Gaussian fits to the 15 min binned residual line profiles from run B. The orange shading denotes the 1σ uncertainty of the model.

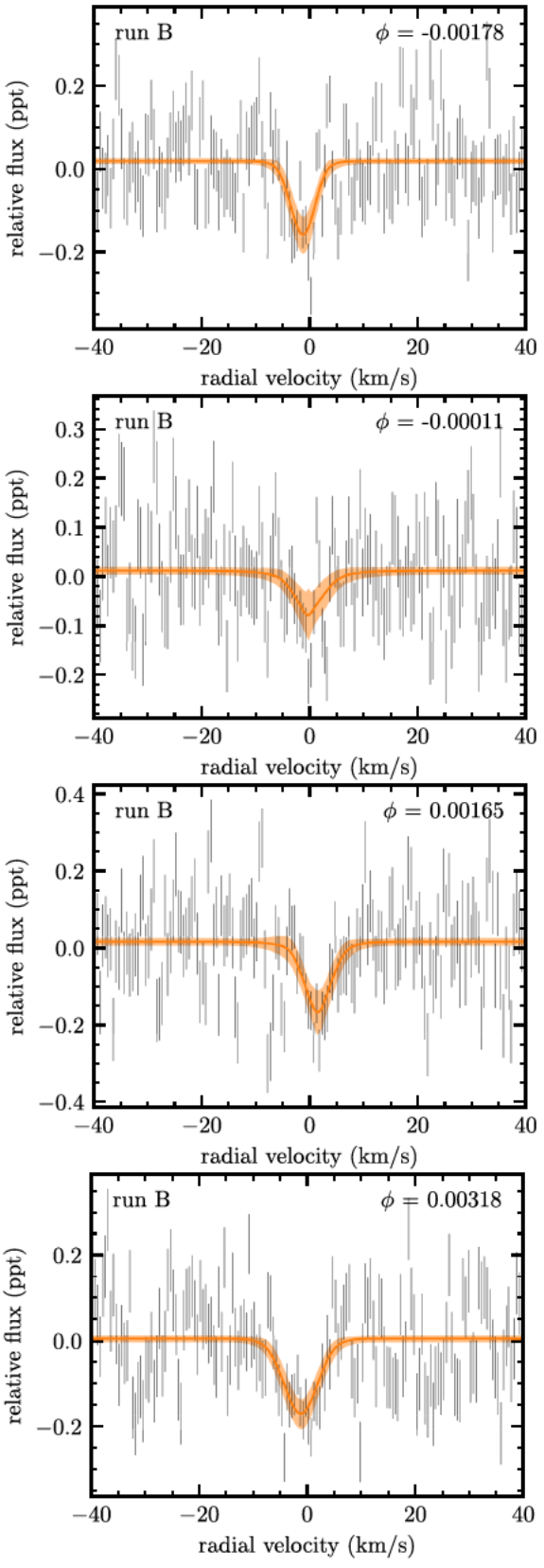


Figure C5. Gaussian fits to the 15 min binned residual line profiles from run B. The orange shading denotes the 1σ uncertainty of the model.

Downloaded from https://academic.oup.com/mnras/article/502/2/2893/6123888 by University of Birmingham user on 09 March 2021

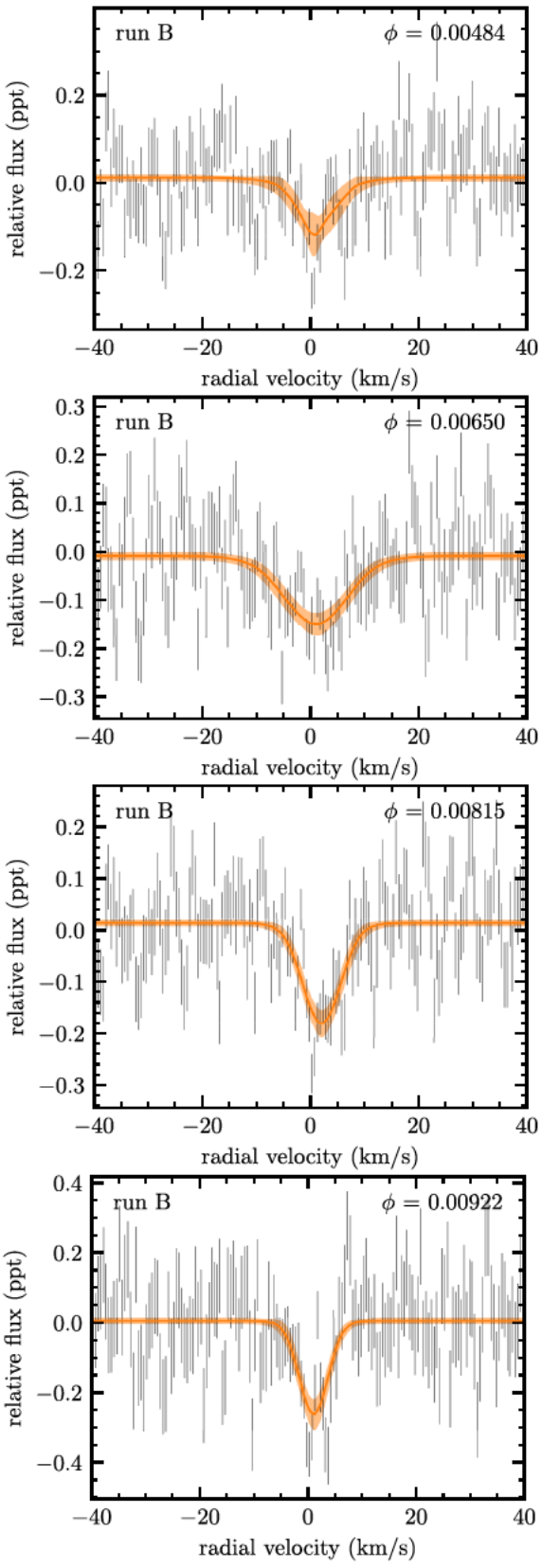


Figure C6. Gaussian fits to the 15 min binned residual line profiles from run B. The orange shading denotes the 1σ uncertainty of the model.

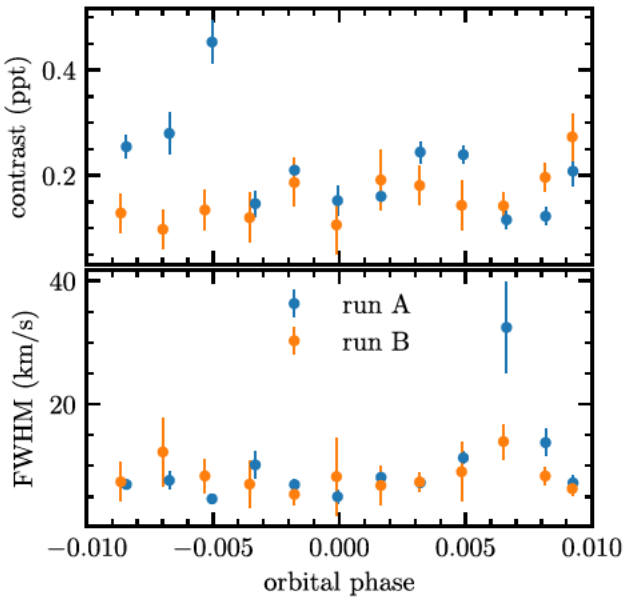


Figure C7. Comparison of the fitted local depth and width from the residual line profiles for runs A and B.

Downloaded from https://academic.oup.com/mnras/article/502/2/2893/6123888 by University of Birmingham user on 09 March 2021

APPENDIX D: GAUSSIAN PROCESS HYPERPARAMETERS

Table D1. Table of GP hyperparameters from the photometric- and radial-velocity analysis.

Parameter	Description	Value	Source
	Photometric analysis		
Sector 1			
$\log \sigma$	GP amplitude	$-0.44^{+0.18}_{-0.17}$	*TESS*
$\log \rho$	GP time-scale	$-9.93^{+0.16}_{-0.13}$	*TESS*
$\log s^2$	Flux variance	$-18.037^{+0.012}_{-0.012}$	*TESS*
Δf	Mean flux	$1.0000054^{+0.0000111}_{-0.0000123}$	*TESS*
Sector 4			
$\log \sigma$	GP amplitude	$-0.58^{+0.25}_{-0.26}$	*TESS*
$\log \rho$	GP time-scale	$-10.47^{+0.16}_{-0.14}$	*TESS*
$\log s^2$	Flux variance	$-18.169^{+0.013}_{-0.012}$	*TESS*
Δf	Mean flux	$0.9999993^{+0.0000078}_{-0.0000078}$	*TESS*
Sector 8			
$\log \sigma$	GP amplitude	$-0.47^{+0.26}_{-0.23}$	*TESS*
$\log \rho$	GP time-scale	$-9.95^{+0.18}_{-0.16}$	*TESS*
$\log s^2$	Flux variance	$-17.903^{+0.013}_{-0.014}$	*TESS*
Δf	Mean flux	$1.0000088^{+0.0000134}_{-0.0000139}$	*TESS*
Sector 11			
$\log \sigma$	GP amplitude	$-2.63^{+0.15}_{-0.14}$	*TESS*
$\log \rho$	GP time-scale	$-10.26^{+0.06}_{-0.06}$	*TESS*
$\log s^2$	Flux variance	$-18.083^{+0.012}_{-0.013}$	*TESS*
Δf	Mean flux	$1.0000049^{+0.0000034}_{-0.0000033}$	*TESS*
Sector 12			
$\log \sigma$	GP amplitude	$-2.52^{+0.28}_{-0.25}$	*TESS*
$\log \rho$	GP time-scale	$-10.71^{+0.08}_{-0.08}$	*TESS*
$\log s^2$	Flux variance	$-17.873^{+0.012}_{-0.011}$	*TESS*
Δf	Mean flux	$1.0000128^{+0.0000023}_{-0.0000023}$	*TESS*
Sector 13			
$\log \sigma$	GP amplitude	$-0.64^{+0.23}_{-0.24}$	*TESS*
$\log \rho$	GP time-scale	$-10.41^{+0.12}_{-0.11}$	*TESS*
$\log s^2$	Flux variance	$-18.211^{+0.011}_{-0.010}$	*TESS*
Δf	Mean flux	$1.0000019^{+0.0000062}_{-0.0000060}$	*TESS*
	Radial velocity analysis		
$\log S_{\rm osc}$ ($\rm km^2\ s^{-2}$)	Oscillation power	$-22.58^{+0.21}_{-0.27}$	*ESPRESSO* RVs
$\log Q_{\rm osc}$	Oscillation damping	$1.58^{+0.23}_{-0.21}$	*ESPRESSO* RVs
$\log S_{\rm bkg}$ ($\rm km^2\ s^{-2}$)	Background activity power	$-18.48^{+0.90}_{-0.68}$	*ESPRESSO* RVs
$\log \omega_{\rm bkg}$ ($\rm d^{-1}$)	Background activity time-scale	$4.07^{+0.32}_{-0.34}$	*ESPRESSO* RVs
$\log \sigma_{\rm A}$ ($\rm km\ s^{-1}$)	White noise term for run A	$-10.31^{+1.25}_{-1.16}$	*ESPRESSO* RVs
$\log \sigma_{\rm B}$ ($\rm km\ s^{-1}$)	White noise term for run B	$-8.29^{+0.67}_{-2.35}$	*ESPRESSO* RVs

This paper has been typeset from a TEX/LATEX file prepared by the author.

Downloaded from https://academic.oup.com/mnras/article/502/2/2893/6123888 by University of Birmingham user on 09 March 2021

CHAPTER 5

A MISCELLANY OF MISALIGNMENTS FOR PLANETS TRANSITING COLD STARS

This Chapter is a draft of a manuscript in preparation for submission to MNRAS. The motivation for this Chapter is discussed in 1.4.3 and 1.5, so we do not repeat this here. In short, one way of learning more about the influence of tidal dissipation on the observed stellar obliquities is to study planets that orbit further from cold stars. This is the topic of this paper.

In Section 5.1 we describe our target sample and their characteristics. In Section 5.2 we describe our spectroscopic and photometric data that we use to derive the orbits, spin-orbit angles, and transit parameters. We analyse the spectra to obtain stellar parameters in Section 5.3; transit parameters in Section 5.4; radial velocity orbit in Section 5.5, and finally the spectroscopic transit analysis in Section 5.6. We report our results in Section 5.7, and offer some preliminary conclusions in Section 5.9. All the following work is my own, with the exception of the analysis presented in Section 5.3, which was done by Barry Smalley at Keele University.

Abstract The obliquity of a star relative to the orbit of a transiting planet (the spin-orbit angle) has long been interpreted as a relic of the dynamical history of the system. The current sample of obliquity measurements has revealed that the spin-orbit angle distribution is stratified by stellar temperature. The prevailing explanation for this dichotomy is that cold stars ($\lesssim$6100 K) more actively partake in an exchange of angular momentum mediated by tides, which tends to align the spin and orbital angular momenta faster than for planets orbiting hot stars. In such a scenario one would expect the temperature stratification to weaken as the tidal evolution timescales increase, which would be the case for planets more widely separated from their stars. Here we present measurements of the projected stellar obliquities of 13 cool stars hosting transiting planets in weaker tidal regimes than previously considered. Our measurements are based on spectroscopic transits observed with the HARPS instrument, and we find that five out of 13

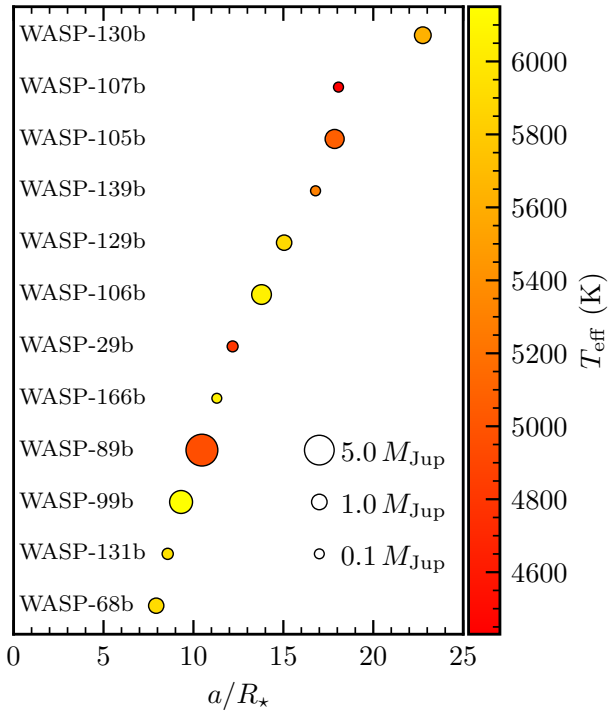


Figure 5.1: Key planetary, stellar, and orbital parameters for the sample considered in this work.

systems are consistent with high obliquities (WASP-29 b, WASP-68 b, WASP-107 b, WASP-131 b, and WASP-139 b). Some of those that are commensurate with low obliquities are likely candidates for disc-driven migration owing to the weak tidal influence (WASP-89 b, WASP-99 b, WASP-105 b, WASP-106 b, WASP-129 b, WASP-130 b, WASP-132 b, WASP-166 b). We show that the distribution of obliquities for cool stars is more diverse than previously seen, bringing it more in line with those of hot stars. Moreover, we use both archival and new CORALIE and HARPS radial velocities to better characterise the planetary eccentricities and additional companions. We detect eccentricities in two of our systems: WASP-89 b and WASP-129 b, both of which are consistent with low obliquity. Five systems also display statistically significant radial velocity drifts which could indicate previously unseen companions. This work represents the largest single contribution of stellar obliquity measurements of cool stars.

5.1 Target selection

The 13 target stars considered in this work and their stellar parameters are listed in Table 5.1. They comprise cool main-sequence stars of mid-K to late-F type with effective temperatures and masses ranging from 4430–6150 K and 0.69–1.24 $M_\odot$. Each of the target stars in Table 5.1 host a transiting close-in giant planet discovered by the WASP survey (Pollacco et al. 2006) between 2010–2019. The orbital and planetary parameters are listed in Table 5.2. The planet masses range from 0.1–5.8 $M_{\rm Jup}$, covering the super-Neptune to hot Jupiter regime. The sample is further illustrated in Figure 5.1.

The planets were primarily selected based on their tidal influence on their star, which is expected to be small. The time over which tidal evolution shapes binary systems is a sharp function of its orbital

Table 5.1: Stellar parameters obtained from a spectroscopic analysis of the combined HARPS data. [a]Stellar masses and radii are taken from the discovery papers, see "Target" column for source. [b]Hellier et al. (2010) [c]Delrez et al. (2014) [d]Hellier et al. (2015) [e]Hellier et al. (2014) [f] Anderson et al. (2017) [g]Smith et al. (2014) [h]Maxted et al. (2016) [i]Hellier et al. (2017) [j]Hellier et al. (2019).

Target	$M_\star^a$ ($M_\odot$)	$R_\star^a$ ($R_\odot$)	$T_{\rm eff}$ (K)	$\log g$ (cgs)	[Fe/H] (dex)	$v \sin i_\star$ (km s^{-1})	$[u, v]$
WASP-29[b]	0.82	0.81	4750 ± 120	4.6 ± 0.2	0.19 ± 0.09	2.0 ± 1.1	[0.78, 0.00]
WASP-68[c]	1.24	1.69	5780 ± 130	4.2 ± 0.1	0.29 ± 0.06	2.4 ± 0.8	[0.62, 0.10]
WASP-89[d]	0.92	0.88	5020 ± 120	4.2 ± 0.1	0.14 ± 0.09	3.4 ± 0.8	[0.75, 0.02]
WASP-99[e]	1.48	1.76	6000 ± 140	4.1 ± 0.1	0.18 ± 0.07	6.6 ± 0.8	[0.59, 0.12]
WASP-105[f]	0.89	0.90	5025 ± 130	4.3 ± 0.1	0.35 ± 0.06	2.7 ± 0.4	[0.74, 0.02]
WASP-106[g]	1.09	1.39	6100 ± 140	4.1 ± 0.1	0.01 ± 0.08	6.3 ± 0.8	[0.56, 0.14]
WASP-107[f]	0.69	0.66	4340 ± 120	4.2 ± 0.1	−0.06 ± 0.09	2.6 ± 0.8	[0.80, -0.01]
WASP-129[h]	1.00	0.90	5920 ± 100	4.1 ± 0.1	0.10 ± 0.08	3.0 ± 0.7	[0.64, 0.10]
WASP-130[i]	1.04	0.96	5570 ± 130	4.6 ± 0.1	0.28 ± 0.06	2.2 ± 0.8	[0.64, 0.09]
WASP-131[i]	1.06	1.53	6020 ± 140	3.7 ± 0.1	−0.11 ± 0.08	2.9 ± 0.8	[0.59, 0.12]
WASP-132[i]	0.80	0.74	4800 ± 150	4.8 ± 0.2	0.36 ± 0.11	2.3 ± 0.5	[0.77, 0.01]
WASP-139[i]	0.92	0.80	5240 ± 130	4.6 ± 0.1	0.19 ± 0.07	1.0 ± 0.9	[0.68, 0.06]
WASP-166[j]	1.19	1.22	6000 ± 100	4.2 ± 0.1	0.19 ± 0.07	4.6 ± 0.7	[0.57, 0.14]

distance scaled by the stellar radius, $\tau \propto (a/R_\star)^5$ (Barker & Ogilvie 2009b). Notably, the combination of the cool hosts and long orbital periods (3.9–11.6 days) means the bulk of the planets orbit at distances where $a/R_\star > 10$. Half of our sample have $a/R_\star > 15$ where the tidal forcing on the star by the planet is weakened (Anderson et al. 2015). For the purposes of this work, we will refer to planets with $a/R_\star > 15$ as *warm Jupiters*. While the term "warm Jupiter" is sometimes used to refer to giant planets on orbits between 10–100 days, there is no universally accepted definition. The definition that we use in this paper is an empirical one based on the difference in tidal influence as seen from the dichotomy in stellar obliquities separated at $a/R_\star \sim 15$ (e.g. Figure 3 in Anderson et al. 2015).

In the following, we summarise the key properties of each system, and new insights since their discovery.

Table 5.2: Adopted planet transit parameters for the systems analysed in this work. [a] $\mathrm{BJD_{TDB}} - 2\,450\,000$. [b] Hellier et al. (2010) [c] Delrez et al. (2014) [d] Hellier et al. (2015) [e] Hellier et al. (2014) [f] Anderson et al. (2017) [g] Smith et al. (2014) [h] Maxted et al. (2016) [i] Hellier et al. (2017) [j] Hellier et al. (2019).

Planet	M_p (M_Jup)	R_p (R_Jup)	P (day)	T_0^a ($\mathrm{BJD_{TDB}}$)	$R_\mathrm{p}/R_\star$	$a/R_\star$	i (°)	b
WASP-29 b[b]	0.24	0.79	3.9227267 ± 0.0000042	5830.18961 ± 0.00016	0.1010	12.18 ± 0.69	88.8 ± 0.7	0.26
WASP-68 b[c]	0.96	1.24	5.0842982 ± 0.0000154	6064.86357 ± 0.00058	0.0755	7.93 ± 0.42	88.1 ± 1.3	0.26
WASP-89 b[d]	5.82	1.04	3.3564228 ± 0.0000025	6207.02192 ± 0.00012	0.1221	10.47 ± 0.47	89.4 ± 0.5	0.10
WASP-99 b[e]	2.78	1.10	5.7525849 ± 0.0000022	8393.71269 ± 0.00023	0.0676	9.31 ± 0.06	89.6 ± 0.4	0.07
WASP-105 b[f]	1.76	0.98	7.8728798 ± 0.0000101	6600.07728 ± 0.00020	0.1095	17.85 ± 0.85	89.7 ± 0.2	0.10
WASP-106 b[g]	1.93	1.08	9.2897151 ± 0.0000100	6649.55050 ± 0.00032	0.0801	13.79 ± 0.44	89.5 ± 0.5	0.13
WASP-107 b[f]	0.12	0.97	5.7214900 ± 0.0000020	6514.41138 ± 0.00010	0.1473	18.07 ± 0.70	89.7 ± 0.2	0.09
WASP-129 b[h]	0.97	0.96	5.7481449 ± 0.0000040	7027.43807 ± 0.00020	0.1068	15.04 ± 0.42	87.7 ± 0.2	0.62
WASP-130 b[i]	1.23	0.91	11.5509801 ± 0.0000102	6921.14384 ± 0.00025	0.0957	22.75 ± 0.81	88.7 ± 0.1	0.53
WASP-131 b[i]	0.27	1.24	5.3220230 ± 0.0000052	6919.82438 ± 0.00039	0.0815	8.57 ± 0.32	85.0 ± 0.3	0.73
WASP-132 b[i]	0.42	0.89	7.1335207 ± 0.0000087	6698.20837 ± 0.00041	0.1208	19.61 ± 0.62	89.6 ± 0.3	0.14
WASP-139 b[i]	0.12	0.82	5.9242620 ± 0.0000041	7196.79408 ± 0.00029	0.1034	16.79 ± 1.04	88.9 ± 0.5	0.33
WASP-166 b[j]	0.10	0.63	5.4435401 ± 0.0000039	7664.32890 ± 0.00060	0.0530	11.30 ± 0.60	88.0 ± 0.7	0.39

5.1.1 WASP-29 b

Discovered by Hellier et al. (2010), the planet is of Saturn-mass and size ($M_p = 0.25 \pm 0.02\,M_{Jup}$, $R_p = 0.79 \pm 0.05\,R_{Jup}$) orbiting a K4 dwarf star with $V = 11.3$. The star is likely old, although its age is only loosely constrained to 7–15 Gyr. Hellier et al. (2010) notes its space velocity of 40 km s^{-1} is typical of a local thin-disc star, thus its age may be consistent with the ~9 Gyr thin-disc age. The planet was also the subject of an investigation into atmospheric escape using far-ultraviolet observations from the *Hubble* Space Telescope. No significant escape of H, Si III, Si IV, Ca II was detected, perhaps in part due to the star's low X-ray luminosity (dos Santos et al. 2021). Gibson et al. (2013) also studied the planet in transmission and found a featureless spectrum from 515–720 nm using spectrophotometric observations from Gemini-South/GMOS.

5.1.2 WASP-68 b

Delrez et al. (2014) reported the discovery of this hot Jupiter planet ($M_p = 0.95 \pm 0.03\,M_{Jup}$, $R_p = 1.24 \pm 0.08\,R_{Jup}$). The star is an evolved $V = 10.7$ G0-type star, with an age of 4.5–7 Gyr based on stellar evolution models.

5.1.3 WASP-89 b

This is the most massive planet in our sample, with $M_p = 5.9 \pm 0.4\,M_{Jup}$, $R_p = 0.88 \pm 0.03\,R_{Jup}$, and eccentricity $e = 0.193 \pm 0.009$ (Hellier et al. 2015). The host star is a faint ($V = 13.1$) magnetically active ($P_{rot} = 20.2 \pm 0.4$ days) K3 dwarf with an estimated age of 0.5–2.8 Gyr based on gyrochronological relations. Hellier et al. (2015) also notes the ~2 Gyr estimate for the circularization timescale for this system is consistent with its non-zero eccentricity and inferred age.

5.1.4 WASP-99 b

Discovered by Hellier et al. (2014), the planet is a hot Jupiter with $M_p = 2.78 \pm 0.13\,M_{Jup}$, $R_p = 1.10 \pm 0.07\,R_{Jup}$. The host star is a $V = 9.8$ F8-type star with an age estimated to be 0.8–2.5 Gyr based on lithium abundance estimates and gyrochronological relations. The latter uses the measured spectroscopic $v \sin i_\star$ value and assuming $i_\star = 90°$. The discovery paper used only one follow-up light curve with poor coverage of the egress to refine the planet ephemeris. In Section 5.4 we provide an updated ephemeris and transit based on an analysis of three sectors of *TESS* photometry to aid our analysis of the spectroscopic transits in Section 5.6.

WASP-105 b

This planet is a warm Jupiter with $M_p = 1.8 \pm 0.1\,M_\odot$, $R_p = 0.96 \pm 0.03\,R_{Jup}$ (Anderson et al. 2017). The host star is a K2 dwarf with low lithium abundance indicative of an old age, although no age estimate was reported in the discovery paper.

5.1.5 WASP-106 b

The discovery of WASP-106 b was reported in Smith et al. (2014). The planet has an orbital period of 9.29 days, with $M_p = 1.925 \pm 0.076\,M_{Jup}$ and $R_p = 1.085^{+0.046}_{-0.028}\,R_{Jup}$. The star is of spectral type F9 with apparent brightness $V = 11.2$. Gyrochronological relations and the star's lithium abundance both suggest an age of 1–2 Gyr, whereas an isochrone placement method suggests 5–9 Gyr.

5.1.6 WASP-107 b

Discovered by Anderson et al. (2017), the planet is an inflated super-Neptune with $M_p = 0.096 \pm 0.005\,M_{Jup}$ ($\sim$31 $M_\oplus$, Piaulet et al. 2021) and $R_p = 0.94 \pm 0.02\,R_{Jup}$. The star is a $V = 11.5$ magnetically active K6 dwarf as evidenced by its measured rotational modulation with period $P_{rot} = 17.0 \pm 1.0$ days seen in WASP and *K2* photometry. The age of the star varies between different studies and methods, with the most recent gyrochronological estimate being 2.7–5.1 Gyr (Piaulet et al. 2021), although isochrones may place it as old as $\sim$12 Gyr (Močnik et al. 2017).

The planet has been the subject of extensive follow-up observations since its discovery. The *HST* transmission spectrum shows subsolar ratio of C/O and absorption of water (Kreidberg et al. 2018); metastable He 10 833 Å (Spake et al. 2018) that has also been confirmed at high resolution with CARMENES (Allart et al. 2019) and *Keck*/HIRES (Kirk et al. 2020); and has featured in theoretical studies of atmospheric chemistry (Fortney et al. 2020; Wang & Dai 2020). WASP-107 b was also observed with *K2* over a period of $\sim$70 days which led to the discovery of infrequent starspot occultations durings transits, pointing to a significant misalignment between the orbit and the stellar spin axis (Dai & Winn 2017; Močnik et al. 2017). The misalignment was only recently formally measured with the Rossiter-McLaughlin effect using *Keck*/HIRES, confirming the orbit is retrograde and polar with a sky-projected spin-orbit angle, $|\lambda| = 118^{+38}_{-19}$ degrees (Rubenzahl et al. 2021). In Section 5.6 we confirm this result based on three transits of WASP-107 b observed with the HARPS spectrograph. A second giant planet companion has also been detected in the outer system (WASP-107 c, Piaulet et al. 2021) with an orbital period $P_c = 2.98$ yr and minimum mass $M_c \sin i = 0.36\,M_{Jup}$, which may have facilitated the misalignment.

5.1.7 WASP-129 b

The planet is a warm Jupiter with $M_p = 1.0 \pm 0.1\,M_{Jup}$, $R_p = 0.93 \pm 0.03\,M_{Jup}$ (Maxted et al. 2016). The host is a $V = 12.3$ star of spectral type G1. Its high density ($\rho \approx 1.4\rho_\odot$) points to enhanced initial helium abundance, with an age of 0.1–1.9 Gyr determined from isochrones.

5.1.8 WASP-130 b

With an orbital period of 11.6 days ($a/R_\star = 22.8$), WASP-130 b is the longest period planet in our sample. Its mass and radius measure $M_p = 1.23 \pm 0.04\,M_{Jup}$, $R_p = 0.89 \pm 0.03\,R_{Jup}$. The host is a $V = 11.1$ metal-rich G6 star where the isochrone placement method puts its age at 0.2–7.9 Gyr. High-contrast imaging with VLT/SPHERE uncovered a neighbouring star at 0.″6, whose brightness corresponds to an M dwarf

with mass $0.3^{+0.03}_{-0.02}\,M_\odot$ assuming the object is gravitationally bound to the system (Bohn et al. 2020). A stellar population model puts the probability of the companion being a background or foreground star at 0.22 %.

5.1.9 WASP-131 b

The planet is significantly inflated considering its mass is similar to Saturn, with $M_\mathrm{p} = 0.27 \pm 0.02\,M_\mathrm{Jup}$ and $R_\mathrm{p} = 1.22 \pm 0.05\,R_\mathrm{Jup}$ (Hellier et al. 2017). The host star is of spectral type G0 with $V = 10.1$. Its low surface gravity ($\log g = 3.9$) suggests it is evolved, with stellar evolution models placing its age in the range 4.5–10 Gyr. This system, too, has a stellar companion separated by 0.″189 detected with high-contrast imaging with VLT/SPHERE (Bohn et al. 2020). Stellar population synthesis models puts the probability of the companion being a background star at 0.01 %. Assuming the system is bound, which is likely, the companion has a mass of $0.62^{+0.05}_{-0.04}\,M_\odot$. The presence of the companion does not, however, affect the derived planetary parameters (Southworth et al. 2020).

5.1.10 WASP-139 b

Also discovered by Hellier et al. (2017), this planet is a super-Neptune/sub-Saturn with $M_\mathrm{p} = 0.117 \pm 0.017\,M_\mathrm{Jup}$ ($\sim$56 $M_\oplus$) and $R_\mathrm{p} = 0.80 \pm 0.05\,R_\mathrm{Jup}$. The star is a $V = 12.4$ K0 dwarf, and the depleted lithium abundance and gyrochronological age constraint (from spectroscopic $v \sin i_\star$) places its age between 0.2–0.9 Gyr. Hellier et al. (2017) performed a velocimetric Rossiter-McLaughlin analysis on a spectroscopic transit of WASP-139 b observed with HARPS. The low SNR of the data prevented an independent detection of its rotation which could mean one of two things: *i)* The $v \sin i_\star$ of the star is much lower than the one determined from spectroscopic broadening ($v \sin i_\star = 4.2 \pm 1.1\,\mathrm{km\,s^{-1}}$). *ii)* Assuming the spectroscopic $v \sin i_\star$ is correct and the system were aligned, the Rossiter-McLaughlin amplitude would be $\sim$28 $\mathrm{m\,s^{-1}}$. The absence of a signal may be because the planet is significantly misaligned with the star and transits across its poles. In Section 5.6 we repeat an analysis of the same data, but instead using the reloaded Rossiter-McLaughlin method.

5.1.11 WASP-166 b

With a mass of $M_\mathrm{p} = 0.101 \pm 0.005\,M_\mathrm{Jup}$ ($\sim$32 $M_\oplus$ and $R_\mathrm{p} = 0.63 \pm 0.03\,R_\mathrm{Jup}$), this super-Neptune is the lowest-mass planet in our sample (Hellier et al. 2019). The star is a bright $V = 9.4$ F9 dwarf, with an estimated age of 1.2–3 Gyr based on an isochrone placement algorithm. Three transits observed with the HARPS spectrograph were also analysed in the discovery paper, where they detected the velocimetric Rossiter-McLaughlin effect and found the planet and star are aligned in the sky-plane, with $\lambda = 3 \pm 5°$ (Hellier et al. 2019). In this paper we use the same data to perform a reanalysis with the reloaded Rossiter-McLaughlin method. The same data were moreover the subject of atmospheric investigations (Seidel et al. 2020; Žák et al. 2019). Seidel et al. (2020) report a 0.455 ± 0.135 % absorption signature

of neutral sodium. Additional photometric transits of WASP-166 b were analysed using *TESS* and NGTS data, refining its ephemeris and transit parameters (Bryant et al. 2020).

5.2 Observations

5.2.1 HARPS spectroscopy

The spectroscopic data underlying this work were gathered with the HARPS instrument on the 3.6-m telescope at ESO La Silla Observatory (Mayor et al. 2003). The data were gathered as part of several investigations into the formation, migration and dynamical histories of close-in giant planets, in particular focusing on newly discovered WASP planets orbiting cool stars in weak-tide regimes. Altogether, the HARPS data were observed in ESO Periods 85-98 as part of the following ESO observing programmes: 0.85.C-0393 (PI Cameron), 0.89.C-0151 (PI Triaud), 091.C-0184 (PI Triaud), 093.C-0474 (PI Triaud), 094.C-0090 (PI Triaud), 095.C-0105 (PI Triaud), 097.C-0434 (PI Triaud), 098.C-0304 (PI Ehrenreich).

Using HARPS we observed between one and three transits of each planet listed in Table 5.2. The integration times were typically 600–900 s, going to 300 s and 1200 s on the brightest and faintest stars, respectively. With this setup, we reached a signal-to-noise ratio (SNR) between 7.1–75.8 per pixel at order 49[a], which is roughly centered at 550 nm. Where recorded, the median seeing of each transit sequence at La Silla ranged between 0.79–1.39 . The details of the observations are recorded in Table 5.3. For each system we also obtained between 5–27 new HARPS radial velocity measurements covering their orbits to provide better constraints on the planet eccentricities.

We reduced the 2D spectra (echellograms) from HARPS with the dedicated Data Reduction Software (DRS). We use the reduced data for three different analyses: *i)* The 1D spectra are used in a uniform spectroscopic analysis to provide updated stellar parameters. Of particular interest is the projected stellar rotation $v \sin i_\star$ which is used in our analysis of the stellar obliquities. *ii)* The 1D spectra are cross-correlated with a depth-weighted binary mask, using a K5 template for the K dwarfs ($T_{\rm eff} < 5100$ K) and a G2 template for the G to late F stars. We focus our attention to the analysis of these cross-correlation functions (CCFs) in Section 5.6, which we use to measure the stellar obliquites. *iii)* The centre of a Gaussian fit to the CCFs denote the stellar radial velocity. In Section 5.5 we analyse these radial velocities to constrain the planetary orbits, and in particular their eccentricities.

5.2.2 CORALIE spectroscopy

In addition to the HARPS data we also use archival radial velocities obtained with the CORALIE spectrograph on the Swiss 1.2-m telescope at the same Observatory (Queloz et al. 2000a). This data was reduced in a similar manner to the HARPS spectra. Most of the CORALIE measurements are published in various discovery papers, but we also include new spectra taken since then as part of follow-up efforts to characterise additional long-period companions.

[a] As displayed in the primary header in the FITS file of the cross-correlation function.

Table 5.3: Summary of spectroscopic data used in this work. [a]SNR per pixel centered at 550 nm.

Target	Transit date	$\overline{\text{SNR}}^a$	t_{exp} (s)	FWHM (km s^{-1})
WASP-29 b	2010 Sep 6	25.4	600	6.70
	2013 Oct 2	18.8	600	6.74
WASP-68 b	2013 Jul 3	32.5	600	7.67
WASP-89 b	2012 Oct 3	7.1	900	7.25
	2013 Jun 15	8.3	900	7.27
	2013 Aug 1	9.0	900	7.10
WASP-99 b	2014 Oct 19	75.8	900	10.81
WASP-105 b	2014 Sep 30	20.0	900	6.82
	2014 Dec 10	19.0	900	6.81
WASP-106 b	2014 Apr 4	19.7	1200	10.72
	2015 Jan 17	20.0	600	10.73
WASP-107 b	2014 Apr 7	13.7	750	7.19
	2018 Feb 1	26.5	800	7.07
	2018 Mar 13	25.2	800	7.08
WASP-129 b	2015 Apr 24	24.1	900	8.20
	2016 Jun 10	22.7	1200	8.21
WASP-130 b	2015 Apr 27	27.6	600	7.54
WASP-131 b	2015 Jun 6	53.3	600	8.40
WASP-132 b	2015 Jun 24	18.5	1200	6.89
WASP-139 b	2014 Oct 29	20.7	1200	7.01
WASP-166 b	2017 Jan 14	47.0	300	9.21
	2017 Mar 4	47.6	300	9.19
	2017 Mar 15	51.9	350	9.19

5.2.3 *TESS* photometry for WASP-99 b

Our analysis of the spectroscopic transits in Section 5.6 is reliant on accurate prior knowledge of the photometric transit parameters, in particular the orbital period, transit time, depth, duration, and inclination. For most targets we obtain the transit parameters from the Exoplanet Orbit Database at `exoplanet.org`. These parameters are reported in Table 5.2.

In the discovery paper of WASP-99 b, Hellier et al. (2014) only had available the original low SNR WASP photometry, as well as one follow-up light curve with a poorly covered egress obtained with the Swiss 1.2-m *Euler* telescope. In contrast, other WASP planet discoveries are typically presented with several ground-based follow-up light curves for a precise characterisation. The poorly covered egress resulted in an uncertain estimate of the transit duration which can bias the spin-orbit angle retrieved from the spectroscopic transit data. To prevent this we use transits of WASP-99 b observed with *TESS* to refine the transit parameters. *TESS* observed the star between 2018 Sep 20 – 2019 Oct 18, 2020 Aug 26 – 2020 Sep 22, and 2020 Sep 22 – 2020 Oct 21, covering 12 transits of WASP-99 b. We downloaded the *TESS* 2-minute (Sector 3) and 20-second cadence (Sector 29, 30) PDCSAP light curves of WASP-99 using the

LIGHTKURVE package (Lightkurve Collaboration et al. 2018) and analyse this data in Section 5.4.

5.3 Spectroscopic stellar parameters

We derive spectroscopic parameters from combining the available HARPS spectra, using already established methods (e.g. Hellier et al. 2019). The results are reported in Table 5.1. The effective temperatures, $T_{\rm eff}$, is measured from the Hα line. The Na D doublet is used to determine the amount of interstellar reddening using the relations of Munari & Zwitter (1997), and is also used to determine the surface gravity, $\log g$. Nine Fe I lines in the range 600–620 nm were selected to determine the metallicity [Fe/H] and projected rotational velocity, $v \sin i_\star$. The $v \sin i_\star$ measurement assumed microturbulence from Bruntt et al. (2012) with a 0.1 km s^{-1} uncertainty. Since our stars span a range of stellar effective temperatures macroturbulence was determined in several ways. For most of our stars we assume the calibration of Doyle et al. (2014) with an uncertainty of 0.7 km s^{-1}. For stars outside this range we used the calibration of Gray (1984) with an uncertainty of 0.3 km s^{-1}. Stars below 5000 K are assumed to have zero macroturbulence as it is expected to be less than that of thermal broadening (Gray 2008). The uncertainty from macroturbulence is added in quadrature to the $v \sin i_\star$ uncertainty.

5.4 Transit modelling of WASP-99 b

We model the *TESS* photometry of WASP-99 using the EXOPLANET probabilistic modelling toolkit (Foreman-Mackey 2019). The transits are modelled by varying the natural logarithms of the orbital period, P; transit mid-point, T_0; the planet-to-star radius ratio, $r/R_\star$; and the transit duration T_{14}. We assume a circular orbit, which is justified by the eccentricity constraint from the radial velocity orbit ($e < 0.031$, 99$^{\rm th}$ percentile). We further assume a quadratic limb darkening law for the intensity distribution across the stellar disc with coefficients $u = 0.59$ and $v = 0.12$ for the linear and quadratic terms, respectively. These coefficients were determined using `LDTK`, which compares the spectroscopic parameters of WASP-99 (Table 5.1) to the PHOENIX stellar atmosphere models (Husser et al. 2013). The data outside of transits were jointly modelled with Gaussian process (GP) regression using CELERITE as implemented in EXOPLANET (Foreman-Mackey et al. 2017). We opted for a kernel function that models the covariance in the data as a damped simple harmonic oscillator implemented as the `SHOTerm` in EXOPLANET. The covariance kernel function is controlled by the hyperparameters S, Q, and ω, which describe the amplitude of the variability, quality factor, and frequency scale, respectively. We fit for the natural logarithms of S and ω, and fix the damping term $Q = 1/\sqrt{2}$. Each *TESS* sector is assigned its own GP term with its associated hyperparameters, as well as flux and white noise scaling terms. We place Gaussian priors on P and T_0 using the values and uncertainties reported in the discovery paper (Hellier et al. 2014). The T_0 prior was converted to the BJD$_{\rm TDB}$ time scale to match the *TESS* time stamps. For all other parameters we use wide Gaussian priors that are several orders of magnitude wider than the final posterior probability distribution, and are therefore practically uninformative relative to the constraint from the data.

We first fit the data using a least squares minimization method. Then, using the maximum likelihood as a starting point, we use Markov chain Monte Carlo (MCMC) to explore correlations between parameters and obtain posterior probability distributions of our parameters marginalised over the others. We launch two independent chains that are tuned for 1000 steps before performing an additional 2000 draws using the No-U-Turn (NUTS) sampling algorithm (Hoffman & Gelman 2014) implemented in PYMC3 (Salvatier et al. 2016). We verify that the chains achieved convergence by assessing the Gelman-Rubin criterion, which for all parameters was <1.001, and that >200 effective (independent) samples have been obtained. The resulting mean and 68 % credible intervals on the fitted and derived parameters for WASP-99 b are given in Tables 5.2.

5.5 Radial velocity orbit analysis

We model the radial velocity data using EXOPLANET. First, we convert all the transit times from the literature and the HARPS and CORALIE time stamps to the $\mathrm{BJD_{TDB}}$ scale using routines in ASTROPY (Astropy Collaboration et al. 2018). The orbital period P and transit time T_0 are varied under Gaussian prior with mean and standard deviations found in Table 5.2. In addition, we fit for the natural logarithm of the radial velocity semi-amplitude K, and eccentricity parameters $\sqrt{e}\cos\omega$ and $\sqrt{e}\sin\omega$. The eccentricity parameters are sampled uniformly between -1 to 1, and we impose a weak Gaussian prior on K centered on the literature values with a standard deviation of $1\,\mathrm{km\,s^{-1}}$. The HARPS and CORALIE data are modelled with their own instrumental offset and white noise scaling terms. CORALIE underwent a fibre upgrade in 2014, so data before and after this technical intervention are treated as separate instruments.

The data span >7 yr for some systems, which means we could be sensitive to radial velocity drifts due to distant stellar or substellar companions. To investigate this possibility we experiment with two additional terms to our model: *i)* time-dependent drift expressed as a linear term, and *ii)* a quadratic term. In each case the offset is instrument-specific as described in our baseline model in the previous paragraph, thus the drift models include one and two extra parameters for the linear and quadratic models, respectively. We perform a maximum likelihood fit for each model and compute the Bayesian Information Criterion (BIC) to compare the drift models to our baseline model. The model with the lowest BIC is favoured, but we only adopt a drift model if the BIC is reduced by more than 6 (Schwarz 1978b). Once a drift model is chosen we run an additional fit using the selected drift model but assuming a circular orbit. Here, too, we compare the BIC between a circular and eccentric model to determine if an eccentric orbit is justified. Eccentric models are adopted again where $|\Delta\mathrm{BIC}| > 6$.

Once the model has been chosen we use MCMC sampling to determine credible intervals for our parameters in a similar fashion to Section 5.4. We launch two independent chains starting at the maximum likelihood solution. We use the NUTS sampler to sample 1000 tuning steps, before sampling an additional 2000 production steps. As before, we verify that our chains have converged and that each parameter has >200 effective samples. The mean values with their 68 % credible intervals as well as the adopted models for each system are summarised in Table 5.4. The best-fitting models to the radial velocity data is shown

in Figure 5.2.

5.6 Spectroscopic transit analysis

5.6.1 Retrieving the spatially resolved light

We use the reloaded Rossiter-McLaughlin method to measure the sky-projected spin-orbit angle, λ (Cegla et al. 2016). This method is based on similar principles to other "Doppler shadow"[b] methods (Albrecht et al. 2007; Collier Cameron et al. 2010a). The transit of a planet in front of a star distorts the stellar absorption line profiles, giving rise to a radial velocity anomaly: the Rossiter-McLaughlin effect (Rossiter 1924; McLaughlin 1924). Since it is a spectroscopic effect it does not exactly translate to a pure Doppler shift in the star's radial velocity. For this reason we do not model the "classical" (i.e. velocimetric) Rossiter-McLaughlin effect, which can be biased one way or another depending on the adopted model (Brown et al. 2017).

Our analysis is on the time-dependent variation in the shape of the CCF (which represents the average stellar line profile) over the duration of the transit. The reloaded Rossiter-McLaughlin method isolates this variation by comparing the in-transit CCFs to a high SNR average out-of-transit CCF, allowing us to retrieve the spatially resolved local stellar photospheric profiles across the transit chord.

By now the method is well-established (e.g. Cegla et al. 2016; Bourrier et al. 2018; Kunovac Hodžić et al. 2021), but here we recall the main steps. The continuum levels of the HARPS CCFs are on an arbitrary scale. In order to compare them we start by normalising the DI CCFs by their individual continuum values, which we define as those regions $> 4\sigma$ from the line centre. We also scale the CCFs by a quadratic limb darkened transit model which we compute using ELLC (Maxted 2016). We use the orbital and planetary parameters listed in Table 5.2, which represent the most recently published values for each system. The adopted limb darkening parameters assuming a quadratic model are listed in Table 5.1, and were computed for the HARPS wavelength range with LDTK (Parviainen & Aigrain 2015), using values of $T_{\rm eff}$, $\log g$ and Fe/H that are listed in the same table.

We shift the CCFs to a common reference frame by removing the Keplerian reflex motion of the star due to the planet. In practice this is done by resampling the CCFs onto a new velocity grid that is corrected for the radial velocity orbit that we derived in Section 5.5. An average line-profile at high signal-to-noise ratio is then created by taking the mean of the observations taken outside of transit on each transit night. For WASP-132 there are no spectra taken outside of transit. For this target we instead used seven spectra taken over the course of a week following the night of transit. The systemic velocity γ is then determined from a Gaussian fit to the reference CCF, which we use to shift the individual CCFs to the reference frame of the star.

Finally, we obtain the residual line profiles by subtracting the in-transit CCFs from the reference line profile. We do this in two iterations. In the first iteration we use the scatter in the residual line profiles

[b] Sometimes referred to as "Doppler tomography", although some astronomers advocate against using "tomography" due to confusion with the term used in other areas of science and medicine.

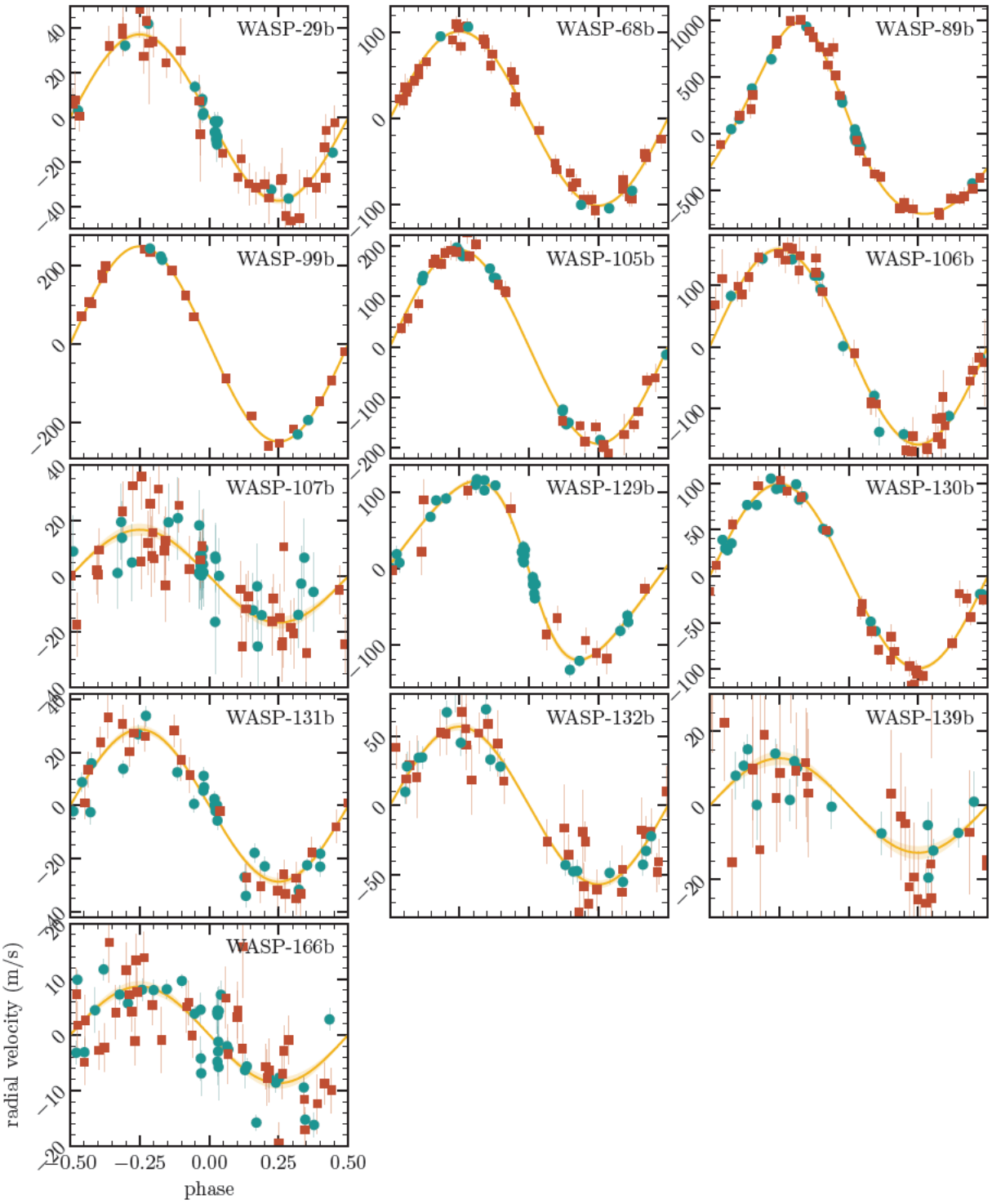


Figure 5.2: Fits to the radial velocity orbits for all planets in our sample. The yellow line and shaded regions are the best-fitting models and the 68 % credible interval, respectively. CORALIE data are shown as red squares, while HARPS data are shown as green circles. Data taken during transit spanning twice the transit duration are not included in the fit and not shown in these figures. In addition to the transit data, all HARPS data shown here (*green*), with the exception of WASP-139 b and WASP-166 b, is previously unpublished and has allowed better constraints on the eccentricities.

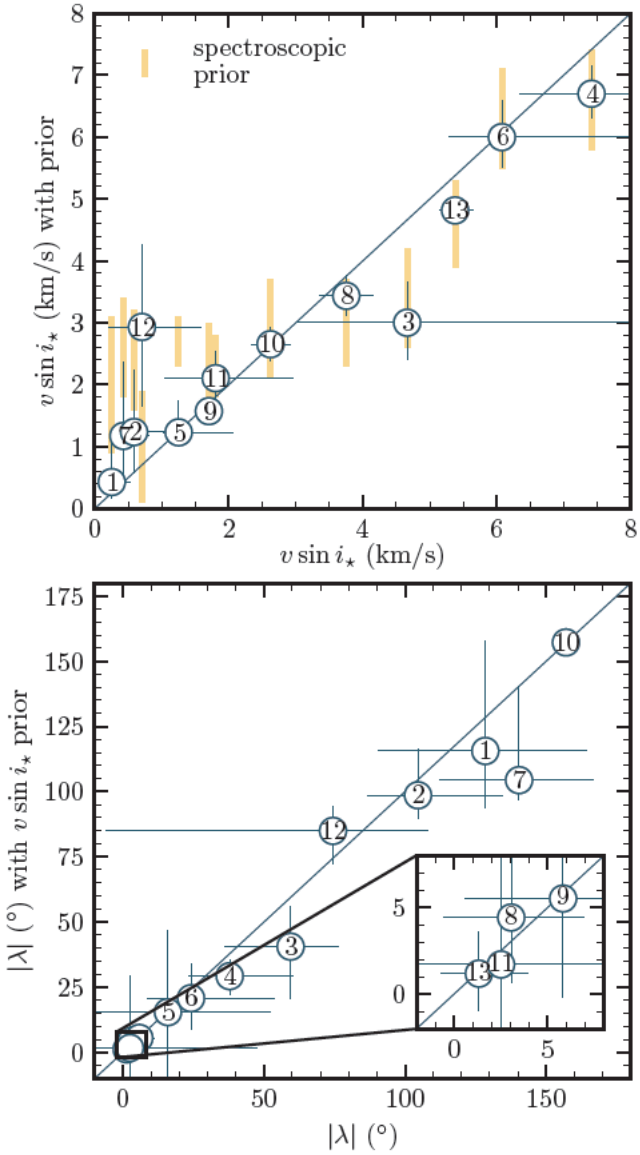


Figure 5.3: Sensitivity of the spectroscopic $v \sin i_\star$ prior on the fitted $v \sin i_\star$ (*top*) and λ (*bottom*) values. The prior (*yellow*) is applied for the vertical axes and is derived from a spectroscopic analysis of the combined CORALIE and HARPS data. The uncertainties denote the 68 % credible interval. Labels: [1]WASP-29 b [2]WASP-68 b [3]WASP-89 b [4]WASP-99 b [5]WASP-105 b [6]WASP-106 b [7]WASP-107 b [8]WASP-129 b [9]WASP-130 b [10]WASP-131 b [11]WASP-132 b [12]WASP-139 b [13]WASP-166 b. Note that the prior values (yellow) are from the new spectroscopic analysis. The fits using $v \sin i_\star$ priors (y-axis) were done before the spectroscopic analysis and therefore used $v \sin i_\star$ from literature.

outside of the transit window to estimate the photon noise uncertainty on the individual CCFs. We then create a new reference line profile which is now a weighted average in order to account for varying SNR during the night, before re-calculating the residual line profiles. The final in-transit residual (local) CCFs represent the spatially resolved line profiles of the star under the transit chord. The movement of the spatially resolved line profiles over the transit chord are shown in Figure 5.4, and are the subject of our further analysis.

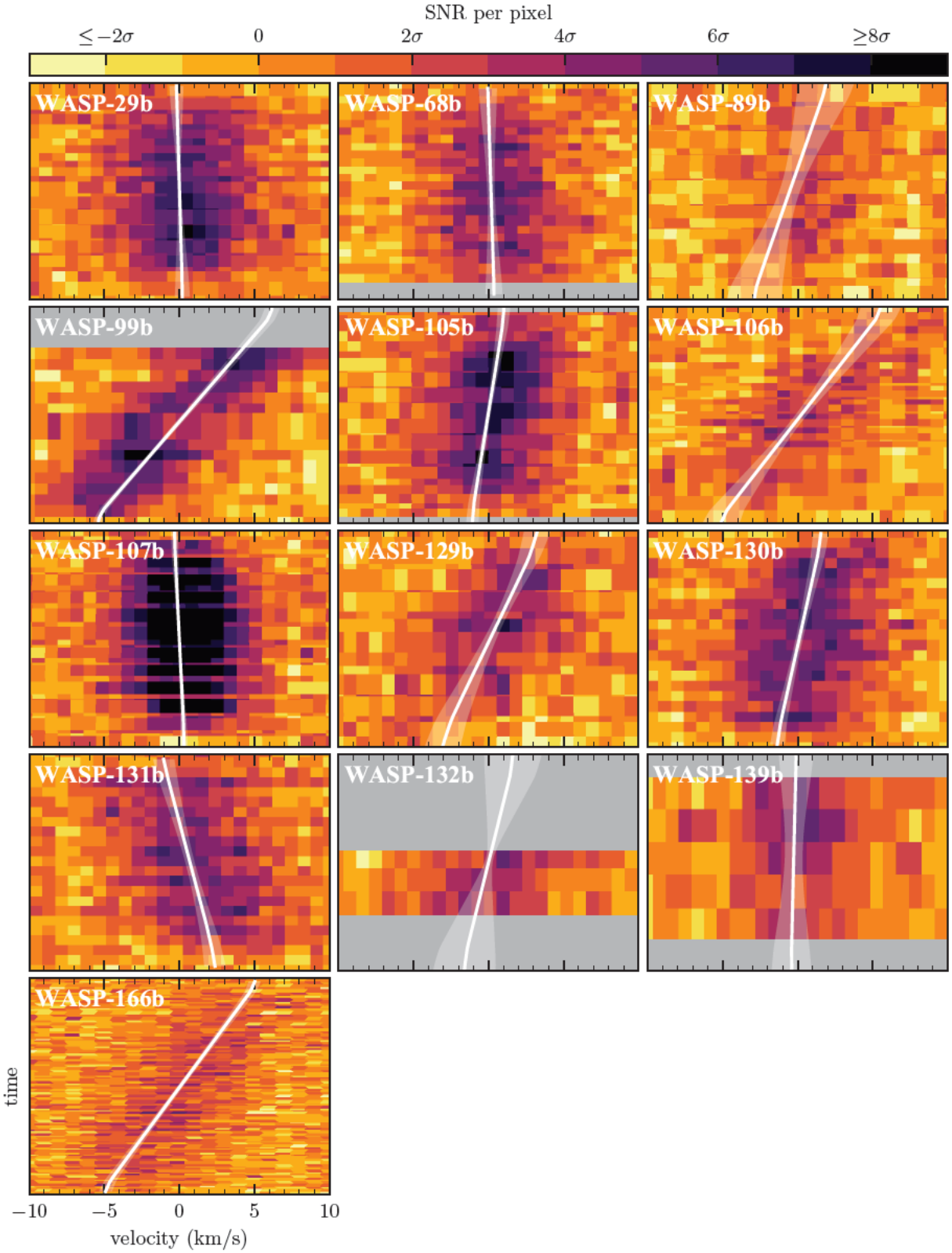


Figure 5.4: Velocity of the stellar surface transited by the planet. The dark regions represent local absorption line profiles on the star that are Doppler shifted by the stellar rotation. The white lines and shaded regions are the best-fitting surface velocity model and the 3σ (99.7 %) credible interval, respectively. Each panel covers the transit duration only and is therefore centered at the transit mid-point. Grey areas denote missing data.

5.6.2 Modelling the stellar surface velocity

In the following we use a similar approach to previous works (Kunovac Hodžić et al. 2020, 2021). We fit Gaussian profiles to the local in-transit line profiles to determine the radial velocity on the surface of the star where it is occulted by the planet. We use Markov chain Monte Carlo (MCMC) sampling to explore the full posterior distribution of the parameters $\boldsymbol{\theta} = \{ A, \mu, \sigma, c \}$ of the Gaussian model, which denote the amplitude, centre, width, and offset, respectively. We use wide priors on our parameters that are typically related to the radial velocity grid or flux range range considered, aimed at returning a conservative estimate of the radial velocity in case the local line centre is poorly resolved. We use a half-normal prior on A and σ as they are restricted to positive values, and a normal prior on μ and c. Similar to previous analyses, we build our model within the PYMC3 probabilistic framework, again taking advantage of the NUTS sampler. For each target we launch two independent chains that are tuned for 1000 steps, starting at the maximum likelihood values. We run the chains for an additional 5000 steps and verify that the Gelman-Rubin convergence criterion is satisfied and that each parameter has >200 effective samples. The line centre μ and its uncertainty is then used for further analysis.

The local stellar surface velocity over the transit chord is determined by the combination of parameters $\boldsymbol{\theta} = \{v \sin i_\star, \lambda, a/R_\star, i, r/R_\star\}$ (Cegla et al. 2016). In this instance we use the affine-invariant MCMC ensemble sampler implemented in EMCEE. $v \sin i_\star$ and λ are sampled uniformly in the range 0–20 km s^{-1} and −180–180°, respectively. We fix $r/R_\star$ to the values reported in Table 5.2 and sample $a/R_\star$ and i with Gaussian priors taken from the same Table. We run 100 "walkers" for 10 000 steps each, discarding the first 2000 steps as burn-in. The chains are thinned by the autocorrelation length of the parameters before finally being merged. The 50$^{\text{th}}$ percentile values and 68 % credible interval are reported in Table 5.4.

We perform an additional run by also placing a Gaussian prior on $v \sin i_\star$ using the spectroscopic values in Table 5.1, which we derived in Section 5.3. We find that the value of λ is largely insensitive to the inclusion of the $v \sin i_\star$ prior, as demonstrated in Figure 5.3, though the uncertainty is vastly improved in a few cases where the data suffers from low SNR. Many of our systems have low impact parameters where there is a degeneracy between a low $v \sin i_\star$ and high λ and vice versa. A prior on $v \sin i_\star$ can be used to lift this degeneracy. For this reason we opt to include the prior in our final adopted models. The best-fitting surface velocity models and the 3σ uncertainty region are overlaid on the residual line profiles in Figure 5.4.

5.7 Results

5.7.1 WASP-129 b is a newly eccentric planet

We report the eccentricity constraints in Table 5.4. Based on the Bayesian Information Criterion (BIC) we find that eccentric orbits are strongly favoured for WASP-89 b ($\Delta \equiv |\Delta\text{BIC}| = 161$) and WASP-129 b ($\Delta = 45$). The eccentricity of WASP-89 b was already detected in the discovery paper owing to the high mass of the planet (Hellier et al. 2015). Here we find $e = 0.181 \pm 0.006$; a measurement consistent with the literature measurement though we improve on the uncertainty by a factor ∼1.5 by cause of additional

HARPS and CORALIE data. The eccentricity of WASP-129 b ($e = 0.208 \pm 0.022$) is a new discovery, also thanks to HARPS radial velocities that have been collected since the planet was announced (Maxted et al. 2016). In addition to these there is some evidence for eccentricity in the orbits of WASP-68 b and WASP-106 b. The BIC improves by 3.3 and 3.5, respectively, which is a positive improvement though not strong enough to adopt a non-circular model. The remaining systems are all in favour of circular orbits at the current sensitivity of the data.

5.7.2 Radial velocity drifts

Five systems show statistically significant radial velocity drifts that can be evidence for additional undiscovered radial velocity companions on wide orbits. These systems are WASP-68, WASP-89, WASP-106, WASP-129, and WASP-132. The radial velocity drifts are illustrated in Figure 5.5 and the rates are reported in Table 5.4. WASP-68 has a strong preference for a linear drift over the 2.3 yr baseline of the radial velocity data ($\Delta = 27$). The same is true for WASP-89 (4.4 yr, $\Delta = 29$) and WASP-129 (2.4 yr, $\Delta = 34$). Quadratic drifts are favoured for WASP-106 (2.3 yr, $\Delta = 6.5$) and WASP-132 (2.1 yr, $\Delta = 86$).

A couple of systems in Table 5.4 have upper limits on the first order drift coefficient that appear significant (e.g. WASP-99 and WASP-130), despite a non-drift model being adopted due to insufficient improvement in the BIC. In the case of WASP-99 this effectively happens due to the short time span of the CORALIE and HARPS data. The model cannot distinguish between two instrumental offsets that are similar, compared to instrumental offsets that are significantly different combined with a high slope parameter. The situation is different for WASP-130. The improvement in the BIC from a non-drift model to a quadratic model is 5.4 and therefore at the cusp of a significant detection. This is particularly interesting in the context of the candidate low-mass stellar companion observed with VLT/SPHERE at 0.″6 separation from WASP-130 A Bohn et al. (2020). The Gaia Early Data Release 3 indicates a distance of 175 pc to WASP-130 A, which corresponds to a projected separation of 104 AU for the candidate companion if bound (Lindegren et al. 2021). Moreover, the orbit of WASP-130 b shows some evidence of eccentricity ($e > 0$; >95 % CI) using the quadratic model, which vanishes when adopting the non-drift model. We recommend follow-up on WASP-130 to characterise the orbit of WASP-130 b further, as well as that of additional companions that may reside in the system.

The remaining systems show no preference for any radial velocity drift models within the sensitivity and time span of the data.

5.7.3 Rotation and stellar obliquities

5.7.3.1 Validation of spins and obliquities

The rotation and obliquity measurements from our analysis of the HARPS cross-correlation functions are shown in Table 5.4. To verify the robustness of our measurements we compare our results to two systems that already have published stellar obliquity measurements, namely WASP-107 and WASP-166. Rubenzahl et al. (2021) analysed one transit of WASP-107 b observed with the Keck/HIRES instrument

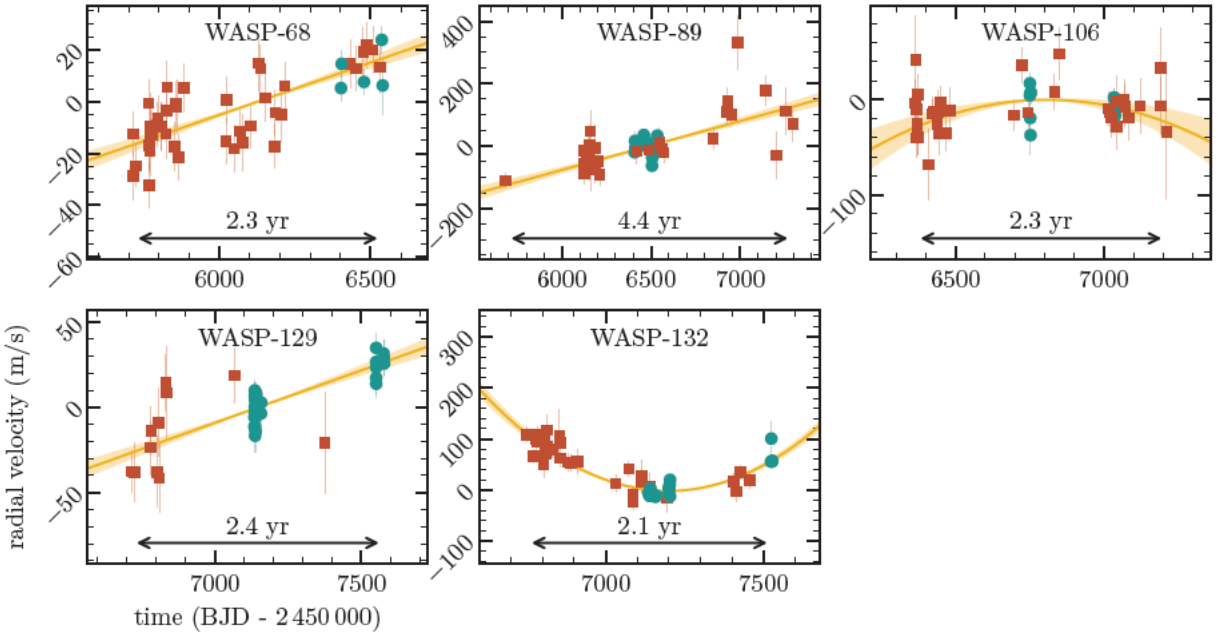


Figure 5.5: Systems where a statistically significant drift is detected. The yellow line and shaded regions are the best-fitting linear or quadratic polynomial models and the 68 % credible interval, respectively. CORALIE data are shown as red squares, while HARPS data are shown as green circles. The constant systemic velocity offset and radial velocity orbits due to known planets have been removed.

and found a polar/retrograde orbit with $|\lambda| = 118.1^{\circ}{}^{+37.8}_{-19.1}$, which confirmed a previous suspicion based on the frequency of transit spot-crossing events seen in *K2* photometry (Dai & Winn 2017). Due to its low impact parameter ($b \approx 0.1$) there is an uncertainty in whether the orbit is oriented such that $\lambda < 0°$ or $\lambda > 0°$, thus only $|\lambda|$ can be meaningfully constrained at the current noise level in the data. In our analysis — based on three WASP-107 b transits observed with HARPS — both solutions ($\lambda < 0°$ and $\lambda > 0°$) diverge significantly from alignment, and when analysed in isolation they provide similar constraints. We find $|\lambda| = 104.4^{\circ}{}^{+36.0}_{-7.8}$ when we apply a Gaussian constraint on $v \sin i_\star$ using the line broadening measurement $2.6 \pm 0.8\,\mathrm{km\,s^{-1}}$. There is a further degeneracy between $|\lambda|$ and $v \sin i_\star$ due to the low impact parameter, i.e. more polar orbits are accompanied by faster rotation and vice versa. Fitting without the constraint on $v \sin i_\star$ favours a slower rotating star with $v \sin i_\star = 0.43^{+38}_{-14}\,\mathrm{km\,s^{-1}}$ and a higher preference for retrograde orbit with $|\lambda| = 140^{\circ}{}^{+28}_{-26}$. Regardless of the prior, our measurement of $v \sin i_\star$ and $|\lambda|$ are consistent with previously measured values and we confirm that WASP-107 b is orbiting retrograde with respect to its parent star.

The projected obliquity of WASP-166 b was previously measured in Hellier et al. (2019) to be $\lambda = 3° \pm 5°$ using the velocimetric Rossiter-McLaughlin effect. Here we use the same data but operate on the CCFs instead of the radial velocities and find a result in agreement with theirs, $\lambda = 1° \pm 2°$.

Finally, we turn our attention to the projected stellar rotational velocities and how they compare to those derived from our spectroscopic analysis, which we show in Figure 5.3. In general the Rossiter-McLaughlin analysis produces $v \sin i_\star$ consistent with the spectroscopic values within their 1σ uncertainties. A couple of things are worth noting in Figure 5.3. A few systems where the $v \sin i_\star$ prior was applied (yellow bar)

are at odds with the $v \sin i_\star$ measurements along the vertical axis shown in Figure 5.3. In particular these include WASP-105 and WASP-139, where the prior and prior-informed measurement are discrepant $>1\sigma$. The reason for this is that the runs with the prior applied were done using literature measurements of $v \sin i_\star$ that were reported in the discovery papers. Since analysing the transits we have carried out a new spectroscopic analysis using our additional HARPS data, and the $v \sin i_\star$ inferred from broadening has changed significantly in WASP-105 and WASP-139. The prior ranges shown in yellow in Figure 5.3 are therefore the newly derived values, but were not used in the original fit. Once the fit is repeated using the new priors, the prior-informed $v \sin i_\star$ measurements for WASP-105 and WASP-139 will be commensurate with the freely fit values.

The measurements of λ are also relatively insensitive to the choice of prior as seen from the clustering along the diagonal line in Figure 5.3, which gives us further confidence in our measurements. In the following we adopt the values of λ with the prior applied, but we will discuss some of the systems individually below.

5.7.3.2 A range of planetary misalignments

Five out of the 13 systems in our sample are consistent with a high degree of alignment, which we here consider to be $\lambda \lesssim 10°$ within their 1σ uncertainties. These are WASP-105 b ($-15^{\circ}{}^{+37^{\circ}}_{-31^{\circ}}$), WASP-106 b ($21^{\circ}{}^{+13^{\circ}}_{-12^{\circ}}$), WASP-129 b ($4° \pm 4°$), WASP-130 b ($6° \pm 6°$), WASP-132 b ($-2^{\circ}{}^{+38^{\circ}}_{-28^{\circ}}$), and WASP-166 b ($1° \pm 2°$). The spin-orbit angle of WASP-132 b is only constrained by four in-transit spectra that are derived from a comparison to out-of-transit spectra from different nights. A follow-up transit of this system is therefore encouraged to measure λ more precisely, particularly in the context of the quadratic radial velocity drift that we have detected in this system.

Another three systems present with prograde orbits of various misalignments. The projected obliquities of WASP-89 b and WASP-99 b are $-41^{\circ}{}^{+20^{\circ}}_{-16^{\circ}}$ and $29^{\circ}{}^{+6^{\circ}}_{-7^{\circ}}$, respectively. Either measurement could still be consistent with alignment at the 3σ level, though the data favour somewhat misaligned configurations. WASP-139 b appears significantly misaligned with $\lambda = -85^{\circ}{}^{+13^{\circ}}_{-9^{\circ}}$. This measurement is based on using the prior $v \sin i_\star = 4.2 \pm 1.1\,\mathrm{km\,s^{-1}}$ from Hellier et al. (2017). In our analysis of the broadening of HARPS spectra in Section 5.3 the $v \sin i_\star$ is significantly adjusted compared to previous values, where we obtain $1.0 \pm 0.9\,\mathrm{km\,s^{-1}}$. The analysis of the transits without imposing a prior is much less constrained: the 68 % credible interval encompasses values of λ ranging from $-105°$ to $0°$. A repeated fit using the new $v \sin i_\star$ prior will therefore be more consistent with a range of possible orientations. If we assume $v \sin i_\star = 1\,\mathrm{km\,s^{-1}}$ and $\sin i_\star \approx 1$, then the rotation period of WASP-139 would be 40.5 days. This would indicate an old age which could be consistent with its low lithium abundance (<0.4 dex). Indeed, two sectors of *TESS* photometry show signs of a ~33 d rotation period with a peak-to-peak amplitude of 3 ppt. If the planet were aligned with the stellar spin the Rossiter-McLaughlin amplitude would produce a $\sim 10\,\mathrm{m\,s^{-1}}$ radial velocity anomaly. The radial velocity uncertainty on each spectrum ranges from 3–5 $\mathrm{m\,s^{-1}}$ and is therefore in principle precise enough to detect an aligned configuration assuming the broadening value is correct. These lines of evidence favour a solution where the planet is misaligned

with the star, which would explain the non-detection of the Rossiter-McLaughlin effect in radial velocity in Hellier et al. (2017), and be consistent with the velocity trace we derive in this work.

Five out of the 13 planets considered in this sample are consistent with orbiting polar and/or retrograde around their star. These are WASP-29 b, WASP-68 b, WASP-107 b, and WASP-131 b. The retrograde orbit of WASP-107 b was discussed in Section 5.7.3.1, so here we turn our attention to the other three. Similar to WASP-107 b, the posterior distribution for λ for WASP-29 b diverges from 0° on both sides and therefore we can only constrain $|\lambda|$. Both solutions are consistent with one another, and we find ($|\lambda| = 115^{\circ}{}^{+42^{\circ}}_{-22^{\circ}}$). The result from the run without the $v \sin i_{\star}$ prior is similar but with somewhat inflated uncertainties, thus the orbit of WASP-29 b is consistent with retrograde. WASP-68 b is also orbiting polar or retrograde to its star with $\lambda = 99^{\circ}{}^{+18^{\circ}}_{-9^{\circ}}$. WASP-131 b has the highest projected spin-orbit angle in our sample and is orbiting its star with $\lambda = 157^{\circ} \pm 4^{\circ}$.

Table 5.4: Orbital parameters from the radial velocity and obliquity analysis presented in this work. Throughout this Table, uncertainties denote the 68 % credible interval, and upper limits denote the 99$^{\text{th}}$ percentile value. Upper limits on e means a circular orbit is adopted. Upper limits on the linear drift parameter means the data does not favour a systemic acceleration term, even if the reported limit appears significant due to a degeneracy with the systemic velocity. Linear or quadratic drift terms are chosen wherever their values and uncertainties are reported. For the obliquity analysis, the column with the $v \sin i_\star$ prior applied is our adopted values.

	radial velocity orbit analysis (§5.5)					CCF analysis (§5.6)			
								$v \sin i_\star$ prior imposed	
Planet	K ($\mathrm{m\,s^{-1}}$)	e	ω (°)	drift$^{(1)}$ ($\mathrm{m\,s^{-1}\,yr^{-1}}$)	drift$^{(2)}$ ($\mathrm{m\,s^{-1}\,yr^{-2}}$)	$v \sin i_\star$ ($\mathrm{km\,s^{-1}}$)	λ (°)	$v \sin i_\star$ ($\mathrm{km\,s^{-1}}$)	λ (°)
WASP-29 b	37.3 ± 1.3	<0.093	–	<0.0	–	$0.25^{+0.28}_{-0.17}$	$128.4^{+35.7}_{-38.1}$	$0.43^{+0.63}_{-0.25}$	$115.6^{+42.1}_{-21.8}$
WASP-68 b	100.6 ± 1.9	<0.052	–	14.8 ± 2.3	–	$0.59^{+0.70}_{-0.30}$	$104.6^{+29.8}_{-17.8}$	$1.24^{+0.99}_{-0.65}$	$98.6^{+17.7}_{-8.7}$
WASP-89 b	848.8 ± 8.7	0.181 ± 0.006	25 ± 3	57.4 ± 8.1	–	$4.66^{+4.72}_{-1.65}$	$-59.4^{+23.1}_{-16.7}$	$3.00^{+0.66}_{-0.60}$	$-40.6^{+20.1}_{-15.5}$
WASP-99 b	250.1 ± 1.7	<0.031	–	<128.0	–	$7.41^{+4.47}_{-1.07}$	$37.8^{+22.6}_{-14.5}$	$6.70^{+0.46}_{-0.38}$	$29.2^{+6.2}_{-6.9}$
WASP-105 b	191.6 ± 2.0	<0.031	–	<34.7	–	$1.25^{+0.80}_{-0.23}$	$-16.0^{+39.2}_{-36.1}$	$1.23^{+0.50}_{-0.21}$	$-15.4^{+37.1}_{-31.4}$
WASP-106 b	159.0 ± 4.0	<0.087	–	2.3 ± 7.0	-19.6 ± 7.9	$6.08^{+3.04}_{-0.78}$	$24.1^{+29.4}_{-15.4}$	$6.00^{+0.59}_{-0.49}$	$20.8^{+13.3}_{-11.8}$
WASP-107 b	16.2 ± 2.1	<0.428	–	4.1 ± 1.0	0.6 ± 0.3	$0.43^{+0.38}_{-0.14}$	$-140.4^{+28.3}_{-26.4}$	$1.17^{+1.19}_{-0.78}$	$-104.4^{+7.8}_{-36.0}$
WASP-129 b	118.2 ± 2.5	0.208 ± 0.022	95 ± 3	22.5 ± 3.2	–	3.75 ± 0.39	$3.1^{+3.9}_{-3.6}$	$3.44^{+0.33}_{-0.32}$	$4.4^{+4.1}_{-3.7}$
WASP-130 b	100.4 ± 2.4	<0.065	–	<89.5	–	1.70 ± 0.18	5.8 ± 5.2	$1.57^{+0.17}_{-0.16}$	$5.5^{+5.5}_{-5.7}$
WASP-131 b	29.2 ± 1.4	<0.110	–	<36.3	–	$2.62^{+0.29}_{-0.28}$	$157.0^{+3.9}_{-4.4}$	$2.65^{+0.28}_{-0.27}$	$157.2^{+3.8}_{-4.2}$
WASP-132 b	57.3 ± 2.6	<0.145	–	-24.4 ± 4.4	74.4 ± 5.2	$1.81^{+1.16}_{-0.77}$	$2.5^{+44.9}_{-36.5}$	$2.11^{+0.44}_{-0.42}$	$-1.7^{+38.3}_{-27.7}$
WASP-139 b	12.7 ± 1.8	<0.468	–	<6.8	–	$0.70^{+0.89}_{-0.50}$	$-74.5^{+80.2}_{-33.4}$	$2.93^{+1.32}_{-1.28}$	$-84.9^{+12.5}_{-9.2}$
WASP-166 b	8.5 ± 1.0	<0.337	–	<4.2	–	$5.38^{+0.28}_{-0.22}$	$1.3^{+2.6}_{-2.0}$	$4.82^{+0.23}_{-0.21}$	$1.2^{+2.4}_{-2.2}$

5.8 Discussion

5.8.1 The origin of misalignments

The study of stellar obliquities can give a glimpse into the early dynamical and formation history of exoplanetary systems (Winn & Fabrycky 2015; Triaud 2018). Planets are formed in protoplanetary discs — the leftover material from star formation. In a classical scenario one would expect such a disc to be aligned with the stellar equator since both the star and disc are formed from the same collapsing clump of rotating gas. Therefore, the expectation is that the angular momenta of planetary orbits and the stellar spin should, too, be aligned. Hot Jupiters are unlikely to form in-situ, so the prevailing theory is that they form beyond the ice line where solid material is more abundant, and instead spiral towards the star through interactions with the protoplanetary disc during the gas phase (Ward 1997). Such disc migration produces planets with low orbital inclinations and eccentricities.

Yet, we frequently observe both hot Jupiters (Triaud et al. 2010; Albrecht et al. 2012) and smaller planets (Winn et al. 2010b; Bourrier et al. 2018; Kunovac Hodžić et al. 2021; Hjorth et al. 2021; Bourrier et al. 2021) on misaligned and/or eccentric orbits. These observations indicate that something happens to the planets either during their formation, or some time after, that causes their orbits to become inclined. Numerous theories have been put forth that describe various pathways for misalignment, such as planet-planet scattering (Rasio & Ford 1996; Chatterjee et al. 2008), the Kozai mechanism (Fabrycky & Tremaine 2007), or secular planet-planet interactions (Wu & Lithwick 2011; Naoz et al. 2011a). These processes fall under the umbrella of disc-free migration, i.e. they occur post formation and are dynamical in nature. Typically, the planet is excited to high eccentricities and inclinations from interactions with other bodies, and later circularises close to the star due to tidal friction. Alternatively the disc itself may become misaligned or warped due to gravitational torques from a distant stellar companion, in which case the planet may still disc-migrate but end up on an inclined orbit (Batygin 2012; Terquem 2013). An open question is to what extent these various processes operate, with some studies already pointing to high-eccentricity migration from planet-planet interactions as a dominant pathway (Nelson et al. 2017).

5.8.2 Tidal realignment

Studies of obliquity trends have revealed several patterns. For example, most of the misaligned hot Jupiters orbit "hot" stars that have a temperature in excess of ≈6100 K (Winn et al. 2010a; Dawson 2014), whereas cold stars tend to host aligned planets. If one studies the population of hot Jupiters orbiting cold stars alone, one finds that planets orbiting further from the star are more frequently misaligned and/or eccentric, though the sample size gets small at larger separations (Triaud 2018). A third pattern is that planet mass tend to be correlated with low obliquity. These patterns can be explained by a combination of ongoing tidal evolution and stellar spin evolution in hot Jupiter systems (Albrecht et al. 2012; Dawson 2014). However, it has been difficult to test this hypothesis due to the drop-off in occurence rate of hot Jupiters on orbital periods beyond a few days where tides are expected to be weaker (Santerne et al. 2016). The timescales of tidal realignment follow a relation of the form $\tau \propto q(a/R_\star)^5$ where $q = M_\star/M_\mathrm{p}$ is the

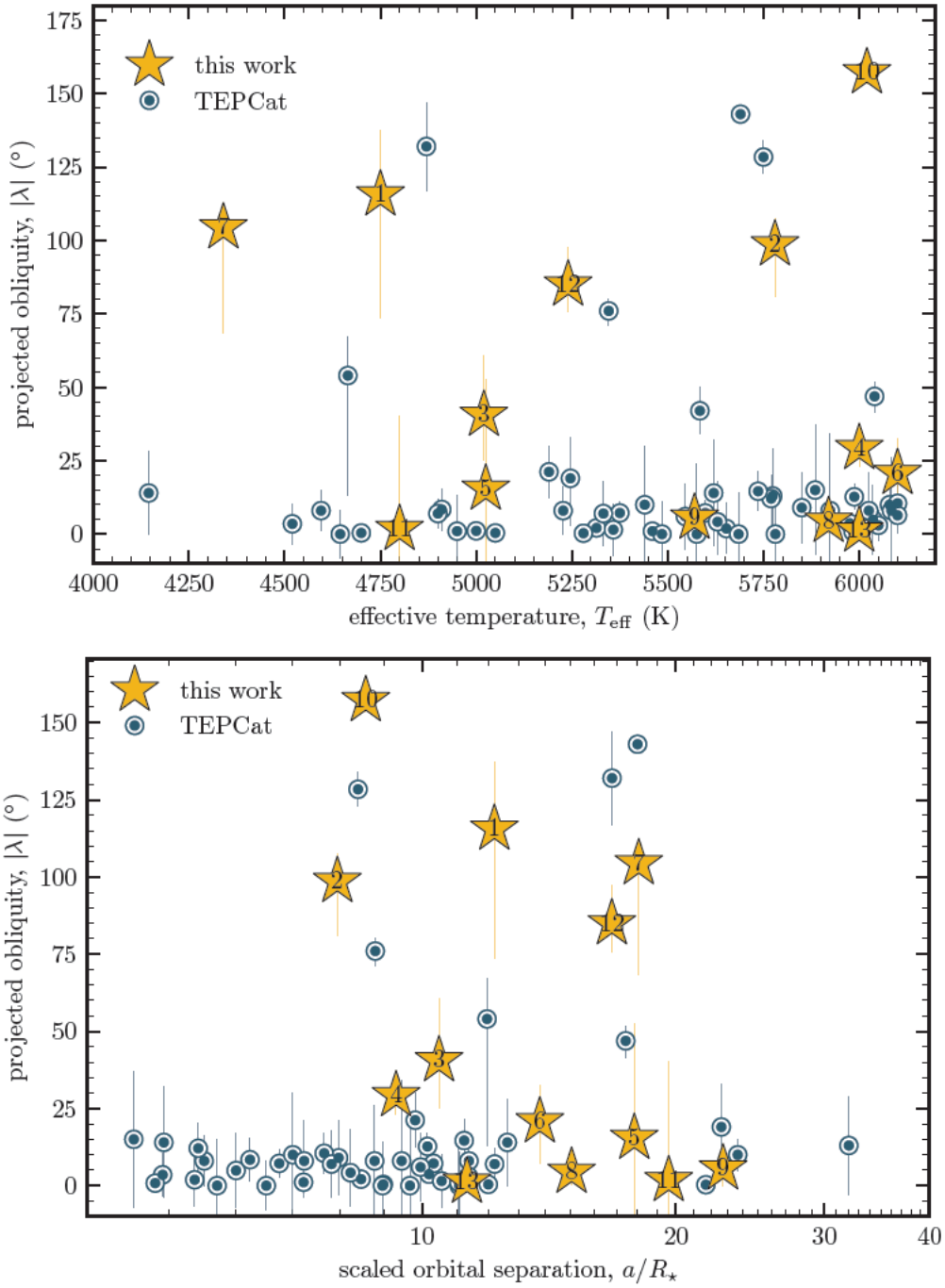


Figure 5.6: Projected obliquities as functions of stellar effective temperature (*top*) and scaled separation (*bottom*). Literature measurements (*blue*) are obtained from TEPCat, and measurements from this work are shown in yellow. The data for WASP-166 b has been previously published, but has not been analysed with the reloaded Rossiter-McLaughlin method. Labels: [1]WASP-29 b [2]WASP-68 b [3]WASP-89 b [4]WASP-99 b [5]WASP-105 b [6]WASP-106 b [7]WASP-107 b [8]WASP-129 b [9]WASP-130 b [10]WASP-131 b [11]WASP-132 b [12]WASP-139 b [13]WASP-166 b.

mass ratio (Barker & Ogilvie 2009b), thus the time for realignment rapidly increases to system lifetime timescales at larger separations. This work considers the obliquities of 13 giant planets orbiting at larger separations (Figure 5.6) and therefore represents a significant leap in our understanding of tidal evolution in hot Jupiter systems.

5.8.3 Origins of our sample

Our main result shows the obliquities of giant planets on "warmer" orbits tend to have a wider variety than has previously been seen, which is in line with the expectation from tidal theory but has until now been difficult to test with Rossiter-McLaughlin measurements. Several of the misaligned systems in this work appear to have polar or close to polar orbits. Recent work shows a surplus of hot Jupiters at $|\lambda| \approx 90°$ and may offer some support of this result (Albrecht et al. 2021). Since the origin of the obliquities is believed to be dynamical in nature, the discovery of radial velocity drifts in five systems is an important addition to our work as these candidate companions may have had a role to play in the initial misalignment. However, we do not see any obvious correlation between misaligned systems and the presence of candidate companions in our sample. Future work may expand on this by using *Gaia* astrometry to search for additional signals.

Among our eccentric targets, WASP-89 b and WASP-129 b, only the former shows a preference for a somewhat misaligned configuration, though the measurement could be consistent with low obliquity and alignment. WASP-89 b is the most massive planet in our sample $M_\mathrm{p} \approx 5.82\,M_\mathrm{Jup}$, thus it may have been able to realign the star within the system lifetime. For WASP-129 b the situation is somewhat different. Given its mass of $M_\mathrm{p} \approx 1\,M_\mathrm{Jup}$ and $a/R_\star \approx 15$, it is unlikely to have been able to realign the star. Its low obliquity may therefore be indicative of its origin. We speculate that WASP-129 b arrived at its present location by gas-driven migration, and may therefore be more similar to the population of warm Jupiters that more frequently have companion planets (Huang et al. 2016). The presence of a candidate long period companion in the radial velocity data may support this picture. The low obliquity and wider separations of WASP-105 b, WASP-106 b, WASP-130 b and WASP-139 b also fall into a similar category, thus these may also be good candidates for disc-migration of giant planets. Nelson et al. (2017) found that ~15 % of hot Jupiters migrate by disc interaction. This fraction is not consistent with our findings. This may indicate that our assumption of equating low obliquity/high-$a/R_\star$ with disc migration may be faulty — indeed the picture is likely more complex than we present here. Alternatively, it may indicate an unknown selection bias in our sample, or that our sample comprises two different populations of close-in giant planets (Huang et al. 2016).

5.9 Conclusion

We have presented spectroscopic transits of 13 giant planets orbiting cool stars in weak-tide regimes. The transits were observed with the HARPS spectrograph between 2010 and 2018, and our analysis is based on the temporal variation in the shape of the cross-correlation functions during transit.

Although we caution that this is still work in progress, we are able to draw some preliminary conclusions from this work. We measure a range of spin-orbit misalignments within our sample, in contrary to the expectation that giant planets orbiting cold stars are aligned with the stellar spin. Five planets (WASP-29 b, WASP-68 b, WASP-107 b, WASP-131 b, and WASP-139 b) are significantly misaligned with polar or retrograde orbits. Another three systems (WASP-89 b, WASP-99 b and WASP-139 b) have low or indeterminate obliquities but are preferentially misaligned, though we cannot rule out alignment. The remaining five systems (WASP-105 b, WASP-106 b, WASP-129 b, WASP-130 b, WASP-132 b, and WASP-166 b) have low obliquities that are consistent with alignment of the orbit and stellar spin. Some of the low obliquity systems are strong candidates for disc-migration owing to the weaker tidal influence at these separations ($a/R_\star > 15$).

We measure statistically significant orbital eccentricities in WASP-89 b ($e = 0.181 \pm 0.006$) and WASP-129 b ($e = 0.208 \pm 0.022$). Of these two, the eccentricity of WASP-129 b is a new discovery. Finally, we detect radial velocity acceleration in WASP-68, WASP-89, WASP-106, WASP-129, and WASP-132, which could indicate additional unseen companions.

This work is expected to be an important addition to the sample of stellar obliquities of cool stars with transiting planets, and will inform our knowledge on the role of tidal evolution in exoplanet systems, the dynamical evolution of close-in giant planets, and the link between hot and warm Jupiters.

CHAPTER 6

ALIGNMENT OF A STAR WITH THE ORBIT OF ITS BINARY COMPANION AND CIRCUMBINARY PLANET

6.1 Background

This Chapter is a small part of a much larger work on the obliquities of the primary component in eclipsing binaries with a low-mass secondaries (EBLMs, Triaud et al. 2013). This was not originally meant to be part of my PhD, but it came to fruition when I decided to apply for a Fulbright Scholarship to go to the US for a six-month research visit. The reason behind this was that I had a vague idea of wanting to go to the US for a postdoc after completing my PhD, so I thought a research visit at a US institution might help me get a foot in the door.

As part of the application process that took place during the autumn of 2018, I had to write a research proposal tailored to a specific University, so Amaury and I sat down to discuss some options. Over the course of Amaury's own PhD while working on the WASP survey, the team had found several hundred eclipsing binary systems composed of a Sun-like primary and a low-mass (M dwarf) secondary (e.g. Triaud et al. 2017). These systems came as a byproduct of looking for planets as they could mimic transit signals given the small size of the secondary stars. After Amaury's PhD he and the WASP team followed up several hundred of these systems with the CORALIE spectrograph to get their mass from the radial velocity orbits (e.g. Triaud et al. 2017; Martin et al. 2019), and gathered additional light curves for the most interesting targets to derive more precise radii than the WASP data allowed (Gómez Maqueo Chew et al. 2014; von Boetticher et al. 2017, 2019; Gill et al. 2019).

One of the primary goals of the EBLM project is to calibrate M dwarf stellar evolution models by deriving an empirical mass-radius-temperature relation for M dwarfs. This can be accomplished by combining primary and secondary eclipse light curves together with the radial velocity orbit of the primary, as we saw in Chapter 2.1.3. However, EBLMs are single-lined binaries, so the derivation of the

absolute dimensions of the secondary still depends on the mass, radius, and temperature of the primary star. The absolute dimensions of the primary may be based on stellar evolution models (e.g. Maxted et al. 2015), or model-independent measurements (Stevens et al. 2018).

Roughly two dozen EBLMs from the WASP sample were observed in spectroscopy with CORALIE during primary eclipse for the Rossiter-McLaughlin effect. The discovery of these systems had not yet been published, so a research proposal started taking shape. *TESS* had recently finished surveying the Southern sky in Cycle 1, which meant light curves with primary and secondary eclipses were now available. These could be combined with the archival CORALIE radial velocity data to get the orbital solution and expand the sample of mass-radius-temperature measurements on M dwarfs significantly. With the orbital solution available, the spectroscopic transits can be used to derive the obliquity of the primary star. This would provide a comprehensive characterisation of the orbit and components of roughly two dozen low-mass eclipsing binaries, which can help constrain dynamical and tidal evolution in binary systems. The obliquity of these stars are also of particular interest because they are potential homes to circumbinary planets. In fact, the EBLM sample makes up the BEBOP (Binaries Escorted By Orbiting Planets) radial velocity survey for circumbinary planets (Martin et al. 2019).

One of the potential host institutions that came up in our talk was The University of Chicago, where one of Amaury's collaborators on BEBOP, David Martin, was on a postdoctoral fellowship. David could assist with some of the data access and interpretation for this project, and he was mentored by Daniel Fabrycky who came with warm recommendations from Amaury as they had worked together previously. We decided to pursue this for my research proposal, so I reached out to Dan at The University of Chicago to inquire if he could host me. I was offered a Fulbright Scholarship from the U.S. - Norway Fulbright Foundation that supported me from September 2019 to March 2020 at The University of Chicago. During this time Dan acted as my second PhD advisor. Dan's and David's backgrounds are more theoretical than what I was used to, so I found our discussions enriching as they provided some new perspectives.

While in Chicago my time was stretched thin because I was still somewhat occupied with working on the π Men analysis, and as a result the EBLM work was not completed within those six months. Upon returning to the UK I decided to put this project on hold and revisit it later as the work in Chapter 5 was of higher priority to my thesis. However, I was not content with not having anything to show for those six months in Chicago, so I was excited when an opportunity arose towards the end of my stay. In February 2020, in the final month before my return to the UK, David Martin had started a new position at The Ohio State University (OSU) and invited me to visit the department for a week. Concurrent to this, both of us were involved in *TESS'* first circumbinary planet discovery (Kostov et al. 2020). Conveniently, the system in question was one of the two dozen systems that was observed with CORALIE during a primary eclipse to measure the Rossiter-McLaughlin effect many years ago. Within the EBLM team the binary is referred to as EBLM J0608-59, though given the planet detection the system is also named after the *TESS* Object of Interest (TOI) number, TOI-1338, which explains the two names referred to in the paper below. This binary system became relevant overnight because of the planet residing in the system, so while visiting David at OSU I decided to focus exclusively on the analysis of this system to publish a

paper on the measurement of the primary star's obliquity. I finished most of the analysis of the CORALIE data within that one week at OSU and started writing the paper shortly after that. This work is also what gave me much more experience and confidence in working on CCFs, which helped immensely when I finally returned to and finished my work on π Men upon returning to the UK.

Monthly Notices of the ROYAL ASTRONOMICAL SOCIETY

MNRAS 497, 1627–1633 (2020)
Advance Access publication 2020 July 15

doi:10.1093/mnras/staa2071

The EBLM project – VII. Spin–orbit alignment for the circumbinary planet host EBLM J0608-59 A/TOI-1338 A

Vedad Kunovac Hodžić,[1,2★†] Amaury H. M. J. Triaud,[1★] David V. Martin,[3‡] Daniel C. Fabrycky,[2] Heather M. Cegla,[4,5] Andrew Collier Cameron,[6] Samuel Gill,[4] Coel Hellier,[7] Veselin B. Kostov,[8,9] Pierre F. L. Maxted,[7] Jerome A. Orosz,[10] Francesco Pepe,[5] Don Pollacco,[4] Didier Queloz,[5,11] Damien Ségransan,[5] Stéphane Udry[5] and William F. Welsh[10]

[1]*School of Physics and Astronomy, University of Birmingham, Edgbaston, Birmingham B15 2TT, UK*
[2]*Department of Astronomy and Astrophysics, University of Chicago, 5640 S. Ellis Avenue, Chicago, IL 60637, USA*
[3]*Department of Astronomy, The Ohio State University, 4055 McPherson Laboratory, Columbus, OH 43210, USA*
[4]*Department of Physics, University of Warwick, Gibbet Hill Road, Coventry CV4 7AL, United Kingdom*
[5]*Observatoire Astronomique de l'Université de Genève, 51 Chemin des Maillettes, CH-1290 Sauverny, Switzerland*
[6]*SUPA, School of Physics & Astronomy, University of St Andrews, North Haugh, St Andrews, Fife, Scotland KY16 9SS, UK*
[7]*Astrophysics Group, Keele University, Staffordshire ST5 5BG, UK*
[8]*NASA Goddard Space Flight Center, 8800 Greenbelt Road, Greenbelt, MD 20771, USA*
[9]*SETI Institute, 189 Bernardo Avenue, Suite 200, Mountain View, CA 94043, USA*
[10]*Department of Astronomy, San Diego State University, 5500 Campanile Drive, San Diego, CA 92182, USA*
[11]*Cavendish Laboratory, J J Thomson Avenue, Cambridge CB3 0HE, UK*

Accepted 2020 July 13. Received 2020 July 12; in original form 2020 April 24

ABSTRACT

A dozen short-period detached binaries are known to host transiting circumbinary planets. In all circumbinary systems so far, the planetary and binary orbits are aligned within a couple of degrees. However, the obliquity of the primary star, which is an important tracer of their formation, evolution, and tidal history, has only been measured in one circumbinary system until now. EBLM J0608-59/TOI-1338 is a low-mass eclipsing binary system with a recently discovered circumbinary planet identified by *TESS*. Here, we perform high-resolution spectroscopy during primary eclipse to measure the projected stellar obliquity of the primary component. The obliquity is low, and thus the primary star is aligned with the binary and planetary orbits with a projected spin–orbit angle $\beta = 2\overset{\circ}{.}8 \pm 17\overset{\circ}{.}1$. The rotation period of 18.1 ± 1.6 d implied by our measurement of $v \sin i_\star$ suggests that the primary has not yet pseudo-synchronized with the binary orbit, but is consistent with gyrochronology and weak tidal interaction with the binary companion. Our result, combined with the known coplanarity of the binary and planet orbits, is suggestive of formation from a single disc. Finally, we considered whether the spectrum of the faint secondary star could affect our measurements. We show through simulations that the effect is negligible for our system, but can lead to strong biases in $v \sin i_\star$ and β for higher flux ratios. We encourage future studies in eclipse spectroscopy test the assumption of a dark secondary for flux ratios $\gtrsim$1 ppt.

Key words: planets and satellites: formation – binaries: eclipsing – stars: individual: (EBLM J0608-59, TOI-1338) – stars: low-mass – stars: rotation.

1 INTRODUCTION

EBLM J0608-59 consists of an inner low-mass binary ($M_1 = 1.13\,M_\odot$, $M_2 = 0.31\,M_\odot$) on a 14.6-d eccentric orbit (Triaud et al. 2017), with an outer Saturn-sized circumbinary planet on a 95-d orbit recently discovered in *TESS* photometry (TOI-1338 AB b; Kostov et al. 2020). The inner binary was first identified as a transiting planet candidate by the WASP survey (Pollacco et al. 2006), but radial velocities measurements soon determined it was instead a G+M single-lined eclipsing binary. Subsequently, EBLM J0608-59 (hereafter J0608-59) was followed up spectroscopically as part of the EBLM project whose goal is to study the properties of low-mass eclipsing binary systems (Triaud et al. 2013, 2017). One of the objectives of the EBLM project is to provide observational constraints on the tidal physics of tight binaries. To study this, we collect three types of observables: rotational velocities $v_{\rm eq} \sin i_{\star,1}$ of the primary stars, precise eccentricities and, in some cases, spin–orbit angles β,[1] which are obtained by measuring the Rossiter–McLaughlin effect (McLaughlin 1924; Rossiter 1924; Kopal 1942).

★ E-mail:
† Fulbright Fellow.
‡ Fellow of the Swiss National Science Foundation.

[1] the notation λ has been used for the spin–orbit angle of exoplanets, with $\lambda = -\beta$. β, defined by Kopal (1942), i.e. the projected angle between the orbital and stellar spin axes, is widely used within the binary star community.

© 2020 The Author(s)
Published by Oxford University Press on behalf of the Royal Astronomical Society

Downloaded from https://academic.oup.com/mnras/article-abstract/497/2/1627/5871829 by Keele University user on 03 August 2020

Despite many spin–orbit measurements obtained on transiting exoplanets (e.g. Winn & Fabrycky 2015; Triaud 2018), not many have been obtained on eclipsing binaries. A list of historical measurements can be found in Albrecht et al. (2011). Hale (1994) notes that binaries with separation >30–40 au are usually found with random spins. For tighter binaries, the most extensive collection of measurements were produced by the BANANA survey (e.g. Albrecht et al. 2014), which mainly targets massive stars, with a recent compilation from the Torun project (Sybilski et al. 2018). So far, most binary pairs appear spin–orbit aligned except DI Hercules (Albrecht et al. 2009), CV Velorum (Albrecht et al. 2014), and AI Phe (Sybilski et al. 2018). The binary sample covered by the EBLM project is distinct from these other efforts in focusing exclusively on small ($M_2/M_1 \lesssim 0.3$) mass ratio binaries with solar-like primaries. So far, three measurements of β have been published by the project: WASP-30, EBLM J1219-39 (Triaud et al. 2013), and EBLM J0218-31 (Gill et al. 2019), where all primary stars were found to be coplanar with their respective orbits. We have collected Rossiter–McLaughlin measurements on dozens of systems whose analysis are ongoing, exploring parameter space in terms of $v_{\rm eq}\sin i_{\star,1}$, eccentricities, and orbital periods.

In this paper, we report a spectroscopic primary eclipse of J0608-59 to measure the stellar obliquity of the primary component with respect to the binary and planet orbits from the Rossiter–McLaughlin effect. J0608-59 is only the second primary star host to a circumbinary planet to have a Rossiter–McLaughlin measurement made, following the 41 d binary Kepler-16, which was found to be aligned (Winn et al. 2011). Additionally, the 7.5 d binary Kepler-47 is also thought to be spin–orbit aligned, based on eclipse spot-crossings (Orosz et al. 2012).

2 OBSERVATIONS

A single spectroscopic primary eclipse of J0608-59 was observed on 2010 November 2 using the 1.2-m Swiss *Euler* Telescope at La Silla, Chile. The CORALIE instrument spans the visible range (390–680 nm) with an average resolving power of $R \sim 55\,000$. We obtained 19 exposures of 900 s each[2] over 5.8 h, capturing the primary eclipse entirely, including two spectra before ingress. The data were reduced using the standard CORALIE Data Reduction Software (DRS; Lovis & Pepe 2007). In brief, a cross-correlation function (CCF) is derived between the observed spectra and a G2 numerical mask. A comparison is made with a reference thorium–argon spectrum, which allows for corrections based on instrumental variations throughout the eclipse (e.g. atmospheric variations since CORALIE is not pressure stabilized). Overall, CORALIE is stable to 5 m s^{-1}, while the median radial velocity error per observation is 26 m s^{-1}.

As a part of the EBLM program, J0608-59 received an additional 19 radial velocity measurements to map out its orbit with CORALIE. From these data, we select three epochs between 2009 November 28–29 and 2010 January 6 as reference spectra due to insufficient data outside the spectroscopic eclipse night. J0608-59 was also selected as a target in the BEBOP radial velocity search for circumbinary planets. An additional 17 CORALIE measurements were made and published in Martin et al. (2019), and an additional seven HARPS measurements have been taken since. Finally, J0608-59 was observed in 12 *TESS* sectors (Kostov et al. 2020), 9 of which were short-cadence data under the Guest Investigator Program G011278 (PI: O. Turner). The BEBOP data were not used in the analysis of this work, but we use orbital parameters (Table 1) from Kostov et al. (2020) that are based on the BEBOP and *TESS* data.

[2]Except the two initial points, which were 600 s.

Table 1. Target and binary orbital parameters. Subscripts 1 and 2 denote the primary and secondary components, respectively. Brackets denote uncertainties on last two digits.

Parameter	Description	Value
Target information		
α	Right ascension	$06^{\rm h}08^{\rm h}31\overset{\rm s}{.}95$
δ	Declination	$-59^\circ32'28\overset{''}{.}1$
$V_{\rm mag}$	Apparent magnitude	11.73
Stellar parameters		
M_1 ($M_\odot$)	Primary mass	1.127(68)
M_2 ($M_\odot$)	Secondary mass	0.313(11)
R_1 ($R_\odot$)	Primary radius	1.331(24)
R_2 ($R_\odot$)	Secondary radius	0.3089(56)
$T_{\rm eff,1}$ (K)	Primary temperature	6050(80)
$T_{\rm eff,2}$ (K)	Secondary temperature	3330(50)
$\log g_1$ (cgs)	Surface gravity	4.00(08)
$[{\rm Fe/H}]_1$	Metallicity	0.01(05)
[a] $v_{\rm eq}\sin i_{\star,1}$ (km s^{-1})	Projected rotation	3.6(0.6)
Age (Gyr)	Isochrone binary age	4.4(0.2)
Orbital parameters		
$P_{\rm bin}$ (d)	Binary orbital period	14.608559(13)
$T_{\rm pri}$ (BJD$-x$[b])	Time of primary eclipse	53336.8242(25)
K_1 (km s^{-1})	RV semi-amplitude	21.6247(34)
$e_{\rm bin}$	Eccentricity	0.15603(15)
$\omega_{\rm bin}$ ($^\circ$)	Periastron angle	117.554(72)
$i_{\rm bin}$ ($^\circ$)	Orbital inclination	89.70(18)
$b_{\rm bin}$ (R_1)	Impact parameter	0.097(57)
$a_{\rm bin}$ (au)	Separation	0.1321(24)
$J_{\rm TESS}$	Surface brightness ratio	0.0926(28)
u	Lin. limb darkening coeff.	0.40
v	Quad. limb darkening coeff.	0.29

[a]Determined from rotational line broadening using HARPS (Kostov et al. 2020).
[b]$x = 2\,450\,000$.

3 LINE PROFILE ANALYSIS

Radial velocity measurements are typically determined from a cross-correlation technique. The resulting CCFs are fitted with Gaussian profiles to determine the effective radial velocity, i.e. treating any distortion of the line profiles as a pure Doppler shift of the line centre. The Rossiter–McLaughlin effect is, however, a spectroscopic effect where the line profiles are distorted depending on the position of the occulting body on the stellar disc.

While many techniques have been put forth to improve on the modelling of the anomalous radial velocity during a spectroscopic transit/eclipse to account for these effects (e.g. Albrecht et al. 2007; Hirano et al. 2011), other methods have been developed for modelling the spectral line distortions directly. These methods are commonly referred to as Doppler tomography or Doppler shadow (Collier Cameron et al. 2010; Cegla et al. 2016a; Hirano et al. 2020). Here, we use the *reloaded* Rossiter–McLaughlin technique from Cegla et al. (2016a) to directly retrieve the occulted light from the stellar disc with no assumptions on the shape of the line profiles compared to other methods. For this and future analyses, we have written a dedicated

Downloaded from https://academic.oup.com/mnras/article-abstract/497/2/1627/5871829 by Keele University user on 03 August 2020

software package, `elle`,[3] and plan to release a user-friendly public version in a forthcoming paper.

3.1 Retrieving the occulted light

We work on the disc-integrated CCFs output from the CORALIE DRS. We start by removing the Keplerian velocity due to the binary orbit by resampling the CCFs on a common velocity grid at the spectrograph resolution of $\sim$1.8 km s^{-1}. The orbital parameters to compute the Keplerian model are obtained from Kostov et al. (2020), who analysed the full *TESS* Cycle 1 photometry and CORALIE/HARPS radial velocities, modelling both the binary orbit as well as the circumbinary planet orbit using a photodynamical model. Their fit did not detect any significant binary apsidal motion, and produced a $\chi^2_\nu \approx 1$, indicating very good agreement on the data despite that $\sim$10 yr separating the first CORALIE observations from the *TESS* photometry. From this, we can rule out any significant changes in the binary ephemeris, such as radial velocity drifts and associated light traveltime effects due to distant massive companions.

The CCFs are scaled by their respective continuum flux to compare their relative flux variations. We define the continuum level as the median flux 4σ outside the computed line profile centres (radial velocity), where σ denotes the width of the Gaussian fit from the CORALIE DRS. In the same fashion, we also estimate the CCF error by computing the standard deviation of the continuum flux. Furthermore, we also normalize the CCFs by the theoretical primary eclipse limb-darkened light curve to account for the loss of light during eclipse, where the light curve was again computed using orbital elements from Kostov et al. (2020).

As with any Doppler shadow method, the in-eclipse CCFs need to be compared to a high SNR template CCF (typically an average over several out-of-eclipse spectra) that represents the intrinsic rotationally broadened stellar spectrum. The Rossiter–McLaughlin sequence we use in this work only has two spectra taken outside of the eclipse window, both observed at high airmass, $z > 1.8$, and at shorter integration times than in-eclipse observations. Upon inspection of the normalized CCFs we noticed – other than lower SNR – that these two observations had CCF contrasts (depths) 3–4 per cent smaller than the remaining sample from the same night.

To avoid biasing our measurements due to the anomalous CCF contrast, we do not use the two spectra at the beginning of night to build our reference. Instead, we average the two spectra together to determine the systemic velocity at the night of the spectroscopic eclipse, $\gamma_{\rm RM}$. Then, we identify three individual spectra taken at different nights with the same exposure time as our in-eclipse observations, and verify that their CCF contrast, FWHM, and SNR match the data taken during eclipse. The three reference spectra are resampled to the same grid as with the in-eclipse spectra, but shifted to $\gamma_{\rm RM}$ to account for any stellar activity between the observations. The three spectra are then averaged together, weighted by their errors, to create a master out-of-eclipse template, CCF$_{\rm out}$. The in-eclipse spectra and CCF$_{\rm out}$ – now in the same reference frame – are then shifted by $\gamma_{\rm RM}$ to bring the CCFs to the stellar rest frame. The residual line profiles are then calculated from the difference between CCF$_{\rm out}$ and the in-eclipse, disc-integrated CCFs. The resulting in-eclipse residual profiles,[4] hereafter CCF$_{\rm in}$, represent the light on the stellar disc occulted by the star and are shown in Fig. 1, clearly displaying the trace of the secondary star as it moves across the primary's disc.

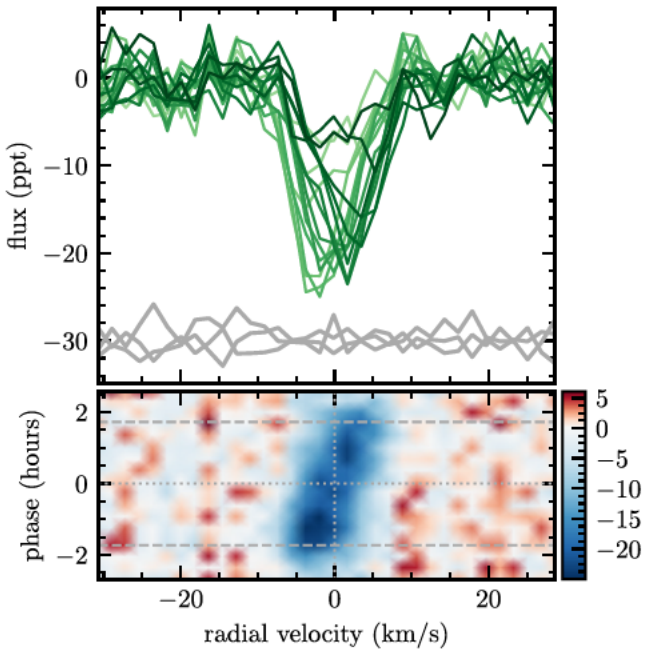


Figure 1. *Upper panel:* The retrieved residual line profiles hidden beneath the eclipsing secondary star, with colours getting darker with time. The grey profiles at the bottom are the residuals from the reference spectra with an arbitrary offset. *Lower panel:* Another view showing the residual flux as a function of time on the vertical axis, displaying the trace, or Doppler shadow, of the eclipsing body moving across the rotating stellar disc. The grey-dashed lines denote the second and third contact points, and the dotted lines denote the mid-transit point and minimum limb angle. The colour bar shows the CCF flux.

We compute their local radial velocity by fitting Gaussian profiles to the CCF$_{\rm in}$. To obtain realistic uncertainties and avoid fitting spurious signals (particularly an issue for low-SNR data, such as profiles at the stellar limb) we use a Markov chain Monte Carlo (MCMC) sampling method to explore the full posterior distribution and propagate uncertainties in the 'nuisance'[5] parameters to the final radial velocity. We build our Gaussian model in the `pyMC3` framework (Salvatier, Wiecki & Fonnesbeck 2016), varying the line centre, μ; width, σ; contrast A; continuum level, c, and CCF error, ϵ. We sample these five parameters using the No-U-Turn sampler (Hoffman & Gelman 2014). To avoid cherry-picking the local profiles that provide a good fit (and thus keep for further analysis), we use wide, informative priors on our parameters aimed at returning a conservative estimate of the radial velocity in case of a non-detection of the local line centre. The priors for A, σ, and ϵ are drawn from the half-normal distribution as they are both restricted to positive values, and draw from the normal distribution for μ and c. The resulting local surface velocities over the eclipse duration are shown in Fig. 2.

3.2 Surface velocity modelling

The surface velocity model is computed using the semi-analytical prescription in Cegla et al. (2016a). Here, we create a 51 × 51 grid

[3] https://github.com/vedad/elle

[4] These are no longer disc-integrated profiles since the disc-integrated contribution has been removed.

[5] While the depths and widths of the Gaussian can be useful for diagnostic purposes, we are mainly interested in the line profile centre, μ, and its uncertainty.

Downloaded from https://academic.oup.com/mnras/article-abstract/497/2/1627/5871829 by Keele University user on 03 August 2020

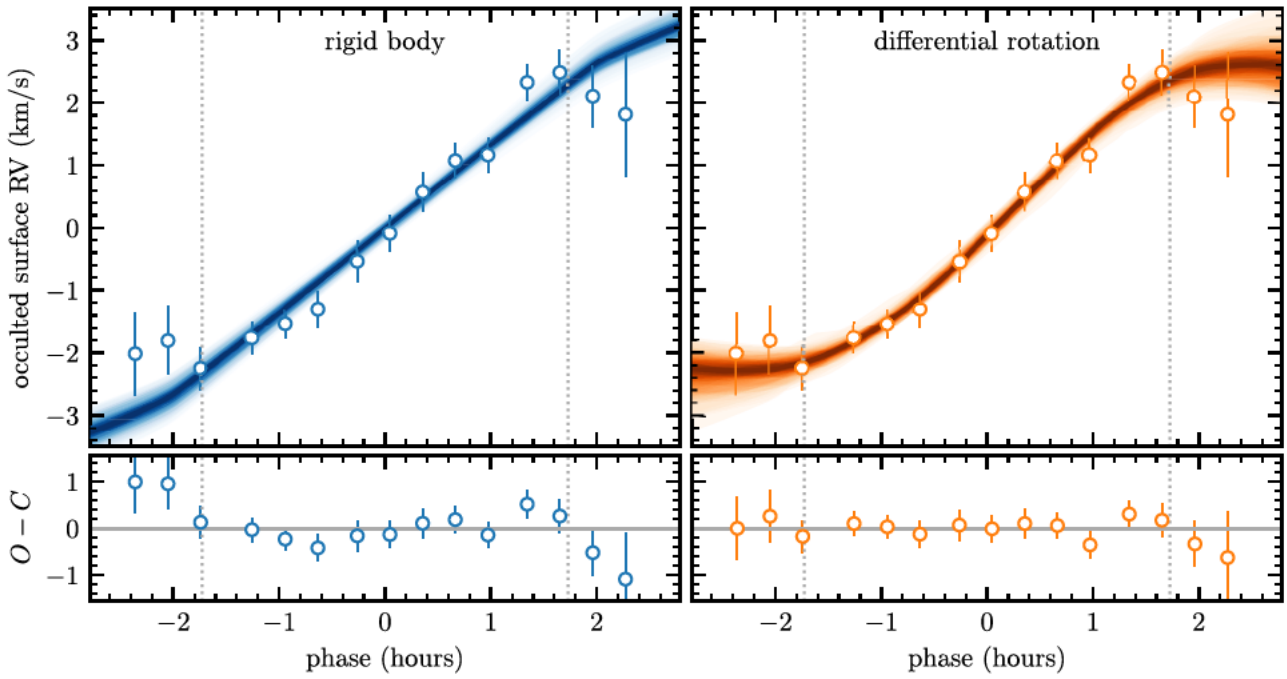


Figure 2. *Upper panels:* The local radial velocities during eclipse, obtained from Gaussian fits to the residual profiles in Fig. 1, for the rigid body model (*left*) and differential rotation model (*right*). The shading denotes the 50th–99th percentiles of the models. The dotted lines denote the second and third contacts, while the horizontal axis is delineated by the eclipse duration. *Lower panels:* Residuals from the maximum likelihood fits of each model. The differential rotation model reduces χ^2_ν from 1.2 to 0.5, and improves the Bayesian Information Criterion (BIC) by 5.5.

that spans the size of the eclipsing body, and co-moving with its centre. At every epoch, the brightness-weighted rotational velocity at a given position is computed by summing the cells covering the stellar disc occulted by the eclipsing body. We assume the star follows a quadratic limb darkening function, with coefficients $c_1 = 0.40$, $c_2 = 0.29$ obtained from interpolating $T_{\rm eff}$, $\log g$, and [Fe/H] in the *V*-band tables from Claret & Bloemen (2011), using the online tool from (Eastman, Gaudi & Agol 2013).[6] Oversampling and averaging our model within each 900 s exposure did not impact our results.

The theoretical surface velocity at any point on a rotating rigid body is computed from a combination of the orbital phase, $\phi(P, T_0)$; orbital inclination, $i_{\rm orb}$; the stellar (primary) radius scaled by the binary separation, R_1/a; projected stellar equatorial velocity, $v_{\rm eq}\sin i_{\star,1}$; and the projected spin–orbit angle, β. While many of these parameters are known very precisely from Kostov et al. (2020; see Table 1), the impact parameter $b = a\cos i_{\rm bin}/R_1$ is known to correlate with both $v_{\rm eq}\sin i_{\star,1}$ and β when b is close to zero. We therefore vary R_1/a and $i_{\rm orb}$ with their Gaussian uncertainties during the fit, and let $v_{\rm eq}\sin i_{\star,1}$ and β float freely. We fix the ephemerides P, T_0, but checked that our results were insensitive to their influence by perturbing them by their 1σ uncertainties. We sample these four parameters using the `emcee` MCMC sampler (Foreman-Mackey et al. 2013) to obtain their full posterior distributions, using 200 walkers that are run for ∼50 times the autocorrelation length. The final posterior distributions are obtained after discarding a number of burn-in steps determined visually, and thinning the individual walkers by the autocorrelation length of the parameters. We also attempt to model the data assuming the rotation rate varies as a function of stellar latitude (differential rotation). In this case, we can independently sample the equatorial velocity, $v_{\rm eq}$, and the stellar inclination, $i_{\star,1}$. Additionally, we sample the relative shear, $\alpha = (\Omega_{\rm eq} - \Omega_{\rm pole})/\Omega_{\rm eq}$, which describes the relative rotation rate between the poles and the equator.[7] We varied the parameters uniformly in $v_{\rm eq} \in [0, 5.3]\,{\rm km\,s^{-1}}$, $\beta \in [-180, 180]°$, $i_{\star,1} \in [0, 180]°$, and $\alpha \in [-2, 1]$, where $\alpha < 0$ signifies antisolar differential rotation, i.e. that the polar latitudes rotate faster than the equator. The upper limit on $v_{\rm eq}$ was set to the predicted pseudo-synchronous rotation period, which is expected at 12.7 d.

4 RESULTS AND DISCUSSION

4.1 Stellar obliquity and rotation

The trace of the secondary star in Fig. 1 is clearly indicative of a prograde orbit as it moves from blue-shifted to red-shifted areas on the stellar disc of the primary. We summarize our results in Table 2. From the data modelling outlined in Section 3, we find a projected rotation and projected stellar obliquity, $\beta = 2\overset{\circ}{.}8 \pm 17\overset{\circ}{.}1$ when assuming rigid body rotation. The three largest sources of angular momentum in the system are the binary and planetary orbits, followed by the primary's rotation – whose magnitudes contribute in approximate ratios of 6000:4:1. Given that the binary and planet orbits are co-planar, with mutual a inclination $|\Delta i| = 0.3°$, the largest angular momentum vectors are thus found to be aligned. Kostov et al. (2020) reported $v_{\rm eq}\sin i_{\star,1} = 3.6 + -0.6\,{\rm km\,s^{-1}}$ from rotational broadening, based on high-resolution spectra from HARPS obtained through the BEBOP survey (ESO prog. ID 1101.C-0721, PI: Triaud; Martin et al. 2019), thus the two measurements agree very well. Our measurement of $v_{\rm eq}\sin i_{\star,1}$ combined with the stellar radius

[6] http://astroutils.astronomy.ohio-state.edu/exofast/limbdark.shtml

[7] $\alpha \sim 0.2$ for the Sun.

Downloaded from https://academic.oup.com/mnras/article-abstract/497/2/1627/5871829 by Keele University user on 03 August 2020

Table 2. Derived spin–orbit parameters. The bold values denote adopted values and model.

Model	$v_{\rm eq}$ (km s^{-1})	$i_{\star,1}$ (°)	β (°)	α	ψ (°)	$P_{\rm rot}$ (d)	χ^2	BIC
Rigid body	$\mathbf{3.69^{+0.35}_{-0.25}}$	**90**[a]	$\mathbf{2.9^{+16.0}_{-15.8}}$	**0**[a]	–	$\mathbf{18.3^{+1.4}_{-1.6}}$	**15.9**	**−9.2**
Differential rotation	$3.89^{+0.87}_{-0.68}$	$137.1^{+13.7}_{-74.8}$	$9.7^{+12.4}_{-11.8}$	$[-1.85, -0.91]$[b]	$53.0^{+10.5}_{-16.4}$	$17.3^{+3.7}_{-3.2}$	4.9	−14.8

[a]Fixed under rigid body assumption. [b]68 per cent confidence interval.

suggests a present-day rotation period of 18.1 ± 1.6 d, assuming a stellar inclination of 90°.

The rigid body model in the left-hand panel of Fig. 2 does not accurately predict the surface velocity at the limbs. One could rightly expect the behaviour at the limb to depend on the particular choice of limb darkening models and its parameters, as well as the size of planet grid. We addressed each of these scenarios by varying the limb darkening coefficients within Gaussian uncertainties of 0.1, using a power-2 limb darkening law (e.g. Maxted 2018), and increasing the planet grid size up to 91 × 91. None made any detectable impact on our results. Moreover, the centre-to-limb variation due to convective blueshift (Cegla et al. 2016a,b) is expected to be symmetric around the mid-transit time, while the data at both limbs seem to be antisymmetric (dragged towards zero velocity), and thus cannot explain the effect. Most likely the effect is due to correlated noise of an unknown origin, possibly originating from nightly differences between the reference and eclipse spectra. Nevertheless, we verified that our results stayed consistent when only fitting the data between the second and third eclipse contact points, obtaining differences within the 1σ uncertainties of the parameters.

4.2 Formation scenario

Tidal evolution has three relevant effects on a binary: *(i)* alignment of stellar spin axes, *(ii)* synchronization of stellar rotation rates, and *(iii)* circularization of the orbit. The first two effects are believed to occur on a roughly similar time-scale, whereas the circularization is a much slower process, owing to there being significantly more angular momentum in the orbit than in the stars (Hut 1981). J0608-59 is too widely separated ($R_1/a_{\rm bin} = 0.023$) for circularization to have occurred within our estimated lifetime of ∼4 Gyr,[8] and so its eccentricity of $e_{\rm bin} = 0.156$ is not surprising.

For non-circular binaries, such as J0608-59, tides do not synchronize the rotation rates with the orbital period (14.61 d). Instead, the stellar rotation will over time pseudo-synchronize with the orbital motion at periastron (Hut 1981). Using their equation (42), the pseudo-synchronous rotation period is 12.7 d for J0608-59. This is significantly shorter than our derived rotation period of 18.1 ± 1.6 d. On the other hand, using the gyrochronological age–rotation relation for single stars from Mamajek & Hillenbrand (2008), the predicted rotation period from stellar spin-down is estimated to be 19.6 ± 2.4 d for our ∼4 Gyr star, which may provide a plausible explanation for the measured rotation rate given the binary separation. We therefore suggest that the primary star's rotation rate is largely unaffected by tides from the binary companion, but rather driven by magnetic braking. This result is consistent with fig. 10 of Torres, Andersen & Giménez (2010), showing that binaries with $R_1/a \lesssim 0.1$ are not necessarily pseudo-synchronized, and also remain eccentric.

The fact that the star is not pseudo-synchronized may appear at odds with an aligned projected obliquity of ∼0°. However, we present two simple explanations for this apparent discrepancy. First, the stellar obliquity may too be unaffected by tides, but rather the binary was primordially aligned and such alignment persisted through its evolution. This points to the two stars having formed from gravitational fragmentation within a single disc. If they are formed at an initially wider separation (predicted by e.g. Bate, Bonnell & Bromm 2002), then their orbital shrinkage would be due to accretion and disc migration, and not a more violent scattering event, such that the stellar alignment and circumbinary planet are preserved (Martin 2019). An alternate explanation is that the time-scale of spin alignment, at least in the case of J0608-59, is noticeably shorter than that of pseudo-synchronization.

The Kepler-16 circumbinary planet system, by comparison, has a wider binary ($R_1/a_{\rm bin} = 0.013$) that is also eccentric and spin–orbit aligned, but contrarily has a rotation period equal to that expected from pseudo-synchronization (∼35 d). However, Winn et al. (2011) point out that this rotation rate also agrees well with the expectation from gyrochronology. Our result may support the view that the rotation of Kepler-16 A is only coincidental with the pseudo-synchronous rotation period and has not been synchronized by tides, but has rather spun down to its present rate due to the natural spin-down of stars from magnetic braking. The Kepler-47 circumbinary system is comparatively much tighter ($R_1/a_{\rm bin} = 0.053$) than both J0608-59 and Kepler-16. Tides are most likely responsible for its small eccentricity (0.023), near synchronization ($P_{\rm bin}$= 7.448 d and $P_{\rm rot}$= 7.775 d), and spin–orbit alignment (<20°).

4.3 Differential rotation and true obliquity

Although unlikely, it is worth mentioning that the true stellar obliquity may be non-zero, i.e. that the star is pointing either towards or away from us and is thus still realigning. Ordinarily, an independent measurement of the rotation period from spot modulation, together with a projected equatorial rotational velocity from the Rossiter–McLaughlin analysis, can provide a measurement of the stellar inclination. However, Kostov et al. (2020) show that neither *TESS* nor ASAS-SN photometry display any clear periodicity. We show our fit to the differential rotation model in the right-hand panel of Fig. 2. The fit favours a higher stellar inclination, $i_{\star,1} = 137.1^{+13.7}_{-74.8}$°, with true obliquity $\psi = 50\overset{\circ}{.}4 \pm 13\overset{\circ}{.}4$ and latitudes rotating antisolar with $\alpha < 0$ at the 99th percentile. The implied rotation period here is $17.3^{+3.7}_{-3.2}$ d, which is similar to the rigid body case. The fit improves the Bayesian Information Criterion by 5.5, showing an improvement in the model, although the reduced $\chi^2_\nu = 0.45$ suggests we may be overfitting the data. There have only been detections of antisolar differential rotation in three giant stars (Strassmeier, Kratzwald & Weber 2003; Kővári et al. 2013; Kriskovics et al. 2014), with only a small handful of main-sequence Sun-like candidates (Benomar et al. 2018). Ultimately, we are not able to rule out contributions from correlated noise and therefore consider it unlikely that the star is inclined. We conclude that the rigid body model is the most likely scenario and thus the true obliquity of the star is low.

[8]Derived in Kostov et al. (2020) using stellar isochrones.

Downloaded from https://academic.oup.com/mnras/article-abstract/497/2/1627/5871829 by Keele University user on 03 August 2020

4.4 Spectral contamination from secondary star

The systems that make up the EBLM sample (including J0608-59) are single-lined binaries, where the spectrum from the secondary star is too faint to be detected in individual observations. However, if the flux emission from the secondary star exceeds that of the noise in the data, the faint signal of the secondary spectrum may be imprinted in the spectrum that is dominated by the light from the primary star, and impact the shape of the final CCF. Since the reloaded Rossiter–McLaughlin method depends on detecting changes in the CCF shape during eclipse, this may impact our measurements. It is worth noting that for the vast majority of the binary orbit this is still not a problem, as the relative radial velocity motion between the two stars is so large that the line core from the secondary star falls outside the line core of the primary star and will not affect the CCF shape. Most of the contamination will occur close to conjunctions, where their radial velocity curves cross.

The apparent magnitude of the system in the CORALIE V band is $m_{V,1} = 11.73$. Assuming an age of 5 Gyr, Triaud et al. (2017) predict an apparent brightness for the secondary star $m_{V,2} = 19.75$, which gives an estimated secondary-to-primary flux ratio of ∼1 ppt through the relation

$$\Delta m_V = -2.5 \log\left(\frac{F_{V,2}}{F_{V,1}}\right).$$

The fitted noise of the residual CCFs in Fig. 1 is ∼2.5 ppt, which yields an SNR < 0.5 for the spectrum from the secondary star. The impact of the secondary spectrum should therefore not affect our measurements of $v_{\rm eq}\sin i_{\star,1}$ and β. Despite this, we carry out a simulation to quantify the impact of the secondary spectrum, and how it changes with increasing flux ratio. We simulate a series of CCFs for the primary star during eclipse, centred at the radial velocity of the primary star in the barycentric reference frame, assuming Gaussian profiles with depths and widths determined by their typical observed values. We add uncertainties to the CCFs according to the typically fitted error, ϵ from the MCMC analysis in Section 3.1. We add a CCF from the secondary star, where we assume that the contrast and full width at half-maximum (FWHM) is the same as for the primary, with flux ratio δF, and centred at the predicted radial velocity of the secondary star from the Keplerian orbit, again in the barycentric reference frame. Finally, we assume Gaussian profiles for the distortion due to the Rossiter–McLaughlin effect, with contrasts and FWHM as fitted in Section 3.1, and their radial velocity centres translated to the barycentric reference frame. This contribution is subtracted from our combined CCF from the two stars to simulate the missing light from the occulted disc.

We apply the reloaded Rossiter–McLaughlin effect outlined in Section 3 to our simulated CCFs, which, as described above, include contributions from both stars and the distortion of the line profiles due to an occulted disc. We vary the flux ratio of the secondary using $F_2/F_1 = \{1, 5, 10\}$ ppt, and repeat the MCMC sampling procedure from before to obtain posterior distributions for $v_{\rm eq}\sin i_{\star,1}$ and β. The posterior distributions are shown in Fig. 3. The simulation with $F_2/F_1 = 1$ ppt matches the observed data remarkably well, and does not show any significant bias in the derived parameters when compared to the simulation with a dark secondary. However, the posterior distributions for both parameters become significantly biased for higher flux ratios. Our simulations show that care must be taken for eclipse spectroscopy with luminous secondaries, and potentially even for eclipse spectroscopy of exoplanets due to the hot day-side temperatures of some ultrahot Jupiters, which can reach similar temperatures to M or even K dwarfs. Assuming a flux ratio

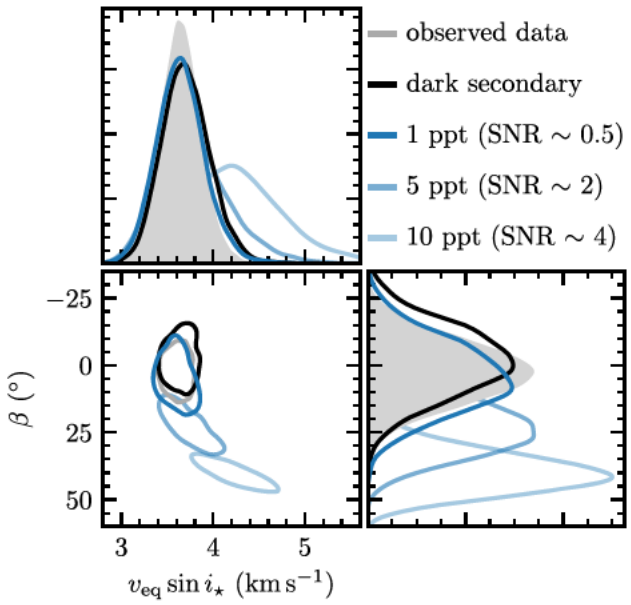


Figure 3. Simulation of the impact of varying levels of emission flux from the secondary star on the retrieved values for $v_{\rm eq}\sin i_{\star,1}$ and β. The posterior distribution for the observed data is shown in grey, and is compared to the simulation with no contamination from a secondary spectrum in black. The coloured lines show the simulated effect for increasing relative flux contribution from the occulting body. The estimated flux contamination for J0608-59 is ∼1 ppt, which agrees very well with the simulated data. The lower left-hand panel shows the 1σ contours.

of ∼15 ppt, as for the Kepler-16 system (Doyle et al. 2011), the secondary spectrum could bias the measurement of β to >30° at 3σ significance, and overestimate $v_{\rm eq}\sin i_{\star,1}$ by ≃30 per cent.

A few caveats are worth mentioning with the simulations. First, the relative depth and width of the secondary CCF are assumed to be the same as for the primary CCF. This may not always be the case when the spectral types of the stars are very different. Taking a G-M binary as an example, the convolution of an M dwarf spectrum with a G2 mask can yield shallower (thus lower SNR) CCFs than assumed here due the cross-correlation with template lines that are not present in M dwarf spectra. In practice, the simulations we carry out here present a worst-case scenario. Secondly, the impact of the secondary spectrum will also depend on the specific orbital characteristics, in particular the eccentricity and argument of periastron, which determine where and how much the two spectra will overlap.

5 CONCLUSIONS

We have presented a stellar obliquity measurement of the primary star in the EBLM J0608-59/TOI-1338 eclipsing binary system, recently discovered to host a circumbinary planet. High-resolution spectroscopy during primary eclipse supports a low obliquity, consistent with alignment with the binary and planet orbits. The binary orbit has not pseudo-synchronized, which indicates that the obliquity of the star has not been influenced by tides, and is thus likely primordial. Moreover, we have simulated the effect of an unresolved secondary spectrum on our analysis of eclipse spectra, and show that the effect is negligible for our data. However, secondaries that contribute with flux of just a few thousandths of that of their primaries can strongly bias measurements of $v_{\rm eq}\sin i_{\star,1}$ and β.

J0608-59 is but one of ∼20 EBLM systems for which we are currently studying stellar obliquities from Rossiter–McLaughlin

Downloaded from https://academic.oup.com/mnras/article-abstract/497/2/1627/5871829 by Keele University user on 03 August 2020

sequences observed with CORALIE and HARPS, and currently the only one known to host a circumbinary planet. However, our sample has significant overlap with the BEBOP Doppler survey for circumbinary planets therefore we may soon find more similar systems. In a forthcoming paper, we will present obliquity measurements on ∼20 systems observed with CORALIE and HARPS, which will allow us to place constraints on tidal evolution in low-mass binaries and their circumbinary planets.

ACKNOWLEDGEMENTS

We are very grateful to the anonymous referee for carefully reading our manuscript and providing constructive comments that led to additional analysis that substantially improved the paper. This work includes data obtained from CORALIE, an instrument mounted on the Swiss *Euler* 1.2m telescope, a project of the University of Geneva, funded by the Swiss National Science Foundation. This work was in part funded by the U.S.–Norway Fulbright Foundation and a NASA *TESS* GI grant G022253 (PI: Martin). AHMJT received funding from the European Research Council (ERC) under the European Union's Horizon 2020 research and innovation programme (grant 803193/BEBOP), and from a Leverhulme Trust Research Project grant (RPG-2018-418). VKH is also supported by a Birmingham Doctoral Scholarship, and by a studentship from Birmingham's School of Physics & Astronomy. DVM received funding from the Swiss National Science Foundation (grant P 400P2 186735). SG has been supported by STFC through consolidated grants ST/L000733/1 and ST/P000495/1.

DATA AVAILABILITY

The data underlying this article will be shared on reasonable request to the corresponding author.

REFERENCES

Albrecht S., Reffert S., Snellen I., Quirrenbach A., Mitchell D. S., 2007, A&A, 474, 565
Albrecht S., Reffert S., Snellen I. A. G., Winn J. N., 2009, Nature, 461, 373
Albrecht S. et al., 2011, ApJ, 738, 50
Albrecht S. et al., 2014, ApJ, 785, 83
Bate M. R., Bonnell I. A., Bromm V., 2002, MNRAS, 336, 705
Benomar O. et al., 2018, Science, 361, 1231
Cegla H. M., Lovis C., Bourrier V., Beeck B., Watson C. A., Pepe F., 2016a, A&A, 588, A127
Cegla H. M., Oshagh M., Watson C. A., Figueira P., Santos N. C., Shelyag S., 2016b, ApJ, 819, 67
Claret A., Bloemen S., 2011, A&A, 529, A75
Collier Cameron A., Bruce V. A., Miller G. R. M., Triaud A. H. M. J., Queloz D., 2010, MNRAS, 403, 151
Doyle L. R. et al., 2011, Science, 333, 1602
Eastman J., Gaudi B. S., Agol E., 2013, PASP, 125, 83
Foreman-Mackey D., Hogg D. W., Lang D., Goodman J., 2013, PASP, 125, 306
Gill S. et al., 2019, A&A, 626, A119
Hale A., 1994, AJ, 107, 306
Hirano T., Suto Y., Winn J. N., Taruya A., Narita N., Albrecht S., Sato B., 2011, ApJ, 742, 69
Hirano T. et al., 2020, ApJ , 890, L27
Hoffman M. D., Gelman A., 2014, J. Mach. Learn. Res., 15, 1593
Hut P., 1981, A&A, 99, 126
Kopal Z., 1942, ApJ, 96, 399
Kostov V. B. et al., 2020, AJ, 159, 253
Kriskovics L., Kővári Z., Vida K., Granzer T., Oláh K., 2014, A&A, 571, A74
Kővári Z., Korhonen H., Strassmeier K. G., Weber M., Kriskovics L., Savanov I., 2013, A&A, 551, A2
Lovis C., Pepe F., 2007, A&A, 468, 1115
Mamajek E. E., Hillenbrand L. A., 2008, ApJ, 687, 1264
Martin D. V., 2019, MNRAS, 488, 3482
Martin D. V. et al., 2019, A&A, 624, A68
Maxted P. F. L., 2018, A&A, 616, A39
McLaughlin D. B., 1924, ApJ, 60, 22
Orosz J. A. et al., 2012, Science, 337, 1511
Pollacco D. L. et al., 2006, PASP, 118, 1407
Rossiter R. A., 1924, ApJ, 60, 15
Salvatier J., Wiecki T. V., Fonnesbeck C., 2016, Peer J Comput. Sci., 2, e55
Strassmeier K. G., Kratzwald L., Weber M., 2003, A&A, 408, 1103
Sybilski P., Pawłaszek R. K., Sybilska A., Konacki M., Hełminiak K. G., Kozłowski S. K., Ratajczak M., 2018, MNRAS, 478, 1942
Torres G., Andersen J., Giménez A., 2010, A&AR, 18, 67
Triaud A. H. M. J., 2018, Handbook of Exoplanets, Springer, p. 2
Triaud A. H. M. J. et al., 2013, A&A, 549, A18
Triaud A. H. M. J. et al., 2017, A&A, 608, A129
Winn J. N., Fabrycky D. C., 2015, ARA&A, 53, 409
Winn J. N. et al., 2011, ApJ, 741, L1

This paper has been typeset from a TEX/LATEX file prepared by the author.

Downloaded from https://academic.oup.com/mnras/article-abstract/497/2/1627/5871829 by Keele University user on 03 August 2020

Chapter 7

Final remarks

In this final Chapter I reflect on how some of the results presented in this thesis are connected. Finally I conclude by presenting some thoughts on future prospects.

7.1 Conclusions

Most of the work presented in this thesis are published articles that include their own sections dedicated to conclusions, so I refer the interested reader to those sections. However, in this thesis I have presented various pieces of work that at first glance do not necessarily tackle the same scientific question, so some thoughts on how they can be reconciled may be warranted. For example, the bulk of Chapter 3 concerns the discoveries of brown dwarfs, while the final paper of that Chapter is an exoplanet discovery. Chapters 4 to 6 are somewhat easier to reconcile as they all investigate spin-orbit misalignments and what these measurements can tell about the dynamical history of the systems. Yet the companions studied in this thesis span the mass continuum from the Earth-regime to low-mass stars, so the obliquity does not necessarily probe the same processes in each system considered.

One commonality between these pieces of work is that they all in one way or another provide leads to questions on how formation of planets, brown dwarfs, or stars occur. The picture of planet formation is clearly more complex than once thought, as can be seen from the diversity of planetary systems that have been discovered (Figure 1.5).

One topic that has come under scrutiny in recent years is the connection between brown dwarfs and giant planets (e.g. Chabrier et al. 2014; Ma & Ge 2014). As the population of known brown dwarf companions to Sun-like stars has grown, a picture has started taking shape that casts doubt on the current definition of a brown dwarf, i.e. substellar objects with masses in the range ~13–80 $M_{\rm Jup}$ (Chabrier et al. 2014). The different classes of planets tend to be distinguished by their formation, and there is a growing body of evidence that indicate that such a definition is needed for brown dwarfs as well (Ma & Ge 2014).

The largest piece of evidence for this is the brown dwarf desert, which is a lack of intermediate-mass brown dwarfs ($35\,M_{\rm Jup} < m \sin i < 55\,M_{\rm Jup}$) on orbits below 100 days (Grether & Lineweaver 2006; Sahlmann et al. 2011; Ma & Ge 2014). The occurence rate of brown dwarfs on either side increases of this mass range increases, which seems to indicate they belong to two separate populations. This is also supported by their different eccentricity distributions, which may provide support for the low-mass and high-mass brown dwarfs originating from two different formation channels (Ma & Ge 2014). In this context, WASP-128 b (Hodžić et al. 2018) and 2M1510 AB (Triaud et al. 2020) add some new discoveries to this landscape that will be important for future work in this area. Individually, these two discoveries also provide new tests for substellar evolution models which are used to understand giant planets and brown dwarfs alike.

My work on the obliquities is important to understand the difference in the formation and orbital evolution of low-mass planets compared to giant planets. As we have seen in Chapter 1.4.3 tidal dissipation in stars can shape the obliquity distribution in hot Jupiter systems (e.g. Winn et al. 2010a; Dawson 2014). Ideally we would like to understand *how much* they are affected by tides at a population level, which will then allow a better understanding of the underlying processes that misaligned (or did not) the planet or star. One way forward is to acquire measurements of the stellar obliquity for a range of planetary masses, stellar masses, orbital separations; ideally with accurate and precise ages which are notoriously difficult to determine. Chapter 5 is a step in this direction, and I expect this work and future measurements will improve our knowledge on the origin of hot Jupiters.

Stars hosting small planets are less concerned with tidal evolution (Barker & Ogilvie 2009b), so the hope is that their obliquity distribution will be more telling of its formation than what we have seen in hot Jupiters. However, we have only just started to probe this region of parameter space. One reason for this is that most small planets were discovered by *Kepler* where the stars are too faint to measure precise stellar obliquities with the Rossiter-McLaughlin effect. As a result, obliquities in systems with low-mass planets were determined via asteroseismology (e.g. Chaplin et al. 2013), or new techniques that study spot-crossing events in transit (Sanchis-Ojeda et al. 2012; Dai et al. 2018). Both these methods are limited in scope due to a small sample size. Since 2018, new sub-Neptune planets are instead provided by *TESS* and these planets orbit brighter stars so that spectroscopic follow-up is more feasible. Chapter 4.2 (Kunovac Hodžić et al. 2021) is a demonstration of this prospect, which is the second-lowest mass-ratio system for which the Rossiter-McLaughlin effect has been measured (after TRAPPIST-1, Hirano et al. (2020), Lim et al. in prep.). However, as seen in Kunovac Hodžić et al. (2021), a misaligned orbit for a small planet does still not provide a clear-cut answer to its formation as inclined outer companions can actively participate in their misalignment (Xuan & Wyatt 2020; De Rosa et al. 2020; Damasso et al. 2020). Future work may therefore have to consider similar effects in systems where outer companions have not yet been detected. In this context, future data releases of *Gaia* may be able to constrain the presence of such companions. The role of new spectrographs such as *ESPRESSO* and *EXPRES* cannot be understated when expanding the sample to small planets, which boasts single-measurement photon-noise limited precision of $10\,\mathrm{cm\,s^{-1}}$ (Pepe et al. 2020) and $30\,\mathrm{cm\,s^{-1}}$ (Blackman et al. 2020; Petersburg et al.

2020), respectively.

Binary star formation is thought to occur from fragmentation of the collapsing molecular gas cloud (Hoyle 1953) or disc-fragmentation (Kratter & Matzner 2006) and may therefore be different to the formation pathway for planets. However, as we saw for the formation of brown dwarfs, nature does not care about the labels we assign various objects. It is therefore of interest to explore how various observables change as a function of the mass ratio of the system so we can better understand their differences in formation. Studying the evolution of binary orbits by measuring rotation periods, eccentricities and stellar obliquities may further aid our understanding on the role of tides in other systems such as hot Jupiters. Chapter 6 is a step in this direction, and more work is expected on similar systems in future work.

7.2 Future prospects

7.2.1 Young systems

Recent years has seen an avalanche of exoplanets transiting young stars, i.e. those with ages $\lesssim$800 Myr, first with the *K2* mission (David et al. 2016a,b, 2018a,b, 2019a,b; Livingston et al. 2018, 2019; Mann et al. 2016a,b, 2017; Obermeier et al. 2016; Pepper et al. 2017; Rizzuto et al. 2018), and more recently with *TESS* (Benatti et al. 2019; Bouma et al. 2020; Mann et al. 2020; Plavchan et al. 2020; Newton et al. 2019, 2021; Tofflemire et al. 2021). The ages of these planets range from ~5–10 Myr at the youngest end (David et al. 2016b; Mann et al. 2016a) to ~700 Myr in open clusters such as Hyades and Praesepe (Mann et al. 2016b, 2017, 2018; Livingston et al. 2018, 2019; Obermeier et al. 2016; Pepper et al. 2017; Rizzuto et al. 2018).

Young systems are thought to be particularly useful at constraining the migration of planets. Disc-free migration mechanisms such as planet-planet scattering and Kozai-Lidov are expected to happen on timescales of several tens to hundreds of Myr (Naoz et al. 2011a; Fabrycky & Tremaine 2007), so catching planets in their youth close to their star can provide some constraint on the timescales of different types of migration. Most of the young planets observed until now are generally much less massive than Jupiter and orbit close to their star, which can either be evidence of *in-situ* formation or rapid radial migration due to disc-interaction within the first 5–10 Myr (David et al. 2016b; Mann et al. 2016a).

Some young systems have already been observed in spectroscopy during transit for the Rossiter-McLaughlin effect, these include AU Mic b (Addison et al. 2020; Hirano et al. 2020; Martioli et al. 2020; Palle et al. 2020), DS Tuc Ab (Montet et al. 2020; Zhou et al. 2020), TOI-942 b (Wirth et al. 2021), HIP 67522 b (Heitzmann et al. 2021), TOI-1726 c (Dai et al. 2020), and Kepler-63 b (Sanchis-Ojeda et al. 2013). With the exception of Kepler-63, all planets appear well-aligned with the spin of the star which seems to favour migration due to disc-interaction. Of these, Kepler-63 is the oldest system at ~250 Myr and further measurements may constrain the timescales of dynamical migration scenarios. However, young stars are typically chromospherically active, causing significant rotational varibility whose period can be determined from photometry. They are also typically fast rotators, which makes spectroscopic

measurements of $v \sin i_\star$ trivial. Together, these can constrain the inclination of the star which alone can tell whether the planet is aligned or not (Masuda & Winn 2020; Newton et al. 2021; Tofflemire et al. 2021).

7.2.2 Sub-Neptunes and multiplanetary systems

As alluded to in Section 7.1, we have now reached a point where we can start probing the obliquity distribution in stars hosting small planets. One exciting prospect about such systems is that they tend to be closely packed systems of multiple planets which can rule out high eccentricity migration from dynamical scattering that are believed to produce hot Jupiters on inclined orbits. Indeed, the general expectation is that a close system of multiple planets migrate though disc-interaction and should have low obliquities, as has been observed in a few systems (Hirano et al. 2012; Sanchis-Ojeda et al. 2012; Chaplin et al. 2013). That is not to say that close multiple planet systems cannot be misaligned, as has been demonstrated in Kepler-53 (Huber et al. 2013), HD 3167 (Dalal et al. 2019), and most recently in K2-290 (Hjorth et al. 2021). A few explanations have been invoked for such systems, including orbital tilting due inclined outer companions (Gratia & Fabrycky 2017); the disc may be torqued due to an inclined stellar companion (Batygin 2012; Lai 2014; Zanazzi & Lai 2018), or the star itself may be tilted from magnetic star-disc interactions (Lai et al. 2011). More measurements of the obliquity in systems with multiple planets as well as constraints on outer planetary and stellar companions may therefore be useful to constrain such scenarios.

7.2.3 True obliquities

The Rossiter-McLaughlin effect only measures the obliquity projected along the line-of-sight, λ, shown in Figure 1.6. In many cases it is the true obliquity, ψ, which is the quantity of interest. Recent work has shown misaligned systems show a preference for ψ close to 90° (Albrecht et al. 2021), which may hold clues to the dynamical evolution of the planetary orbit (Fabrycky & Tremaine 2007) or tidal evolution of the star (Lai 2012). Future work may therefore include revisiting some of the previously measured systems to determine the true obliquities.

The largest obstacle to determining the true obliquity is knowing the stellar inclination, which is mostly down to the difficulty in determining the rotation period of the star. The rotation period is most often found from a photometric timeseries, which in some cases may be available from *TESS* and is worth exploring for the literature sample of Rossiter-McLaughlin measurements. In cases where the rotational modulation may not be found from photometry it can also be determined from spectral activity indices or precise radial velocity data.

Bibliography

ALMA Partnership et al., 2015, The Astrophysical Journal, 808, L3

Addison B. C., et al., 2020, arXiv e-prints, 2006, arXiv:2006.13675

Albrecht S., Reffert S., Snellen I., Quirrenbach A., Mitchell D. S., 2007, Astronomy and Astrophysics, 474, 565

Albrecht S., Reffert S., Snellen I. A. G., Winn J. N., 2009, Nature, 461, 373

Albrecht S., et al., 2012, The Astrophysical Journal, 757, 18

Albrecht S. H., Marcussen M. L., Winn J. N., Dawson R. I., Knudstrup E., 2021, arXiv e-prints, 2105, arXiv:2105.09327

Allart R., et al., 2019, Astronomy and Astrophysics, 623, A58

Anderson D. R., et al., 2011, ApJ, 726, L19

Anderson D. R., et al., 2015, The Astrophysical Journal, 800, L9

Anderson D. R., et al., 2017, Astronomy and Astrophysics, 604, A110

Anderson K. R., Winn J. N., Penev K., 2021, The Astrophysical Journal, 914, 56

Andrae R., Schulze-Hartung T., Melchior P., 2010, arXiv:1012.3754 [astro-ph, physics:physics, stat]

Angus R., Morton T., Aigrain S., Foreman-Mackey D., Rajpaul V., 2018, Monthly Notices of the Royal Astronomical Society, 474, 2094

Astropy Collaboration et al., 2018, The Astronomical Journal, 156, 123

Baglin A., et al., 2006, COSPAR, 36, 3749

Bailey E., Batygin K., Brown M. E., 2016, The Astronomical Journal, 152, 126

Bakos G., Noyes R. W., Kovács G., Stanek K. Z., Sasselov D. D., Domsa I., 2004, Publications of the Astronomical Society of the Pacific, 116, 266

Bakos G. Á., et al., 2007, The Astrophysical Journal, 670, 826

Bakos G. Á., et al., 2013, Publications of the Astronomical Society of the Pacific, 125, 154

Ballot J., García R. A., Lambert P., 2006, Monthly Notices of the Royal Astronomical Society, 369, 1281

Ballot J., Appourchaux T., Toutain T., Guittet M., 2008, Astronomy and Astrophysics, 486, 867

Baraffe I., Chabrier G., Barman T. S., Allard F., Hauschildt P. H., 2003, A&A, 402, 701

Baranne A., et al., 1996, A&AS, 119, 373

Barker A. J., Ogilvie G. I., 2009a, MNRAS, 395, 2268

Barker A. J., Ogilvie G. I., 2009b, Monthly Notices of the Royal Astronomical Society, 395, 2268

Barnes J. W., 2009, The Astrophysical Journal, 705, 683

Barnes J. R., et al., 2014, Monthly Notices of the Royal Astronomical Society, 439, 3094

Basu S., Chaplin W. J., 2017, Asteroseismic Data Analysis: Foundations and Techniques. Princeton University Press

Basu S., Mazumdar A., Antia H. M., Demarque P., 2004, Monthly Notices of the Royal Astronomical Society, 350, 277

Batygin K., 2012, Nature, 491, 418

Batygin K., Morbidelli A., Holman M. J., 2015, The Astrophysical Journal, 799, 120

Bayliss D., et al., 2017, AJ, 153, 15

Becker J. C., Vanderburg A., Adams F. C., Rappaport S. A., Schwengeler H. M., 2015, The Astrophysical Journal Letters, 812, L18

Beeck B., Cameron R. H., Reiners A., Schüssler M., 2013, Astronomy and Astrophysics, 558, A49

Benatti S., et al., 2019, Astronomy and Astrophysics, 630, A81

Birkby J. L., 2018, arXiv e-prints, 1806, arXiv:1806.04617

Blackman R. T., et al., 2020, The Astronomical Journal, 159, 238

Bodenheimer P., Hubickyj O., Lissauer J. J., 2000, Icarus, 143, 2

Bohn A. J., Southworth J., Ginski C., Kenworthy M. A., Maxted P. F. L., Evans D. F., 2020, Astronomy and Astrophysics, 635, A73

Borucki W. J., et al., 2010, Science, 327, 977

Bouchy F., Pepe F., Queloz D., 2001, Astronomy and Astrophysics, 374, 733

Bouchy F., Bazot M., Santos N. C., Vauclair S., Sosnowska D., 2005, Astronomy and Astrophysics, 440, 609

Boué G., Montalto M., Boisse I., Oshagh M., Santos N. C., 2013, Astronomy and Astrophysics, 550, A53

Bouma L. G., et al., 2020, The Astronomical Journal, 160, 239

Bourrier V., et al., 2018, Nature, 553, 477

Bourrier V., et al., 2021, Astronomy & Astrophysics, 654, A152

Brown D. J. A., et al., 2017, Monthly Notices of the Royal Astronomical Society, 464, 810

Bruntt H., et al., 2012, Monthly Notices of the Royal Astronomical Society, 423, 122

Bryant E. M., et al., 2020, Monthly Notices of the Royal Astronomical Society, 494, 5872

Burdanov A., Delrez L., Gillon M., Jehin E., 2018, SPECULOOS Exoplanet Search and Its Prototype on TRAPPIST. Springer International Publishing, doi:10.1007/978-3-319-55333-7_130

Burgasser A. J., Mamajek E. E., 2017, The Astrophysical Journal, 845, 110

Burrows A., et al., 1997, The Astrophysical Journal, 491, 856

Butler R. P., Marcy G. W., Williams E., McCarthy C., Dosanjh P., Vogt S. S., 1996, Publications of the Astronomical Society of the Pacific, 108, 500

Cañas C. I., et al., 2018, preprint, (arXiv:1805.08820)

Campante T. L., et al., 2016, The Astrophysical Journal, 819, 85

Carmichael T. W., et al., 2020, The Astronomical Journal, 160, 53

Carmichael T. W., et al., 2021, The Astronomical Journal, 161, 97

Cegla H., 2019, Geosciences, 9, 114

Cegla H. M., Lovis C., Bourrier V., Beeck B., Watson C. A., Pepe F., 2016, Astronomy and Astrophysics, 588, A127

Cegla H. M., et al., 2018, The Astrophysical Journal, 866, 55

Chabrier G., Johansen A., Janson M., Rafikov R., 2014, Protostars and Planets VI, pp 619–642

Chambers J., 2010, Exoplanets, pp 297–317

Chaplin W. J., et al., 2013, The Astrophysical Journal, 766, 101

Charbonneau D., Brown T. M., Latham D. W., Mayor M., 2000, ApJ, 529, L45

Chatterjee S., Ford E. B., Matsumura S., Rasio F. A., 2008, The Astrophysical Journal, 686, 580

Chen J., Kipping D., 2017, The Astrophysical Journal, 834, 17

Claret A., 2000, Astronomy and Astrophysics, 363, 1081

Claret A., Bloemen S., 2011, Astronomy and Astrophysics, 529, A75

Collaboration G., et al., 2016, Astronomy and Astrophysics, 595, A1

Collier Cameron A., Jardine M., 2018, Monthly Notices of the Royal Astronomical Society, 476, 2542

Collier Cameron A., et al., 2006, MNRAS, 373, 799

Collier Cameron A., Bruce V. A., Miller G. R. M., Triaud A. H. M. J., Queloz D., 2010a, Monthly Notices of the Royal Astronomical Society, 403, 151

Collier Cameron A., et al., 2010b, Monthly Notices of the Royal Astronomical Society, 407, 507

Costa E., Méndez R. A., Jao W. C., Henry T. J., Subasavage J. P., Ianna P. A., 2006, The Astronomical Journal, 132, 1234

D'Angelo G., Durisen R. H., Lissauer J. J., 2010, Giant Planet Formation. The University of Arizona Press

Dai F., Winn J. N., 2017, The Astronomical Journal, 153, 205

Dai F., Winn J. N., Berta-Thompson Z., Sanchis-Ojeda R., Albrecht S., 2018, The Astronomical Journal, 155, 177

Dai F., et al., 2020, The Astronomical Journal, 160, 193

Dalal S., Hébrard G., Lecavelier des Étangs A., Petit A. C., Bourrier V., Laskar J., König P.-C., Correia A. C. M., 2019, Astronomy and Astrophysics, 631, A28

Damasso M., et al., 2020, arXiv e-prints, 2007, arXiv:2007.06410

David T. J., et al., 2016a, The Astronomical Journal, 151, 112

David T. J., et al., 2016b, Nature, 534, 658

David T. J., et al., 2018a, The Astronomical Journal, 155, 222

David T. J., et al., 2018b, The Astronomical Journal, 156, 302

David T. J., Petigura E. A., Luger R., Foreman-Mackey D., Livingston J. H., Mamajek E. E., Hillenbrand L. A., 2019a, arXiv e-prints, p. arXiv:1910.04563

David T. J., et al., 2019b, The Astronomical Journal, 158, 79

Dawson R. I., 2014, The Astrophysical Journal, 790, L31

Dawson R. I., Johnson J. A., 2012, The Astrophysical Journal, 756, 122

De Rosa R. J., Dawson R., Nielsen E. L., 2020, arXiv e-prints, 2007, arXiv:2007.08549

Delrez L., et al., 2014, Astronomy and Astrophysics, 563, A143

Delrez L., et al., 2018, Monthly Notices of the Royal Astronomical Society, 475, 3577

Demory B.-O., et al., 2013, The Astrophysical Journal, 776, L25

Désert J.-M., et al., 2011, The Astrophysical Journal Supplement Series, 197, 14

Doyle A. P., Davies G. R., Smalley B., Chaplin W. J., Elsworth Y., 2014, MNRAS, 444, 3592

Eastman J., Gaudi B. S., Agol E., 2013, Publications of the Astronomical Society of the Pacific, 125, 83

Eastman J. D., et al., 2019, EXOFASTv2: A Public, Generalized, Publication-Quality Exoplanet Modeling Code

Ehrenreich D., et al., 2020, Nature, 580, 597

El-Badry K., Rix H.-W., 2018, Monthly Notices of the Royal Astronomical Society, 480, 4884

Espinoza N., Kossakowski D., Brahm R., 2019, Monthly Notices of the Royal Astronomical Society, 490, 2262

Fabrycky D., Tremaine S., 2007, The Astrophysical Journal, 669, 1298

Farr W. M., et al., 2018, The Astrophysical Journal, 865, L20

Fischer D. A., Valenti J., 2005, The Astrophysical Journal, 622, 1102

Fischer D. A., et al., 2016, Publications of the Astronomical Society of the Pacific, 128, 066001

Foreman-Mackey D., 2019, Astrophysics Source Code Library, p. ascl:1910.005

Foreman-Mackey D., Hogg D. W., Lang D., Goodman J., 2013, PASP, 125, 306

Foreman-Mackey D., Agol E., Ambikasaran S., Angus R., 2017, The Astronomical Journal, 154, 220

Fortney J. J., Visscher C., Marley M. S., Hood C. E., Line M. R., Thorngren D. P., Freedman R. S., Lupu R., 2020, The Astronomical Journal, 160, 288

Fressin F., et al., 2013, The Astrophysical Journal, 766, 81

Fulton B. J., et al., 2017, The Astronomical Journal, 154, 109

Gandolfi D., et al., 2018, Astronomy and Astrophysics, 619, L10

Gaudi B. S., et al., 2017, Nature, 546, 514

Gelman A., Carlin J., Stern H., Rubin D., 2003, Bayesian Data Analysis, Second Edition. Chapman & Hall/CRC Texts in Statistical Science, Taylor & Francis, https://books.google.co.uk/books?id=TNYhnkXQSjAC

Gibson N. P., Aigrain S., Barstow J. K., Evans T. M., Fletcher L. N., Irwin P. G. J., 2013, Monthly Notices of the Royal Astronomical Society, 428, 3680

Gill S., et al., 2019, Astronomy and Astrophysics, 626, A119

Gillen E., et al., 2014, Astronomy & Astrophysics, Volume 562, id.A50, $<$NUMPAGES$>$19$<$/NUMPAGES$>$ pp., 562, A50

Gillen E., Hillenbrand L. A., David T. J., Aigrain S., Rebull L., Stauffer J., Cody A. M., Queloz D., 2017, The Astrophysical Journal, 849, 11

Gillon M., et al., 2016, Nature, 533, 221

Gillon M., et al., 2017, Nature, 542, 456

Giménez A., 2006, The Astrophysical Journal, 650, 408
Gizon L., Solanki S. K., 2003, The Astrophysical Journal, 589, 1009
Goldreich P., Tremaine S., 1979, The Astrophysical Journal, 233, 857
Goldreich P., Tremaine S., 1980, The Astrophysical Journal, 241, 425
Gómez Maqueo Chew Y., et al., 2014, Astronomy and Astrophysics, 572, A50
Goodman J., Weare J., 2010, Communications in Applied Mathematics and Computational Science, Vol.~5, No.~1, p.~65-80, 2010, 5, 65
Gratia P., Fabrycky D., 2017, Monthly Notices of the Royal Astronomical Society, 464, 1709
Gray D. F., 1984, The Astrophysical Journal, 281, 719
Gray D. F., 2005, The Observation and Analysis of Stellar Photospheres. Cambridge University Press
Gray D. F., 2008, The Observation and Analysis of Stellar Photospheres, third edn. Cambridge University Press
Grether D., Lineweaver C. H., 2006, ApJ, 640, 1051
Grimm S. L., et al., 2018, Astronomy and Astrophysics, 613
Grunblatt S. K., Howard A. W., Haywood R. D., 2015, The Astrophysical Journal, 808, 127
Günther M. N., Daylan T., 2019, Astrophysics Source Code Library, p. ascl:1903.003
Hall O. J., et al., 2021, arXiv e-prints, 2104, arXiv:2104.10919
Haswell C. A., 2010, Transiting Exoplanets. Cambridge University Press
Haywood R. D., et al., 2014, Monthly Notices of the Royal Astronomical Society, 443, 2517
Hébrard G., et al., 2008, Astronomy and Astrophysics, 488, 763
Hébrard G., et al., 2011, Astronomy and Astrophysics, 527, L11
Heitzmann A., et al., 2021, arXiv:2109.04174 [astro-ph]
Hellier C., et al., 2010, The Astrophysical Journal Letters, 723, L60
Hellier C., et al., 2014, Monthly Notices of the Royal Astronomical Society, 440, 1982
Hellier C., et al., 2015, The Astronomical Journal, 150, 18
Hellier C., et al., 2017, Monthly Notices of the Royal Astronomical Society, 465, 3693
Hellier C., et al., 2019, Monthly Notices of the Royal Astronomical Society, 488, 3067
Hilditch R. W., 2001, An Introduction to Close Binary Stars. Cambridge University Press
Hirano T., Suto Y., Taruya A., Narita N., Sato B., Johnson J. A., Winn J. N., 2010, The Astrophysical Journal, 709, 458
Hirano T., Suto Y., Winn J. N., Taruya A., Narita N., Albrecht S., Sato B., 2011, The Astrophysical Journal, 742, 69
Hirano T., et al., 2012, The Astrophysical Journal Letters, 759, L36
Hirano T., et al., 2020, The Astrophysical Journal, 890, L27
Hjorth M., Albrecht S., Hirano T., Winn J. N., Dawson R. I., Zanazzi J. J., Knudstrup E., Sato B., 2021, Proceedings of the National Academy of Science, 118, 2017418118
Hodžić V., et al., 2018, Monthly Notices of the Royal Astronomical Society, 481, 5091
Hoffman M. D., Gelman A., 2014, Journal of Machine Learning Research, 15, 1593

Howard A. W., et al., 2010, Science, 330, 653

Hoyle F., 1953, The Astrophysical Journal, 118, 513

Huang C., Wu Y., Triaud A. H. M. J., 2016, The Astrophysical Journal, 825, 98

Huang C. X., et al., 2018, The Astrophysical Journal Letters, 868, L39

Huber D., et al., 2013, Science, 342, 331

Husser T.-O., Wende-von Berg S., Dreizler S., Homeier D., Reiners A., Barman T., Hauschildt P. H., 2013, A&A, 553, A6

Hut P., 1981, Astronomy and Astrophysics, 99, 126

Ida S., Lin D. N. C., 2004, The Astrophysical Journal, 604, 388

Ikuta K., et al., 2020, The Astrophysical Journal, 902, 73

Irwin J. M., et al., 2011, The Astrophysical Journal, 742, 123

Izidoro A., Ogihara M., Raymond S. N., Morbidelli A., Pierens A., Bitsch B., Cossou C., Hersant F., 2017, Monthly Notices of the Royal Astronomical Society, 470, 1750

Johnson M. C., Cochran W. D., Albrecht S., Dodson-Robinson S. E., Winn J. N., Gullikson K., 2014, The Astrophysical Journal, 790, 30

Jones H. R. A., Paul Butler R., Tinney C. G., Marcy G. W., Penny A. J., McCarthy C., Carter B. D., Pourbaix D., 2002, Monthly Notices of the Royal Astronomical Society, 333, 871

Kamiaka S., Benomar O., Suto Y., Dai F., Masuda K., Winn J. N., 2019, The Astronomical Journal, 157, 137

Kempton E. M. R., et al., 2018, Publications of the Astronomical Society of the Pacific, 130, 114401

Kennedy G. M., et al., 2019, Nature Astronomy, 3, 230

Kipping D. M., 2013, Monthly Notices of the Royal Astronomical Society, 434, L51

Kirk J., Alam M. K., López-Morales M., Zeng L., 2020, The Astronomical Journal, 159, 115

Kleine T., Münker C., Mezger K., Palme H., 2002, Nature, 418, 952

Kleine T., et al., 2009, Geochimica et Cosmochimica Acta, 73, 5150

Kokubo E., Ida S., 2002, The Astrophysical Journal, 581, 666

Kopal Z., 1959, Close binary systems. Springer

Kostov V. B., et al., 2020, The Astronomical Journal, 159, 253

Kozai Y., 1962, The Astronomical Journal, 67, 591

Kraft R. P., 1967, ApJ, 150, 551

Kratter K., Lodato G., 2016, Annual Review of Astronomy and Astrophysics, 54, 271

Kratter K. M., Matzner C. D., 2006, Monthly Notices of the Royal Astronomical Society, 373, 1563

Kreidberg L., 2015, Publications of the Astronomical Society of the Pacific, 127, 1161

Kreidberg L., Line M. R., Thorngren D., Morley C. V., Stevenson K. B., 2018, The Astrophysical Journal Letters, 858, L6

Kunovac Hodžić V., et al., 2020, Monthly Notices of the Royal Astronomical Society, 497, 1627

Kunovac Hodžić V., Triaud A. H. M. J., Cegla H. M., Chaplin W. J., Davies G. R., 2021, Monthly Notices of the Royal Astronomical Society, 502, 2893

Kurucz R. L., 1979, The Astrophysical Journal Supplement Series, 40, 1
Lafarga M., et al., 2020, Astronomy and Astrophysics, 636, A36
Lai D., 2012, Monthly Notices of the Royal Astronomical Society, 423, 486
Lai D., 2014, Monthly Notices of the Royal Astronomical Society, 440, 3532
Lai D., Foucart F., Lin D. N. C., 2011, Monthly Notices of the Royal Astronomical Society, 412, 2790
Lambrechts M., Johansen A., 2012, Astronomy and Astrophysics, 544, A32
Laskar J., 1994, Astronomy and Astrophysics, 287, L9
Lee E. J., Chiang E., 2017, The Astrophysical Journal, 842, 40
Lee E. J., Chiang E., Ormel C. W., 2014, The Astrophysical Journal, 797, 95
Leighton R. B., Noyes R. W., Simon G. W., 1962, The Astrophysical Journal, 135, 474
Leleu A., et al., 2021, Astronomy and Astrophysics, 649, A26
Lidov M. L., 1962, Planetary and Space Science, 9, 719
Lightkurve Collaboration et al., 2018, Astrophysics Source Code Library, p. ascl:1812.013
Lin D. N. C., Papaloizou J., 1986, The Astrophysical Journal, 309, 846
Lindegren L., et al., 2021, Astronomy and Astrophysics, 649, A2
Livingston J. H., et al., 2018, The Astronomical Journal, 155, 115
Livingston J. H., et al., 2019, Monthly Notices of the Royal Astronomical Society, 484, 8
Lopez E. D., Fortney J. J., Miller N., 2012, The Astrophysical Journal, 761, 59
Louden E. M., Winn J. N., Petigura E. A., Isaacson H., Howard A. W., Masuda K., Albrecht S., Kosiarek M. R., 2021, The Astronomical Journal, 161, 68
Lovis C., Fischer D., 2010, Radial Velocity Techniques for Exoplanets. The University of Arizona Press
Lubow S. H., Ida S., 2010, arXiv e-prints, p. arXiv:1004.4137
Luger R., Agol E., Kruse E., Barnes R., Becker A., Foreman-Mackey D., Deming D., 2016, The Astronomical Journal, 152, 100
Luger R., et al., 2017, Nature Astronomy, 1, 0129
Luger R., Agol E., Foreman-Mackey D., Fleming D. P., Lustig-Yaeger J., Deitrick R., 2019, The Astronomical Journal, 157, 64
Lynden-Bell D., Pringle J. E., 1974, Monthly Notices of the Royal Astronomical Society, 168, 603
Ma B., Ge J., 2014, MNRAS, 439, 2781
Madhusudhan N., 2012, The Astrophysical Journal, 758, 36
Mamajek E. E., 2009, AIP Conference Proceedings, 1158, 3
Mamajek E. E., Hillenbrand L. A., 2008, The Astrophysical Journal, 687, 1264
Mancini L., et al., 2018, Astronomy and Astrophysics, 613, A41
Mann A. W., et al., 2016a, The Astronomical Journal, 152, 61
Mann A. W., et al., 2016b, The Astrophysical Journal, 818, 46
Mann A. W., et al., 2017, The Astronomical Journal, 153, 64
Mann A. W., et al., 2018, The Astronomical Journal, 155, 4
Mann A. W., et al., 2020, The Astronomical Journal, 160, 179

Martin D. V., 2018, Handbook of Exoplanets, p. 156
Martin D. V., et al., 2019, Astronomy and Astrophysics, 624, A68
Martin D. V., et al., 2021, Monthly Notices of the Royal Astronomical Society, 507, 4132
Martioli E., et al., 2020, Astronomy and Astrophysics, 641, L1
Masuda K., 2015, The Astrophysical Journal, 805, 28
Masuda K., Hirano T., 2021, arXiv e-prints, 2103, arXiv:2103.05216
Masuda K., Winn J. N., 2020, The Astronomical Journal, 159, 81
Matsumura S., Thommes E. W., Chatterjee S., Rasio F. A., 2010, The Astrophysical Journal, 714, 194
Maxted P. F. L., 2016, A&A, 591, A111
Maxted P. F. L., 2018, Astronomy and Astrophysics, 616, A39
Maxted P. F. L., Serenelli A. M., Southworth J., 2015, A&A, 575, A36
Maxted P. F. L., et al., 2016, Astronomy and Astrophysics, 591, A55
Mayor M., Queloz D., 1995, Nature, 378, 355
Mayor M., et al., 2003, The Messenger, 114, 20
Mayor M., et al., 2011, arXiv e-prints, 1109, arXiv:1109.2497
Mazeh T., Perets H. B., McQuillan A., Goldstein E. S., 2015, The Astrophysical Journal, 801, 3
McLaughlin D. B., 1924, The Astrophysical Journal, 60, 22
McQuillan A., Mazeh T., Aigrain S., 2014, The Astrophysical Journal Supplement Series, 211, 24
Močnik T., Hellier C., Anderson D. R., Clark B. J. M., Southworth J., 2017, Monthly Notices of the Royal Astronomical Society, 469, 1622
Montet B. T., et al., 2020, The Astronomical Journal, 159, 112
Moré J. J., 1978, in Watson G. A., ed., Numerical Analysis. Lecture Notes in Mathematics. Springer, Berlin, Heidelberg, pp 105–116, doi:10.1007/BFb0067700
Munari U., Zwitter T., 1997, Astronomy and Astrophysics, 318, 269
Muñoz D. J., Perets H. B., 2018, The Astronomical Journal, 156, 253
Murchikova L., Tremaine S., 2020, The Astronomical Journal, 160, 160
Murray C. D., Correia A. C. M., 2010, Keplerian Orbits and Dynamics of Exoplanets. Exoplanets, University of Arizona Press, pp 15–23
Nagasawa M., Ida S., Bessho T., 2008, The Astrophysical Journal, 678, 498
Naoz S., Farr W. M., Lithwick Y., Rasio F. A., Teyssandier J., 2011a, Nature, 473, 187
Naoz S., Farr W. M., Lithwick Y., Rasio F. A., Teyssandier J., 2011b, Nature, 473, 187
Nelson B. E., Ford E. B., Rasio F. A., 2017, The Astronomical Journal, 154, 106
Newton E. R., et al., 2019, The Astrophysical Journal, 880, L17
Newton E. R., et al., 2021, The Astronomical Journal, 161, 65
Obermeier C., et al., 2016, The Astronomical Journal, 152, 223
Ogilvie G. I., 2014, Annual Review of Astronomy and Astrophysics, 52, 171
Ohta Y., Taruya A., Suto Y., 2005, The Astrophysical Journal, 622, 1118
Orosz J. A., et al., 2012, Science, 337, 1511

Osborn A., Bayliss D., 2020, Monthly Notices of the Royal Astronomical Society, 491, 4481

Paardekooper S.-J., Leinhardt Z. M., Thébault P., Baruteau C., 2012, The Astrophysical Journal Letters, 754, L16

Palle E., et al., 2020, Astronomy and Astrophysics, 643, A25

Parviainen H., Aigrain S., 2015, Monthly Notices of the Royal Astronomical Society, 453, 3821

Penev K., Bouma L. G., Winn J. N., Hartman J. D., 2018, The Astronomical Journal, 155, 165

Pepe F., et al., 2020, arXiv e-prints, 2010, arXiv:2010.00316

Pepper J., et al., 2007, Publications of the Astronomical Society of the Pacific, 119, 923

Pepper J., et al., 2017, The Astronomical Journal, 153, 177

Perryman M., 2011, The Exoplanet Handbook. Cambridge University Press

Petersburg R. R., et al., 2020, The Astronomical Journal, 159, 187

Petigura E. A., et al., 2018, The Astronomical Journal, 155, 89

Petrovich C., Deibert E., Wu Y., 2019, The Astronomical Journal, 157, 180

Piaulet C., et al., 2021, The Astronomical Journal, 161, 70

Plavchan P., et al., 2020, Nature, 582, 497

Pollacco D. L., et al., 2006, PASP, 118, 1407

Pollack J. B., Hubickyj O., Bodenheimer P., Lissauer J. J., Podolak M., Greenzweig Y., 1996, Icarus, 124, 62

Queloz D., et al., 2000a, Astronomy and Astrophysics, 354, 99

Queloz D., Eggenberger A., Mayor M., Perrier C., Beuzit J. L., Naef D., Sivan J. P., Udry S., 2000b, Astronomy and Astrophysics, 359, L13

Quirrenbach A., et al., 2016, Proceedings of the SPIE, 9908, 990812

Quirrenbach A., et al., 2018, Proceedings of the SPIE, 10702, 107020W

Rajpaul V., Aigrain S., Osborne M. A., Reece S., Roberts S., 2015, Monthly Notices of the Royal Astronomical Society, 452, 2269

Rajpaul V. M., et al., 2021, Monthly Notices of the Royal Astronomical Society, 507, 1847

Rasio F. A., Ford E. B., 1996, Science, 274, 954

Rasmussen C. E., Williams C. K. I., 2006, Gaussian Processes for Machine Learning. Cambridge University Press

Raymond S. N., Kokubo E., Morbidelli A., Morishima R., Walsh K. J., 2014, Protostars and Planets VI, p. 595

Raymond S. N., Boulet T., Izidoro A., Esteves L., Bitsch B., 2018, Monthly Notices of the Royal Astronomical Society, 479, L81

Ricker G. R., et al., 2015, Journal of Astronomical Telescopes, Instruments, and Systems, 1, 014003

Rizzuto A. C., Vanderburg A., Mann A. W., Kraus A. L., Dressing C. D., Agüeros M. A., Douglas S. T., Krolikowski D. M., 2018, The Astronomical Journal, 156, 195

Roberge A., Kamp I., 2010, Protoplanetary and Debris Disks. The University of Arizona Press

Roberts S., Osborne M., Ebden M., Reece S., Gibson N., Aigrain S., 2013, Philosophical Transactions

of the Royal Society A: Mathematical, Physical and Engineering Sciences, 371, 20110550
Rossiter R. A., 1924, The Astrophysical Journal, 60, 15
Roy A., Chakraborty A., Mahadevan S., Chaturvedi P., Prasad N. J. S. S. V., Shah V., Pathan F. M., Anandarao B. G., 2016, Proceedings of the SPIE, 9908, 99086R
Rubenzahl R. A., et al., 2021, The Astronomical Journal, 161, 119
Sahlmann J., et al., 2011, A&A, 525, A95
Salvatier J., Wiecki T. V., Fonnesbeck C., 2016, PeerJ Computer Science, 2, e55
Sanchis-Ojeda R., Winn J. N., 2011, The Astrophysical Journal, 743, 61
Sanchis-Ojeda R., Winn J. N., Holman M. J., Carter J. A., Osip D. J., Fuentes C. I., 2011, The Astrophysical Journal, 733, 127
Sanchis-Ojeda R., et al., 2012, Nature, 487, 449
Sanchis-Ojeda R., et al., 2013, The Astrophysical Journal, 775, 54
Santerne A., et al., 2016, Astronomy and Astrophysics, 587, A64
Santos N. C., Israelian G., Mayor M., 2004, Astronomy and Astrophysics, 415, 1153
Schlaufman K. C., 2010, The Astrophysical Journal, 719, 602
Schwarz G., 1978a, Annals of Statistics, 6, 461
Schwarz G., 1978b, The Annals of Statistics, 6, 461
Seidel J. V., et al., 2020, Astronomy and Astrophysics, 641, L7
Shallue C. J., Vanderburg A., 2018, The Astronomical Journal, 155, 94
Smith A. M. S., et al., 2014, Astronomy and Astrophysics, 570, A64
Smith A. M. S., Eigmüller P., Oshagh M., Southworth J., 2020, Research Notes of the American Astronomical Society, 4, 23
Snellen I. A. G., de Kok R. J., de Mooij E. J. W., Albrecht S., 2010, Nature, 465, 1049
Souami D., Souchay J., 2012, Astronomy and Astrophysics, 543, A133
Southworth J., 2013, Astronomy and Astrophysics, 557, A119
Southworth J., Wheatley P. J., Sams G., 2007, Monthly Notices of the Royal Astronomical Society, 379, L11
Southworth J., Bohn A. J., Kenworthy M. A., Ginski C., Mancini L., 2020, Astronomy and Astrophysics, 635, A74
Spake J. J., et al., 2018, Nature, 557, 68
Speagle J. S., 2020, Monthly Notices of the Royal Astronomical Society, 493, 3132
Stassun K. G., Mathieu R. D., Valenti J. A., 2006, Nature, 440, 311
Stassun K. G., et al., 2018, The Astronomical Journal, 156, 102
Stevens D. J., Gaudi B. S., Stassun K. G., 2018, The Astrophysical Journal, 862, 53
Stevenson K. B., et al., 2012, The Astrophysical Journal, 754, 136
Suárez Mascareño A., et al., 2020, arXiv e-prints, 2005, arXiv:2005.12114
Swayne M. I., Maxted P. F. L., Hodžić V. K., Triaud A. H. M. J., 2020, Monthly Notices of the Royal Astronomical Society, 498, L15

Terquem C., 2013, Monthly Notices of the Royal Astronomical Society, 435, 798

Terquem C., Ajmia A., 2010, Monthly Notices of the Royal Astronomical Society, 404, 409

Tofflemire B. M., et al., 2021, arXiv e-prints, 2102, arXiv:2102.06066

Tokovinin A., Moe M., 2020, Monthly Notices of the Royal Astronomical Society, 491, 5158

Torres G., Andersen J., Giménez A., 2010, Astronomy and Astrophysics Review, 18, 67

Triaud A. H. M. J., 2018, Handbook of Exoplanets, p. 2

Triaud A. H. M. J., et al., 2009, Astronomy and Astrophysics, 506, 377

Triaud A. H. M. J., et al., 2010, Astronomy and Astrophysics, 524, A25

Triaud A. H. M. J., et al., 2013, A&A, 549, A18

Triaud A. H. M. J., et al., 2017, MNRAS, 467, 1714

Triaud A. H. M. J., et al., 2020, Nature Astronomy, pp 1–8

Valenti J. A., Fischer D. A., 2005, The Astrophysical Journal Supplement Series, 159, 141

Van Eylen V., Albrecht S., 2015, The Astrophysical Journal, 808, 126

Van Eylen V., et al., 2014, The Astrophysical Journal, 782, 14

Van Eylen V., Agentoft C., Lundkvist M. S., Kjeldsen H., Owen J. E., Fulton B. J., Petigura E., Snellen I., 2018, Monthly Notices of the Royal Astronomical Society, 479, 4786

Van Eylen V., et al., 2019, The Astronomical Journal, 157, 61

Van Grootel V., et al., 2018, The Astrophysical Journal, 853, 30

Vida K., Kővári Z., Pál A., Oláh K., Kriskovics L., 2017, The Astrophysical Journal, 841, 124

Virtanen P., et al., 2020, Nature Methods, 17, 261

Wang L., Dai F., 2020, arXiv e-prints, 2101, arXiv:2101.00045

Ward W. R., 1997, Icarus, 126, 261

Weiss L. M., Petigura E. A., 2020, The Astrophysical Journal Letters, 893, L1

Weiss L. M., et al., 2018, The Astronomical Journal, 155, 48

Williams K. A., Bolte M., Koester D., 2009, The Astrophysical Journal, 693, 355

Winn J. N., 2010, Exoplanet Transits and Occultations. Exoplanets, University of Arizona Press, pp 55–77

Winn J. N., Fabrycky D. C., 2015, Annual Review of Astronomy and Astrophysics, 53, 409

Winn J. N., et al., 2005, The Astrophysical Journal, 631, 1215

Winn J. N., et al., 2009a, The Astrophysical Journal, 700, 302

Winn J. N., Johnson J. A., Albrecht S., Howard A. W., Marcy G. W., Crossfield I. J., Holman M. J., 2009b, The Astrophysical Journal, 703, L99

Winn J. N., Fabrycky D., Albrecht S., Johnson J. A., 2010a, The Astrophysical Journal, 718, L145

Winn J. N., et al., 2010b, The Astrophysical Journal, 723, L223

Winn J. N., et al., 2011, The Astrophysical Journal, 737, L18

Winn J. N., et al., 2017, The Astronomical Journal, 154, 270

Wirth C. P., et al., 2021, The Astrophysical Journal, 917, L34

Wittenmyer R. A., et al., 2020, Monthly Notices of the Royal Astronomical Society, 492, 377

Wolszczan A., 1994, Science, 264, 538

Wolszczan A., Frail D. A., 1992, Nature, 355, 145

Wright J. T., Marcy G. W., Howard A. W., Johnson J. A., Morton T. D., Fischer D. A., 2012, The Astrophysical Journal, 753, 160

Wu Y., Lithwick Y., 2011, The Astrophysical Journal, 735, 109

Wu Y., Murray N., 2003, The Astrophysical Journal, 589, 605

Xuan J. W., Wyatt M. C., 2020, Monthly Notices of the Royal Astronomical Society

Zahn J.-P., 1975, Astronomy and Astrophysics, 41, 329

Zahn J.-P., 1977, Astronomy and Astrophysics, 57, 383

Žák J., Kabáth P., Boffin H. M. J., Ivanov V. D., Skarka M., 2019, The Astronomical Journal, 158, 120

Zanazzi J. J., Lai D., 2018, Monthly Notices of the Royal Astronomical Society, 478, 835

Zhou G., et al., 2020, The Astrophysical Journal Letters, 892, L21

Zhu W., 2020, The Astronomical Journal, 159, 188

Zucker S., Mazeh T., 1994, The Astrophysical Journal, 420, 806

de Kort J. J. M. A., 1954, Ricerche Astronomiche, 3, 109

dos Santos L. A., et al., 2021, Astronomy & Astrophysics, Volume 649, id.A40, $<$NUMPAGES$>$10$<$/NUMPAGES$>$ pp., 649, A40

von Boetticher A., et al., 2017, Astronomy and Astrophysics, 604, L6

von Boetticher A., et al., 2019, Astronomy and Astrophysics, 625, A150